TECHNISCHE UNIVERSITÄT DARMSTADT

Investigations of phase transitions in magnetic materials by magnetic-field- and temperature-dependent x-ray diffraction

Untersuchungen von Phasenübergängen in magnetischen Materialien durch magnetfeld- und temperaturabhängige Röntgenbeugung

Zur Erlangung des Grades eines Doktors der Naturwissenschaften (Dr. rer. nat)
Genehmigte Dissertation im Fachbereich Material- und Geowissenschaften von Tom Faske aus Löbau

Tag der Einreichung: 16.11.2022, Tag der Prüfung: 27.01.2023
Darmstadt 2023

1. Gutachten: Prof. Dr. Wolfgang Donner
2. Gutachten: Prof. i.R. Dr. Mehmet Acet

Investigations of phase transitions in magnetic materials by magnetic-field- and temperature-dependent x-ray diffraction

Untersuchungen von Phasenübergängen in magnetischen Materialien durch magnetfeld- und temperaturabhängige Röntgenbeugung

Genehmigte kumulative Dissertation von M.Sc. Tom Faske

1. Gutachten:	Prof. Dr. Wolfgang Donner
2. Gutachten:	Prof. i.R. Dr. Mehmet Acet

Tag der Einreichung:	16.11.2022
Tag der Prüfung:	27.01.2023

Darmstadt – D 17

Erklärungen laut Promotionsordnung

§8 Abs. 1 lit. c PromO

Ich versichere hiermit, dass die elektronische Version meiner Dissertation mit der schriftlichen Version übereinstimmt.

§8 Abs. 1 lit. d PromO

Ich versichere hiermit, dass zu einem vorherigen Zeitpunkt noch keine Promotion versucht wurde. In diesem Fall sind nähere Angaben über Zeitpunkt, Hochschule, Dissertationsthema und Ergebnis dieses Versuchs mitzuteilen.

§9 Abs. 1 PromO

Ich versichere hiermit, dass die vorliegende Dissertation selbstständig und nur unter Verwendung der angegebenen Quellen verfasst wurde.

§9 Abs. 2 PromO

Die Arbeit hat bisher noch nicht zu Prüfungszwecken gedient.

Darmstadt, 16.11.2022

_____

T. Faske

Zusammenfassung

Gegenstand dieser Doktorarbeit ist der Aufbau eines laborbasierten Röntgendiffraktometers mit Magnet und einer Probenumgebung für Untersuchungen magnetischer Materialien in einem breiten Temperaturbereich. Der Fokus liegt dabei im Besonderen auf der Vielseitigkeit und zugänglichen Nutzbarkeit des Instruments. Das Röntgendiffraktometer stellt dabei ein wichtiges Analysetool für die Bestimmung der kristallographischen Struktur und Gitterparameter der Einheitszelle dar, und ermöglicht die Bestimmung davon abgeleiteter Größen, wie Dehnung und thermischer Ausdehnung als Funktion von Temperatur und Magnetfeld. Unter bestimmten äußeren Bedingungen, die in diesem Diffraktometer erzeugt werden können, durchlaufen einige Materialien eine strukturelle oder magnetische Phasenumwandlung. Diese Phasenumwandlungen und ihre Auswirkungen auf die kristallographischen Strukturparameter, können *in situ* in diesem Diffraktometer untersucht werden. Fallbeispiele für magnetoelastische und magnetostrukturelle Phasenübergänge im weiten Temperaturbereich zwischen 25 K und 600 K und unter verschiedenen magnetischen Feldern zeugen von der Leistung und den Möglichkeiten des Diffraktometers.

Das fertiggestellte Röntgendiffraktometer ist mit einem 5.5 T starken Magneten und einem Kryoofen für Messungen in einem Temperaturbereich zwischen 11–700 K ausgestattet. Durch das Messen in Transmissionsgeometrie sind die relativen Reflexintensitäten zuverlässig, sodass eine Bestimmung und Verfeinerung von Strukturparametern, und sogar das Lösen von Kristallstrukturen aus den Beugungsdaten möglich ist. Der schnelle ortsempfindliche Silizium-Streifendetektor deckt einen großen Winkelbereich ab, was schnelle Messungen ermöglicht. Die Energieauflösung kann bei Bedarf durch einen Austausch der Röntgenspiegeloptik gegen einen Monochromatorkristall auf Kosten des Photonenflusses vergrößert werden. Zudem sind alle Hardwarekomponenten über die Kontrollsoftware ansteuerbar, sodass der Betrieb des Diffraktometers mithilfe von Makros für Messreihen unter frei wählbaren Bedingungen automatisiert werden kann.

In den ersten Fallstudien werden mit MnB, FeB und $LaFe_{11.4}Si_{1.6}$ Verbindungen mit magnetoelastischen Phasenübergängen untersucht. Diese Verbindungen durchlaufen keine strukturellen Phasenumwandlungen während der magnetischen Ordnung, weisen aber große elastische Verzerrungen auf. Synchrotron- und Neutronenstreuexperimente ergänzen die Charakterisierung mithilfe des laborbasierten Diffraktometers mit Magnet und zeigen auf, dass es sich um Phasenumwandlungen erster Ordnung handelt. Spinfluktuationen sind die gemeinsame Triebkraft hinter den Magnetovolumeneffekten und Anomalien während der Phasenübergänge von MnB, FeB und $LaFe_{11.4}Si_{1.6}$. Obwohl alle beobachteten Effekte auf Spinfluktuationen beruhen, sind die eigentlich dahintersteckenden Phänomene unterschiedlich, was an entsprechender Stelle erläutert wird.

Die zweite Gruppe an Fallbeispielen handelt von der Familie der $(La,Ce)Fe_{12}B_6$-Verbindungen. Sie durchlaufen bei niedrigen Temperaturen einen magnetfeldinduzierten Phasenübergang, gekoppelt mit einer riesigen Magnetostriktion. Der Ursprung der anisotropen Ausdehnung liegt in der magnetfeldinduzierten Umwandlung in eine neue ferromagnetische Struktur. Aus den magnetfeldabhängigen Röntgenbeugungsdaten kann die Struktur gelöst und ein Modell für den Umwandlungsmechanismus als martensitartige Umwandlung aufgestellt werden. Das Modell erklärt außerdem das schubweise Wachstum der ferromagnetischen Phase in der Matrix der sie umgebenden Körner. Der dadurch entstehende Kinetic Arrest der ferromagnetischen Phase führt zu einer Verzögerung und damit verbundenen Hysterese der Phasenumwandlung.

Abstract

The subject of this doctoral work is the assembly of a laboratory-based x-ray diffractometer with magnet and non-ambient sample temperature environment for investigations of magnetic materials. A special focus is on the versatility and accessibility of the instrument. The x-ray diffractometer serves as important analysis tool for the determination of the crystallographic unit cell and derived parameters like strain or expansion as function of the temperature and magnetic field. Some materials undergo structural or magnetic phase transformations under specific conditions, which can be induced within the x-ray diffractometer. These phase transformations, and their effect on crystallographic parameters of the investigated materials can be followed *in situ* in the instrument. Several case studies of investigations of magnetoelastic and magnetostructural phase transitions at temperatures between 25 to 600 K under various magnetic fields highlight the performance and capabilities of the instrument.

The final x-ray diffractometer setup is equipped with a 5.5 T magnet and cryofurnace for non-ambient measurements in the range between 11–700 K. Measurements in transmission geometry result in reliable reflection intensities that allow for the refinement of structural parameters, and even structure solution from the diffraction data. The fast position-sensitive Si strip detector has a large angular coverage, and allows for quick data collections. High resolution data can be collected with the use of a monochromator crystal at the expense of photon flux instead of the high flux x-ray mirror optics. Integration of all diffractometer components into the control software enables the use of macros for automated data collection for a series of different measurement conditions.

The first set of case studies is related to materials with a magnetoelastic phase transition, MnB, FeB and $LaFe_{11.4}Si_{1.6}$, which exhibit no structural change over the course of the magnetic ordering, but a large elastic response. Synchrotron and neutron scattering studies complement the characterization with the lab-based diffractometer with magnet, and reveal the first-order character of the phase transition. Spin fluctuations are the connecting driving force behind the magnetovolume effects and anomalies over the course of the phase transition in MnB, FeB and $LaFe_{11.4}Si_{1.6}$. The term spin fluctuations, however, describes different phenomena in the investigated materials and is clarified accordingly.

The second set of case studies is related to the $(La,Ce)Fe_{12}B_6$ class of materials. They undergo a magnetic-field-induced phase transition at low temperatures that is coupled with a huge magnetostriction. The origin behind this anisotropic expansion over the course of the phase transition is determined as magnetic-field-induced magnetostructural phase transition into a new ferromagnetic structure. The structure is determined from the x-ray diffraction data collected in magnetic fields. A model for the transformation mechanism in the form of a martensitic-like phase transition is proposed. The model also explains the burst-like growth of ferromagnetic phase in the matrix of surrounding grain boundaries. A kinetic arrest of the ferromagnetic structure occurs, and results in a delay and large hysteresis of the magnetostructural phase transition.

Acknowledgements

First and foremost, I thank **Prof. Dr. Wolfgang Donner** for supervising me during my Ph.D. time, and for giving me the opportunity to join the Structure Research group. His constant support and the many valuable discussions we had over the years are not a given, and highly appreciated. Without his patience I would not have been able to finish this thesis.

Furthermore, I would like to express my gratitude to **Prof. i.R. Dr. Mehmet Acet** for agreeing to co-referee this work. I would also like to thank **Prof. Dr. Lambert Alff** and **Prof. Dr. Oliver Clemens** for accepting to being members of the examination committee.

I thank the entire Structure Research group for their support, company and many great activities over the years. Special thanks go to **Jean-Christophe Jaud** and **Heinz Mohren** for their technical assistance in all technical and diffractometer aspects. I thank my colleagues **Dr. Constantin Wansorra**, **Dr. Florian Pforr**, **Marcel Urban**, **David Koch, Leif Carstensen** and **Marco Léal** for all the fruitful, but also fun, discussions, and activities in and outside of the institute. I also thank **Elisabeth Albrecht** for her great work during her master's thesis. **Sabine Foro**, **Maria Bense**, **Claudia Fasel**, **Ingrid Swoboda** and **Antje Pappenhagen** I thank for the lovely coffee meetings that became a staple of every morning for many years, as well as **Ulrike Kunz** and **Dr. Stefan Lauterbach** for the "after lunch coffee".

I also thank the former members of the "Großraumbüro" and ATFT group for the great company, fun activities, but also scientific discussions that went well beyond my own research topic. Especially, **Dr. Philipp Kehne**, **Dr. Márton Major**, **Nico Kaiser**, **Tobias Vogel**, **Corinna Müller**, **Benjamin Krah**, **Eszter Piros**, **Dr. Juliette Cardoletti** and **Dr. Peter Swekis**.

Special thanks go to the mechanical and electronical workshop, who were the backbone of the many small projects that in the end became the complete x-ray diffractometer.

Andreas Hönl and **Stefan Diefenbach** I thank for the IT support, and saving my failing computers more than once.

Apart from the Structure Research group, I would like to extend my gratitude to all the colleagues I collaborated with over the years at the Materials and Earth Sciences department, especially from the LOEWE RESPONSE project. A huge thanks to **Dr. Léopold Diop** for teaching me about magnetism, and for the many collaborations and fruitful discussions we had over the years at the Laue camera. **Dr. Iliya Radulov** I thank for the magnetization measurements and many discussions. **Dr. Bahar Fayyazi** I thank for the great crystals from the Fe-Sn series with their beautiful structures and our collaborations. **Dr. Michael Duerrschnabel** and **Prof. Dr. Leopoldo Molina-Luna** I thank for the TEM analyses and collaborations on Fe-Sn.

Many fruitful collaborations came from the Functional Materials group, so I thank all of the colleagues I worked with: **Dr. Lukas Pfeuffer**, **Dr. Andreas Taubel**, **Dr. Konstantin Skokov**, **Dr. Fernando Maccari**, **Dr. Maximilian Fries**, **Dr. Simon Sawatzki**, and **Prof. Dr. Oliver Gutfleisch** as head of the group.

I am also grateful for the international collaborations and great joint publications with my colleagues **Dr. Joshua Bocarsly** from UC Santa Barbara, **Dr. Narendirakumar Narayanan** from the Australian National University, **Dr. Johann Cedervall** from Uppsala University and **Prof. Dr. Sergey Taskaev** from Chelyabinsk State University, proving that science does not know borders.

I am thankful for the financial support of my work by the LOEWE projects RESPONSE and FLAME, and thank the DFG for equipment grant No. INST 163/442-1 FUGG.

Finally, I want to thank all my **family** and **friends** who supported me during this time. Last but not least, my deepest gratitude goes to **Jana** for her support and care over the past years.

Statement of personal contribution

The statements of contribution of this cumulative dissertation are based on the definitions used in the Contributor Roles Taxonomy (CRediT), as given in Table 0.1. They are provided for all authors of the five selected publications.

Publication A (1):

T. Faske, W. Donner, «X-ray diffractometer for the investigation of temperature- and magnetic field-induced structural phase transitions», *Journal of Applied Crystallography* **51**, 761 (2018), DOI: https://doi.org/10.1107/S1600576718004892.

T. Faske: Project administration, Conceptualization, Resources, Methodology, Investigation, Formal analysis, Writing - Original Draft, Writing - Review & Editing; **W. Donner**: Project administration, Supervision, Resources, Funding acquisition, Writing - Review & Editing.

Publication B (2):

T. Faske, I. A. Radulov, M. Hölzel, O. Gutfleisch, W. Donner, «Direct observation of paramagnetic spin fluctuations in LaFe13−xSix», *Journal of Physics: Condensed Matter* **32**, 115802 (2020), DOI: https://doi.org/10.1088/1361-648X/ab5a99.

T. Faske: Project administration, Conceptualization, Resources, Methodology, Investigation, Formal analysis, Writing - Original Draft, Writing - Review & Editing; **I. A. Radulov**: Resources, Investigation, Writing - Review & Editing; **M. Hölzel**: Resources, Investigation, Writing - Review & Editing; **O. Gutfleisch**: Funding acquisition, Writing - Review & Editing; **W. Donner**: Project administration, Supervision, Resources, Funding acquisition, Writing - Review & Editing.

Publication C (3):

J. D. Bocarsly, E. E. Levin, S. A. Humphrey, **T. Faske**, W. Donner, S. D. Wilson, R. Seshadri, «Magnetostructural Coupling Drives Magnetocaloric Behavior: The Case of MnB versus FeB», *Chemistry of Materials* **31**, 4873 (2019), DOI: 10.1021/acs.chemmater.9b01476.

J. D. Bocarsly: Conceptualization, Methodology, Resources, Investigation, Formal analysis, Project administration, Writing - Original Draft, Writing - Review & Editing; **E. E. Levin**: Investigation, Writing – Review & Editing; **S. A. Humphrey**: Investigation, Writing – Review & Editing; **T. Faske**: Resources, Methodology, Investigation, Formal analysis, Writing - Review & Editing; **W. Donner**: Resources, Writing - Review & Editing; **S. D. Wilson**: Conceptualization, Supervision, Writing – Review & Editing; **R. Seshadri**: Conceptualization, Supervision, Resources, Funding acquisition, Writing – Review & Editing.

Publication D (4):

L.V.B. Diop, **T. Faske**, M. Amara, D. Koch, O. Isnard, W. Donner, «Evidence for a coupled magnetic-crystallographic transition in La0.9Ce0.1Fe12B6», *Physical Review B* **104**, 134412 (2021), DOI: https://doi.org/10.1103/PhysRevB.104.134412.

L.V.B. Diop: Conceptualization, Methodology, Resources, Investigation, Formal analysis, Project administration, Writing - Original Draft preparation, Supervision, Writing - Review & Editing; **T. Faske**: Methodology, Investigation, Formal analysis, Writing - Review & Editing; **M. Amara**: Methodology, Investigation, Writing - Review & Editing; **D. Koch**: Investigation,

Writing - Review & Editing; **O. Isnard**: Investigation, Writing - Review & Editing; **W. Donner**: Supervision, Writing - Review & Editing.

Publication E (5):

L.V.B. Diop, **T. Faske**, O. Isnard, W. Donner, «Magnetic-field-induced structural phase transition and giant magnetoresistance in La0.85Ce0.15Fe12B6», *Physical Review Materials* **5**, 104401 (2021), DOI: https://doi.org/10.1103/PhysRevMaterials.5.104401.

L.V.B. Diop: Conceptualization, Methodology, Resources, Investigation, Formal analysis, Project administration, Writing - Original Draft preparation, Supervision, Writing - Review & Editing; **T. Faske**: Methodology, Investigation, Formal analysis, Writing - Review & Editing; **O. Isnard**: Investigation, Writing - Review & Editing; **W. Donner**: Supervision, Writing - Review & Editing.

Table 0.1: Nomenclature of Contributor Roles Taxonomy (CRediT) (6).

Term	Definition
Conceptualization	Ideas, formulation or evolution of overarching research goals and aims
Methodology	Development or design of methodology; creation of models
Formal analysis	Application of statistical, mathematical, computational, or other formal techniques to analyze or synthesize study data
Investigation	Conducting a research and investigation process, specifically performing the experiments, or data collection
Resources	Provision of study materials, reagents, materials, patients, laboratory samples, animals, instrumentation, computing resources, or other analysis tools
Writing – original draft	Preparation, creation and/or presentation of the published work, specifically writing the initial draft (including substantive translation)
Writing – review and editing	Preparation, creation and/or presentation of the published work by those from the original research group, specifically critical review, commentary or revision – including, pre- or post-publication stages
Visualization	Preparation, creation and/or presentation of the published work, specifically visualization/ data presentation
Supervision	Oversight and leadership responsibility for the research activity planning and execution including mentorship external to the core team
Project administration	Management and coordination responsibility for the research activity planning and execution
Funding acquisition	Acquisition of the financial support for the project leading to this publication

Nomenclature

Symbols

a, b, c	Crystallographic unit cell parameters
α, β, γ	Angles in crystallographic unit cells
α_L or α_t	Linear thermal expansion coefficient
α_V	Volumetric thermal expansion coefficient
B or B_{iso}	Debye-Waller factor
C	Curie constant
C_{edge}	Detector channel number closer to an edge
C_{center}	Center detector channel number
d_{min}	Smallest attainable lattice plane distance
E_{mag}–E_{nonmag}	Magnetic stabilization energy
$f_{mag}(Q)$	Magnetic form factor
λ	Wavelength
Θ_e	Detector encoder position
Θ_o	Angular offset with respect to the diffractometer zero position
θ_p	Paramagnetic Curie temperature
H	Magnetic field
I	Intensity
I_{Bragg}	Intensity of a Bragg reflection
I_{calc}	Calculated reflection intensity
I_{diff}	Intensity difference
I_{mag}	Magnetic contribution to reflection intensity
I_{nuc}	Nuclear contribution to reflection intensity
I_{obs}	Observed reflection intensity
k	Propagation vector
$\Delta L/L$	Critical magnetic-field-induced strain induced at the Curie temperature
M	Magnetization
M_0	Spontaneous magnetization
μ_{eff}	Paramagnetic effective moment
μ_B	Magnetic moment
ν_0	Spontaneous volume magnetostriction
ν_h	Forced volume magnetostriction
ξ	Spin fluctuation amplitude
ξ_{th}	Thermal spin fluctuation amplitude
ξ_{zp}	Zero-point spin fluctuation amplitude
Q	Momentum transfer
r	Rhodes-Wohlfarth ratio
R	Radius of the detection circle
R_{Bragg}	Residual factor from Rietveld refinement for the peak positions
R_{exp}	Expected residual factor from Rietveld refinement
R_f	Residual factor from Rietveld refinement for reflection profiles
R_{mag}	Residual factor from Rietveld refinement for the magnetic structure
R_{wp}	Weighted profile residual factor from Rietveld refinement
ρ	Magnetoresistance

$S^{\alpha,\beta}(Q,\omega)$	Magnetic scattering function
S_{el}	Electronic contribution to entropy
S_M	Magnetic contribution to entropy
S_p	Number of carriers in the disordered (paramagnetic) state
S_{tot}	Total entropy
S_0	Number of carriers in the ordered (ferromagnetic) state
Σ_M	Magnetic deformation
T	Temperature
T_C	Curie temperature
T_{comp}	Overcompensation temperature of thermal contraction
T_N	Néel temperature
T_t or T_{tr}	Transition temperature
V	Unit cell volume
W_{FM}	Weight fraction of ferromagnetic phase
W_{PM}	Weight fraction of paramagnetic phase
χ	Paramagnetic susceptibility
χ^2	Goodness of fit in Rietveld refinements
Z	Number of formula units per unit cell
ω	Energy transfer

Acronyms

ac	Alternating current
ACMS	Alternating current magnetic susceptibility
CRediT	Contributor Roles Taxonomy
CW	Curie-Weiss
DFT	Density functional theory
DLM	Disordered local moments
dc	Direct current
FCC	Field-cooled cooling
FM	Ferromagnetic
FWHM	Full width at half maximum
GME	Giant magnetocaloric effect
GOF	Goodness of fit
HT	High-temperature
iCOHP	Integrated crystal orbital Hamilton population
IEM	Itinerant-electron metamagnetic
JM	Joulian magnetostriction
LT	Low-temperature
MCE	Magnetocaloric effect
MR	Magnetoresistance
MU	Moriya-Usami
NJM	Non-Joulian magnetostriction
NTE	Negative thermal expansion
PM	Paramagnetic
PPMS	Physical property measurement system
QENS	Quasi-elastic neutron scattering
RT	Room temperature
SCR	Self-consistent renormalization
SEW	Stoner-Edwards-Wohlfarth
TEM	Transmission electron microscopy
VSM	Vibrating sample magnetometer
XRD	X-ray diffraction
ZFC	Zero-field cooling
ZFCW	Zero-field-cooled warming

Table of contents

1. Introduction

1.1. Motivation

Ever since their discovery in 1895 by Wilhelm Röntgen (7), x-rays have been an exciting tool to look at, through, and into materials, and (living) objects spanning many orders of magnitude in size. Numerous analysis techniques based on x-rays have been developed over the last century, but none has become as widespread and universally powerful as x-ray diffraction (XRD). The ability to investigate the periodic arrangements of atoms in a material of basically any shape and size is astounding. Material properties can be predicted from the crystal structure, and complete synthesis batches can be checked for yield and sample purity. Many further uses for XRD are well-established *e.g.*, qualitative and quantitative phase analysis, determining residual sample stress and strain, texture analysis, determining crystallite sizes, determining the amount and structure of amorphous phases, thin film analyses, *e.g.*, film thickness, surface roughness, interface roughness, and many more (8–13).

Research on magnetic materials is a hot topic in the scientific community, and applications are manifold, ranging from permanent magnet candidates (14–17), solid-state refrigeration using the magnetocaloric effect (MCE) (18–24), magnetic read-out units (25–28) to magnetostrictive actuators (29–32), to name just a few. Basic research, however, is equally important, and many materials exhibit exotic phenomena that are worth to be investigated and understood even with no immediate application in mind. It has been proven time and time again that even well-known materials can sometimes hold secrets that only surface many years, decades or sometimes centuries after their initial discovery. MgB_2 is a prime example for this, as its superconducting properties were only discovered in 2001 (33), whereas it was first synthesized and reported already in 1953 (34). Basic research is also important for validation of theories that can then be applied to more complex systems. Moriya and Takahashi's theory for spin fluctuations in itinerant-electron magnetic materials is an example for such a theory. It was first proposed in 1973 (35–37) and experimentally verified initially only for the basic MnSi system (38). Further verifications for some more complex structures in the form of Heusler alloys were published only recently (39, 40).

XRD can serve as complementary analysis tool for investigation of these magnetic materials. Determining the crystal structure is as important as following the progress of structural phase transitions in magnetocalorics (20–22, 41). Accurate determination of magnetostriction is also possible (42–45), and further structure-property relationships like microscopic strain, and completeness of transformation can be deduced (46–48). Ultimately, it is a tool to determine and judge the usefulness of a candidate material for a given application.

It can, furthermore, be useful to apply an external magnetic field during an XRD measurement, especially for inducing certain magnetic or magnetostructural phase transformations, or investigating the forced magnetostriction (49–56). This helps to better understand what happens during applications like solid-state refrigeration, where a material undergoes a phase transition by moving in an out of a magnetic field, or *vice versa* (57). Furthermore, it enables correlation between microscopic structural data of the sample with macroscopic measurements, like magnetization or bulk magnetostriction determined with a strain gauge.

While the existence of a diffractometer setup with magnet is more than justified by the sheer number of analysis use cases, such an instrument with non-ambient temperature capabilities and magnet is not available from commercial suppliers of x-ray diffractometers. Numerous challenges are imposed by the size of the magnet, and the large stray magnetic field in its vicinity. However, it is possible, and well-established to perform experiments under magnetic fields at large-scale facilities. Due to spacious beamline design, and large photon or neutron fluxes available, experiments are typically fast, and possible in large continuous (58–65) or pulsed magnetic fields (66–75). The issue with large-scale facilities, however, is limited access, both in actual "beam time" granted at the facility, as well as the rather scarce availability of measurement days over the course of a year. This results in only few, and well pre-characterized samples being analyzed, instead of being able to *e.g.*, screen different batches of syntheses and testing different sample and sample preparation types. While a few other custom-built lab-based XRD setups with magnet exist, they are scattered all over the world (76–79, 81), and none of them is located in Europe. Furthermore, their diffractometer technology oftentimes is not state-of-the-art and comes with various drawbacks. This leaves a clear gap for a modern x-ray diffractometer setup with magnet and non-ambient temperature capabilities covering a wide sample parameter space.

1.2. Objectives

At the beginning of this doctoral work, x-ray diffractometer systems with magnet and cryostat were rare and hardly accessible outside of major research facilities. Only five setups worldwide, none of them located in Europe, were reported in literature (76–79, 81). Hence, the primary focus of this work has been to develop a lab-based x-ray diffraction setup with magnet and non-ambient temperature capabilities for the investigation of magnetic-field- and temperature-induced structural phase transitions and concomitant magnetovolume effects. The objectives of the research performed within the framework of this dissertation are as follows:

- Development of an x-ray diffractometer with magnet and cryostat.
- Improvement of the accessibility of the diffractometer by remotely controlling all diffractometer components, to make the system readily available for other users and collaborations worldwide.
- Investigation of magnetovolume effects of materials undergoing magnetoelastic and magnetostructural phase transitions, *e.g.*, potential candidates for the use in magnetocaloric refrigeration.

1.3. Structure of this thesis

In this doctoral work, the development of a one-of-a-kind x-ray diffractometer with magnet and cryofurnace has been realized. The x-ray diffractometer has proven to be a crucial analysis tool for the determination of magnetostriction, and the investigation of temperature- and magnetic-field-dependent phase transitions of different material systems. The results were published in several articles, and, out of these, five publications were selected for this cumulative dissertation. Although the selected articles seem to be quite different at first glance, they are connected by the common theme, "magnetoelastic and magnetostructural phase transitions". The publications selected for this cumulative thesis are as follows:

Chapter 3.2: Publication A: X-ray diffractometer for the investigation of temperature- and magnetic field-induced structural phase transitions
T. Faske, W. Donner, Journal of Applied Crystallography **51**, 761 (2018).

Chapter 4.2: Publication B: Direct observation of paramagnetic spin fluctuations in $LaFe_{13-x}Si_x$
T. Faske, I. A. Radulov, M. Hölzel, O. Gutfleisch, W. Donner, Journal of Physics: Condensed Matter **32**, 115802 (2020).

Chapter 4.3: Publication C: Magnetostructural Coupling Drives Magnetocaloric Behavior: The Case of MnB versus FeB
J. D. Bocarsly, E. E. Levin, S. A. Humphrey, **T. Faske**, W. Donner, S. D. Wilson, and R. Seshadri, Chemistry of Materials 31, 4873 (2019).

Chapter 5.2: Publication D: Evidence for a coupled magnetic-crystallographic transition in $La_{0.9}Ce_{0.1}Fe_{12}B_6$
L.V.B. Diop, **T. Faske**, M. Amara, D. Koch, O. Isnard, and W. Donner, Physical Review B **104**, 134412 (2021).

Chapter 5.3: Publication E: Magnetic-field-induced structural phase transition and giant magnetoresistance in $La_{0.85}Ce_{0.15}Fe_{12}B_6$
L.V.B. Diop, **T. Faske**, O. Isnard, and W. Donner, Physical Review Materials **5**, 104401 (2021).

Publication A is the key publication that in detail describes the x-ray diffractometer with magnet that was assembled during this work, and served as valuable analysis tool for the other publications selected for this thesis. Publications B – E were selected as case studies that highlight the quality, capabilities, and importance of the x-ray diffractometer with magnet. The articles cover different material classes that undergo magnetostructural phase transitions under very different conditions, *e.g.*, at temperatures spanning from 25 K to as high as 600 K, and with or without an applied magnetic field.

The outline of this thesis is as follows:
Chapter 2 gives an overview of the state of research for the topics relevant for this work, lists challenges that are associated with assembly of an x-ray diffractometer setup with magnet, and compares existing lab-based instruments.

Chapter 3 is dedicated to the x-ray diffractometer with magnet assembled for this work. An extended synopsis containing also the important updates to the setup that were implemented since the release of Publication A, and a summary of the final diffractometer setup is followed by a reprint of the publication. This, and all other publications are adapted to the layout of this thesis to make it easier for the reader to follow.

Chapter 4 contains the first set of case studies performed with the diffractometer with magnet, that were published as Publications B and C. The research question at hand is the nature and driving force of the magnetoelastic phase transition in $LaFe_{13-x}Si_x$, MnB and FeB. Reprints of the publications are preceded by a synopsis.

Chapter 5 contains the second set of case studies about the magnetic-field induced structural phase transition and the transformation mechanism in the $La_{1-x}Ce_xFe_{12}B_6$ system, which were published in Publications D and E. A synopsis of the publications is followed by reprints.

Chapter 6, finally, presents the conclusions drawn from the x-ray diffractometer setup with magnet and investigated phase transitions, and shows a perspective for future research.

2. State of research

This chapter focuses on an overview of the current state of research on topics relevant for this work. In the first part, a general framework for magnetic phase transitions, and associated effects like hysteresis and magnetovolume effects is given, followed by an overview of the possibilities for investigations of phase transitions by XRD. In the second part, an overview of x-ray diffraction in magnetic fields together with experimental challenges imposed by the magnet attachment is shown. Some research groups already solved the issues associated with building a lab-based x-ray diffractometer with magnet. These setups, but also their limitations are presented, revealing the need for the state-of-the art instrument that was successfully assembled during this work.

2.1. Phase transitions in magnetic materials

Phase transitions are changes in a system that occur over a small range of a control variable, or order parameter, which in magnetic materials is usually the magnetization M (82). Transformations are classified according to the presence or absence of a discontinuity in the order parameter M, see Figure 2.1. A ferromagnetic (FM) material with first-order transition has a discontinuity of M at a certain transition temperature T_t, at which it transforms between a low-temperature phase with high magnetization, and a high-temperature phase with low magnetization (57). The magnetic material responds to an applied magnetic field H with a shift of T_t by stabilizing the phase with higher magnetization (83). The low-temperature phase would be stable up to its Curie Temperature T_C, see the extrapolation of M as green dashed line in Figure 2.1, but transforms to the high-temperature paramagnetic (PM) phase before, at $T_t < T_C$.

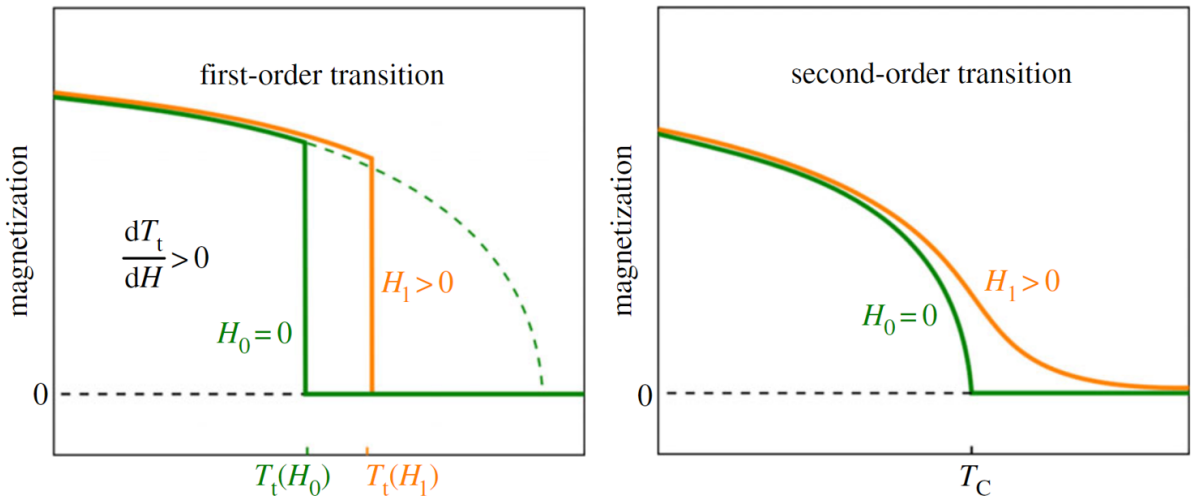

Figure 2.1: Schematic of the temperature dependence of the order parameter magnetization in a magnetic material with and without magnetic field for a first-order transition (left), and second-order transition (right). Adapted from (57).

In contrast to a first-order phase transition, a schematic of the magnetic behavior of a FM material with second-order transition is shown in Figure 2.1(right). There is no discontinuity

of M, instead the magnetization continuously decreases upon heating, and finally vanishes at T_C. Application of a magnetic field leads to a partial alignment of magnetic moments in the PM phase, which results in a small field-induced magnetization. The PM-FM transition in the element Gd is a classical example for such a second-order phase transition (84).

2.1.1. Magnetostructural phase transitions

First-order magnetostructural phase transitions are a special case of phase transitions observed in magnetic materials, as is shown in the classification of phase transitions in Figure 2.2. While magnetic ordering from the PM to FM state is a classical example for a continuous *i.e.*, second-order, transition, for some materials magnetic ordering is accompanied by a structural phase transition due to a strong coupling between magnetism and structure. This coupling of several degrees of freedom inevitably leads to a first-order character of the phase transition (85).

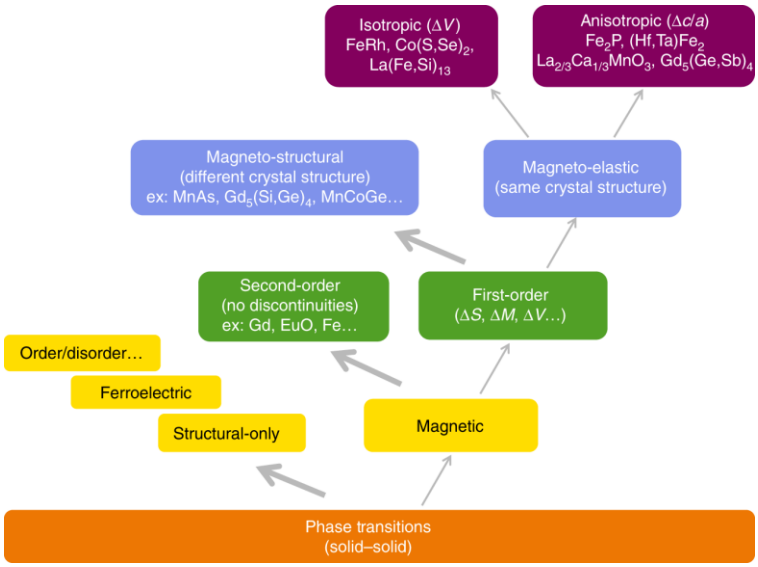

Figure 2.2: Classification of solid-state phase transitions. Several types of magnetic phase transitions are classified with special focus on the magnetoelasticity branch, where several sub-classes are distinguished (86).

Materials with magnetostructural phase transitions are of technological interest because of their responsiveness to at least three external stimuli, temperature, pressure and an applied magnetic field, that can be used to control the phase transition (87). Magnetostructural phase transitions were heavily investigated in recent years, and many examples exist in the literature. Of great interest are these materials for use in magnetic refrigeration using the MCE, which has the prospect of replacing conventional vapor-compression refrigerators due to, among other advantages, potentially higher efficiencies (88). Candidate materials for use in magnetic refrigeration, however, have to fulfill many requirements to be viable, and so, no definitive solution has so far been established (57). From the vast field of examples of materials undergoing magnetostructural phase transitions, the following families of compounds are among the most common: Heusler alloys, such as Ni-Mn-In-(Co), and Ni-Mn-Sn (20, 89–92), MnAs (93, 94), $Gd_5(Si,Ge)_4$ (95, 96), MnCoGe (97, 98), and $La_{1-x}Sr_xMnO_3$ (99).

2.1.2. Magnetoelastic phase transitions

Magnetoelastic phase transitions are first-order phase transitions without change in the crystal structure, but with large isotropic or anisotropic length changes during the metamagnetic transition. Interatomic distances, and as a result, the crystallographic unit cell dimensions change over the magnetic ordering temperature due to a strong coupling between structure and magnetism. Two sub-types of magnetoelastic transitions exist, as is shown in Figure 2.2.

The first type is a magnetoelastic phase transition with isotropic unit cell expansion or contraction. This type of distortion is special, as it only exists in materials with cubic symmetry. Since cubic materials only have a single unit cell parameter a, length changes are automatically coupled with an isotropic distortion. A length change along only one direction in cubic compounds would directly result in a symmetry reduction and, therefore, structural phase transition. Examples for isotropic magnetoelastic materials are FeRh (100–103), Mn_3GaC (104, 105), $LaFe_{13-x}Si_x$ (106), and $LaFe_{13-x}Si_x$-based alloys, such as $La(Fe,Co)_{13-x}Si_x$ (107, 108), and $La(Fe,Mn)_{13-x}Si_xH_y$ (109, 110).

The second type of magnetoelastic materials are those with anisotropic distortions during the phase transition. Such anisotropic distortions occur in all crystal classes of lower than cubic symmetry. A further subdivision between materials undergoing anisotropic unit cell distortions is possible, but not shown in Figure 2.2. For some materials, the anisotropic distortions during the metamagnetic transition are positive along one crystallographic direction and negative along another direction, resulting in a net conservation of unit cell volume, despite being strongly distorted. Such materials are compounds belonging to the Fe_2P-type family, *e.g.*, $(Mn,Fe)_2(P,As)$ (111), $(Mn,Fe)_2(P,Si,B)$ (112), or $(Mn,V,Fe)_2(P,Si,B)$ (23). Examples for materials with a net unit cell volume change coupled with their anisotropic magnetoelastic transition are $(Hf,Ta)Fe_2$ (113), the $La_{1-x}Ca_xMnO_3$ family of manganites (114), and $Gd_5(Ge,Sb)_4$ (115).

2.1.3. Hysteresis

An important aspect of a magnetic phase transition is the thermal hysteresis that occurs over the course of the transition. A hysteresis can be seen as an energy barrier due to latent heat that a material needs to overcome in order to transform from one state to another (85). Depending on the size of this energy barrier, this can lead to significant shifts in the transition temperature between cooling and heating cycles. A system undergoing a first-order coupled magnetostructural phase transition has to overcome a larger energy barrier for its transformation, and, therefore, such materials typically exhibit a large hysteresis (116). Examples being the Heusler alloys (20, 89–92), and the $Gd_5(Si,Ge)_4$ alloys (95, 96).

A smaller hysteresis is observed for materials undergoing a first-order magnetoelastic transition, like FeRh (100–103), $LaFe_{13-x}Si_x$ and derived alloys (107–110), or the Fe_2P-type family of compounds (23, 111, 112). These compounds have a first-order metamagnetic phase transition without change in their crystal structure, but with significant variations of the unit cell parameters between the PM and FM phases. The last type of materials, classified by the size of their hysteresis, are materials with a second-order transition. Such materials do, by definition, not show a hysteresis due to intrinsic effects. For these types of transitions, the total entropy change ΔS_{tot}, an important metric for the MCE, is smaller, as the transition is broad and not abrupt like first-order transitions. Examples are Gd and Gd-containing rare-earth alloys (84), and Sr-substituted manganites from the $La_{1-x}Ca_xMnO_3$ family (117).

The technological importance of a hysteresis lies in the use of a material in an application with frequent switching between both states. Such an application is *e.g.*, solid refrigeration, which relies on MCE. Here, a reversible transition within a small temperature and magnetic field range is needed, so, a hysteresis effectively results in a loss of efficiency for the MCE (57, 118, 119). Many individual factors influence the width of a materials' hysteresis, but they can be classified into two main groups, *intrinsic* and *extrinsic* factors, as shown in Figure 2.3 (57).

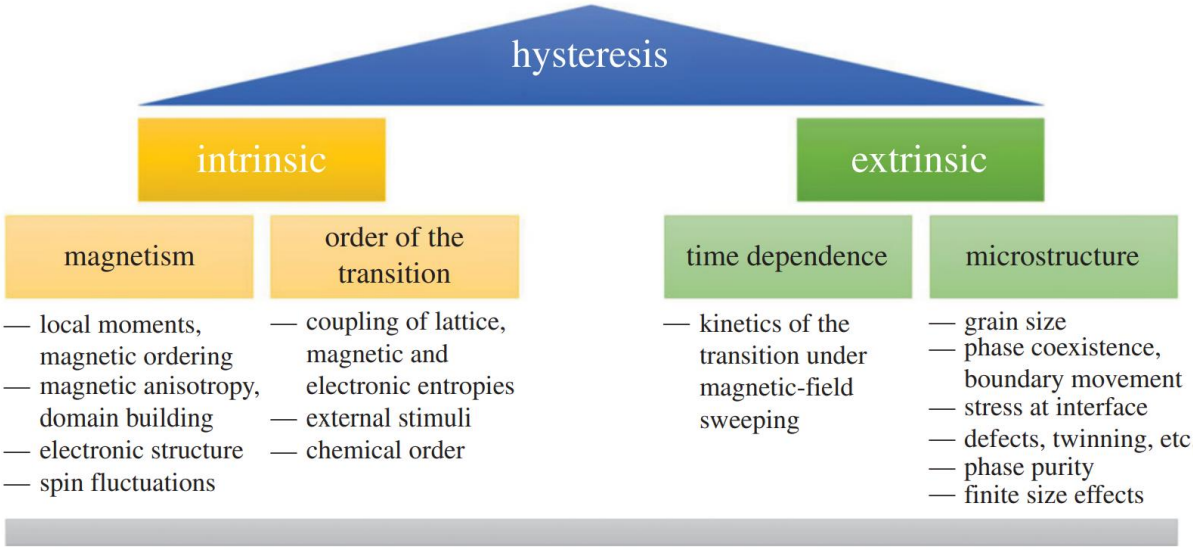

Figure 2.3: Intrinsic and extrinsic factor influencing the hysteresis of a magnetic phase transition (57).

Intrinsic factors that influence the width of a hysteresis are properties specific to a material. They are dependent on the chemical composition and crystal structure, which define other properties, like the electronic structure and magnetism, as well as the order of the phase transition. Extrinsic factors that influence the width of a hysteresis are related to the time dependence of the phase transition, and to a large extent the microstructure of the material. Extrinsic factors all act as a further broadening of an experimentally observed hysteresis of a 'real' material as compared to the intrinsic properties in an 'ideal' material (120). For an XRD experiment, the factors grain size, interfacial stress, and phase coexistence are of great importance, as the sample is prepared as powder, and a broadening of the hysteresis as observed from XRD is to be expected (121).

For application in solid-state refrigeration using the MCE, the goal is to engineer a material with large ΔS_{tot} at the transition, and as narrow as possible hysteresis, preferably by reaching a tricritical point (122, 123). A material at the tricritical point has no hysteresis, but the benefits of a large ΔS_{tot} of a first-order transition, maximizing the efficiency of the MCE. However, for application in solid-state cooling, not only the hysteresis has to be optimized. Several other requirements have to be fulfilled by a candidate material, be it economical, ecological, mechanical, and many more. Design of a material for solid-state refrigeration, therefore, requires large combined efforts (57). XRD, especially *in situ* XRD with magnetic field, can significantly contribute to these combined efforts. An experimental observation of the structural hysteresis of a material as function of T and H allows for a phase specific view on lattice parameters and phase fractions, which is invaluable information for a better understanding of the phase transformation mechanism.

2.1.4. Magnetovolume effects

Magnetovolume effects result from the interplay between magnetism and structure in crystals (124). Magnetic ordering in a material is accompanied by a volume change. This relative difference between unit cell volume with, and (hypothetically) without magnetic interactions, $\Delta V/V_0$, is also called spontaneous volume magnetostriction ν_0 (125).
Application of a magnetic field to a magnet causes a further anisotropic distortion, that *below* the magnetic saturation is known as Joule magnetostriction (JM) (126). A characteristic of JM is volume conservation, so, an elongation parallel to the magnetic field direction is always accompanied by a shrinkage in the transverse direction. This behavior is caused by magnetization reorientation, *i.e.*, self-accommodation of magnetic domains along the magnetic field direction (127).
Recently, a non-volume-conserving type of magnetostriction was discovered in single crystals of Fe-Ga, that was reported as non-Joulian magnetostriction (NJM) (127, 128). This NJM is caused by reorientation of magnetoelastically self-sufficient micro-cells within the crystal. These micro-cells are made up from nanometer-sized lamellar structures consisting of modulated martensite of the Fe-Ga crystal (129).
Above magnetic saturation, applied external magnetic fields induce an additional small volume change, the so-called forced volume magnetostriction $\nu_h(M, T_C)$.
Over the years, several models have been developed that describe the magnetovolume coupling. In the following, some models and their applications are presented.

2.1.5. Spin fluctuations in itinerant-electron systems

Predicting and explaining the magnetic properties of itinerant-electron magnets has been a topic of interest already for many decades (130, 131). A successful approach was the self-consistent renormalization (SCR) spin fluctuation theory of Moriya and Kawabata in the 1970s and 1980s (35, 132, 133). This theory was the first to include collective magnetic excitations *i.e.*, spin fluctuations, and their coupling, to successfully describe the temperature dependence of magnetic properties like the paramagnetic susceptibility χ, known as the Curie-Weiss law. While thermal spin fluctuations are included in the SCR theory of Moriya and Kawabata, zero-point fluctuations are generally neglected. A complete description of itinerant-electron systems with thermal and zero-point spin fluctuations was later realized by Takahashi (124, 134, 135). A key assumption of Takahashi's theory is the net conservation of the squared sum of the spin fluctuation amplitudes $\xi_{th}^2 + \xi_{zp}^2 = const.$ (124, 132), ξ_{th} being the thermal, and ξ_{zp} the zero-point spin fluctuation amplitude.
Magnetovolume effects in itinerant-electron system were initially also described without the implementation of spin fluctuations in the Stoner-Edwards-Wohlfarth (SEW) theory (136, 137). The magnetic ground-state is well described by the SEW theory, but, due to not considering thermal spin fluctuations, the magnetovolume behavior does not match experiments at higher temperatures, especially above T_C. Corrections to the SEW theory were implemented by Moriya and Usami (MU theory) (138) by including the influence of thermal spin fluctuations on ν_0, and their contribution to thermal expansion above T_C. Although a description of the magnetic contribution to the thermal expansion in the PM state is generally given by the MU theory, experiments also do not match the predicted magnetovolume behavior at higher temperatures. Takahashi's approach of including zero-point spin fluctuations further improved the spin fluctuation theory for itinerant-electron systems. The theory also implemented additional

temperature dependencies for the magnetovolume coupling constants, and now separates between spontaneous and forced magnetovolume coupling constants (139).
While Takahashi's theory was established already several decades ago, initially only the general assumption $\xi_{th}^2 + \xi_{zp}^2 = const.$ was confirmed for the MnSi system by Ziebeck *et al.* (38), and no direct confirmation for the theory was reported. Later publications mainly report on the indirect implications of spin fluctuations on the thermal expansion properties of itinerant-electron systems, without direct confirmation of Takahashi's theory. For example, Wada *et al.* have demonstrated that the presence of spin fluctuations acts as internal magnetic pressure that heavily alters the thermal expansion of the itinerant-electron magnetic materials $Y(Mn_{1-x}Al_x)_2$ and $Y_{1-x}Sc_xMn_2$ (140), but without direct connection to the spin fluctuation theory. According to Takahashi's theory, the magnetic pressure that spin fluctuations exert on itinerant-electron materials expresses itself in a M^4-dependence of $\Delta L/L$, the critical strain induced by an applied magnetic field at T_C (139).
More recently, the large impact of spin fluctuations on magnetoelastic phase transitions, without explicitly mentioning Takahashi's theory, was reported for several material classes, examples being rare-earth manganites (141, 142), the $(Mn,Fe)_2(P,Si)$ system (143, 144), and several Heusler alloys (145, 146).
Only very recently, Sakon *et al.* experimentally observed the M^4-dependence of the critical forced magnetostriction $\Delta L/L$ as predicted by Takahashi's theory for the Heusler alloys Ni_2MnGa with, and Ni_2MnIn, and Ni_2MnSn without martensitic phase transition (39, 40, 147). They determined the temperature-dependent magnetostriction under different magnetic fields with a strain gauge on bulk samples.
So far, no determination of forced magnetostriction by XRD for confirmation of Takahashi's theory is reported in literature. It is to be assumed that the lack of availability of x-ray diffractometers with magnet plays an important part in that. XRD on powders in a magnetic field, however, could be favorable to confirm Takahashi's theory for more material classes, since many itinerant-electron systems have large volume expansions during their metamagnetic transitions, that might result in pulverization of bulk samples.

2.1.6. Martensitic phase transitions and kinetic arrest

Martensitic phase transitions are a special type of diffusionless first-order phase transitions in which the structural transformation is realized through a rapid and cooperative shear-type displacement of atoms. Originally discovered in steels (148), the range of compound classes in which martensitic phase transformations were found extends from other ferrous alloys, to Heusler alloys, ceramics, and recently even molecular crystals (149).
Magnetovolume effects as large as ~10% in a moderate magnetic field of 1 T were observed for the martensitic phase transition in the magnetic Heusler alloy Ni_2MnGa (150). The large strain associated with the transition, and the fact that the martensitic transition can be manipulated by temperature, magnetic field, and applied pressure (151), make Ni_2MnGa a prime candidate for use as magnetic shape memory alloy (152, 153). Driving force for the martensitic transformations in Heusler alloys is a phonon instability due to interactions between optical and acoustic phonon states (154–156).
Martensitic phases of Heusler alloys have tetragonal or lower crystal symmetry, with structures derived from the cubic parent phase. The symmetry reduction during the phase transition leads to (nano-scale) twinning, and a distribution of martensite orientations related to the initial orientation of the parent phase (157). Application of a magnetic field causes reorientation of

martensite variants through domain wall movements in the magnetic field direction, which leads to large irreversible and reversible strains (150). These kinds of strains induced by martensite variant reorientation are independent of forced magnetostriction described in the previous chapters, and factors that need to be considered additionally.
A feature that is characteristic, but not exclusive to martensitic phase transitions is kinetic arrest (158–161). Kinetic arrest describes a retardation of a phase transition with nucleation and growth mechanism, *i.e.*, a first-order transition. After first seeds of a transformed material appear in a matrix of untransformed grains or domains, the untransformed matrix induces large stresses, acting as additional energy barrier for the transformation. This phenomenon is especially severe for transformations with large spontaneous magnetostrictions, like they are observed for Heusler alloys. In addition, microstructural effects like particle shape, and defects play a crucial role for the extent of kinetic arrest (162).

2.1.7. Investigation of phase transitions with non-ambient x-ray diffraction

Non-ambient XRD experiments are a widely used tool to investigate phase transformations in materials, chemical reactions, or in general the response of a material to an external stimulus. Low- and high-temperature attachments for lab-based diffractometers are commonly available from a wide range of suppliers, and already in use for many decades (163–166). They enable to perform *in situ* characterizations without the need to visit large-scale facilities or at least serve as pre-characterization step to identify samples best suited for *in situ* XRD experiments at a beamline, where a wide selection of non-ambient attachments usually is available.
Examples of studies using non-ambient XRD are numerous. High-temperature studies enable the investigation of formation of new phases or *in situ* investigations of reactions (167–170). With the growing field of battery research, *in operando* measurements during cycling of battery cells has also become a popular use of XRD to determine possible degradation pathways or side-products that occur during the (dis)charge reactions (171–174). Low-temperature XRD experiments are also frequently performed to investigate phase transformations, or follow interatomic distances, and unit cell parameters as function of temperature to determine thermal contraction (166, 175, 176).
Many materials also undergo changes in ordering of their magnetic moments at lower temperatures. These materials can have exotic magnetic states (177–180), or be simple ferromagnets; for x-ray diffraction there is no difference, since x-rays are not sensitive to the magnetic structure, and only the underlying crystal structure of a material is probed. Distortions in the crystal structure, or deviation from linearity of unit cell contraction upon cooling, however, often hint at the changes in the magnetic structure even if the crystal structure does not change (106, 143, 176, 181). The vast field of magnetic materials is, therefore, also available for investigations with temperature-dependent XRD as complementary, but powerful analysis technique. The main use of XRD for investigations of phase transitions in magnetic materials are determination of crystal structures, lattice parameters, and phase fractions. These fundamental microscopic properties help to get a better understanding of the behavior of magnetic materials. The hysteresis can be determined directly from the phase fractions of low- and high-temperature phase. Typically, it is deduced from macroscopic measurements of strain or magnetization on bulk samples. The results, however, are averaged, isotropic values, and often erroneous in the case of non-phase pure samples. Furthermore, temperature-dependent XRD can be used to determine the crystal structures after the phase transition, which are the basis for modelling of materials properties and phase transformation mechanisms (157, 182,

183). It is also possible to accurately determine the anisotropic spontaneous magnetostriction that is otherwise only obtainable from single crystal investigations (42–45). Many further structure-property relationships like microscopic strain, and completeness of transformation can be also deduced from the XRD data (46–48), making it a well-established and invaluable tool for characterization of phase transitions in (magnetic) materials.

2.2. X-ray diffraction in magnetic fields

X-ray diffraction in magnetic fields is a useful tool for analyzing field-induced phase transitions (49, 50, 184) and/or measuring the microscopic magnetostriction of a material (68, 185, 186). Numerous research applications benefit from a diffractometer setup with magnet, so it is desirable to consider assembling such a diffractometer. However, such setups are not readily available, and diffraction experiments under magnetic field are typically performed at large-scale facilities (58, 66, 69, 187, 188). This chapter presents the main challenges that need to be overcome in order to assemble an x-ray diffractometer with magnet, and gives an overview over the few installations scattered around the world that already existed prior to this work.

2.2.1. Challenges

There are numerous challenges associated with building an x-ray diffractometer with a magnet sample environment. So many, that, in fact, no supplier of x-ray diffractometers has a solution in its shelves. Such a diffractometer can, therefore, only be custom-built, and each and every challenge has to be overcome by clever design choices.

Space: One of the most basic, but nevertheless very important, challenges associated with assembling an x-ray diffractometer setup with magnet is *space*. Regardless of the type of magnet chosen for the installation, be it permanent or (superconducting) electromagnet, the typical dimensions of a magnet are rather large (189). Standard diffractometer cabinets tend to be compact, so that the diffractometer footprint is small inside a laboratory. Most diffractometer setups are, furthermore, optimized for space, so that there is typically only as much distance between x-ray source and detector as needed for the diffraction geometry of the system. And, additionally, there is rarely more free space than needed *e.g.*, for a non-ambient temperature sample environment like a heating chamber, instead of a regular sample holder. Enough space is not only needed for fitting in the magnet, but also to be able to place all moving and electronic parts as far away as possible from the magnet, to reduce the impact of stray magnetic fields. This will be discussed more in-depth in the chapter, *stray magnetic fields*. The issue of space alone renders most, if not all, standard diffractometer setups unsuitable for a potential upgrade with a magnet sample environment, so that a custom diffractometer has to be assembled.

Magnet type: Another challenge for building an x-ray diffractometer with magnet is choosing a suitable magnet. The magnet would ideally have a fast ramp up/down speed and large $\mu_0 H_{\max}$, so a (superconducting) electromagnet is the most obvious choice. Its bulky dimensions and the vibrations induced by the compressor that is cooling the magnet to superconducting temperatures will have to be considered. Further points of consideration are the angular coverage of the scattering window, the height of the beam flight tube and the available space for potential sample cryostats.

Stray magnetic fields: A magnet with $\mu_0 H$ in the order of several tesla generates strong, long-range stray magnetic fields. Especially at risk are highly sensitive electronic parts. Since $\mu_0 H$ decreases with distance to the center of the magnet, it is crucial to place the x-ray source and all sensitive electronic parts, like the detector, as far away as possible from the magnet. Stray magnetic fields may cause electronic parts to malfunction or break, whereas the x-ray source is affected by a Lorentzian force exerted on the accelerated electron beam that is used for x-ray generation. The electron beam is deflected by the Lorentzian force which causes a shift of the

focal point of the x-ray beam, potentially resulting in a field-dependent misalignment of the x-ray diffractometer. Not all components that are sensitive to magnetic fields may be placed far enough away from the magnet, however, so they have to be shielded against the stray magnetic fields. Magnetic shielding is typically achieved by encapsulating the to-be-shielded component in a cage made from a material with large permeability (190).

Diffraction geometry: The diffraction geometry, *i.e.*, spatial arrangement of x-ray source, sample and detector, while potentially ensuring an optical focusing condition of the x-ray beam, is another fundamental aspect during the planning phase of a diffractometer. It is especially important for this kind of setup, because the magnet imposes severe geometrical restrictions on the instrument. Other points to be aware of are the large distances, and how the focusing of the x-ray beam should be handled under such conditions. Certain geometries, like the Bragg-Brentano geometry, rely heavily on accurately meeting the parafocusing condition, otherwise a severe reflection broadening is observed. Furthermore, the chosen diffraction geometry should allow for high quality counting statistics, in order to be able to perform quantitative diffraction data analysis (8). Such analyses include crystal structure solution and refinement (191–194) and phase quantification (195–197) using the Rietveld refinement method (198). High quality counting statistics are achieved by exposing a large number of particles in many different orientations to the x-ray beam, so, a large x-ray spot size and/or sample rotation or movement in the x-ray beam are desirable (199).

Sample preparation: Closely tied to the diffraction geometry is the sample preparation. One has to ensure sample stability and data reproducibility even under large magnetic fields and/or possibly non-ambient temperatures.

X-ray source: The topic of x-ray sources might seem trivial at first glance, since x-ray tubes are available with only a limited selection of possible anode materials for standard laboratory diffractometers. The most common types are Co, Cu, Mo, or Ag anodes, but even for these different anode materials there are a lot more options than it appears. Each x-ray tube anode material is available with different filament shapes – broad, normal, fine, and long-fine focus – which heavily impact the beam size and shape at the sample position. Furthermore, these x-ray tubes can be mounted with their filament oriented either parallelly or perpendicularly with respect to the beam path of the diffractometer, producing an x-ray beam with either a point or line focus. And, finally, one has to decide which x-ray wavelength to use, because even for a given anode material there is usually the choice between K_α and K_β radiations as most intense characteristic wavelengths in the tube's x-ray spectrum. Factors influencing the decision which x-ray wavelength and filament type to choose for the custom magnet diffractometer are: the long x-ray beam path and concomitant large air scattering, possible sample absorption effects, and the sensitivity of the detector for the chosen radiation wavelength.

Monochromator: The monochromator is another integral part of an x-ray diffractometer. It can be a metal filter, (bent) crystal, or multi-layer optics, also called x-ray mirror. They are expected to be unaffected by the stray magnetic field, provided that they are tightly fixed. All types of monochromators have different properties with respect to the x-ray spectrum purity and intensity of the resulting monochromatic x-ray beam. Energy resolution and intensity are inversely proportional to each other. The trade-off between resolution and intensity has to be carefully balanced for a given research question, as lower intensities typically result in longer data collection times. Diffractograms collected with "impure" x-ray radiation, however, contain

duplicates of reflections from characteristic x-ray wavelengths other than $K_{\alpha 1}$ (like $K_{\alpha 2}$ or K_{β}) that might hide subtle features in the pattern.

Detector: A wide range of x-ray detectors utilizing different detection principles are available on the market, *e.g.*, CCD cameras, scintillation counters, image plates, Si-strip, and semiconductor pixel detectors, to name just a few of them. While all detectors have their strengths and weaknesses, the most important quality for an x-ray diffractometer setup with magnet is stability in the stray magnetic field. Desired but not mandatory properties would be a large detection area, fast read-out times, and a high sensitivity for the chosen x-ray wavelength, all of which would speed up data collection times.

Temperature control: While not being essential for the diffractometer setup with magnet, having the option to measure at non-ambient temperatures would be a valuable asset, and broaden the field of research applications for the diffractometer. It would allow the investigation of temperature- and/or field-induced phase transitions (200–203), and measurement of temperature-dependent magnetostriction (125, 204, 205). The main challenges for the custom diffractometer setup are the geometrical restrictions imposed by the magnet, and the stray magnetic field. The means of temperature control, *e.g.*, a furnace or cryostat, would also have to serve as sample holder, and would have to be incorporated into the diffraction geometry, while ideally still allowing for sample movement/rotation.

Diffractometer control/Automation: The last but not least difficult to solve challenge is the means of diffractometer control. Since the diffractometer is custom-built, no standard software from diffractometer manufacturers can be used to control the individual diffractometer parts. Every aspect of the hardware has to be incorporated into the software individually; be it shutter control, sample movement, detector read-out, or more advanced features like remote temperature, and magnetic field control. This would allow for programming of macros for measurement series under various conditions without the need of user interference, and thus greatly increase measurement efficiency and user convenience.

2.2.2. Existing lab-based x-ray diffractometer setups with magnet

The challenges listed in Chapter 2.2.1 were solved by others prior to this work, and several lab-based x-ray diffractometer setups with magnet exist at universities scattered all over the world (76–79, 81). All setups are custom-built, and every instrument is designed on a different basis. Many more diffraction setups with magnet are available at beamlines in large-scale facilities like synchrotrons with continuous (58–61), and pulsed (66–75) magnets, and also neutron beamlines (62–65) with magnets reaching $\mu_0 H_{max}$>30 T. These are out of scope for this work, however, and will not be discussed in detail.

The first in-house setup for peak scans on single crystals with a 0.9 T split-pair superconducting magnet was developed by Tajima *et al.* in 1990 (206), which was later upgraded to an 8 T magnet on a triple axis diffractometer (56). Single crystal samples of sufficient size are required for this setup, so the practical use is somewhat limited. Many materials undergoing magnetoelastic or magnetostructural transitions with large magnetostriction tend to crack or pulverize during the transition, making the reversible analysis of single crystals impossible (207–209).

The first lab-based powder XRD instrument with 5 T magnet and low-temperature attachment was reported by Watanabe *et al.* from Tohoku in 1998 (80). It utilizes the Bragg-Brentano diffraction geometry. A high-temperature attachment for measurements from RT up to 473 K was later added as an alternative sample environment, making it the only setup capable of measuring above RT (81). Seamless switching between low- and high-temperature measurements, however, is not possible with this instrument. A second diffractometer with 10 T magnet from same group was reported in 2011 (77). This time a Debye-Scherrer camera was used as basis for the instrument, so, measurements are performed in transmission geometry, and are limited to ambient temperature. The camera is not shielded against the stray magnetic fields, and reflection intensities are significantly lower at large fields. Furthermore, an image plate detector with offline read-out is used, which requires removal, and remounting of the image plate in between every measurement. The reproducibility of the peak position accuracy is therefore questionable.

Another setup in Bragg-Brentano geometry was reported by Holm *et al*. from Ames in 2003 (54, 76). This setup has a 3.5 T magnet, low-temperature capabilities, and shielding against stray magnetic fields. A goniometer even allows for sample positioning and alignment to overcome some instrumental error sources leading to systematic peak shifts. Some are introduced by the Bragg-Brentano geometry in general, and others are the result of a shift of the sample position due to thermal contraction of the sample holder during cooling. The use of a continuous-flow cryostat allows for quick sample cooling, and a low T_{min} of 2.2 K, but consumes large amounts of liquid He.

The most recent setup with magnet was reported in 2016 by Shahee *et al*. from Indore (79). The diffractometer is equipped with an 8 T magnet, and uses a parallel beam geometry, which causes less aberrations for reflection measurements than a convergent beam, as is used for Bragg-Brentano geometry. The scintillation counter detector is appropriately shielded against the stray magnetic fields, and low-temperature capabilities are available in the form of a continuous-flow cryostat for measurements down to $T_{min} = 2$ K.

Table 2.1: Comparison of laboratory x-ray diffractometer setups with magnet existing prior to this work.

	X-ray source	Geometry	Detector	T [K]	$\mu_0 H_{max}$ [T]	Magnetic shielding
Tohoku (80)	Cu sealed tube graphite monochromator	Bragg-Brentano	Scintillation counter	9–320 283–473	5	yes
Tohoku (77)	various sealed tubes K_β filter	Debye-Scherrer	Image plate	RT	10	no
Ames (76)	Mo rotating anode graphite monochromator	Bragg-Brentano	Scintillation counter	2.2–315	3.5	yes
Indore (79)	Mo rotating anode multi-layer mirror	Parallel beam	Scintillation counter	2–300	8	yes

A comparison of all powder XRD setups with magnet is listed in Table 2.1. Most instruments use reflection geometries with all their disadvantages. The powder samples are fixed with vacuum grease that freezes only at low temperatures. Orientation of sample particles in the magnetic field is, therefore, a common issue of many of the instruments. Furthermore, the reflection resolution with FWHM of >0.1° can only be considered to lie in the medium range. Coupled with the fact that no setup uses $K_{\alpha 1}$-only radiation, the overall peak overlap is large, especially for low-symmetry materials. Scintillation counter detectors are almost exclusively used, and since they are point detectors, measurement scans consist of many steps resulting in long measurement times. The use of continuous-flow cryostats consumes large amounts of liquid He, and might be considered unsustainable given the large economic footprint of He, and the volatility of the He market (210). The shielding against stray magnetic fields is oftentimes not sufficient to completely avoid reflection shifts, and lattice parameter accuracy at large magnetic fields is, therefore, questionable. To summarize, all diffractometer setups fulfill their purpose of enabling XRD measurements in magnetic fields. The technology used is, however, oftentimes not state-of-the-art, and there is potential for a modern XRD instrument to overcome some of the limitations of the existing systems.

3. X-ray diffractometer with magnet

The key development for this work was the assembly of an x-ray diffractometer with 5.5 T superconducting magnet and sample cryostat to cover a wide parameter space in magnetic field and temperature. The diffractometer is described in detail in Publication A, which is reprinted in Chapter 3.2. Since the release of Publication A, several updates and improvements in both hard- and software of the diffractometer were realized. These updates are included in the synopsis in Chapter 3.1.1, and the final x-ray diffractometer setup is shown and summarized in Chapter 3.1.2.

3.1. Synopsis of Publication A

3.1.1. Synopsis of Publication A und Experimental Updates

Chapter 2.2.1 introduced challenges related to building an x-ray diffractometer with magnet. This chapter now describes how these challenges were overcome for the diffractometer assembled for this work, while also considering the experimental updates that were implemented since release of Publication A.

Prior to this work, there was no lab-based x-ray diffractometer with magnet based in Europe, limiting access to XRD experiments under magnetic fields to large-scale facilities. Publication A introduces and describes the custom-built x-ray diffractometer setup with magnet. Its completion is the main achievement of this work. The publication highlights the performance and customizability of the diffractometer setup with the choice between two monochromator units; one for high resolution and one for high flux applications. Diffractometer stability is shown up to magnetic fields of 5.0 T. The monochromator performances are demonstrated for the field- and temperature-dependent lattice parameter determination of $LaFe_{11.6}Si_{1.4}$, and the field- and temperature-induced martensitic phase transition of $Ni_{50}Mn_{33.4}In_{16.6}$.

Space: The diffractometer assembled for this work was custom-built, and not based on an existing x-ray diffractometer setup. Limitations regarding the spacing of the main building blocks of the diffractometer – x-ray source, magnet, and detector –, which would have been imposed by a "standard" diffractometer cabinet basis, could therefore be avoided. The lab-based diffractometers with magnet that existed prior to this setup followed a similar approach, apart from the instrument reported in (76). This diffractometer, however, is equipped with the "weakest" magnet of all the diffractometer setups, with a magnetic field strength of up to 3.5 T. So, it is likely that the magnet dimensions are smaller compared to the other setups, and the magnet could, therefore, fit into the existing diffractometer system.

Magnet type: The magnet chosen for this setup is a compact superconducting split-pair magnet (HTS-110) with vertical magnetic fields up to 5.5 T. The maximum field $\mu_0 H_{max}$ is in the medium range compared to other setups (56, 76, 77, 80, 206), however, it is cooled cryogen-free, ensuring a green footprint, and reduced operational cost compared to conventional He-cooled magnets. With its compact size, it allows for a moderate source – detector distance of 80 cm. A

Ø40 mm bore ensures compatibility with most sample cryostats used for diffraction experiments. With a height of 10 mm, the flight tube for the direct beam and scattered x-rays is large enough for the use of a line focus x-ray beam shape, which allows for a significantly larger coverage of sample area with x-rays compared to a point focus beam. The scattering angle is limited to 94°, which is enough Q coverage for high resolution using harder x-ray radiation, like Mo K_α ($d_{\min} = 0.49$ Å), or Ag K_α ($d_{\min} = 0.40$ Å), but would not be enough using Cu K_α ($d_{\min} = 1.05$ Å).

Stray magnetic fields: Shielding of the x-ray source against stray magnetic fields has proven to be essential for this diffractometer setup. It was known from other lab-based instruments with magnet, that magnetic shielding might be needed (56, 76, 77, 79, 80, 206); the extend, however, could only be assessed after assembly of the complete setup. Initially, the stray magnetic fields affected both, the image plate detector and the x-ray source. Read-out of the image plate was only possible after ramp-down of the magnet after each data collection, since no signal could be detected as a result of the magnetic field affecting the photo multiplier tube in the read-out unit of the detector. This led to a significant increase in experimental times, and caused ageing of samples that are dependent on their magnetic field and temperature history, like Heusler alloys (211, 212). After upgrading the detector by replacing the image plate with a DECTRIS MYTHEN2 R 1K Si strip detector (213) (from now on called MYTHEN2), however, it is no longer necessary to ramp-down the magnetic field after exposure. The MYTHEN2 can withstand stray magnetic fields of up to 1000 mT (which was tested with a loaner MYTHEN2 under supervision of a DECTRIS technician).
This leaves only the x-ray source to be shielded against the stray magnetic fields, which, in this case, cannot be circumvented. If left unshielded, the direct x-ray beam shifts to an extend that the sample is no longer hit and no signal can be detected, see Figure 3.1 (left). As explained in Chapter 2.2.1, the primary x-ray beam shifts due to the Lorentzian force exerted on the accelerated electron beam inside the x-ray tube, which causes a field-dependent movement of the focal point.

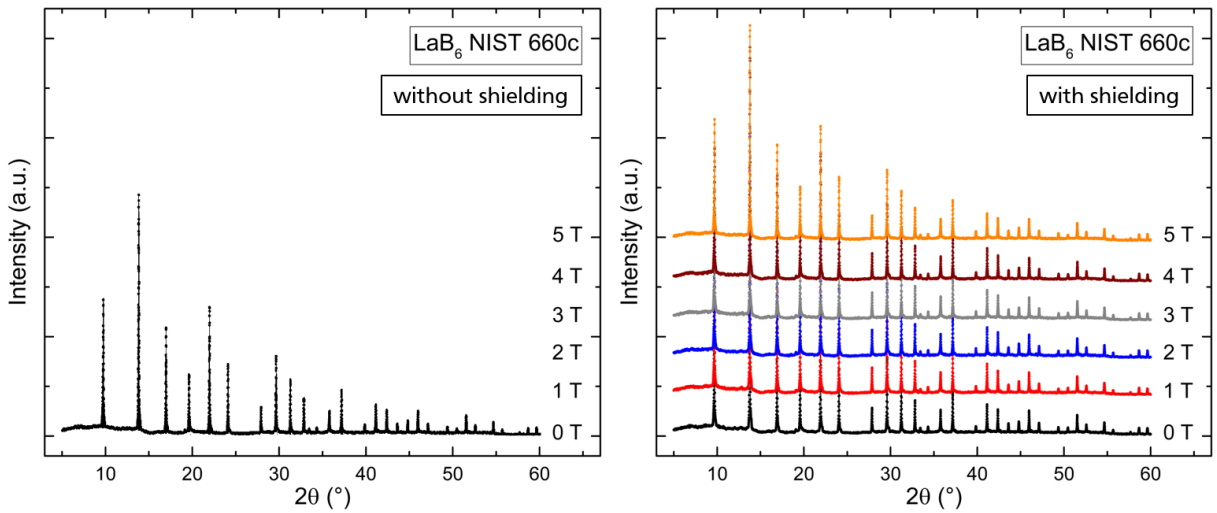

Figure 3.1: Diffraction patterns of LaB_6 without (left), and with (right) magnetic shielding of the x-ray source under increasing magnetic fields. Adapted from Publication A.

A 2 mm thick housing made from high permeable μ-metal (Sekels), see Figure 3.9, is enough to almost completely avoid the effects of the stray magnetic fields on the x-ray source. The residual stray magnetic field of 1 mT at $\mu_0 H_{\max}$ still causes a slight systematic shift the x-ray

beam, and, as a direct consequence, of reflections in the diffraction pattern. The magnitude of the shift of <0.02°, however, is small enough to easily be corrected for in a Rietveld refinement. As an additional layer of security regarding potential instrumental errors as function of sample temperature and magnetic field, all samples are prepared as mixtures with NIST 640d Si standard reference powder with known lattice parameters.

Diffraction geometry: Most setups with magnet are arranged in the Bragg-Brentano geometry, *i.e.*, working with samples in reflection mode. While this is a popular diffraction geometry in general, it comes with disadvantages that are especially pronounced for instruments with magnet. Samples are typically prepared by scattering loose powder on a flat, horizontal sample holder or using pressed powder pellets. As the magnetic field requires fixing of the sample powder in order to avoid movement or reorientation of the particles, the samples are often diluted with vacuum grease that freezes at low temperatures (80). This procedure does not work for elevated temperatures, and, thus, limits these diffractometers to low temperature studies. Other disadvantages include the height displacement, and resulting diffraction peak shifts, as well as the sample transparency error (214), and pronounced preferred orientation effects (8). These issues result in diffraction patterns that are not quantitatively analyzable, and, therefore, cannot be interpreted by Rietveld refinement for structural analysis – making it impossible to accurately characterize new phases induced by the magnetic field. One of the biggest disadvantages of reflection geometries is that the diffracted x-ray beam is only focused onto a single detector position at a time, making it necessary to perform step scans, and limiting the detector selection to point detectors.
With all of the aforementioned disadvantages of a reflection geometry in mind, the diffractometer assembled for this work is arranged in a different geometry, *i.e.*, a modified transmission geometry, see Figure 3.2.

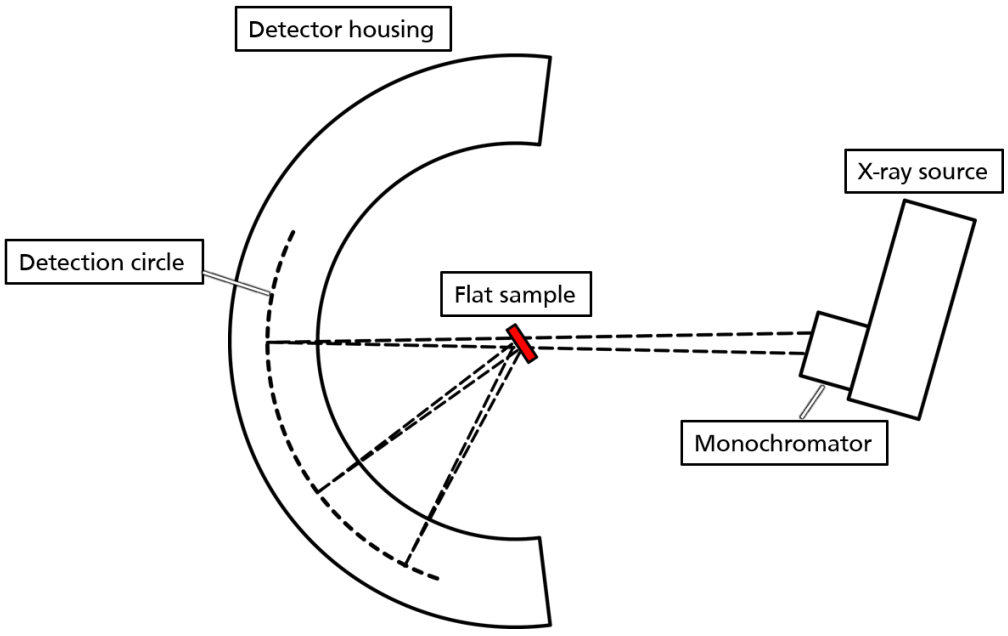

Figure 3.2: Schematic of the focusing circle of the transmission geometry for this diffractometer setup.

A traditional transmission geometry is Debye-Scherrer geometry, utilizing a capillary sample, and focusing diffracted x-rays onto the detection circle independently of the sample. Capillary samples inside a magnet are impractical, however, especially when mounted on a cold finger of a cryostat, so a flat-plate transmission technique was developed. Its main advantage is that

the sample is always exposed to the x-ray beam, regardless of a potential shift of the primary x-ray beam, as the flat-plate surface area is larger than the beam size. Furthermore, by directly focusing onto the detector, it is possible to utilize position-sensitive detectors instead of point detectors, which greatly speeds up measurement times. This was initially exploited with the image plate recording an entire diffraction pattern simultaneously, as described in Publication A. The image plate has since been replaced by a MYTHEN2, which is described more in detail later.
In Publication A, a curved sample holder with curved samples was described. The long-term stability of samples glued on a curved carbon sheet was unreliable, however, especially over several temperature cycles. After a redesign, the current sample holder is, therefore, optimized for flat samples. The disadvantage of using flat samples is a small broadening of the reflections in the diffraction patterns due to the introduction of a parallax error. The parallax error is a result of the intentional rocking motion of the cryofurnace, *i.e.*, sample holder, by ±15° over the course of a measurement. However, since the broadening effect is quite small, the advantages of sample rocking, *i.e.*, improvement of the counting statistics by exposing more powder particles to the x-ray beam, outweigh the disadvantages.

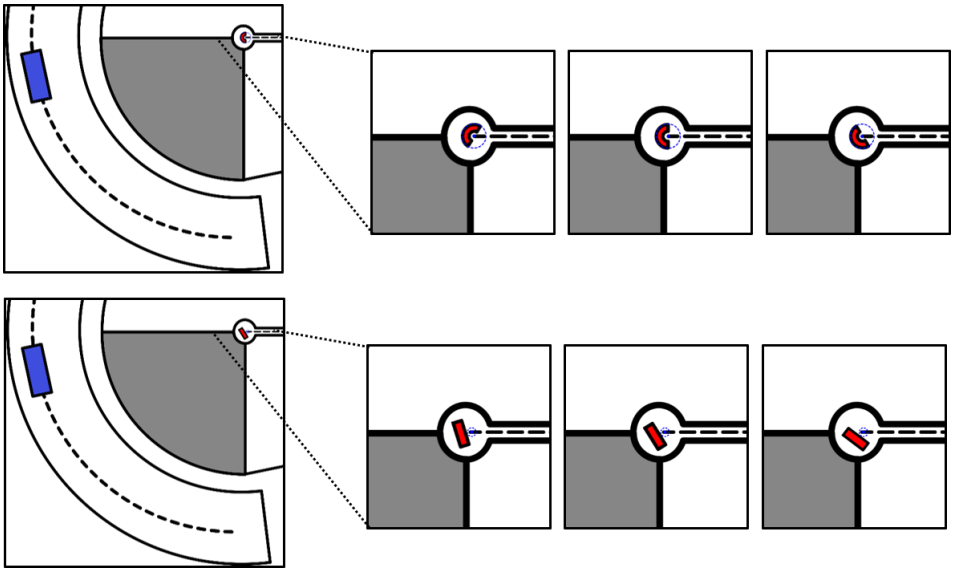

Figure 3.3.: Schematic of the sample rocking by ±15° in the magnet bore during a measurement with a curved (top) and flat sample (bottom).

In addition to the rocking motion that is schematically shown in Figure 3.3 for curved and flat samples, the flat sample has an incidence angle of 45° with respect to the incoming x-ray beam. This incidence angle allows for a larger amount of powder particles to be exposed to the x-ray beam, and results in a further improvement of the counting statistics, and, thus, a reduced influence of a possible preferred orientation. All of these features combined result in the relative reflection intensities being reliable, which is a requirement for Rietveld refinement for structural analysis.

Sample preparation: Sample preparation was a potential pitfall of the transmission geometry, as a suitable glue and substrate for the powder particles had to be determined. The substrate should contribute as little as possible to the diffraction pattern, while still having large heat conduction properties, to ensure a stable and controllable sample temperature. The solution is a carbon sheet that is clamped into a brass frame and attached to the end of the brass cold finger of the cryostat, see Figure 3.4. The carbon sheet used is partly crystalline and contributes

to the diffraction patterns as an additional graphite phase, but, can be described as additional phase in a potential Rietveld analysis.

Figure 3.4.: Cold finger of the cryofurnace with flat sample clamped into a brass frame.

Sample powder is sieved to $<40\ \mu$m and mixed with NIST 640d Si standard reference powder that is used as internal standard. The added Si with known lattice parameters allows for correction of the zero-point error of the sample, and potential shift of the x-ray beam in the residual stray magnetic field at large magnetic fields. The type of glue used depends on the temperature range, since not all glues can withstand temperatures >350 K. Details of the sample preparation procedure are given in Supplemental Chapter 7.1.
Since the sample in total must not be too thick, in order to avoid too large x-ray absorption, the amount of sample powder needed is far less than for the other diffractometer setups with magnet. Several mg of sample are enough, which is especially useful for hard-to-synthesize samples with sometimes only little synthesis yield.

X-ray source: With the diffractometer being arranged in transmission geometry, and the long distance between source and detector, hard x-ray radiation is heavily favored for this setup. A Mo anode was chosen as trade-off between wavelength and general flux of the x-ray tube compared to a potential Ag source. The use of a long fine focus x-ray tube enables the exposure of a large sample area with $\sim$6 mm beam height at the sample position. Compared to the other x-ray diffractometer setups with magnet, this setup uses a relatively low power x-ray source and, thus, has a lower x-ray flux in the primary beam. The other setups often use 18 kW rotating anodes, which, although they produce brighter primary beams, consume much more energy and require frequent maintenance, which all contribute to overall high operational costs. Despite the fact that the primary x-ray beam of this work's diffractometer has less initial flux, total measurement times are still faster by at least a factor of 4–10 compared to the other setups. That is due to the use of position-sensitive detectors that cover a large angular range simultaneously, making this setup the fastest, and most efficient of all lab-based diffractometer with magnet.

Monochromator: Selection of a monochromator for an x-ray diffractometer is always a compromise between (energy) resolution and flux of the resulting monochromatic x-ray beam. Laboratory XRD is usually performed with the K_α radiation of the anode material of the x-ray source, since it is the most intense characteristic wavelength of a sealed-tube x-ray source. However, K_α radiations are actually two distinct but rather similar wavelengths, and, thus, the

monochromator selection gains an additional layer of thought. There is an "x-ray energy selection threshold" below which certain monochromator crystals can separate $K_{\alpha 1}$ and $K_{\alpha 2}$ radiations. Above this threshold, a monochromator still has its uses, as it functions like a filter, filtering out unwanted x-ray wavelengths, *e.g.*, hard radiations from the Bremsstrahlung of the x-ray source. All reflections in a diffraction pattern, however, will consist of $K_{\alpha 1}$ and $K_{\alpha 2}$ contributions, and are, therefore, doubled – making it sometimes impossible to follow subtle peak splitting during phase transitions with a symmetry reduction (215).

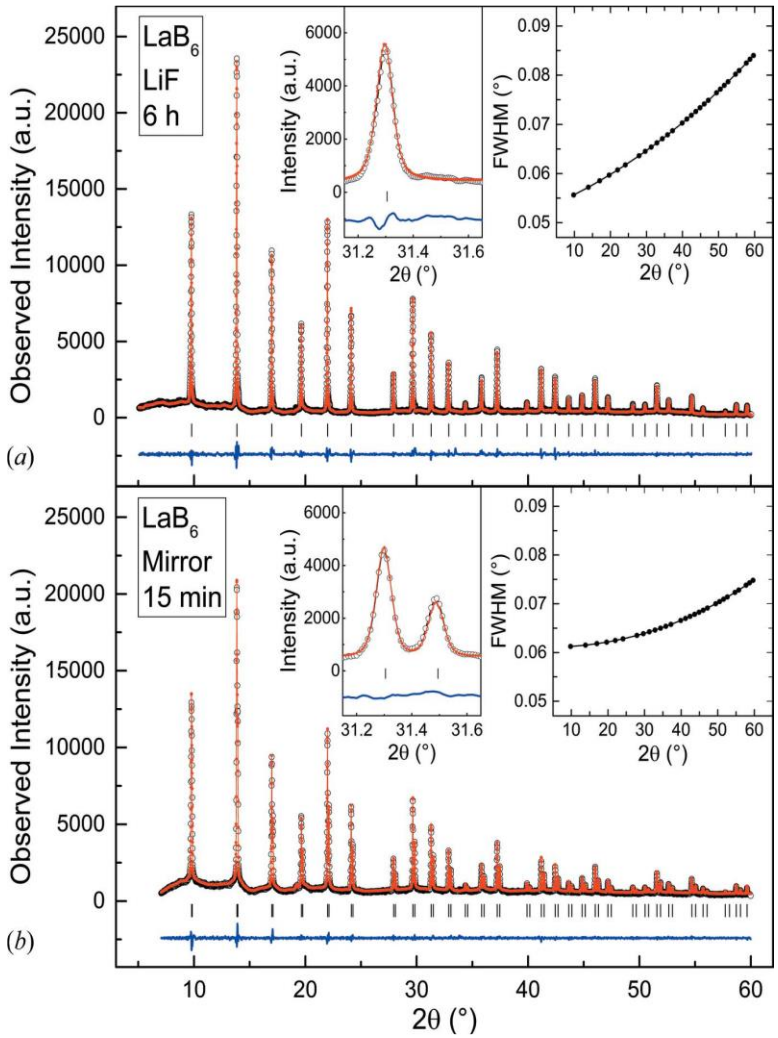

Figure 3.5.: Rietveld refinements of x-ray powder diffraction patterns of the same NIST 660c LaB_6 standard sample collected at $T = 295$ K with (a) a LiF(200) monochromator crystal for 6 h and (b) a focusing x-ray mirror for 15 min. The insets show the 2θ range from ~31.2 to ~31.6° to highlight both the difference in energy resolution between the monochromators and the reflection full width at half maximum for these measurements as function of the diffraction angle. Reprinted from Publication A.

For this setup, two interchangeable monochromator units are available. They offer the flexibility of adapting the diffractometer resolution to the research question at hand. Both monochromator units produce an x-ray beam that is focused onto the detection circle. A LiF(200) monochromator allows for data collection with $K_{\alpha 1}$ radiation only, for use in high resolution experiments. The focusing x-ray mirror optic, however, provides the highest flux possible, and, therefore, lowest measurement times – at the cost of the presence of the K_{α} doublet in diffraction patterns. Figure 3.5 shows a comparison between the two monochromator units in terms of peak widths, typical measurement times, and "Rietveld-ability" of the collected

data.
Other lab-based diffractometer setups with magnets do not offer this flexibility regarding their monochromator units. Neither of these instruments features a monochromator for $K_{\alpha 1}$-only measurements, making the diffractometer assembled for this work the best solution for high resolution experiments. The peak widths with the x-ray mirror optic are also considerably smaller compared to the other setups, which makes the presence of the K_α doublet in the diffraction patterns much less of a drawback.

Detector: The detector is another integral part of any x-ray diffractometer, and other instruments with magnets almost without exception use scintillation counters, *i.e.*, point detectors (56, 76, 79, 80, 206). As a result, measurements have to be performed as step scans, and require a minimum of 1 h data collection time per temperature/magnetic field, despite the use of rotating anode x-ray sources. The only exception is the Debye-Scherrer camera reported in (77), that uses an image plate with offline read-out unit. All of these detectors have in common that they use indirect methods of x-ray detection, and all utilize a photomultiplier for signal amplification. This leads to arbitrary intensities, low signal-to-noise ratios, and inherently low maximum count rates for these detectors. Overall, the data quality, and signal/noise ratio for the these previously existing setups is less compared to this work's diffractometer.
The online readable image plate detector system that was installed and described in Publication A has since been replaced with a hybrid photon counting MYTHEN2 detector, see Figure 3.6. This was a significant update for a number of reasons. The MYTHEN2 consists of 1280 individual 50 μm-wide Si strips (8 mm high), and covers $\sim$11 °2θ with the given distance to the sample. The detector is mounted in place of the former read-out unit of the imaging plate system, and reuses the rail and encoder system inside the *OBI* housing (216), which was used to precisely position the former read-out unit. With the integration into the *SPEC* (217) environment, the detector can now be positioned using commands in the *SPEC* console of the control PC, and thus programmed for single exposures at a fixed 2θ position or step scans to collect complete diffraction patterns up to $2\theta_{max} = 78°$.

Figure 3.6.: DECTRIS MYTHEN2 R 1K Si strip detector (218).

The main advantage of the MYTHEN2 detector compared to the imaging plate are the vastly reduced exposure times, due to the combination of large height of 8 mm per Si strip, high quantum efficiency of $\sim$80% for Mo K_α radiation, and fast read-out time of $<$10 ms, which all factor into the collected diffraction signal and measurement speed. Another major advantage is

the ability to withstand stray magnetic fields of up to ~1000 mT. Since stray magnetic fields at the detector position reach only up to 300 mT at maximum field strength of the magnet, the MYTHEN2 detector can be used without having to ramp down the magnet after each exposure. This speeds up measurement protocols, and eliminates the need for unnecessary additional magnetization cycles, which is especially useful for samples exhibiting ageing effects over several magnetization or temperature cycles. With a channel width of 50 μm (compared to ~100–150 μm for the image plates), which translates to a step size of 0.0097°, the MYTHEN2 also features a greater angular resolution. Furthermore, the detector has a maximum count rate of 10^7 ph/s/strip, which allows for the use as alignment tool of the non-attenuated direct beam.

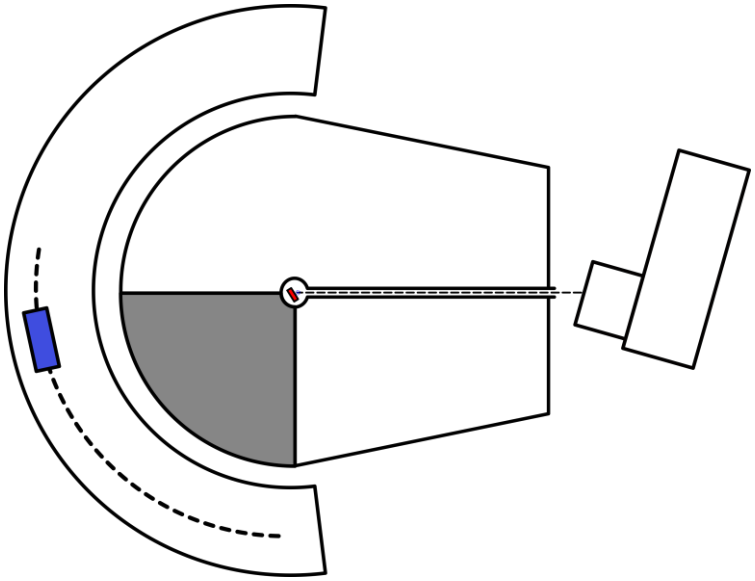

Figure 3.7.: Schematic of the x-ray diffractometer with magnet and MYTHEN2 strip detector (blue) inside the *OBI* housing. The scattering slit in the magnet (grey area) allows for diffraction of x-rays up to ~90 °2θ.

Figure 3.7 shows a schematic the final diffraction geometry with MYTHEN2 detector in the *OBI* housing. Since the detector is not bent like the image plate was, only the center channel is tangent on the diffraction circle. The channels further to the edges are subject to a parallax error, which is corrected after data acquisition with the following equation:

$$\Theta_e = \Theta_o - \arctan\left(\frac{50\ \mu m \cdot (C_{edge} - C_{center})}{R}\right), \tag{3.1}$$

where the encoder position Θ_e is corrected by the angular offset with respect to the diffractometer zero position Θ_o, C_{edge} is a channel number closer to an edge, C_{center} is the channel number of the center channel, and R is the distance of the detector module from the center of the diffraction circle.

Typical diffraction experiments with the MYTHEN2 detector consist of step scans with 5-6 steps of the detector, each covering ~11 °2θ with an overlap of ~0.5 °2θ, summed up to a total diffraction range of 50–60 °2θ. The Python script used for angular correction, data summation, and data export is given in Supplemental Chapter 7.2.

Temperature control: For measurements at non-ambient temperatures, a cryogen-free closed-cycle He cryostat was chosen. Some setups follow a similar approach (80), while others use liquid He-based cryostats (76, 79). Liquid He-based cooling allows for faster sample cooling and lower achievable T_{min}, but requires the use of the costly consumable He. Furthermore, only one setup has an optional high temperature attachment (81) that can replace the cryostat. The

other setups are limited to measurements below ambient temperatures. However, especially for the investigation of near room temperature phase transitions, as are sought after for magnetic refrigeration, the ability to measure above ambient temperatures often is a necessity.
The sample cryostat that was initially installed allowed for measurements in a temperature range from 20–310 K. Since the release of Publication A, the cryostat has been replaced with a cryofurnace (model CH-204-N, SHI cryogenics). This cryofurnace is a two-stage closed-cycle He cryostat for low-temperature measurements down to 11 K, but also features an integrated thermal bridge for heating samples >300 K, up to T_{max} = 700 K. The unmounted cryofurnace can be seen in Figure 3.8. Without the thermal bridge, the He cryostat could not withstand the additional heat input of the sample heater for temperatures above room temperature.

Figure 3.8.: Unmounted cryofurnace lifted with a Bowden cable. The inset shows the thermal bridge that prevents heating up of the first stage of the closed-cycle He cryostat while the sample is heated >300 K.

The cryofurnace allows for a continuous change of sample temperature in the range 11–700 K, and, thus, vastly increases the sample parameter space compared to the previous cryostat. Switching between low and high temperature measurements is seamless with this cryofurnace, and there is no need for a realignment of the sample. Any temperature-dependent zero-point errors that occur as a result of the thermal contraction/expansion of the cold finger are accounted for in a Rietveld refinement including the internal Si standard. High-temperature studies like the ones performed for Publication C and Ref. (219) would not have been possible without this upgrade.
As a further improvement of data quality, the whole cryofurnace is rotated by±15° over the course of a measurement, as explained in subchapter *Diffraction Geometry*. This motorized rotation increases the number of sample particles exposed to the x-ray beam, and, thus, results

in an improved counting statistic. The cryofurnace is rotated while mounted on a rack, see Figure 3.9, that also serves as positioning tool for alignment of the sample inside the magnet.

Diffractometer control/Automation: Diffractometer control is not mentioned for the other diffractometer setups with magnet, except for the instrument in Ames (76). There, a Rigaku TTRAX system is the basis for the diffractometer, and the corresponding control software is used. The general alignment and measurement procedure is also explained for the setup in Indore (79). Both setups require several manual alignment steps before each measurement, so it is assumed that no automation of temperature and magnetic field measurement series is implemented.
For the diffractometer assembled for this work, no realignment is needed after changing temperature and/or magnetic field, performing a series of measurements is, therefore, possible – and indeed integrated into the control software. All hardware components of the diffractometer are integrated into the *SPEC* environment, so that all parameters, like *e.g.*, temperature, magnetic field strength, shutter status, cryostat rotation, or detector position, can be accessed via the control PC, after initial mounting of the sample. This allows for the convenient use of macros, which let the user program a series of measurements with the desired temperature and magnetic field protocols. An example macro for a temperature series under different magnetic fields is given in Supplemental Chapter 7.3.

3.1.2. Final x-ray diffractometer setup

The final x-ray diffractometer setup after implementation of all the updates and improvements since Publication A is summarized in the following section and shown in Figure 3.9.

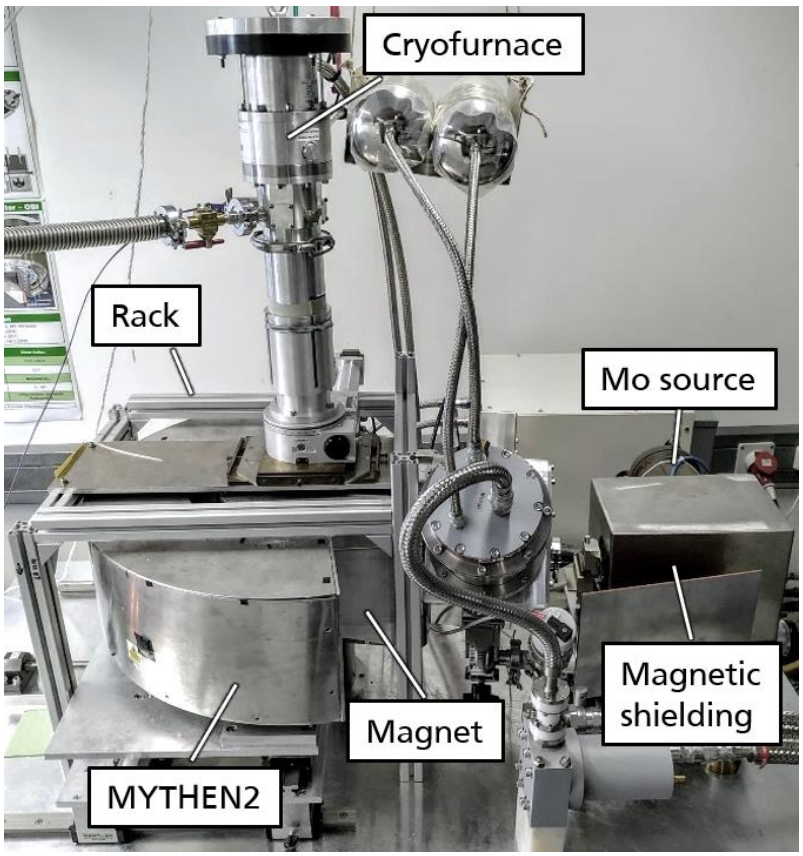

Figure 3.9.: Final setup of the x-ray diffractometer with magnet, cryofurnace, furnace rack and magnetic shielding.

The final instrument configuration is as follows:

- long fine focus Mo sealed x-ray tube with magnetic shielding
- evacuated x-ray mirror (high flux) or LiF(200) monochromator (high resolution)
- superconducting magnet, up to 5.5 T magnetic field strength
- flat samples glued on carbon sheet
- cryofurnace with supporting rack, 11–700 K
- MYTHEN2 detector inside the *OBI* housing
- hardware control of all components using the *SPEC* environment

Conclusions: The x-ray diffractometer with magnet that was assembled for this work is a unique instrument and different from all the other existing lab-based setups in many ways. It is arranged in transmission geometry with the advantages of requiring less sample, having more reliable relative peak intensities and less geometrical errors causing reflection shifts. Focusing onto the detector circle allows for the use of position-sensitive detectors, which is taken advantage of in the form of the MYTHEN2 detector that covers ~11 °2θ per detector position. Despite using a sealed-tube x-ray source with less photon brightness than a rotating anode, measurement times with this setup are vastly shorter than for other setups, while having a higher reflection resolution, and the ability to switch to a $K_{\alpha 1}$-only monochromator for even higher resolution. The $\mu_0 H_{max}$ of 5.5 T for the installed magnet is in the medium range compared to other setups, which can achieve magnetic field strengths of up to 10 T. The temperature range of this setup, however, is the largest, spanning 11–700 K. And the ability to seamlessly switch between low and high temperature measurements with the same cryostat, and without having to realign the instrument in between is a great asset. The internal Si reference standard that is mixed with every sample enables the correction of systematic errors of the setup, which allows for high precision and accuracy of determined lattice parameters, regardless of magnetic field and temperature. Together with the reliable reflection intensities from transmission geometry with a line focus x-ray beam, and the sample rotation employed during the measurements – quantitative phase analyses using the Rietveld method are possible and encouraged, as demonstrated in Publications D and E. An example input file for the *FULLPROF* software for a standard Rietveld refinement is shown in Supplemental Chapter 7.4. Computer control of all diffractometer components allows for the use of macros to perform complex series of measurements under different temperatures and/or magnetic fields. To summarize, this unique setup allows for quick and reproducible measurements over a wide temperature range in moderate magnetic fields of up to 5.5 T.

3.2. Publication A: X-ray diffractometer for the investigation of temperature- and magnetic field-induced structural phase transitions

X-ray diffractometer for the investigation of temperature- and magnetic field-induced structural phase transitions

Tom Faske[1] and Wolfgang Donner[1]

[1]Institut für Material- und Geowissenschaften, Technische Universität Darmstadt, Alarich-Weiss-Straße 2, Darmstadt, 64287, Germany

Correspondence email: faske@st.tu-darmstadt.de

Received 29 January 2018
Accepted 26 March 2018
DOI: 10.1107/S1600576718004892

Reprinted with permission from *J. Appl. Crystallogr*. 2018, 51, 761–767.

Abstract This article reports the development and characterization of a laboratory-based high-resolution X-ray powder diffractometer equipped with a 5.5 T magnet and closed-cycle helium cryostat that is primarily designed for the investigation of magneto-structural phase transitions. Unique features of the diffractometer include the position-sensitive detector, allowing the collection of an entire diffraction pattern at once, and the high energy resolution with Mo $K_{\alpha 1}$ radiation. The ability to utilize a lower energy resolution but higher photon flux by switching to an X-ray mirror monochromator makes it a versatile setup for a variety of compounds. In this contribution, details of the design and performance of the instrument are presented along with its specifications.

3.2.1. Introduction

With the rise of research focussed on the development of solid-state magnetic refrigerators in the last three decades (91, 220–222) came an increased need in structural characterisation of the involved materials under magnetic fields. Magnetocaloric cooling has the prospect of being more energy efficient than conventional gas compressor refrigerators (221). An integral part of a refrigerator utilising the magnetocaloric effect (MCE) is a material that undergoes a magneto-structural phase transition, preferably close to room temperature (91, 223). The phase transition is induced by an applied external magnetic field, which shifts the transition temperature, often the Curie temperature T_C. A magnetic field induced shift of T_C to higher temperatures leads to a *direct* MCE, while a decrease of T_C with increasing applied field can lead to the so-called *inverse* MCE (224).

Well-established characterisation tools for the investigation of structural changes occurring during the phase transition of magnetocaloric materials are x-ray and neutron diffraction. Due to space and weight restrictions often encountered for standard laboratory setups, diffraction experiments at non-ambient temperatures and under high magnetic fields are often performed at large-scale facilities (225, 226). There are few laboratory-based x-ray powder diffractometers equipped with powerful magnets where $\mu_0 H$ can be larger than 2 T (76, 77, 79, 81). Holm *et al.* (76) were the first to report on an x-ray diffractometer for the investigation of magneto-structural phase transitions in magnetic fields of up to 3.5 T. The diffractometer features Bragg-Brentano geometry with a point detector and Mo K_α x-ray radiations, similar to the setup recently reported by Shahee *et al.* (79). Due to the use of low energy resolution monochromators in these setups, $K_{\alpha1}$ and $K_{\alpha2}$ reflections are present in the respective diffractograms. The split reflections due to K_α doublets potentially hide information about phase transitions with subtle features (227) or multiple phases (48). Point detectors have the disadvantage of long measurement durations and they require an especially strong shielding against stray magnetic field (76). Mitsui *et al.* (77, 81) reported on two modified Debye-Scherrer cameras for the use in strong magnetic fields of up to 10 T, which allow for recording of an entire diffraction pattern on a conventional photographic film. Development of the photographic film, however, requires the removal from the Debye-Scherrer camera and comes with an increased angular uncertainty.

Here we report on the development of a laboratory-based high-resolution x-ray diffractometer for measurements in magnetic fields of up to 5.5 T in a temperature range of 20 – 310 K. The energy resolution of the monochromatic x-rays can be selected with different sets of monochromators enabling experiments with either Mo $K_{\alpha1}$ only ($\lambda \approx 0.7093$ Å) or Mo K_α radiations. Detection of the entire diffraction pattern at once is realised by an on-site readable image plate detector.

The paper is structured as follows: the description of the instrument is followed by details about the monochromator setups and magnetic shielding. An example measurement of NIST 660c LaB_6 gauges the capabilities of the diffractometer for both energy resolution modes and application examples of two prominent magnetocaloric materials highlight the usefulness of being able to select the energy resolution.

3.2.2. Instrumentation and Methodology

3.2.2.1. Instrumentation

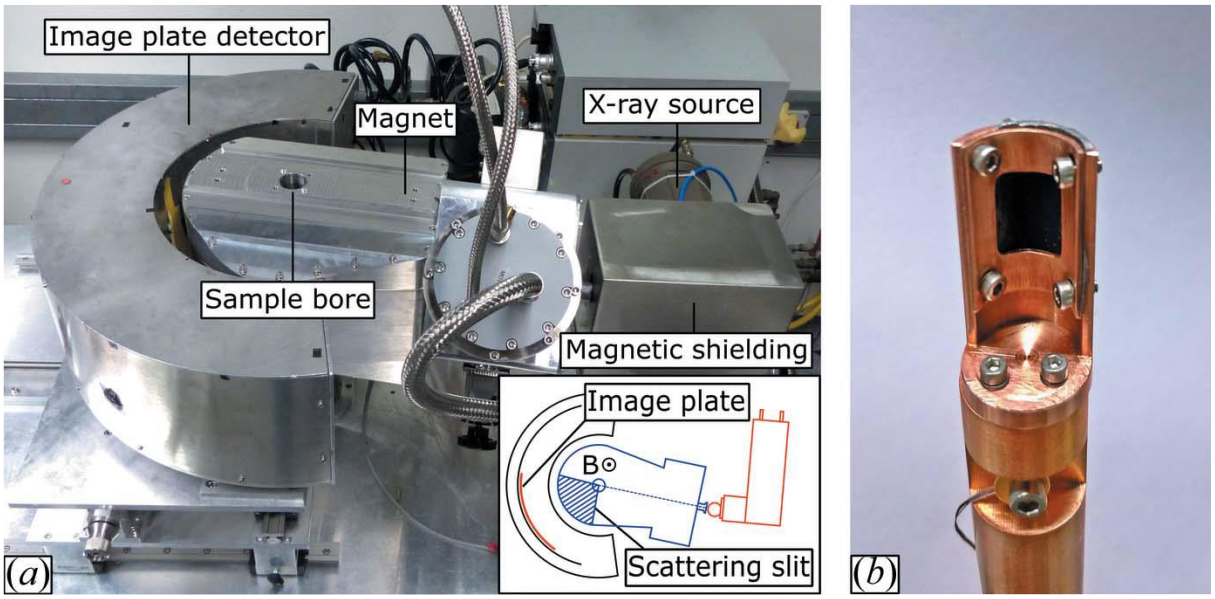

Figure 3.10.: (a) Photograph of the X-ray diffractometer setup with magnet while no sample is mounted with an inset showing a drawing of the scattering geometry and indicating the magnetic field line direction perpendicular to the scattering plane. The shaded area in the inset displays the scattering slit for diffracted x-ray photons. (b) Photograph of the cold finger of the sample cryostat with a powder sample glued onto off-centre cylindrically bent carbon foil.

Figure 3.10(a) shows the instrument which is comprised of two integral components, the X-ray diffractometer and a split-coil superconducting magnet. The diffractometer is arranged in transmission Debye-Scherrer geometry, using a standard long-fine focus Mo x-ray tube (50 kV, 40 mA) for low air scattering and sample absorption. Two monochromator setups are available, a LiF(200) single crystal monochromator for high energy resolution ($K_{\alpha 1}$ only) or a focusing x-ray mirror (AXO DRESDEN) as high flux, low energy resolution (K_{α} doublet) alternative. The sample is positioned 455 mm away from the monochromator in the centre of the detector circle (R = 345 mm). The cold finger of a closed cycle cryostat (Janis Research) serves as a sample holder (see Figure 3.10(b)). Sample powder of an appropriate particle size of <40 μm is glued onto carbon foil for better heat conduction. The carbon foil is cylindrically bent and positioned outside of the rotation axis of the sample holder. The entire cryostat is rotated by ±15 degrees during the measurement so that an effective sample area of ~10 horizontal (H) x 7 vertical (V) mm² is exposed to the 0.3 (H) x 7 (V) mm² x-ray beam. During rotation, the exposed sample area always remains in the centre of the detector circle. Regulation of the sample temperature is possible in the range between T = 20±0.001 and 310±0.01 K. The position sensitive image plate detector *OBI* (216), formerly deployed at beamline *B2* of the *HASYLAB* synchrotron, serves as detection unit. The detector features a 10 mm vertical slit through which the 380 (H) x 40 (V) mm² cylindrically bent image plate (R = 345 mm) is exposed to the diffracted x-ray photons. The image plate allows for the simultaneous collection of diffracted X-rays in a 63° 2θ arc covering reciprocal space up to Q = 8.85 Å^{-1}. A built-in read-out unit scans of the image plate with a spot size of 30 (H) x 300 (V) μm², with an effective step size of 0.002°. Averaging of three neighbouring data points yields the final angular resolution of 0.006°.

The second integral component of the setup is a custom-built compact split-coil

superconducting magnet (HTS-110 Ltd.) (228) positioned between the X-ray source and the detector. The sample cryostat is mounted within a 40 mm wide cylindrical bore. The diffracted X-rays reach the detector through a continuous scattering slit covering 94 degrees, shown in the inset of Figure 3.10(a). The magnetic field of up to 5.5 ± 0.02 T is homogeneous over ± 5 (V and H) mm at the sample position and applied perpendicularly to the scattering plane, either pointing up- or downwards. Stray magnetic fields of up to 13 mT at the filament position of the X-ray source require the source and monochromator units to be shielded by a custom housing made from mu-metal (Sekels GmbH). The housing nearly cancels the shift and intensity loss of the primary beam due to the stray magnetic field.
The control of the diffractometer, sample temperature and magnetic field strength is carried out within the *SPEC* environment (217) which is often used at synchrotron facilities.

3.2.2.2. Setup Characterisation

3.2.2.2.1. Test Systems

We gauged the different energy resolution modes with a NIST 660c LaB_6 standard sample and two examples from promising material classes for magnetocaloric application, $Ni_{50}Mn_{33.4}In_{16.6}$ and $LaFe_{11.6}Si_{1.4}$.
The $Ni_{50}Mn_{50-x}In_x$ family of Heusler alloys has a cubic $L2_1$-type ($Fm\bar{3}m$, $a \approx 6$ Å) high temperature phase in the composition range of $15.5 < x < 25$ (41) and different low temperature martensite structures for compositions $x < 17.0$ (229). Martensitic phase transformations are diffusionless and can be described by “shuffling” or cooperative displacement of several atomic layers creating large supercells (230). Most of these superstructures are incommensurate and can only be approximated by conventional three-dimensional unit cells (231, 232). The low-temperature phase of $Ni_{50}Mn_{33.4}In_{16.6}$ is a 7M incommensurably modulated martensite (226) described in space group $I2/m$ with $a \approx 4.40$ Å, $b \approx 5.62$ Å, $c \approx 4.33$ Å, $\beta \approx 92.76°$, $q = 0.344c^*$. The name 7M originates from the six superstructure satellites appearing in diffraction patterns between main reflections, most easily observed with electron diffraction (230, 233, 234). The bulk sample of $Ni_{50}Mn_{33.4}In_{16.6}$ transforms into the 7M martensite below 230 K, which we determined by thermo-magnetization (M-T) measurement. Rietveld structural analysis of the diffraction patterns containing the 7M modulated phase were performed with the *Jana2006* software package (235).
The $LaFe_{13-x}Si_x$ ($1.0 \leq x \leq 2.0$) family of intermetallic compounds crystallises in the cubic $NaZn_{13}$ structure type in space group $Fm\bar{3}c$ with $a \approx 11.48$ Å and is paramagnetic at room temperature. It exhibits an itinerant electron metamagnetic transition at low temperatures, which is coupled with a large unit cell expansion $\Delta V/V \approx 1\%$, while retaining the $NaZn_{13}$ structure type (236). The nature of the magneto-structural phase transition and the transition temperature T_C depend on the Si content (19). The investigated compound $LaFe_{11.6}Si_{1.4}$ has a first order transition around $T \approx 195$ K, which we determined from an M-T measurement of bulk sample.

3.2.2.2.2. Monochromator Setups

The x-ray diffractometer can be set up in two energy resolution modes realized by two different monochromator setups. A high energy resolution of the primary x-ray beam (Mo $K_{\alpha 1}$ only) is achieved with a LiF(200) single crystal monochromator when the $K_{\alpha 2}$ radiation is cut off with a 0.3 mm slit right before hitting the sample. In case high energy resolution does not provide any

particular advantage for the purpose of the investigation, a high flux alternative in the form of a horizontally bent X-ray mirror can be employed. The mirror monochromator focusses the Mo K_α radiations onto the detector circle. Since an image plate detects the photons, the entire diffraction pattern in an angular range of –5 to 63° is recorded as soon as the sample is exposed to the monochromatic x-ray beam. The read-out unit is part of the detector with a fixed effective step size of 0.002 °, which allows for the same high angular resolution even for short exposure times.

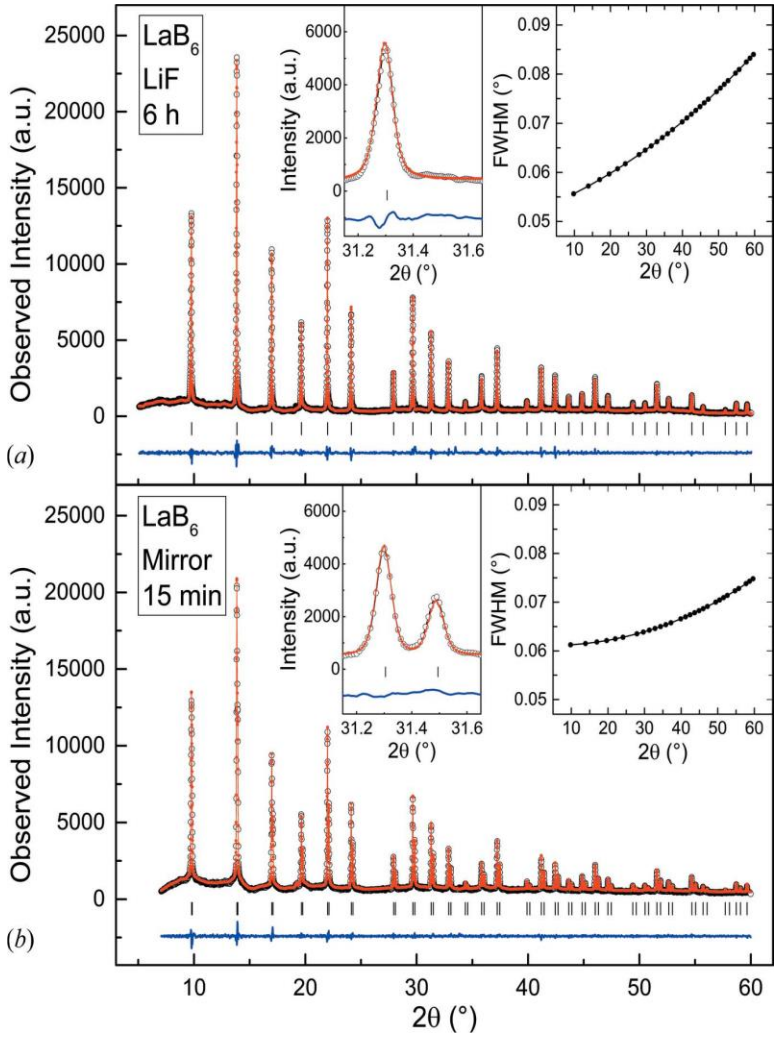

Figure 3.11.: Rietveld refinements of x-ray powder diffraction patterns of the same NIST 660c LaB6 standard sample collected at T = 295 K with (a) a LiF(200) monochromator crystal for 6 h and (b) a focusing x-ray mirror for 15 min. The insets show the 2θ range from ˜31.2 to ˜31.6° to highlight both the difference in energy resolution between the monochromators and the reflection full width at half maximum for these measurements as function of the diffraction angle.

Figure 3.11 shows a comparison between the two monochromator setups using NIST (National Institute of Standards and Technology) 660c LaB_6 standard reference material collected at T = 295 K and the corresponding Rietveld refinements performed with the *FULLPROF* software suite (237). We chose exposure times for each measurement yielding comparable observed intensities. This resulted in a measurement time with the LiF monochromator of 6 h (Figure 3.11(a)), while a 15 min exposure was sufficient for the x-ray mirror (Figure 3.11(b)). The (310) reflection shown in the inset of Figure 3.11(a) illustrates that only Mo $K_{\alpha1}$ radiation was present with the LiF monochromator. In the diffraction pattern in Figure 3.11(b), however, the reflections are clearly split into $K_{\alpha1}/K_{\alpha2}$ doublets and the background beneath each reflection is

slightly larger due to the lower energy resolution of the x-ray mirror. Also shown as insets in Figure 3.11(a) and Figure 3.11(b) are the reflection full widths at half maximum (FWHM) taken from the Rietveld refinement output of the corresponding LaB_6 measurements. For both monochromator setups the reflection FWHM are well below 0.1° even at $2\theta = 60°$, which demonstrates the high angular resolution regardless of the monochromator used. The reflection width for Debye-Scherrer geometry depends on, assuming a nearly parallel primary x-ray beam from the LiF crystal, the beam size at the sample position (238). The x-ray mirror monochromator, however, focusses the beam onto the detector circle in order to cover a large sample area while retaining an excellent angular resolution. Focussing the beam results in slightly narrower reflections than for the LiF monochromator setup with nearly parallel beam.

3.2.2.2.3. **Magnetic Shielding**

The superconducting magnet is not equipped with an iron-yoke to close the magnetic field lines due to space restrictions. All components of the diffractometer are therefore exposed to rather large magnetic stray fields, reaching up to 200 mT at the detector position. The image plate itself is not affected by the magnetic field, but the read-out unit features a photo multiplier tube, which must not be operated in such large magnetic fields to prevent damage. The magnetic field, therefore, has to be ramped down to 0 T before read out of the image plate, slightly prolonging each measurement under magnetic field, see Section 3.2.2.2.4 for more details.

The only other unit of the diffractometer affected by the stray magnetic field is the x-ray source. More precisely, a Lorentzian force is exerted on the accelerated electrons in the x-ray tube. The resulting electron deflexion causes a focal point shift in the x-ray tube and therefore a shift of the primary beam trajectory proportional to the magnetic field strength (76). The divergence slit in front of the sample is fixed, so a primary beam deviation leads to a drop in observed intensity and systematic shift of all reflections. Without additional magnetic shielding of the x-ray tube, the photon flux at the sample position is reduced to zero when the magnet is operated above 3 T. The corresponding stray magnetic field at the x-ray tube filament positioned 350 mm away is $\sim$10 mT. In order to reduce the stray magnetic field a custom housing has been built for the x-ray tube (Sekels GmbH). The housing is made from μ-metal, a soft magnetic Ni/Fe alloy, with 2 mm wall thickness. It surrounds the tube and monochromator unit, leaving a hole for the monochromatic beam. The housing reduces the stray magnetic field strength to 1 mT at the tube filament position when the magnet is powered to 5.5 T. At 1 mT stray magnetic field, the systematic shift of reflections ($<0.02°$) and intensity loss ($<5\%$) of the primary beam are almost negligible.

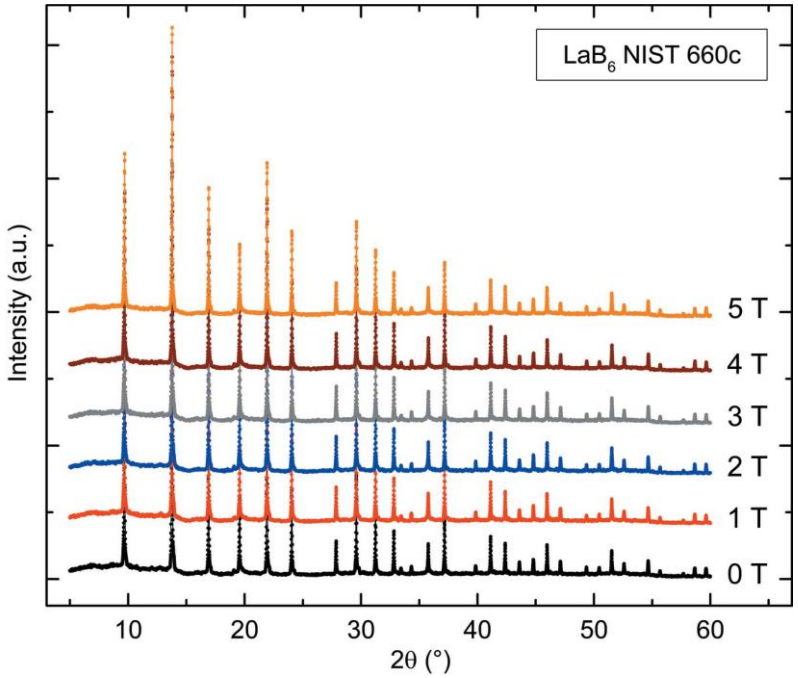

Figure 3.12.: X-ray diffraction patterns of a NIST 660c LaB_6 standard sample collected at $T = 295$ K with Mo $K_{\alpha 1}$ radiation (LiF(200) monochromator) under 0, 1, 2, 3, 4 and 5 T applied magnetic field with additional shielding of the x-ray tube against stray magnetic field.

Figure 3.12 shows the x-ray diffraction patterns of a NIST 660c reference LaB_6 sample collected with the LiF monochromator under magnetic fields of 0 – 5 T for 6 h each after the installation of the magnetic shielding for the x-ray tube. The total observed intensity, relative intensities and reflection positions stay unchanged even at long exposure times. Even the relative intensities of ferromagnetic sample powders stay the same for all magnetic fields, proving the stability of the sample stage and importance of using a strong adhesive to prevent rotation of the powder particles. Measurements with the x-ray mirror monochromator under magnetic field are equally stable.

3.2.2.2.4. Measurement Procedure

The magnet has to be ramped down before read-out of the image plate to prevent damage on the detector photomultiplier tube. Investigations of phase transitions as function of applied magnetic field therefore require a specific experimental sequence to avoid hysteresis effects. A typical procedure for measurements over magnetic field induced phase transitions is: cool to desired temperature with or without magnetic field → x-ray exposure under magnetic field → ramp down the magnet → read-out of the image plate → heat above transition temperature → cool back to desired temperature with or without magnetic field.

3.2.3. Measurement Results

3.2.3.1. High-Resolution Setup

The data quality of the high energy resolution LiF(200) setup at low temperatures and applied magnetic fields was gauged with a sample of $Ni_{50}Mn_{33.4}In_{16.6}$. We mixed the Heusler alloy with NIST 640d certified Si powder to detect possible peak shifts due to deviation of the x-ray beam trajectory in large magnetic fields, as mentioned in Section 3.2.2.2.3.

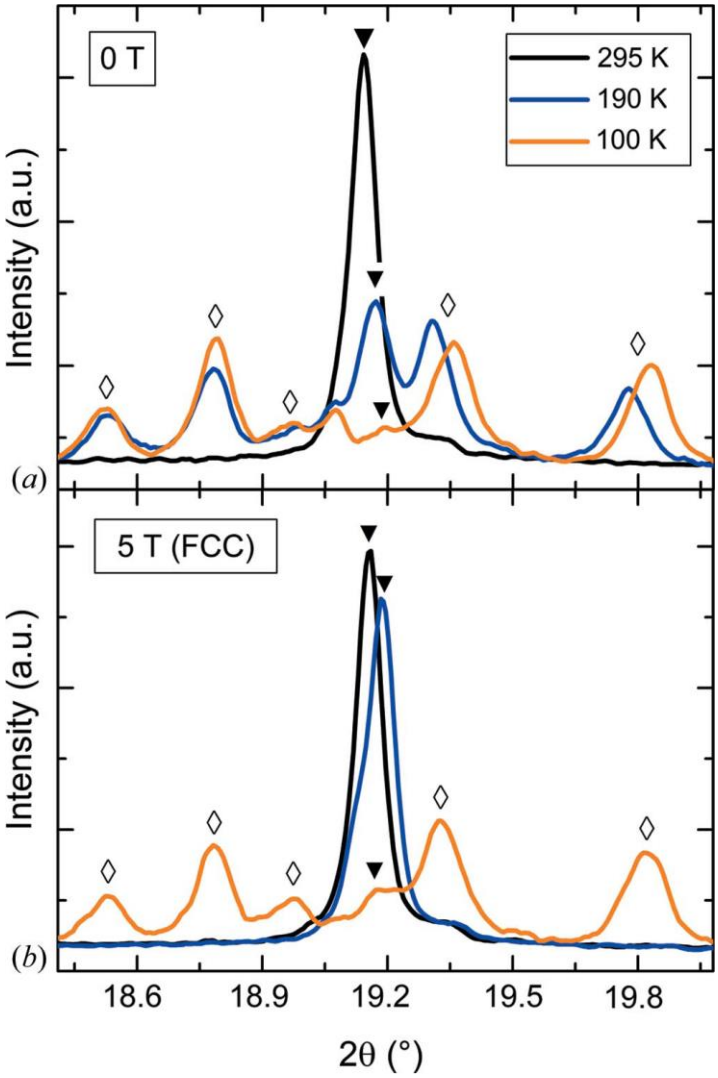

Figure 3.13.: X-ray diffraction patterns of $Ni_{50}Mn_{33.4}In_{16.6}$ in the range from ~18.5 to ~19.9° measured at T = 295, 190 and 100 K under (a) no external magnetic field (ZFC) and (b) 5 T magnetic field applied during cooling (FC). Marked reflections belong to the high-temperature austenite (▼) and low-temperature martensite (◊) phases. We multiplied the intensity of martensite reflections by a factor of 2 for clarity. The starting temperature of the structural phase transition of ~200 K decreases by ~10 K/T during field-cooled cooling.

X-ray diffraction patterns of $Ni_{50}Mn_{33.4}In_{16.6}$ were collected in the temperature range from 295 to 50 K during cooling at magnetic fields of $\mu_0 H$ = 0, 1, 3 and 5 T in 10 K steps. Figure 3.13(a) shows the 2θ range from ~18.5 to 19.9° of the x-ray diffraction patterns collected at T = 295, 190 and 100 K during cooling under $\mu_0 H$ = 0 T. The austenite phase fraction decreases with decreasing temperature while martensite reflections start appearing in the diffractogram collected at T = 200 K (not shown here). The shift of the phase transition temperature compared to the bulk value from T = 230 to 200 K is a known size and stress effect for particles of Heusler alloys (121). At large enough stresses, the transition would be suppressed entirely, a so-called kinetic arrest of the austenite structure (239). Even in the diffraction pattern collected at T = 100 K, 100 K below the onset of the transition, traces of the austenite reflection are present, suggesting a partial arrest of the austenite phase. Figure 3.13(b) shows the same diffractogram range for the sample cooled under $\mu_0 H$ = 5 T. Applying a magnetic field during cooling causes the transition temperature to decrease, as $Ni_{50}Mn_{33.4}In_{16.6}$ exhibits the *inverse* MCE (226). The austenite phase is stabilized down to 140 K (not shown here), resulting in a shift of transition temperature onset of ~10 K/T. At T = 100 K under a magnetic field of 5 T

the remaining intensity of the austenite reflection is larger than at $\mu_0 H = 0$ T suggesting a larger degree of kinetic arrest.
Resolving the features of the split reflections in the x-ray diffraction patterns shown in Figure 3.13 is only possible with the high energy resolution monochromator setup. Presence of the K_α doublet would make it impossible to assign the correct phases to the reflection 'bump' otherwise appearing in this narrow 2θ range of less than 1.5°.

3.2.3.2. High-Flux Setup

The high-flux mirror monochromator setup is a viable alternative whenever the presence of the Mo K_α doublet does not negatively affect the analysis parameters of interest. Several structural parameters can be followed accurately as a function of temperature and applied magnetic field, despite the presence of K_α doublets. Included are phase fractions, lattice parameters, atomic positions and Debye-Waller factors. The x-ray photon flux with the mirror is ~15 times higher than with the LiF(200) monochromator. Exposure times in the range of 15–30 min are therefore sufficient while retaining an excellent angular resolution, as shown in the example diffraction pattern in Figure 3.11(b).
$LaFe_{11.6}Si_{1.4}$ powder was thoroughly ground and sieved to <40 μm particle size and then glued together with NIST 640d Si powder on carbon foil. X-ray diffraction patterns were collected without an applied magnetic field in the temperature range from 295 to 50 K during cooling with varying temperature step sizes. Smaller temperature steps were used close to and during the magneto-structural phase transition, which was roughly estimated for a bulk sample from an *M*–*T* measurement to occur around ~195 K.
The temperature dependence of the lattice parameter of $LaFe_{11.6}Si_{1.4}$ was determined from Rietveld refinements and is shown in Figure 3.14(a). The experimental error bars of the lattice parameters are included, but of the order of 10^{-4} and thus too small to be visible. In the range from 300 to 220 K, the lattice parameter decreases slightly due to thermal contraction but starts to increase below 220 K. A drastic expansion of ~0.8% occurs in the temperature range from 194 to 184 K due to the first order magneto-structural phase transition. The ordering of Fe magnetic moments is accompanied by a large spontaneous volume magnetostriction. Below the Curie temperature T_C, the thermal contraction is overcompensated by the magneto-volume effect due to further increase in Fe magnetic moment resulting in a net unit cell expansion down to 0 K (225).

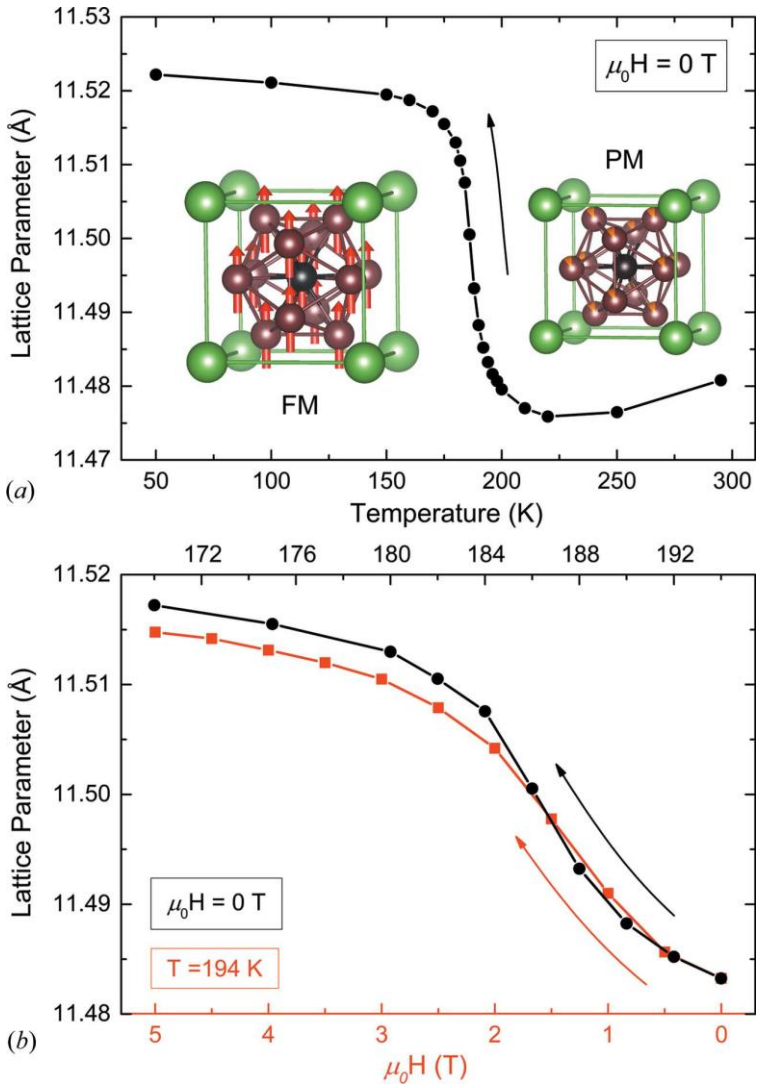

Figure 3.14.: (a) Lattice parameter of $LaFe_{11.6}Si_{1.4}$ from 295 to 50 K under no external magnetic field extracted from x-ray diffraction patterns collected for 30 min each. The first order magneto-structural phase transition in the range from T = ~194 to ~180 K is accompanied by a ~0.8% lattice parameter expansion. The insets show structural models of the paramagnetic (PM) high-temperature and simple ferromagnetic (FM) low-temperature phase. There are three occupied crystallographic sites, one La site (8*a*, green) and two Fe sites (8*b*, grey and 96*i*, brown) of which the 96*i* site has shared occupancy with Si (orange). Only one-eighth of each unit cell is shown for clarity. (b) Lattice parameter in the range of the transition from T = 194 to 170 K (black) and isothermal at T = 194 K as a function of applied magnetic field from 0 to 5 T (red). The transition to the FM phase and associated lattice parameter expansion is induced due to an increase of T_c with increasing magnetic field at a rate of ~4 K/T.

The magneto-structural phase transition can also be induced by applying a magnetic field close to, but still above T_C, as $LaFe_{11.6}Si_{1.4}$ exhibits the *direct* MCE. Figure 3.14(b) shows the comparison of lattice parameter evolution between the temperature and magnetic field induced phase transition of $LaFe_{11.6}Si_{1.4}$. The starting temperature for both series was 194 K. Cooling (black) induces the phase transition and accompanied lattice parameter expansion in the temperature range from ~194 to ~180 K. Applying an increasing magnetic field at T = 194 K (red) induces a similar unit cell expansion. The transition is complete at $\mu_0 H$ = 2.5 T. Higher magnetic fields cause the lattice parameter to only slightly expand further due to an increase in Fe magnetic moment, very similar to the low temperature behaviour without an applied magnetic field.

3.2.4. Summary and Outlook

The installation and application of a new laboratory-based x-ray powder diffractometer with a 5.5 T magnet is presented in detail. Temperature- and magnetic-field induced phase transformations can be followed with two different monochromator setups, which provide either high energy resolution or high photon flux, while retaining an excellent angular resolution regardless of the monochromator used.
To further increase the parameter space, a cryofurnace setup will be installed in the near future for measurements in a continuous temperature range of 700 down to 9 K with or without magnetic field.
In situ studies of phase transformations will be possible with an update of the detector unit to a MYTHEN 1K silicon strip detector (213). MYTHEN 1K detectors are not affected by the stray magnetic field present in our setup and feature up to 1280 Si channels (0.05 x 8 mm^2) with a short read-out time of <0.1 ms and a quantum efficiency for Mo K_α radiations of ≈80%. Collection of diffracted x-ray photons over 8 mm height will result in a significant gain in intensity compared to the current image plate detector. The detector upgrade will therefore enable an even faster collection of x-ray diffraction patterns without the need of ramping down the magnet.

Acknowledgements The authors thank Dr M. Acet (University of Duisburg-Essen) for proving the powder sample of $Ni_{50}Mn_{33.4}In_{16.6}$, and Dr I. Radulov for providing the polycrystalline sample as well as the *M-T* measurements of $LaFe_{11.6}Si_{1.4}$. We also thank H. Mohren, M. Weber and J.-C. Jaud for providing engineering support and technical assistance in the instrument design and realisation.

Funding information The following funding is acknowledged: LOEWE RESPONSE; DFG (grant No. INST 163/442-1 FUGG).

4. Magnetoelastic coupling in $LaFe_{11.6}Si_{1.4}$, MnB and FeB

This chapter focuses on the first set of selected studies conducted with the lab-based x-ray diffractometer with magnet. A synopsis of the main findings resulting from the x-ray diffraction in magnetic fields, and contributions to the research field is then followed by a reprint of the publications. Publications B and C cover the material systems $LaFe_{13-x}Si_x$ and MnB/FeB, respectively. A central point of these publications is the nature of the magnetic phase transition in the investigated compounds. It was found that spin fluctuations are an important driving force in the PM-FM phase transitions in these systems, and, hence, an applied magnetic field has a large influence on their magnetoelasticity.

4.1. Synopsis of Publications B and C

These articles are comprehensive studies of the magnetoelastic coupling in $LaFe_{11.6}Si_{1.4}$, MnB, and FeB. These materials are serious candidates for the technological use of the MCE they exhibit upon their first-order magnetic transition (3). Although the temperature range of the magnetic ordering – and, hence, the application range – is vastly different for these material classes: $LaFe_{11.6}Si_{1.4}$ has a low temperature PM-FM transition at ~200 K, whereas MnB and the isostructural FeB display magnetic ordering at elevated temperatures of ~560 K.

The aim of these studies was to understand the first-order magnetic phase transition, and associated magnetoelastic coupling in these material classes, and correlate the findings with the fact that these materials exhibit large MCE. The materials chosen for these investigations were $LaFe_{11.6}Si_{1.4}$, MnB, and FeB. They share the property of undergoing a first-order magnetic PM-FM phase transition without structural change during the transition.

MnB and the isostructural FeB show remarkably different magnetoelastic behavior, despite having similar FM ordering temperatures. To understand the differences in their magnetoelastic response, MnB and FeB were investigated with high-resolution synchrotron diffraction, and lab-based magnetic-field-dependent high temperature XRD, complemented by DFT calculations in Publication C.

The lattice parameters of orthorhombic MnB were determined from high-temperature, high-resolution synchrotron powder diffraction measurements, and were found to evolve anisotropically, and non-linearly upon heating in the FM phase region. The largest changes were observed in the vicinity of the first-order metamagnetic transition, see Figure 4.1(a). Above T_C, the lattice parameters continued to evolve monotonically. A large ΔS_M of –10.7 J Kg^{-1} K^{-1} at 5 T was determined for MnB for the magnetic ordering temperature region, even without an accompanied structural phase transition, see Figure 4.1(c).

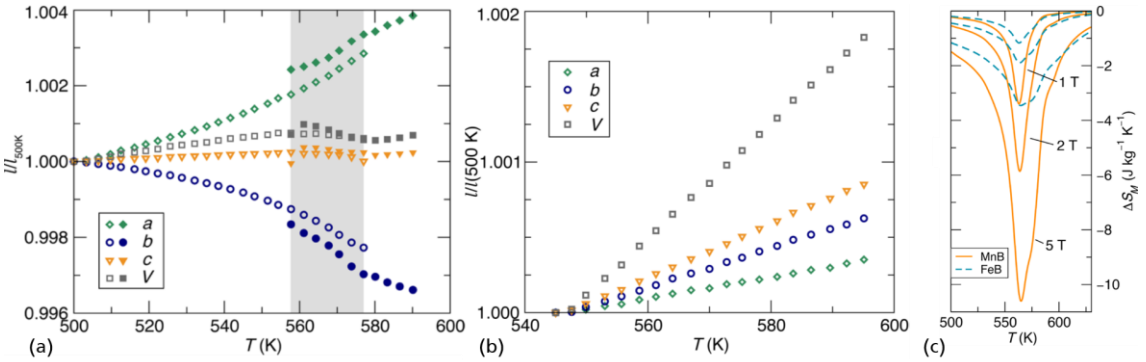

Figure 4.1.: (a) Results of parametric two-phase Rietveld refinement of temperature-dependent synchrotron diffraction data for MnB. Lattice parameters are shown relative to their 500 K value, and show highly anisotropic thermal expansion including large negative thermal expansion in the *b* direction. Furthermore, phase coexistence between two isostructural phases is seen in a 19 K window around the magnetic transition temperature, indicated with a gray box. (b) Lattice parameters from parametric Rietveld refinement of temperature-dependent synchrotron diffraction data for FeB. In contrast to MnB the lattice parameters of FeB all show linear, moderate positive thermal expansion, with no obvious anomaly at the magnetic transition temperature. Some anisotropy in thermal expansion can be seen, evidenced by a larger coefficient of thermal expansion in the *c* direction than the *a* and *b* direction. (c) Comparison of $-\Delta S_M$ of MnB and FeB. Adapted from Publication C.

The isostructural FeB compound behaved very differently. All lattice parameters expanded linearly upon heating in the FM region, and no change of lattice parameter expansion slope could be observed, even over the magnetic transition temperature. ΔS_M of the magnetic transition in FeB showed an about three times smaller magnitude compared to MnB. The results of magnetic-field-dependent XRD revealed a similarly different picture for MnB and FeB. Whereas the metamagnetic transition, and coupled anisotropic lattice parameter changes could be induced by applying a magnetic field close to T_C for MnB, no such response to the magnetic field could be observed for FeB, see Figure 4.2.

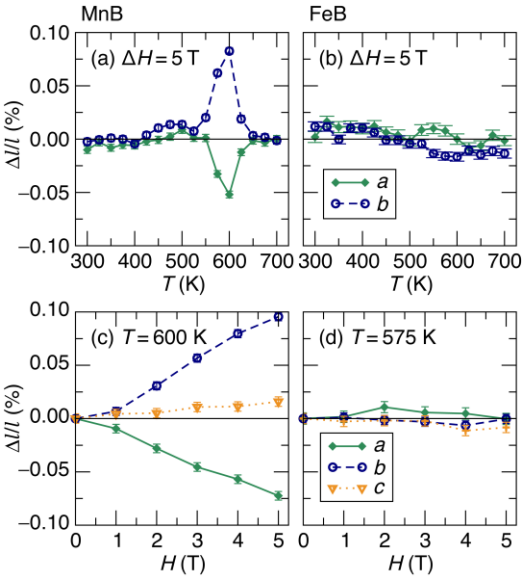

Figure 4.2.: Changes in lattice parameters induced by magnetic field. The top row shows the relative change in lattice parameters upon application of a 5 T field, monitored as a function of temperature. (a) MnB shows large induced magnetoelasticity around its magnetic transition temperature, with a positive change in the *b* lattice parameter and a negative change in the *a* lattice parameter. No changes are clearly resolvable above the noise in FeB (b). The bottom panel shows how the lattice parameters evolve with magnetic field at fixed temperature near the magnetic transition temperature. Once again, the changes are not clearly resolved in FeB (d), but are seen to be large in MnB (c). Reprinted from Publication C.

These fundamental differences between MnB and FeB result from the difference in strain exerted on the B–B bonds by the differently sized metal ions, as was revealed by the DFT calculations. There is a competition between the Mn magnetic moment and the B–B bond length. In the FM region, the large magnetic moment causes a large magnetovolume effect, and neighboring B–B bonds are stretched beyond their "natural" length. Upon heating in the FM phase, fluctuations of the magnetic moments set in, which grow stronger in the vicinity of T_C. These magnetic fluctuations cause a weakening of the magnetic stabilization of the strained B–B bonds. The B atoms are oriented in zigzag chains along the crystallographic *b* axis, and the *b* lattice parameter, hence, shrinks upon relaxation of the B–B bonds. In the PM phase, just above T_C, the B–B bonds are fully relaxed, which was observed by a sudden drastic drop of the *b* lattice parameter. The strain is compensated by an increase of the *a* and *c* lattice parameters, so that the total unit cell volume shows a small non-linearity, but no sudden change, as shown in Figure 4.1(a). No such competition between magnetism and bonding occurs for FeB, presumably because of the smaller atom size of Fe. B–B bonds in FeB are, therefore, less strained by the metal ion, and no relaxation occurs during the magnetic transition. This lack of elastic contribution S_{el} to ΔS_{tot} during the magnetic phase transition of FeB is reflected in the overall smaller absolute value of ΔS_{tot} compared to MnB, see Figure 4.1(c). MnB, however, has a strong magnetoelastic coupling, and both entropy terms, ΔS_{el} and ΔS_M, contribute equally to ΔS_{tot} of the system. The strong magnetoelastic coupling in MnB can, therefore, be directly linked to a large magnetocaloric performance. As the overall volume strain over the metamagnetic transition of MnB is small, and no structural phase transition occurs, the transition itself is less kinetically arrested than systems experiencing large volumetric and microstructural strain, such as Heusler alloys (159, 160, 239). This could explain the small hysteresis of the metamagnetic transition of MnB and FeB.

A similar picture presents itself for $LaFe_{11.6}Si_{1.4}$, which was investigated in Publication B. $LaFe_{11.6}Si_{1.4}$, and the whole $LaFe_{13-x}Si_x$ system up to $x = 2.2$, were thoroughly investigated in the recent past, especially since the discovery of the giant magnetocaloric effect (GME) in these materials (19, 236). It was known that this material class is an itinerant-electron system, and exhibits a metamagnetic PM-FM transition, which is, depending on Si concentration, either of first-order for $x \leq 1.6$, or second-order for $x > 1.6$ (236), but without structural transformation in either case. The driving force of the magnetoelastic phase transition that leads to the GME was investigated in Publication B with (diffuse) neutron scattering and magnetic-field-dependent XRD. Short-range magnetic correlations in the PM state, and the internal magnetic pressure they exert on the structure were determined as the origin of these peculiar material properties.

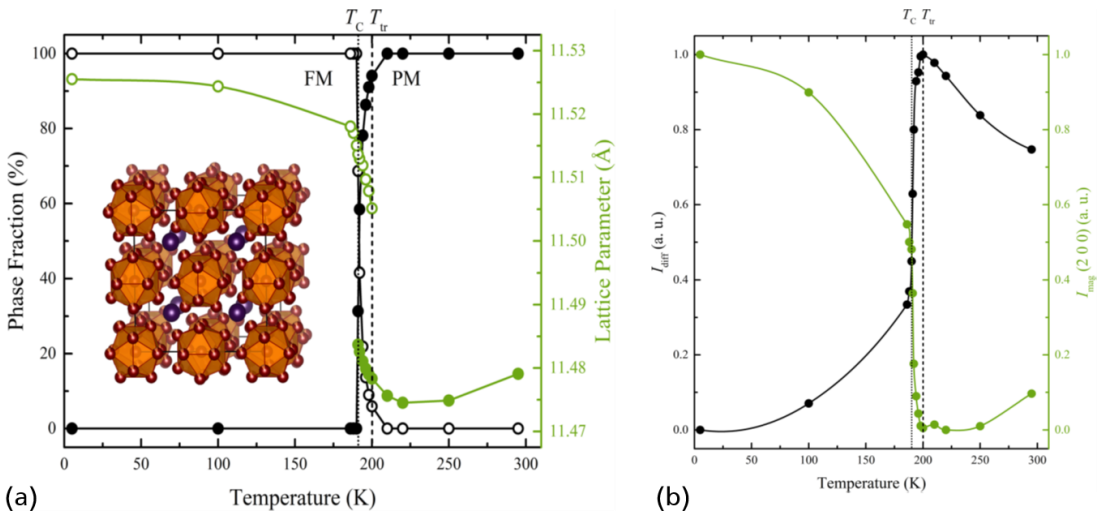

Figure 4.3.: (a) Phase fraction (left) and lattice parameter (right) of the paramagnetic PM (filled circles) and ferromagnetic FM phase (open circles) obtained from Rietveld refinements of neutron diffraction data of bulk $LaFe_{11.6}Si_{1.4}$. The dashed line marks the onset of magnetic transition at temperature T_{tr} = 200 K. The dotted line shows the Curie temperature T_C = 190 K. Symbols are connected by spline curves serving as guides to the eye. The inset shows the crystal structure of $LaFe_{11.6}Si_{1.4}$ with two distinct Fe atoms (wine), Si (orange) partially occupying the Fe position on polyhedral corners and La (purple) occupying large voids in between Fe/Si polyhedra (240). (b) Evaluation of the temperature dependence of magnetic scattering intensity from neutron diffraction data of bulk $LaFe_{11.6}Si_{1.4}$. Integrated magnetic diffuse scattering I_{diff} (left) and normalized 2 0 0 magnetic Bragg reflection intensity I_{mag}(2 0 0) (right) are shown. The dashed line marks the onset of magnetic transition at temperature T_{tr} = 200 K. The dotted line shows the Curie temperature T_C = 190 K. Symbols are connected by spline curves serving as guides to the eye. Adapted from Publication B.

Strong magnetoelastic coupling was observed for $LaFe_{11.6}Si_{1.4}$. Upon cooling, the *a* lattice parameter of the cubic structure contracts non-linearly already as far as 100 K above the metamagnetic phase transition. Thermal contraction of the unit cell volume is overcompensated by magnetic effects already 20 K above T_C, see Figure 4.3(a). Short-range spin fluctuations were determined to be main driving force behind this unusual thermal evolution of *a* lattice parameter. These spin fluctuations were directly observed as diffuse contribution in the neutron scattering pattern of $LaFe_{11.6}Si_{1.4}$ above T_C. Correlation of the integrated diffuse intensity with the magnetic contribution of the (2 0 0) Bragg peak revealed an inverse relation suggesting a magnetic origin of the diffusely scattered signal, see Figure 4.3(b). The fluctuations were present already at 295 K, the highest temperature for the neutron scattering experiments, which is consistent with the fact that thermal contraction at this temperature is already non-linear.

Magnetic-field-dependent XRD with the setup assembled for this work allowed for the determination of forced magnetostriction of the $LaFe_{11.6}Si_{1.4}$ material that was also used for the neutron scattering experiments. Correlation of $\Delta L/L$ with M^2 and M^4 revealed that the magnetic strain follows Takahashi's theory of spin fluctuations (124), see Figure 4.4. Following the interpretation of Takahashi's theory, this correlation of strain *vs*. M^4 proved the growing internal magnetic pressure due to longer correlation lengths of PM spin fluctuations as T_C is approached, which is not explained by magnetovolume coupling as described by classical SEW theory (137). Interestingly, all materials investigated for this part of the work, $LaFe_{11.6}Si_{1.4}$, MnB, and FeB, had a small hysteresis in common, but still exhibited a large ΔS_M at their metamagnetic transition. This behavior is typical for materials close to a tricritical point, which are characterized by being at the border between first- and second-order, and thus having no hysteresis while still displaying large ΔS_M (241–243).

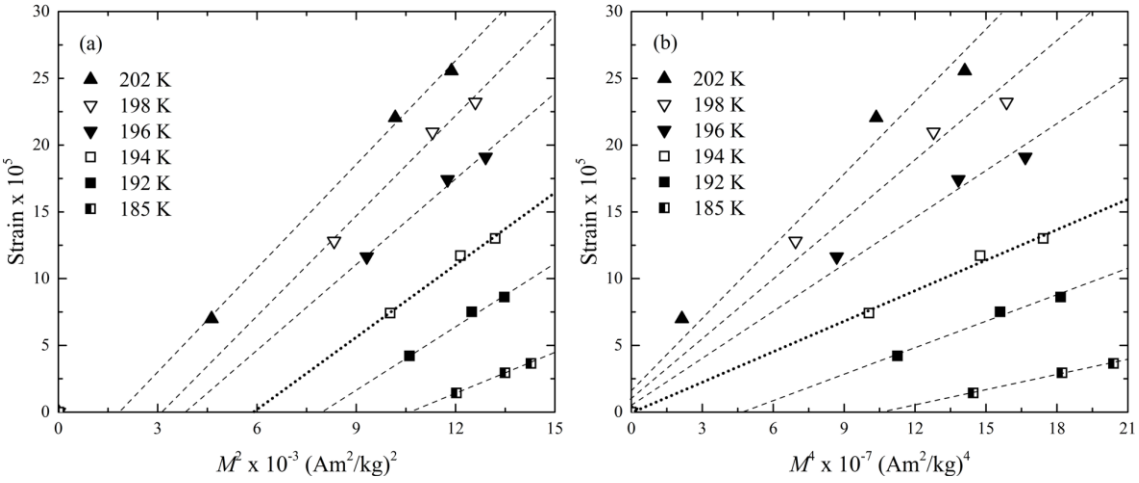

Figure 4.4.: Forced magnetostriction $\Delta L/L$ of $LaFe_{11.6}Si_{1.4}$ determined from magnetic field-dependent XRD (a) as a function of M^2 and (b) as function of M^4. The dashed straight lines are linear fits for each temperature and the dotted line highlights the linear fit at T_C = 194 K. Reprinted from Publication B.

Although being close to a tricritical point, the metamagnetic transitions in the investigated materials were still clearly of first order, as can be observed directly in the diffraction patterns. For first-order transitions a nucleation and growth process of the FM phase in PM matrix is expected (244), and close to T_C there is a distinct two-phase region in which PM and FM phase were present simultaneously, see Figure 4.5. This was most obvious for MnB and $LaFe_{11.6}Si_{1.4}$, for which a clear splitting of the reflections in the diffraction patterns due to the large magnetoelastic effect was observed.

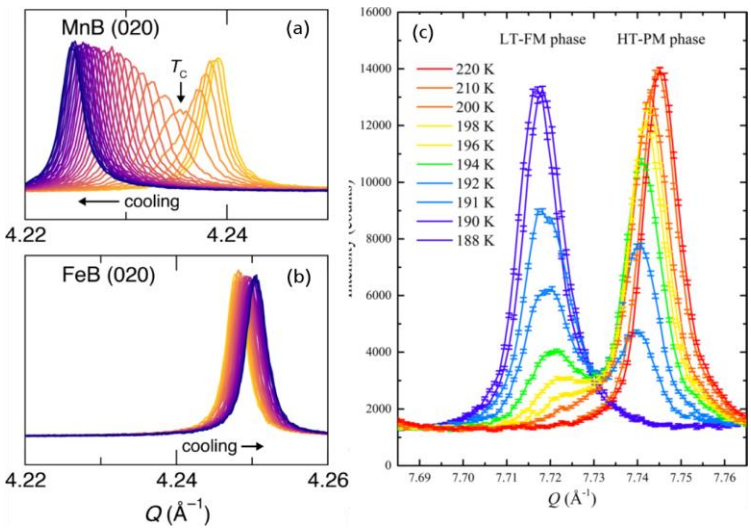

Figure 4.5.: Temperature evolution of the (020) peak in MnB and FeB through the magnetic transition temperature. In MnB, the peak shifts dramatically to the left upon cooling (a), and broadens near the magnetic transition temperature. In FeB, the peak shifts to the right upon cooling (b), including at the magnetic transition temperature. (c) Splitting and shift of high Q nuclear reflection (10 8 6) of $LaFe_{11.6}Si_{1.4}$ on cooling over the magnetic ordering temperature. The high-temperature paramagnetic HT-PM and low-temperature ferromagnetic LT-FM phase coexist in the temperature range from 200 to 191 K. Adapted from Publications B and C.

Over the course of the metamagnetic transition, both systems also showed a distinct evolution of lattice parameters of the PM phase, see Figure 4.1(a) and Figure 4.3(a). From neutron scattering and forced magnetostriction measurements of $LaFe_{11.6}Si_{1.4}$ it was revealed that this abnormal PM lattice evolution close to T_C originates from short-range PM spin fluctuations. Although this was not confirmed through direct measurements for MnB, the lattice parameter

evolution indicates that PM spin fluctuations might also play an important role in its metamagnetic transition.

In fact, with the recent discovery of their role in the first-order phase transition in many other systems (143, 245–247), spin fluctuations could be a universal driving force of all first-order itinerant-electron metamagnetic phase transitions, as was predicted by Takahashi's theory. Specifically, for the $LaFe_{13-x}Si_x$ system it was recently further confirmed that spin fluctuations are the driving force of the phase transition (248). By using quasi-elastic neutron scattering (QENS) and ultra-fast x-ray diffraction experiments it was found that picosecond magnetic fluctuations precede the magnetic transition, and the electronic degree of freedom is responsible for the phase transition. In Publication B, we proposed that the PM fluctuations are increasingly suppressed with larger Si concentrations x, especially for compositions $x>1.6$, which have a second-order transition. The QENS data of $LaFe_{11.6}Si_{1.4}$ and $LaFe_{11.2}Si_{1.8}$ confirm this statement. Spin fluctuations in $LaFe_{11.2}Si_{1.8}$ disappear just above T_C, and are significantly weaker than in $LaFe_{11.6}Si_{1.4}$.

To conclude, in Publications B and C we found that a structural transition is not mandatory in order to achieve large ΔS_{tot}, which is one of the requirements for a large MCE. We found that a strong magnetoelastic coupling, *i.e.*, large change in lattice parameters and response to external magnetic field upon a first-order metamagnetic transition, is the ideal case for a magnetocaloric use. Structural phase transitions over the metamagnetic transition, while allowing for potentially larger ΔS_{tot}, should be avoided, as they are oftentimes accompanied by a large hysteresis due to kinetic arrest. Spin fluctuations in the PM regime are an important driving force of magnetoelastic transitions, but rarely investigated.

Magnetic-field dependent XRD proved to be a vital analysis tool for both investigated material classes, $LaFe_{11.6}Si_{1.4}$ and MnB/FeB, as it provided micro- and crystal structural information that is not accessible from macroscopic bulk sample measurements, and allowed for the determination of anisotropic magnetostriction parameters. Furthermore, XRD enabled a view on each phase separately in the two-phase region, which is a central part of understanding the first-order metamagnetic transitions in the investigated materials. Only the x-ray diffractometer assembled for this work has the necessary temperature range to reach the magnetic phase transition of MnB and FeB at >560 K, compared to other lab-based setups. And the fact that seamless switching between high- and low-temperature measurements is (only) possible with this diffractometer, was especially important for the study on $LaFe_{11.6}Si_{1.4}$.

4.2. Publication B: Direct observation of paramagnetic spin fluctuations in $LaFe_{13-x}Si_x$

Direct observation of paramagnetic spin fluctuations in $LaFe_{13-x}Si_x$

Tom Faske[1], Iliya A. Radulov[1], Markus Hölzel[2], Oliver Gutfleisch[1], Wolfgang Donner[1]

[1]Fachbereich Material- und Geowissenschaften, Technische Universität Darmstadt, Alarich-Weiss-Strasse 2, D-64287 Darmstadt, Germany
[2]Forschungsneutronenquelle Heinz Maier-Leibnitz (FRM II), Technische Universität München, Lichtenbergstrasse 1, D-85747 Garching, Germany

Correspondence email: wolfgang.donner@tu-darmstadt.de

Received 26 August 2019
Accepted 22 November 2019
DOI: 10.1088/1361-648X/ab5a99

Reprinted with permission from *J. Phys: Condensed Matter* 2020, 32, 115802.

Abstract Spin fluctuations are a crucial driving force for magnetic phase transitions, but their presence usually is indirectly deduced from macroscopic variables like volume, magnetization or electrical resistivity. Here we report on the direct observation of spin fluctuations in the paramagnetic regime of the magnetocaloric model system $LaFe_{11.6}Si_{1.4}$ in the form of neutron diffuse scattering. To confirm the magnetic origin of the diffuse scattering, we correlate the temperature dependence of the diffuse intensity with *ac* magnetic susceptibility and x-ray diffraction experiments under magnetic field. Strong spin fluctuations are already observable at 295 K and their presence alters the thermal contraction behavior of $LaFe_{11.6}Si_{1.4}$ down to the Curie temperature of the first-order magneto-structural transition at 190 K. We explain the influence of the spin fluctuation amplitude on the lattice parameter in the framework of the internal magnetic pressure model and find that the critical forced magnetostriction follows Takashi's spin fluctuation theory for itinerant electron systems.

4.2.1. Introduction

The $LaFe_{13-x}Si_x$ system has been widely investigated in recent years because of the giant magnetocaloric effect (GME) that was observed for compositions $1.0 \leq x \leq 1.8$ (19, 236). A potential application of materials exhibiting a GME is magnetic refrigeration – a technology that has the prospect of replacing conventional gas compressor refrigerators due to higher efficiency and environmental sustainability (91, 221, 249, 250).

In our contribution, we present details on the mechanism of the phase transition in the $LaFe_{13-x}Si_x$ system by investigating the magnetostructural coupling and internal pressure related to spin fluctuations in $LaFe_{11.6}Si_{1.4}$.

$LaFe_{13-x}Si_x$ is a ferromagnetic material with a composition-dependent Curie temperature T_C. It is described as an itinerant-electron system in which the magnetic transition from the paramagnetic (PM) to a ferromagnetic (FM) state can be induced by either temperature or magnetic field, if applied just above T_C (236, 251, 252).The magnetic transition is of first-order for compositions $x \leq 1.6$ (253) and, if induced by a magnetic field, is referred to as an itinerant-electron metamagnetic (IEM) transition (236, 252). The change in internal energy during the IEM transition results in the GME and is dominated by changes in the electronic structure (254).

$LaFe_{11.6}Si_{1.4}$ exhibits a first-order PM–FM transition at $T_C \approx 190$ K that is accompanied by a giant spontaneous magnetostriction of ~1.2% due to magnetovolume coupling (106, 225, 253). It crystallizes in the cubic $NaZn_{13}$-type structure ($Fm\bar{3}c$ #226) in which the Fe atoms are located on two inequivalent Wyckoff sites (8*b* and 96*i*) with the La and Si atoms occupying the 8*a* and 96*i* sites, respectively(255). The PM and FM phases are isostructural, apart from the difference in unit cell volume. The magnetically ordered phase has a simple FM spin structure and therefore no magnetic superlattice reflections appear in neutron diffraction patterns of the FM phase (225).

The paramagnetic state of $LaFe_{13-x}Si_x$ was recently described with a disordered local moment (DLM) model with a fluctuating Fe moment of ~1.9 μ_B (254, 256). In accordance with this model, the temperature dependence of the reciprocal paramagnetic susceptibility χ^{-1} was found to obey the Curie-Weiss (CW) law for compositions $x>1.6$ (253, 257–259). Compositions of $LaFe_{13-x}Si_x$ with $x \leq 1.6$ also show CW behavior in the high-temperature regime, but in addition they exhibit a paramagnetic Curie temperature θ_p, as defined by the Bean-Rodbell model of magnetoelastic coupling (253, 260). $\theta_p < T_C$ is characteristic for first-order transitions, and the larger $T_C - \theta_p$, the stronger the first-order character of the transition. Spin fluctuations terminate the FM state for first-order transitions before magnetic excitations realize the disappearance of collective magnetization and PM and FM phase therefore have different Curie temperatures (259). For second-order transitions $\theta_p = T_C$ and no deviation from CW behavior is observed (253).

The two main contributions to spin fluctuations are thermally excited spin fluctuations and zero-point fluctuations. On cooling, one would expect the amplitude of thermal spin fluctuations ξ_{th} to decrease, whereas the amplitude of zero-point fluctuations ξ_{zp} increases, resulting in a net conservation of the squared sum $\xi_{th}^2 + \xi_{zp}^2 = \text{const}$ (124, 132).

Spin fluctuations as a driving force for magnetoelastic phase transitions have recently been discussed for other GME materials, such as rare earth manganites (141, 142), the $(Mn,Fe)_2(P,Si)$ system (143, 144) and Heusler compounds (39, 145, 146).

First-order phase transitions are generally described in terms of their Landau free energy. Spin fluctuations in itinerant-electron systems require a renormalization of the expansion coefficients in a Landau theory (251, 261) and had been introduced in the self-consistent renormalization

(SCR) spin fluctuation theory by Moriya and Kawabata (35, 124). The effect of spin fluctuations can be interpreted as an internal magnetic pressure that modifies the thermal expansion behavior (261, 262). A deviation from linear thermal expansion can therefore be seen as evidence for the presence of strong spin fluctuations as Wada *et al.* have demonstrated for $Y(Mn_{1-x}Al_x)_2$ and $Y_{1-x}Sc_xMn_2$ (140).

Takahashi proposed a theory describing the effect of spin fluctuations on the magnetic properties of itinerant-electron systems (124, 135). According to Takahashi's theory, the magnetic pressure of spin fluctuations expresses itself in a fourth power of magnetization M^4 dependence of the forced magnetostriction $\Delta L/L$ at T_C as seen in the following equation:

$$\frac{\Delta L}{L} = \frac{\nu_h(M, T_C)}{\nu_0} = C \cdot \xi_{th}(0,T_C) \cdot \frac{M^4}{M_0^4(0)} \tag{4.1}$$

where ν_0 and $\nu_h(M, T_C)$ represent the spontaneous and magnetic field-dependent volume contribution to magnetostriction, respectively. C is constant under isothermal conditions and $\xi_{th}(0,T_C)$ is the amplitude of thermal spin fluctuations in zero field. $M_0(0)$ represents the spontaneous magnetization and M the magnetization in a magnetic field.

The effect of spin fluctuations can not only be inferred indirectly in macroscopic variables like the volume or the magnetization: the direct proof for the occurrence of fluctuations is their detection by scattering methods.

Neutron scattering is a universal tool to investigate spin structures, both localized in a magnetically ordered system and disordered in the form of spin waves. The intensity of magnetically scattered neutrons in general is defined by the following equation (4.2): (263)

$$I_{mag}(Q) \sim \left|f_{mag}(Q)\right|^2 \sum_{\alpha,\beta} S^{\alpha,\beta}(Q,\omega)(\delta_{\alpha,\beta} - \widehat{Q}_\alpha \widehat{Q}_\beta) \tag{4.2}$$

where $f_{mag}(Q)$ is the magnetic form factor, Q is the momentum transfer, ω is the energy transfer and the summation runs over the Cartesian directions. $S^{\alpha,\beta}(Q,\omega)$ is the magnetic scattering function which is proportional to the space and time Fourier transform of the spin-spin correlation function. The term $\delta_{\alpha,\beta} - \widehat{Q}_\alpha \widehat{Q}_\beta$ describes that neutron only probe the components of spin perpendicular to Q. If the energy of scattered neutrons is not analyzed, $I_{mag}(Q)$ is a snapshot of the spin correlations in reciprocal space.

In this contribution, we provide direct experimental evidence for the important role of itinerant spin fluctuations in the magnetic phase transition of $LaFe_{11.6}Si_{1.4}$. We report on evidence for paramagnetic spin fluctuations in $LaFe_{11.6}Si_{1.4}$ observed in the form of magnetic diffuse scattering in our temperature-dependent neutron powder diffraction data. Furthermore, we use x-ray diffraction to detect the effect of spin fluctuations on the lattice parameter, thereby verifying the "internal pressure" effect of the fluctuations. Lastly, we confirm that the short-range magnetic correlations in $LaFe_{11.6}Si_{1.4}$ follow Takahashi's theory of spin fluctuations in itinerant-electron systems by using the example of the magnetization dependence of critical forced magnetostriction.

4.2.2. Experimental

4.2.2.1. Sample Preparation

$LaFe_{11.6}Si_{1.4}$ was synthesized from elemental materials with commercial purity in a Al_2O_3 crucible using an induction furnace, as described in (264). To prevent oxygen contamination, the elemental lanthanum was arc melted prior to induction melting with the other elements. To compensate for lanthanum losses due to evaporation, an excess of 7% La was added. For

better homogeneity, the sample was re-melted twice in an induction oven under Ar pressure of 1 bar. Afterwards the ingots were wrapped in Mo foil and sealed in fused silica tubes under 0.3 bar Ar pressure at RT. To form the desired 1:13 phase ($NaZn_{13}$-type structure), the ingots were annealed for 7 days at 1373 K in a resistive tube furnace and subsequently quenched in water.

4.2.2.2. Magnetic Characterization

The magnetic moment measurements were performed using the vibrating sample magnetometer option of a QD PPMS 14 (Quantum Design Physical Property Measurement System, LOT-QuantumDesign GmbH). A needle shaped sample, cut from the bulk specimen, was used in order to minimize the demagnetization factor due to shape anisotropy. The PM–FM transition temperature T_C was determined from the temperature dependent magnetization measured in a magnetic field of 500 Oe from 300 to 100 K with a temperature sweep rate of 1K/min.
The *ac* magnetic susceptibility was measured by means of an ACMS option of a QD PPMS 14 in an applied magnetic field of 10 kOe. The temperature dependent measurement was performed on cooling from 350 to 100 K in an alternating excitation field with frequency of 1 kHz and amplitude of 10 Oe.

4.2.2.3. Neutron Diffraction

Unpolarized neutron diffraction experiments were performed at the high-resolution diffractometer SPODI at research reactor FRM II, Garching (265). The wavelength was set to $\lambda = 1.5482$ Å by a stack of Ge(551) monochromator crystals. A cylinder (11 x 18 mm, ~11 g) cut from polycrystalline bulk $LaFe_{11.6}Si_{1.4}$ was placed in a cylindrical vanadium container and into a closed-cycle helium cryostat. Diffraction patterns were collected on cooling in the temperature range from 295 to 5 K between 3.2 and 160° in 2θ ($Q = 8.0$ Å^{-1}) with a step size of 0.05°. Rietveld analyses of the neutron diffraction patterns were performed up to $2\theta = 135°$ ($Q = 7.5$ Å^{-1}) using the *FULLPROF* program, which allows for the simultaneous refinement of structural and magnetic profiles (198, 237). The diffraction range Q>7.5 Å^{-1} was excluded from Rietveld analysis due to instrument-related broadening of the reflections, which could not be modelled using the same peak shape function as for the rest of the pattern.

4.2.2.4. X-ray Diffraction

Temperature and magnetic field-dependent x-ray diffraction patterns were collected on a custom-built diffractometer in transmission geometry (Mo K_α radiation, $\lambda_1 = 0.70932$ Å, $\lambda_2 = 0.71332$ Å, MYTHEN2 R 1K detector (Dectris Ltd.), 2θ range from 7 to 67°, step size of 0.009°). A detailed description of the diffractometer can be found in (1). A piece of bulk $LaFe_{11.6}Si_{1.4}$ from the neutron diffraction experiments was crushed and mixed with a NIST640d standard reference silicon powder for correction of geometric errors. The temperature was controlled by means of a closed-cycle helium cryofurnace (SHI Cryogenics Group) in the range from 400 to 12 K. The cooling rate was 2 K/min and the sample temperature was stabilized for 10 min before data collection. Measurements were performed for zero-field cooling (ZFC) and field-cooled cooling (FCC) protocol under 1.0, 3.0 and 5.0 T applied magnetic field. Structural parameters were again refined using the Rietveld option of the *FULLPROF* software.

4.2.3. Results and Discussion

4.2.3.1. Neutron diffraction

In order to probe the magnetostructural coupling in $LaFe_{11.6}Si_{1.4}$, we performed temperature-dependent neutron diffraction experiments. Diffraction patterns of bulk $LaFe_{11.6}Si_{1.4}$ were collected on cooling between 295 K and 5 K. Typical neutron diffraction patterns and corresponding Rietveld analyses are shown in Figure 4.6(a) for T = 295 K and Figure 4.6(b) for T = 5 K. Phase purity is confirmed aside from ~1 wt.% fraction of α-Fe side phase. The small goodness-of-fit (χ^2) and residual (R) values from Rietveld refinement of profile (R_f), peak positions (R_{Bragg}) and (below T_C) magnetic structure (R_{mag}) suggest an excellent data quality and a well-fitting structure model. The temperature of the onset of magnetic transition T_{tr} = 200 K is identified by a splitting of all Bragg reflections, see Figure 4.6(c). PM and FM phase coexist in the temperature range from 200 to 191 K and the magnetic transition is complete at the Curie temperature T_C = 190 K.

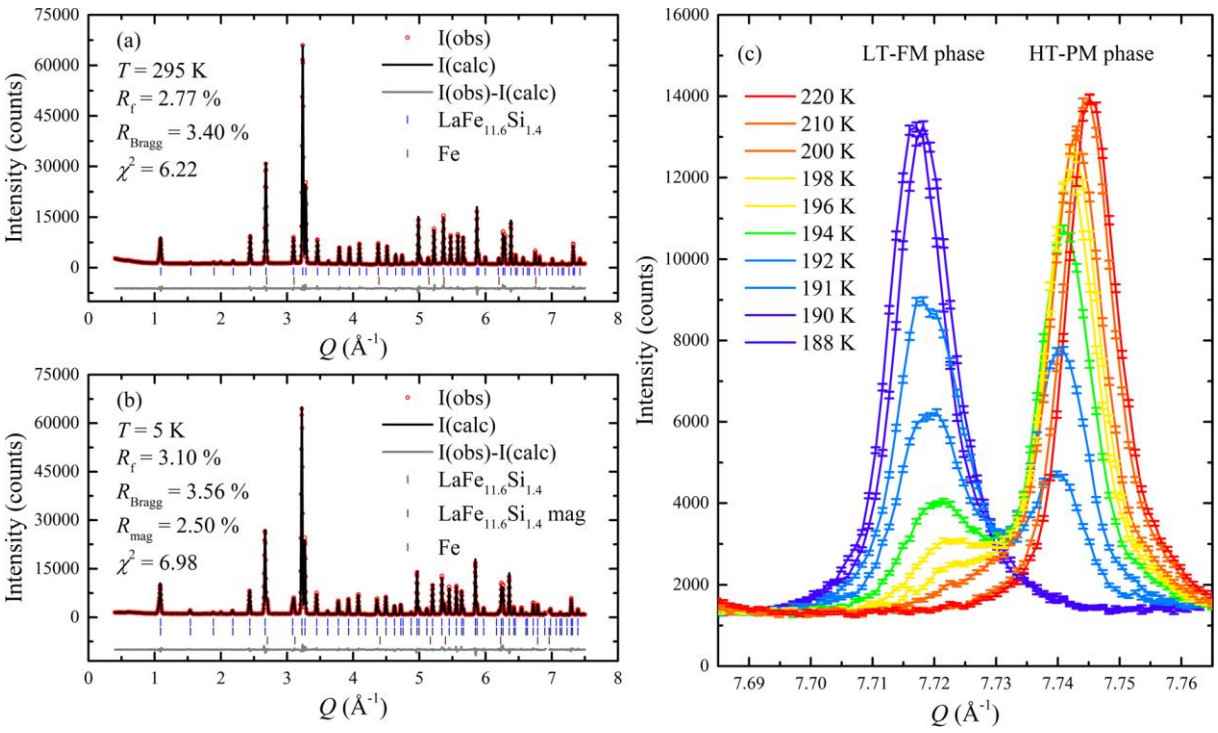

Figure 4.6.: Rietveld refinement of the neutron diffraction pattern of $LaFe_{11.6}Si_{1.4}$ collected at (a) T = 295 K and (b) T = 5 K. Observed (red dots), calculated (black line) and difference (grey line) patterns are given, as well as reflection positions for $LaFe_{11.6}Si_{1.4}$ (blue), magnetic $LaFe_{11.6}Si_{1.4}$ (dark blue) and a side phase of ~1 wt.% α-Fe (wine). (c) Splitting and shift of high Q nuclear reflection 10 8 6 of $LaFe_{11.6}Si_{1.4}$ on cooling over the magnetic ordering temperature. The high-temperature paramagnetic HT-PM and low-temperature ferromagnetic LT-FM phase coexist in the temperature range from 200 to 191 K.

First traces of the FM phase appear in the neutron diffraction pattern at T_{tr}, identified by a splitting and shift of all reflections to lower Q due to giant spontaneous magnetostriction, see Figure 4.6(c). The observed coexistence of PM and FM phase is characteristic for a nucleation and growth process of first-order phase transitions, as it is expected for $LaFe_{11.6}Si_{1.4}$ (225, 253). The lattice parameter of the FM phase a(FM) is significantly larger than that of the PM phase a(PM), see Figure 4.7 and it further expands on cooling in the two-phase region, due to the increasing spontaneous Fe magnetic moment (225).

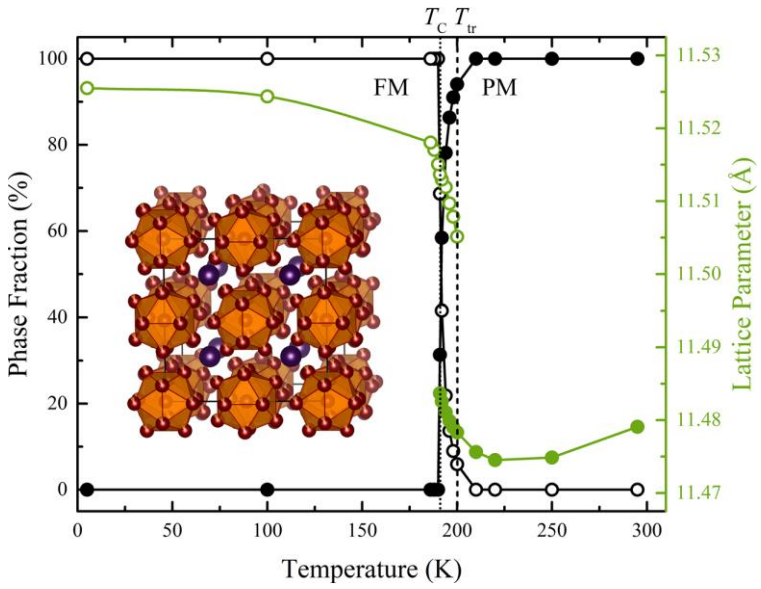

Figure 4.7.: Phase fraction (left) and lattice parameter (right) of the paramagnetic PM (filled circles) and ferromagnetic FM phase (open circles) obtained from Rietveld refinements of neutron diffraction data of bulk $LaFe_{11.6}Si_{1.4}$. The dashed line marks the onset of magnetic transition at temperature T_{tr} = 200 K. The dotted line shows the Curie temperature T_C = 190 K. Symbols are connected by spline curves serving as guides to the eye. The inset shows the crystal structure of $LaFe_{11.6}Si_{1.4}$ with two distinct Fe atoms (wine), Si (orange) partially occupying the Fe position on polyhedral corners and La (purple) occupying large voids in between Fe/Si polyhedra (240).

Apart from ~1% volume expansion, the crystal structure of the PM phase of $LaFe_{11.6}Si_{1.4}$ is retained in the FM phase. Figure 4.8(a) shows a contour plot of the temperature dependence of the low Q region from 295 to 5 K. The neutron diffraction patterns of the PM and FM phases display the same number of reflections, however, several Bragg reflections such as 2 0 0 and 2 2 0 gain intensity during the magnetic transition.

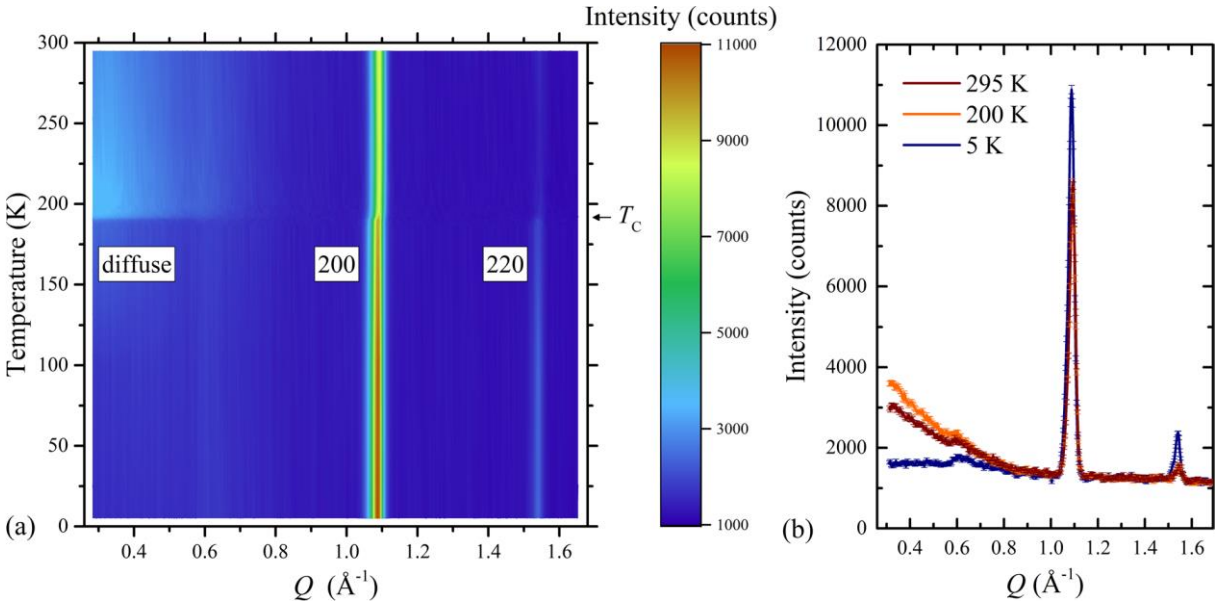

Figure 4.8.: (a) Contour plot of neutron diffraction data measured for bulk $LaFe_{11.6}Si_{1.4}$ on cooling in the temperature range 295 to 5 K. Small angle diffuse scattering (top-left) and Bragg reflections 2 0 0 and 2 2 0 are marked. (b) Raw neutron diffraction patterns collected at 295, 200 and 5 K.

Strong diffuse intensity I_{diff} is present above T_C in the low Q range up to $Q \approx 0.8$ Å^{-1}, see Figure 4.8(b). On cooling from 295 K, I_{diff} first increases and peaks at $T = 200$ K $= T_{tr}$ but sharply

drops thereafter. Simultaneously to the decrease in I_{diff}, the 2 0 0 and 2 2 0 Bragg reflections gain intensity due to FM contributions. The integrated intensity of Bragg reflections I_{Bragg}(h k l) in neutron diffraction consists of two contributions: I_{Bragg}(h K l) = I_{nuc}(h K l) + I_{mag}(h k l), where I_{nuc}(h k l) is the nuclear and I_{mag}(h k l) the magnetic contribution due to long-range spin ordering. The close relation between I_{diff} and I_{mag}(h k l) is a hint towards a magnetic origin of I_{diff}, such as short-range FM correlations. Neutron diffraction studies published previously on the $LaFe_{13-x}Si_x$ system, however, do not show the low Q region and thus do not allow for comparison with our work (225, 255, 266).

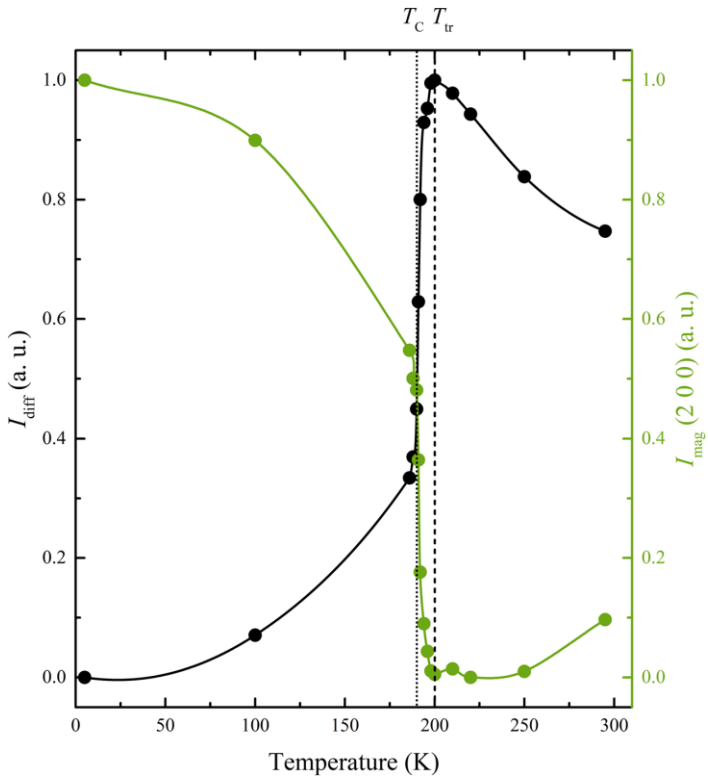

Figure 4.9.: Evaluation of the temperature dependence of magnetic scattering intensity from neutron diffraction data of bulk $LaFe_{11.6}Si_{1.4}$. Integrated magnetic diffuse scattering I_{diff} (left) and normalized 2 0 0 magnetic Bragg reflection intensity I_{mag}(2 0 0) (right) are shown. The dashed line marks the onset of magnetic transition at temperature T_{tr} = 200 K. The dotted line shows the Curie temperature T_C = 190 K. Symbols are connected by spline curves serving as guides to the eye.

We integrate the area under the curve like $I_{diff} = \int_{0.3\ Å^{-1}}^{0.8\ Å^{-1}} I(Q)\ dQ$ in order to quantify the diffuse scattering contribution, see Figure 4.9. Sizable I_{diff} is already present at 295 K (1.55 T_C). Upon cooling, I_{diff} increases approaching T_C and has a maximum at T_{tr} = 200 K (1.05 T_C). I_{diff} sharply drops with the appearance of FM phase in the temperature range between T_{tr} and T_C and is converted into I_{mag}(h k l). At T = 186 K (0.98 T_C), however, despite the magnetic transition being complete, I_{diff} is still ~33 % of the value at T_{tr}, as can be seen in Figure 4.9. A further conversion of the remaining I_{diff} to I_{mag}(h k l) continues down to 5 K. An explanation for significant I_{diff} being present below T_C is that the magnetization is not yet saturated. Consequentially, the conversion of remaining I_{diff} to I_{mag}(h k l) continues in the FM phase down to 5 K. The further increase in I_{diff} far below T_C indicates that the localized Fe magnetic moment increases up to its saturation value of 2.16 μ_B at 0 K (225).

4.2.3.2. Magnetization and *ac* magnetic susceptibility

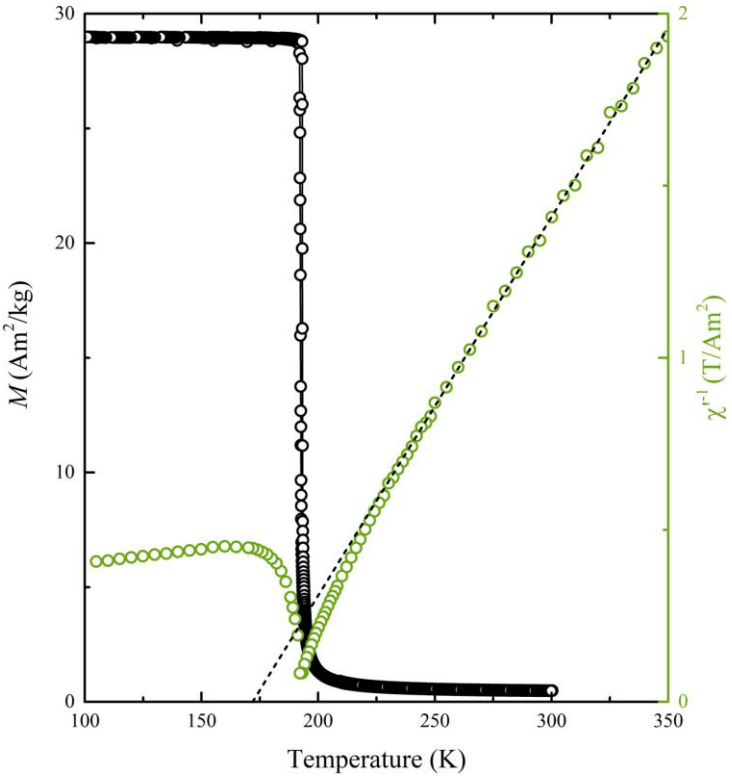

Figure 4.10.: Temperature dependence of the magnetization M (left) of bulk $LaFe_{11.6}Si_{1.4}$ under an applied field $\mu_0 H$ = 0.05 T and the inverse of the real part of the ac susceptibility χ^{-1} (right) measured at 1 T. The dashed line shows a linear fit of χ^{-1} in the paramagnetic regime according to Curie-Weiss law.

As shown in Figure 4.10, the $LaFe_{11.6}Si_{1.4}$ compound shows a sharp PM–FM transition in the *dc* magnetization measurements with a small thermal hysteresis of ~1 K. We can conclude from the sharp transition that the sample is chemically homogeneous. The small remnant magnetization above T_C proves that only low amounts of FM impurities such as α-Fe are present. T_C = 191 K is in perfect agreement with T_C obtained from neutron diffraction.

The spontaneous magnetization amounts to 22.62 μ_B/f.u. at 5 K; consequently, one can extract an average value for the mean Fe magnetic moment. The average moment per Fe atom (μ_{Fe}) is estimated to be 1.95 μ_B/Fe. Magnetic measurements have been recorded at high temperatures, well above the magnetic transition temperature, in order to investigate the magnetic behavior of Fe in the paramagnetic state. At high temperatures, the thermal variation of the reciprocal magnetic susceptibility shows a CW behavior. A linear fit of the experimental data according to a CW law leads to a Curie constant C = 67.9 μ_BK/f.u.T. The effective paramagnetic moment μ_{eff} deduced from the Curie constant is found to be 5.10 μ_B/Fe. The investigation of the magnetic properties in both paramagnetic and ferromagnetic states has led to significantly different values of Fe magnetic moments in magnetically ordered state (μ_{Fe} = 1.95 μ_B/Fe) and in the disordered state (μ_{eff} = 5.10 μ_B/Fe). This leads to a number of spin S_p = 2.10 and S_0 = 0.975 in the paramagnetic and the ferromagnetic state respectively and a corresponding Rhodes-Wohlfarth ratio $r = S_p/S_0$ of 2.15. This points to the itinerant character of magnetism in the present compound.

Since the obtained value of r is larger than 1, we expect that the amplitude of local spin fluctuations varies significantly with temperature in this system, according to the self-consistent renormalization theory of spin fluctuations (267–269). In this model, two extreme regimes

characterized by different values of the Rhodes-Wohlfarth ratio *r*, are described: (i) local moment limit and (ii) weakly ferromagnetic limit. In the local moment limit we have $r = 1$ and in the opposite weakly ferromagnetic limit the theoretical model predicts a divergence of this ratio.

The inverse of the real part of the *ac* susceptibility χ'^{-1} shows CW behavior in the PM regime as predicted for itinerant ferromagnets by Moriya and Kawabata (35) and for the $LaFe_{13-x}Si_x$ system in particular by Fujita (256), but deviates from linearity at $T_{CW} = 225$ K. This change of slope in χ^{-1} close to T_C is expected for first-order transitions according to the Bean-Rodbell model (260). We extracted a paramagnetic Curie temperature $\theta_p = 170$ K that is close to the value reported for $LaFe_{11.8}Si_{1.2}$(253). The large difference $T_C - \theta_p$ confirms the strong first-order nature of the phase transition.

4.2.3.3. Magnetic field and temperature-dependent x-ray diffraction

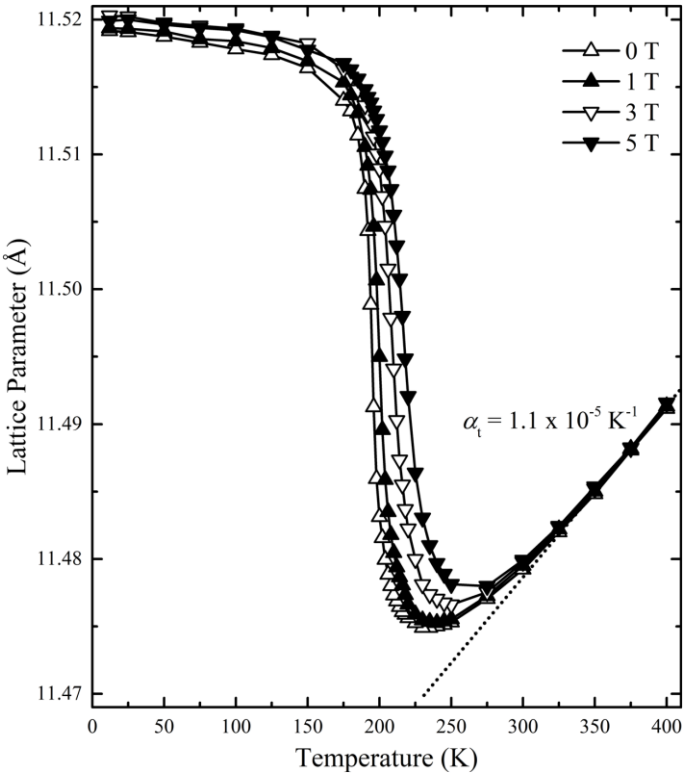

Figure 4.11.: Lattice parameter of $LaFe_{11.6}Si_{1.4}$ powder determined by x-ray diffraction for zero-field cooling (ZFC) and field-cooled cooling (FCC) protocol in magnetic fields of 1, 3 and 5 T. The dotted line shows the extrapolation of linear thermal contraction above T_C.

Figure 4.11 shows the thermal evolution of the lattice parameter of $LaFe_{11.6}Si_{1.4}$ determined from x-ray powder diffraction on cooling for different magnetic fields. Extracting separate lattice parameters a(PM) and a(FM) in the transition region was not possible because of the lower angular resolution of our x-ray compared to our neutron diffraction experiments. The PM–FM transition of $LaFe_{11.6}Si_{1.4}$ powder is not as sharp as for bulk material, which is a known effect for a powder due to decoupling of the particles (121). We found the thermal expansion to be linear for $T>300$ K with an expansion coefficient $\alpha_t = 1.1 \times 10^{-5}$ K^{-1}, independent of magnetic field. Jia *et al.* reported a value of $\alpha_t = 8.2 \times 10^{-6}$ K^{-1} (253) for the temperature range 300–250 K. Our data show, however, that the thermal expansion is not linear in the temperature range used for determination of the reported α_t. Deviation from linear behavior

starts at $T \approx 300$ K, most likely due to the appearance of short-range magnetic correlations. Overcompensation of thermal contraction under zero applied field starts at the temperature $T_{comp} = 225$ K, resulting in a net increase in a(PM) upon further cooling and a sharp expansion at $T_C = 194$ K.

Applying a magnetic field during cooling shifts T_C towards higher temperatures at a rate of ~ 4 K T^{-1}, which is consistent with previous studies. (236, 253) The magnetic transition is broader for larger magnetic fields due to an increasing second-order character of the IEM (236). Simultaneously with T_C, T_{comp} also increases with increasing magnetic field, whereas the high-temperature behavior above $T>300$ K is identical for all magnetic fields. We assume that the magnetic field enhances the short-range magnetic correlations in the PM regime at $T<300$ K of $LaFe_{11.6}Si_{1.4}$. Therefore, T_{comp} increases with increasing field – eventually inducing the IEM transition at $T>T_C(0\ T)$. Below T_C we observe a small increase in a(FM) with increasing magnetic field due to forced magnetostriction and saturation of magnetization far above 0 K.

4.2.4. Discussion

4.2.4.1. Diffuse Scattering

We integrate the diffuse signal shown in Figure 4.8(b) up to $Q = 0.8$ Å^{-1}, which is justified by the fact that the maximum momentum transfer of spin fluctuations in Fe is $Q_{max} \approx 0.75$ Å^{-1} (270). Spin fluctuations transition into the Stoner continuum at larger Q values and our I_{diff}, therefore, covers all essential magnetic fluctuations. We consider the fluctuation-dissipation theorem (271) to show that I_{diff} in our neutron diffraction data is indeed a good proxy for ξ. However, the maximum of the as-observed I_{diff} at T_{tr} does not necessarily translate to a maximum of ξ. The reason being that the PM–FM transformation begins at T_{tr} and spans over a 10 K temperature window. I_{diff} decreases proportionally to the PM fraction (W_{PM}) between T_{tr} and T_C whereas I_{mag}(h k l) increases proportionally to the FM fraction (W_{FM}). If we assume that I_{diff} originates only from the PM phase, we can correct I_{diff} above T_C by dividing through W_{PM}.

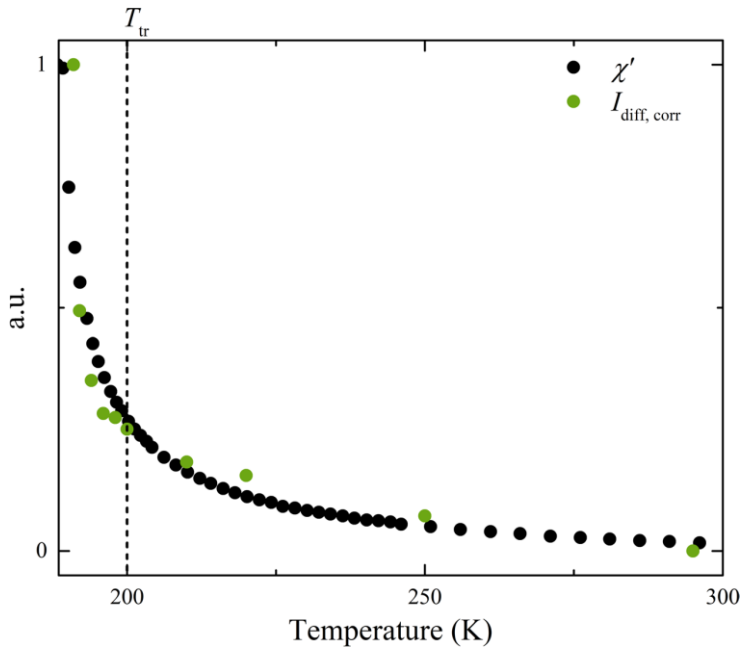

Figure 4.12.: Comparison of the real part of the *ac* magnetic susceptibility χ' under $\mu_0 H = 1$ T (black) and $I_{diff,corr}$ (green) normalized to 1. The dashed line highlights the temperature of onset of magnetic transition $T_{tr} = 200$ K.

Figure 4.12 shows the comparison of $I_{diff,corr} = I_{diff}/W_{PM}$ with the real part of the *ac* susceptibility χ'; the fact that they both show the same temperature dependence is evidence that $I_{diff,corr}$ measures ξ. We can now use $I_{diff,corr}$ instead of equation (4.2), while the error that we make by final integration in space and time is small, since $f_{mag}(Q)$ is a function that decays fast. ξ, consequentially, increases continuously down to T_C.

4.2.4.2. Lattice parameter – internal magnetic pressure

We observe linear thermal contraction for $LaFe_{11.6}Si_{1.4}$ at temperatures above $T > 300$ K. Deviation from linear behavior starts below $T \approx 300$ K and is present in both, our neutron and x-ray diffraction data, see Figure 4.7 and Figure 4.11, respectively. Simultaneously, our neutron diffraction data reveals that strong magnetic fluctuations are present in the form of I_{diff} at $T = 295$ K, see Figure 4.8. I_{diff}, as shown in section 4.2.4.1, is a measure for ξ and increases on cooling, until it diverges at T_C. At the same time, the lattice parameter deviates further from high-temperature linear behavior the closer the temperature gets to T_C. Below $T_{comp} = 225$ K, the lattice parameter even increases upon further cooling. A feature that is likely related is present in our *ac* susceptibility data, where we observe a deviation from CW behavior at the same temperature $T_{CW} = 225$ K, see Figure 4.10.
In the two-phase region we observe a sharp increase in lattice parameter not only for the FM phase, but also for the PM phase. a(FM) is expected to increase due to spontaneous magnetostriction as the Fe magnetic moments assume long-range order (225). The trend of a(PM), however, cannot be explained by magnetostriction. Instead, we use the model of internal magnetic pressure by Wagner and Wohlfarth. According to their theory, spin fluctuations exert a magnetic pressure proportional to ξ and thus influence a system's lattice parameter (261, 262). Since ξ increases, we expect an increasing magnetic pressure on cooling and a larger effect on a(PM) closer to T_C. From our data we find that both ξ and a(PM) increase upon cooling and sharply close to T_C, verifying the theory of internal magnetic pressure. The deviation from linear thermal contraction of $LaFe_{11.6}Si_{1.4}$ can therefore be seen as another measure of ξ.

4.2.4.3. Correlation between magnetization and critical forced magnetostriction

In order to probe the magnetization dependence of critical forced magnetostriction according to equation (4.1), we extracted lattice parameters of $LaFe_{11.6}Si_{1.4}$ powder from Rietveld refinements of our magnetic field and temperature-dependent x-ray diffraction measurements. We derived the forced magnetostriction $\Delta L/L$ from the relative change in lattice parameter in magnetic field compared to zero-field data. The resulting $\Delta L/L$ is shown as a function of M^2 and M^4 in Figure 4.13(a) and Figure 4.13(b), respectively. Magnetization measurements performed separately for $LaFe_{11.6}Si_{1.4}$ powder confirm a broadening of the transition and a slightly larger $T_C = 194$ K, which is still very close to the bulk value.

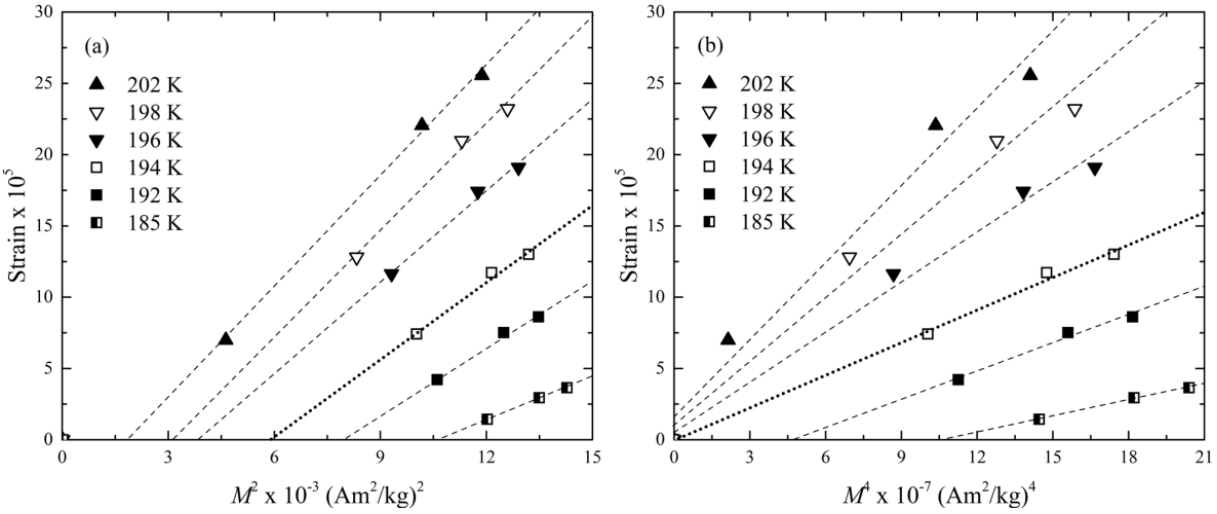

Figure 4.13.: Forced magnetostriction $\Delta L/L$ of $LaFe_{11.6}Si_{1.4}$ determined from magnetic field-dependent XRD (a) as a function of M^2 and (b) as function of M^4. The dashed straight lines are linear fits for each temperature and the dotted line highlights the linear fit at T_C = 194 K.

Classical SEW theory of magnetovolume coupling (neglecting fluctuations) suggests that $\Delta L/L$ vs M^2 follows a straight line through the origin at T_C (137). The forced magnetostriction of $LaFe_{11.6}Si_{1.4}$ indeed follows a straight line vs. M^2 for all temperatures close to T_C, see Figure 4.13(a), however, for none through the origin. This observation is in accordance with Takahashi's SCR spin fluctuation theory. He suggests a change from M^2-linearity behavior to M^4-linearity behavior at T_C, as shown in equation (4.1) (124). The plot of $\Delta L/L$ vs. M^4, see Figure 4.13(b), indeed indicates linearity through the origin at T_C.

4.2.5. Conclusions

Neutron and x-ray diffraction studies on $LaFe_{11.6}Si_{1.4}$ reveal that short-range magnetic correlations in the paramagnetic regime drive the first-order PM–FM transition. These spin fluctuations are observable as neutron diffuse scattering and exist as far as 100 K above the Curie temperature T_C = 190 K. On cooling, the magnetic diffuse intensity I_{diff} and *ac* magnetic susceptibility χ show the same temperature dependence. I_{diff} is, therefore, directly related to the amplitude of short-range magnetic correlations ξ. ξ increases as T_C is approached, creating an internal magnetic pressure that leads to a deviation from linear thermal contraction and an overcompensation close to T_C. Both the PM and FM phase coexist in the temperature range between T_{tr} = 200 K and T_C, in which I_{diff} in the neutron diffraction patterns is transferred to magnetic Bragg intensity I_{mag}. The lattice parameter of PM phase increases sharply in the two-phase region, simultaneously to a large increase in ξ – verifying the pressure effect created by the spin fluctuations. The critical forced magnetostriction at T_C is proportional to the fourth power of magnetization, which is in accordance with Takahashi's SCR spin fluctuation theory.

Paramagnetic spin fluctuations might in general play an important role in driving the magnetocaloric effect in $LaFe_{13-x}Si_x$. We expect that the fluctuations are increasingly suppressed with larger Si concentrations x, especially for compositions x>1.6, which have a second-order transition. However, the evolution of spin fluctuations in the $LaFe_{13-x}Si_x$ system as function of x and, consequentially, the extension to the commercially applied $La(Fe,Mn)_{13-x}Si_xH_y$ system would be a topic for further investigation. It could provide a generalized view on the occurrence of the giant magnetocaloric effect.

Acknowledgements We would like to thank L.V.B. Diop for performing the magnetic calculations and helpful discussions regarding the manuscript and DFG instrument grant INST 163/442-1 FUGG and LOEWE RESPONSE for funding.

4.2.6. Appendix: Supporting Information

Table 4.1.: Structural parameters of $LaFe_{11.6}Si_{1.4}$ obtained from the Rietveld analyses of neutron diffraction patterns collected at T = 295 and 5 K (standard deviations corrected for Berar's criterion in brackets).

Temperature (K)		295	5
Lattice Parameter (Å)		11.4791(1)	11.5255(1)
Atom Name	FeI 8*b*	0, 0, 0	
Wyckoff Site	FeII 96*i*	0, 0.1172(1), 0.1793(1)	0, 0.1168(1), 0.1804(1)
Coordinates (x,y,z)	La 8*a*	0.25, 0.25, 0.25	
Occupancies	FeI	1.00	
	FeII	0.885	
	Si	0.115	
	La	1.00	
Debye-Waller Factors B (Å^2)	FeI	1.20(10)	1.00(10)
	FeII	1.44(5)	1.09(5)
	La	1.3(1)	0.8(1)
Magnetic Moment (μ_B)	FeI	–	1.9(2)
	FeII	–	2.0(1)
R_f		0.0277	0.0310
R_{Bragg}		0.0340	0.0356
R_{mag}		–	0.0250
χ^2		6.22	6.98

4.3. Publication C: Magnetostructural Coupling Drives Magnetocaloric Behavior: The Case of MnB versus FeB

Magnetostructural Coupling Drives Magnetocaloric Behavior: The Case of MnB versus FeB

Joshua D. Bocarsly[1,2], Emily E. Levin[1,2], Samuel A. Humphrey[3], Tom Faske[4], Wolfgang Donner[4], Stephen D. Wilson[1,2], and Ram Seshadri[1,2,5]

[1]Materials Department, University of California, Santa Barbara, California 93106, United States
[2]Materials Research Laboratory, University of California, Santa Barbara, California 93106, United States
[3]Department of Materials, University of Oxford, Oxford OX1 3PH, United Kingdom
[4]Department of Materials and Earth Sciences, Technische Universität Darmstadt, Darmstadt, 64287, Germany
[5]Department of Chemistry and Biochemistry, University of California, Santa Barbara, California 93106, United States

Correspondence email: seshadri@mrl.ucsb.edu

Received 14 April 2019
Accepted 20 June 2019
DOI: 10.1021/acs.chemmater.9b01476

Reprinted with permission from *Chem. Mater*. 2019, 31, 13, 4873–4881.

Abstract Materials with strongly coupled magnetic and structural transitions can display a giant magnetocaloric effect, which is of interest in the design of energy-efficient and environmentally-friendly refrigerators, heat pumps, and thermomagnetic generators. There also exist however, a class of materials with no known magnetostructural transition that nevertheless show remarkable magnetocaloric effects. MnB has been recently suggested as such a compound, displaying a large magnetocaloric effect at its Curie temperature (570 K) showing promise in recovering low-grade waste heat using thermomagnetic generation. In contrast, we show that isostructural FeB displays very similar magnetic ordering characteristics, but is not an effective magnetocaloric. Temperature- and field-dependent diffraction studies reveal dramatic magnetoelastic coupling in MnB, which exists without a magnetostructural transition. No such behavior is seen in FeB. Furthermore, the magnetic transition in MnB is shown to be subtly first-order, albeit with distinct behavior from that displayed by other magnetocalorics with first-order transitions. Density functional theory-based electronic structure calculations point to the magnetoelastic behavior in MnB as arising from a competition between Mn moment formation and B–B bonding.

4.3.1. Introduction

While the Curie transition from a paramagnet to a ferromagnet is canonically a continuous transition, there exist ferromagnets that display discontinuous first-order transitions. This phenomenon can arise when magnetic and structural degrees of freedom are so strongly coupled that the magnetic phase transition is accompanied by a structural transition. Materials displaying such coupled transitions, including MnAs (93, 94), ferromagnetic, hole-doped $LaMnO_3$ (272), $Gd_5(Si, Ge)_4$ (95, 273–276), $(Mn,Fe)_2(P,Si,Ge,As)$ (277–281), and $La(Fe,Si)_{13}H_x$ (19, 282) are of great interest for their unusual functionality, including, variously, colossal magnetoresistance, giant magnetovolume effects, and, most recently, giant magnetocaloric effects. The magnetocaloric properties stem from the fact that this type of first-order transition can often be actuated using a modest magnetic field, leading to relatively small fields ordering a significant fraction of paramagnetic spins. By alternating cycles of adiabatic and isothermal magnetization and demagnetization, these changes in entropy can be leveraged to drive an environmentally-friendly and energy-efficient heat pump (283). Conversely, changes of temperature can be employed to build efficient thermomagnetic waste heat regenerators (284–286). The primary metric for magnetocaloric performance is the peak entropy change that can be accomplished during isothermal application of a given magnetic field, $\Delta S_{M,\mathrm{peak}}(H)$. For commercial applications, earth-abundant materials that have substantial peak isothermal magnetic entropy changes at low fields (*ie.* $H = 1$ T to 2 T) are attractive.

Giant first-order magnetostructural phase transitions are recognized by the usual hallmarks of an abrupt change in the magnetization at the transition temperature accompanied by a peak in heat capacity, thermal hysteresis, and phase coexistence of the two phases at the transition temperature. The structural phase transition may either be from one crystallographic space group to another (*e.g.* the $P6_3/mmc$ to $Pnma$ transition seen in MnAs (94)), or it may involve two phases within the same structure but with distinct lattice parameters (*e.g.* the transition in $(Fe,Mn)_2(P,Si)$ (287)). The latter case is often termed a magnetoelastic transition.

While the giant magnetic entropy changes associated with first-order magnetostructural phase transitions are useful in applications, they pose engineering challenges. The thermal and magnetic hysteresis associated with first-order transitions leads to inefficiencies and rate limitations when the material is cycled between magnetic states. Large changes in structure during cycling can lead to fatigue and mechanical degradation. Furthermore, thermal hysteresis greatly reduces the reversible adiabatic temperature change of a magnetocaloric. While these challenges can often be alleviated using chemical tuning and device engineering (57, 90, 288), a different solution that has gained popularity recently is to change the composition of a first-order material in order to weaken the magnetostructural coupling so that the transition becomes increasingly second-order. At the border between first- and second-order transitions, one may find a tricritical transition which has no hysteresis while maintaining a large ΔS_M (241–243, 280, 287, 289). In contrast, for systems without magnetostructural first-order transitions, the main strategy for improving ΔS_M has been to increase the magnetic moment (290–292). However, there exist several materials such as $AlFe_2B_2$ (293, 294), Mn_5Ge_3 (295), CrO_2 (296), MnCoP (297), and MnB (297, 298) which show promising magnetocaloric properties without any known first-order magnetostructural or magnetoelastic transitions. All of these materials have ΔS_M values that are competitive with, or exceed that of Gd metal despite having gravimetric magnetic moments at saturation that are only between 30% and 60% as large (299). All these materials also have large values of magnetic deformation Σ_M, a density functional theory-based indicator of the strength of magnetostructural coupling (297), suggesting that magnetostructural coupling may play an underappreciated role in the good

magnetocaloric properties of these materials.

Here, we present the case study of MnB *vs.* FeB to demonstrate that magnetostructural coupling is the driving force behind a large magnetocaloric effect, even in a system with no obvious first-order magnetostructural transitions. MnB and FeB are both ferromagnets with the same structure (FeB-type, shown in Figure 4.14) and comparable magnetic properties, but MnB has a large ΔS_M of -10.7 J Kg^{-1} K^{-1} for an applied field of 5 T while FeB has an effect three times smaller. Interestingly, some anomalous structural behavior near the Curie temperature of MnB was reported as early as 1975 (300, 301). However, this phenomenon was not explained, and MnB has not received much attention until recently (297, 298, 302–304).

We use high-resolution temperature-dependent synchrotron powder diffraction and diffraction under a magnetic field to study the magnetostructural coupling in MnB and FeB. We find that despite the similarities between the two compounds, MnB shows dramatic anisotropic coupling between its lattice and magnetism while FeB does not. We employ density functional theory calculations to understand the origin of this magnetostructural coupling as a competition between manganese moment formation (and the associated volume effects) and B–B bonding.

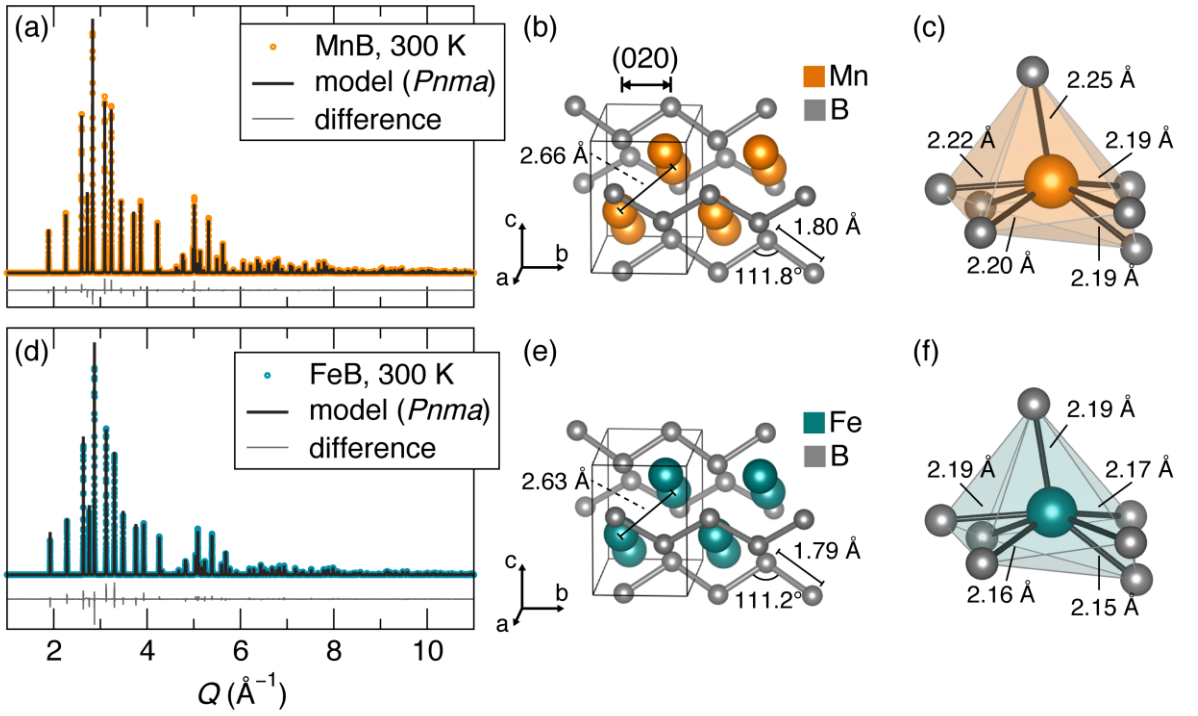

Figure 4.14.: Crystal structures at 300 K of MnB (a-c) and FeB (d-f) determined from high-resolution synchrotron X-ray diffraction. (a) and (c) show the diffraction patterns, along with their Rietveld refinement fits. Both samples have the "FeB" structure (space group *Pnma*, no. 62) consisting of tightly bonded 1-D chains of B atoms with the metal ions arranged around them, as can be seen in (b) and (e). The B–B chain is almost unchanged between the structures, but slightly larger Mn-B contacts lead to the MnB cell having a 4.3% larger unit cell volume. The difference in *a*, *b*, and *c* lattice parameters are 1.1%, 0.97%, and 2.2%, respectively. Refined structures are provided in the Supporting Information as Crystallographic Information Files.

This competition leads MnB to be delicately balanced between competing magnetic and structural considerations, yielding a system where a small stimulus can drive large changes in structure and magnetism. Furthermore, we determine the magnetic transition in MnB is in fact subtly first-order, as revealed by phase coexistence between two isostructural phases with slightly different lattice parameters at the magnetic transition temperature. However, this subtly first-order transition appears to be distinct from the giant magnetostructural or magnetoelastic

transitions seen in other magnetocalorics. The present observation is enabled by the very high resolution of the synchrotron diffraction experiments. We propose that similar behavior may also be revealed in other magnetocaloric compounds if they were to be examined in similar resolution.

4.3.2. Materials and methods

Phase-pure powders of MnB and FeB were prepared by assisted microwave synthesis, as reported previously (297). Briefly, Mn (Alfa Aesar, 99.95%) or Fe (Aldrich, 99.9%) powders were ground in air with 2% stoichiometric excess of crystalline B powder (Alfa Aesar, 99.5%), pressed into pellets, and sealed in evacuated silica ampoules. The ampoules were placed in a carbon-filled crucible and heated in a 1200 W domestic microwave oven (Panasonic, model NN-SN651B) at 70% power (840 W) for 3 min. The pellets were then annealed in evacuated ampoules at 1100 °C for 2 days, followed by air quenching. The samples were confirmed to be phase-pure MnB or FeB prior to and after the final anneal. The excess B required is believed to be due to incomplete reaction of the boron starting material. The samples showed no signs of oxidation or air-sensitivity, and are treated as air stable.

Magnetic measurements were performed on a Quantum Design Physical Property Measurement System (PPMS DynaCool) equipped with a Vibrating Sample Magnetometer (VSM) oven option which allows for the collection of magnetic data between 300 K and 1000 K. The magnetocaloric isothermal entropy change upon magnetization ($\Delta S_M(H, T)$) for each sample was determined using the appropriate Maxwell relation, from magnetization *M vs. T* measurements taken while sweeping temperature through the magnetic transition at several fixed magnetic fields between $H = 0.1$ T and $H = 5$ T. The temperature derivatives of magnetization were calculated using Tikhonov regularization (305), as described in detail previously (306). Raw measurement data are presented in the Supporting Information Figure 4.21.

High-resolution synchrotron powder diffraction data were collected on Beamline BM at the Advanced Photon Source (APS), Argonne National Laboratory using an average wavelength of 0.414581 Å. Room temperature data were collected between 2θ of 0.5° and 50°. Temperature-dependent data was collected between 0.5° and 34° for MnB (10 minute collection time per pattern), and between 0.5° and 28° for FeB (5 minute collection time per pattern). A calibrated Cyberstar Hot Gas Blower was used to control the temperature. Patterns were collected continually while temperature was ramped slowly cooled through the magnetic transition such that one diffraction pattern was taken at every 3 K interval. Resulting patterns were refined using Topas Academic, using sequential and parametric (307) refinement.

Temperature and magnetic-field dependent X-ray powder diffraction measurements were performed on a custom-built laboratory diffractometer in transmission geometry (Mo K_α radiation, $\lambda_1 = 0.709320$ Å, $\lambda_2 = 0.713317$ Å, using the 2θ range from 7° to 67° with a step size of 0.0097°). The instrument has been described in detail elsewhere. (1) The sample powder was mixed with NIST 640d standard reference silicon for correction of geometric errors. Temperature in the range from 300 K to 700 K was controlled by means of a custom SHI closed-cycle Helium cryofurnace. The heating rate between the measurements was 10 K min^{-1} and the sample temperature was stabilized for 15 min. before data collection. Magnetic fields of up to 5 T were applied for isofield warming and cooling protocols, as well as for isothermal field-application experiments. Pawley analyses of the obtained diffraction patterns were carried out sequentially using TOPAS Academic. Example data and fits are available in the Supporting Information Figure 4.26 and Figure 4.27.

Spin-polarized density functional theory calculations were performed using the Vienna Ab initio Simulation Package (*VASP*) (308) using projector augmented wave (PAW) pseudopotentials (309, 310) within the Perdew-Burke-Ernzerhof (PBE) generalized gradient approximation (GGA) (311). First, the eight-atom unit cells of MnB and FeB were relaxed with a force convergence of 0.001 eV $Å^{-1}$ and a starting magnetic moment of 3 μ_B per transition metal ion. This resulted in lattice parameters *a*, *b*, *c* of 5.36, 2.96, and 4.07 Å for MnB and 5.32, 2.93, and 3.96 Å for FeB, which are within reasonable agreement of the room temperature lattice parameters given in Supporting Information Table 4.2. Based on these structures, unit cells with systematically expanded and contracted *b* lattice parameters were generated and ion only relaxations were performed. On these relaxed structures, static spin-polarized and nonspin-polarized calculations were performed. The Crystal Orbital Hamilton Population (COHP) between pairs of B atoms in the chain were calculated with the help of the LOBSTER code (312–316).

4.3.3. Results and Discussions

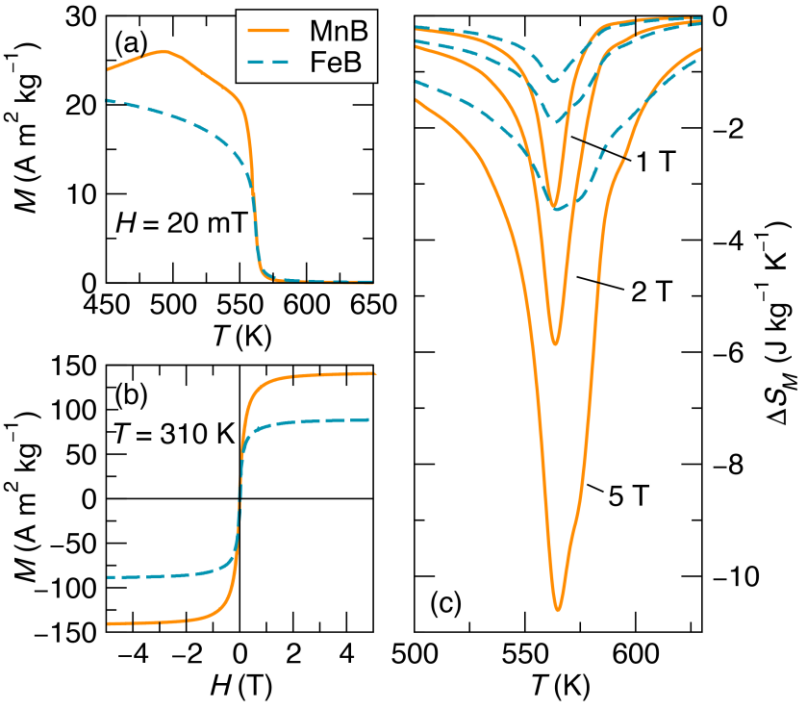

Figure 4.15.: Comparison of the magnetism of MnB and FeB. (a) The two materials show a nearly identical magnetic transition temperature, but MnB shows an unconventional shape of the *M*(*T*) curve. (b) MnB has a saturation magnetization about 50% larger than that of FeB, (c) but shows a peak $-\Delta S_M$ about three times larger.

The results of Rietveld refinement of high-resolution MnB and FeB patterns collected at room temperature are shown in Figure 4.14 and Table 4.2. Both patterns match the known orthorhombic *Pnma* structure ("FeB-type") (317, 318), which consists of 1D zigzag chains of closely spaced (1.8 Å) B atoms running along the *b* crystallographic axis with Mn or Fe arranged in a distorted hexagonal network around these chains. This results in a highly bonded framework, with each metal atom coordinated by seven boron atoms within a sphere of 2.3 Å and six additional metal atoms within 2.7 Å. These diffraction patterns display anisotropic peak widths, which can be well-fit using the Stephens peak-shape function (319) which accounts for (*hkl*)-dependent peak broadening by assuming that different crystallographic directions may have different amounts of inhomogenous strain. The anisotropy in peak shape is consistent with

the highly one-dimensional nature of the crystal structure.
MnB and FeB show very similar bond lengths and contacts, albeit with slightly larger metal-B contacts in MnB leading to larger lattice parameters and a 4.3% larger unit cell volume for MnB. It should be noted the B–B bond lengths and the lattice parameter in their direction of propagation are very similar in the two materials.
Figure 4.15 shows the magnetic characterization of pure samples of MnB and FeB. MnB and FeB show remarkably similar magnetic ordering temperatures (560 K), despite the magnetic behavior appearing to display some key differences. Under low applied fields (less than about 0.1 T), M *vs*. T of FeB behaves as expected for a ferromagnet, uniformly increasing as temperature is lowered. MnB on the other hand, shows an atypical maximum in the magnetization around 500 K, whose origin is not known but may represent a spin reorientation or other magnetic transition. The gravimetric saturated magnetic moment of MnB is about 50% larger than that of FeB (1.65 μ_B/Mn and 1.05 μ_B/Fe). This difference in saturated moment is not nearly enough to explain the dramatic difference in the magnetocaloric properties, with MnB showing a three times larger magnitude of peak ΔS_M. No resolvable thermal hysteresis was seen in either material.
The large ΔS_M in MnB compared to FeB is surprising, given the similarities in structure, ordering temperature and ordered magnetic moment. However, when the temperaturedependence of the synchrotron X-ray diffraction is examined (Figure 4.16), striking differences become evident. In FeB, all of the peaks shift uniformly towards higher Q upon cooling through the magnetic transition, demonstrating conventional positive thermal expansion. In MnB, different peaks shift in different directions, indicating highly anisotropic effects. Furthermore, pronounced kinks are visible in the thermal evolution of most of the peaks at the magnetic transition temperature, suggesting that the crystal structure is much more strongly linked to the magnetism in MnB than in FeB.
Figure 4.17 shows the temperature evolution of the (020) peak of the two compounds which corresponds to the lattice spacing parallel to the B–B chain direction. In MnB, this peak shifts towards lower Q upon cooling, showing a negative coefficient of thermal expansion in the b lattice parameter.

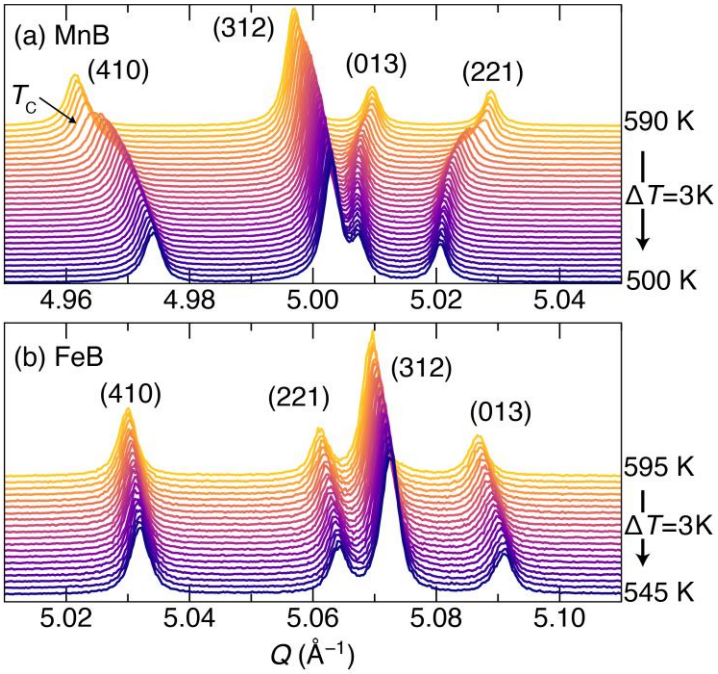

Figure 4.16.: A section of the temperature-dependent diffraction dataset for (a) MnB and (b) FeB. MnB shows highly anisotropic thermal evolution of the diffraction peaks, including pronounced kinks at the Curie temperature. FeB, on the other hand, shows only conventional thermal expansion.

Furthermore, around the magnetic transition temperature, the peak broadens dramatically and can be seen to form a distinct shoulder (Figure 4.17(b)), indicating that two closely spaced peaks are present. This effect is subtle enough that it would be undetectable at the resolution of most diffraction experiments, including laboratory X-ray diffraction or powder neutron diffraction. However, with the resolution of the present experiment, the splitting of one peak into two around the magnetic transition temperature is seen on all peaks with substantial *h* or *k* character. In addition to the data shown in Figure 4.16, a pattern taken at the fixed temperature 576.1 K after temperature equilibration also shows this two-phase coexistence, confirming that it is not a transient effect (Figure 4.22). This behavior indicates that there is a region of phase coexistence between two phases around the magnetic transition in MnB, a hallmark that the transition is actually first-order. In FeB, on the other hand, no such behavior is observed.

In order to examine the thermal evolution of the structure, parametric Rietveld refinements on both data sets were performed, allowing the noise in the refined parameters to be minimized. Results for FeB are shown in the Supporting Information Figure 4.22. The lattice parameters and unit cell volume of FeB display well-behaved linear thermal expansion of all three cell parameters, with no observable change in slope at the magnetic transition temperature. Some anisotropy is seen in the thermal expansion, with average coefficients of thermal expansion of 7, 12, and 17 ppm K^{-1} in the *a*, *b*, and *c* directions, respectively. In contrast, the results of parametric refinement for MnB (Figure 4.18) demonstrate anomalous behavior. If the refinement for MnB is set up so that only one crystallographic phase exists in each pattern, the patterns well below and well above the transition are described appropriately, but near the transition, R_{wp} (a measure of the error in a Rietveld fit) increases dramatically, even if the peak profile is allowed to refine independently for each temperature (Supporting Information Figure 4.24(a)).

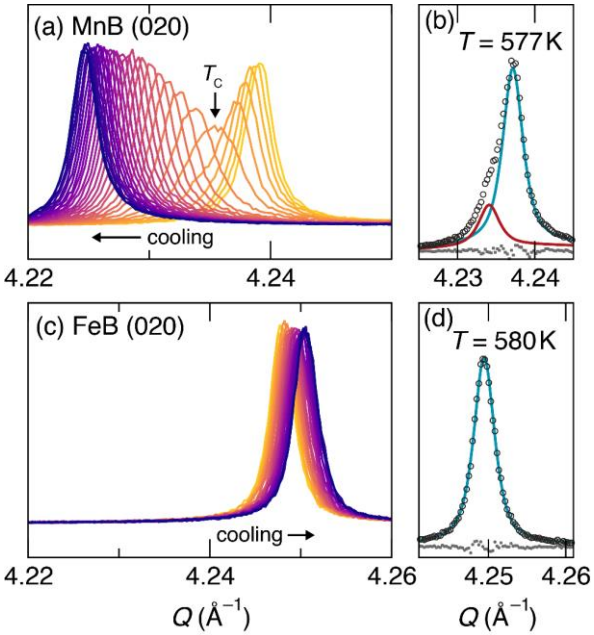

Figure 4.17.: Temperature evolution of the (020) peak in MnB and FeB through the magnetic transition temperature. In MnB, the peak shifts dramatically to the left upon cooling (a), and broadens near the magnetic transition temperature. Below and above the magnetic transition, the peak has a well-behaved Lorentzian shape, but near the Curie temperature, it requires two peaks to fit, indicating coexistence of two phases (b). In FeB, the peak shifts to the right upon cooling (c) and maintains a constant-width Lorentzian shape at all temperatures, including at the magnetic transition temperature (d).

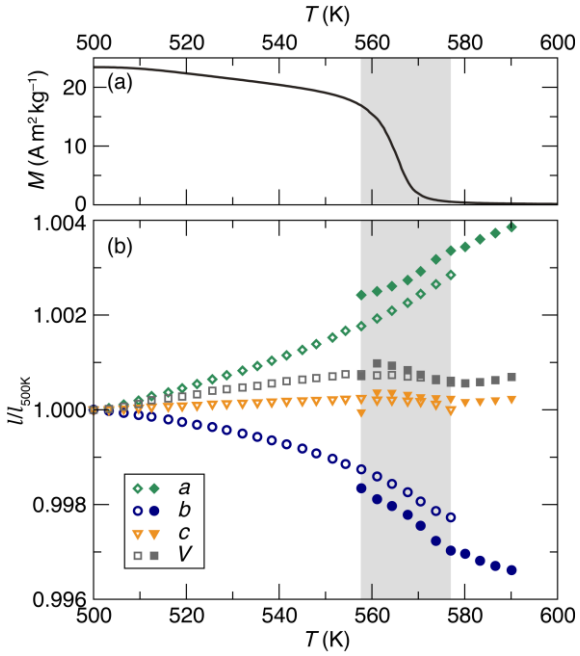

Figure 4.18.: Results of parametric two-phase Rietveld refinement of temperature-dependent synchrotron diffraction data for MnB, compared with magnetization data. (a) Magnetization as a function of temperature under an applied field $H = 20$ mT. (b) MnB lattice parameters are shown relative to their 500 K value, and show highly anisotropic thermal expansion including large negative thermal expansion in the b direction. Furthermore, phase coexistence between two isostructural phases is seen in a 19 K window around the magnetic transition temperature, indicated with a gray box.

However, if two isostructural *Pnma* phases with slightly different lattice parameters (about 0.05% difference in the a and b directions) are included in the fit, the R_{wp} remains constant across the magnetic transition. The two phases are found to coexist in a temperature region

between 558 K and 577 K, transitioning from 100% of the low-temperature phase at 558 K to 100% of the high-temperature phase at 577 K (Supporting Information Figure 4.24(b)). As can be seen in Figure 4.18, the temperature-range of this two-phase transition corresponds exactly to the width of the magnetic transition. Taken together, these observations confirm that the magnetic transition in MnB is first-order. The phase coexistence over a temperature span of 20 K is reminiscent of the first-order transitions in shape memory alloys, where strain buildup causes the transformation to occur progressively, rather than all at once (121). However, it is important to note that the differences in lattice parameters of the coexisting MnB phases are not anywhere near as large as those seen in magnetocalorics displaying giant magnetocaloric effects at coupled first-order magnetostructural or magnetoelastic transitions (often 1% or more). In fact, the changes in lattice parameters between the two phases are less than the thermal expansion of each phase within the phase coexistence region, and therefore the structural part of the phase transition cannot be considered primary. Rather, this transition appears to represent a different kind of first-order phase transition than those previously seen in magnetocalorics. Its origin and behavior are the subject of ongoing investigation.

Outside of the two-phase coexistence region, the thermal evolution of the lattice parameters of MnB is also unusual. The *a* lattice parameter experiences a very large positive thermal expansion across the full temperature range, with an average linear coefficient of thermal expansion of 43 ppm K^{-1} across the dataset. On the other hand, the b lattice parameter shows a similarly large negative coefficient of thermal expansion, –38 ppm K^{-1}. In the *a* and *b* directions, the positive or negative thermal expansion is strongest at the magnetic transition temperature. The *c* lattice parameter is relatively invariant with temperature, and the overall unit cell volume shows slight positive expansion. Both the *c* lattice parameter and the volume show some irregular behavior at the magnetic transition temperature.

Like the lattice parameters, the bond lengths in MnB show anisotropic thermal evolution (Supporting Information Figure 4.25). Notably, the closest Mn–B and B–B contacts decrease slightly as temperature is increased, as does the average Mn–Mn distance. However, the changes in bond length are all small, and with no dramatic changes at the transition temperature that would indicate a change in bond order. Rather, these anisotropic changes in bonding indicate that some electronic redistribution is occurring as temperature is changing, as will be discussed in the final section.

The structure evolution of MnB is clearly strongly affected by the magnetism, as evidenced by the structural anomalies seen at the magnetic transition temperature. For this reason, MnB was originally compared to invar (Fe-Ni) alloys, wherein low thermal expansion is known to be caused by a magnetovolume effect (300, 301). The magnetovolume effect, which is based on theories of itinerant electron magnetism, relies on the fact that large magnetization causes lattice parameters to expand (136, 138). At low temperatures, the moment is at its largest, and its effect on expanding the crystal lattice is also at its largest. As temperature increases, fluctuations set in and the magnetic moment weakens, causing a negative contribution to the thermal expansion. This contribution may partially or completely offset the normal thermal expansion of the material due to anharmonic phonons. Above the magnetic Curie temperature, the thermal expansion typically returns abruptly to positive. In MnB however, magnetostructural effects manifest in quite a different way. The thermal expansion is marked by a change in cell shape, inducing both a strong negative thermal expansion in the *b* direction and a strong positive thermal expansion in the *a* direction. In addition, these effects persist, although somewhat weakened in magnitude, at least 150 °C (see Supporting Information Figure 4.28) above the magnetic transition temperature, which is quite unusual, even in

magnetocalorics with exceptionally large magnetostructural coupling (1, 138, 320, 321). This persistence suggests that the magnetism in MnB has at least partly local character, and that the magnetostructural interaction is related to a coupling between the moment magnitude and the Mn ion size. This coupling may persist above the Curie temperature because the local moments still exist in the paramagnetic regime.

4.3.3.1. Field Induced Magnetoelasticity

In order to directly probe magnetostructural coupling in MnB, we carried out X-ray diffraction experiments as a function of temperature under a magnetic field. Diffraction patterns were collected between 300 K and 700 K under no applied field and under an applied field of 5 T. The difference in lattice parameters fit from these patterns is shown in the top panel of Figure 4.19.

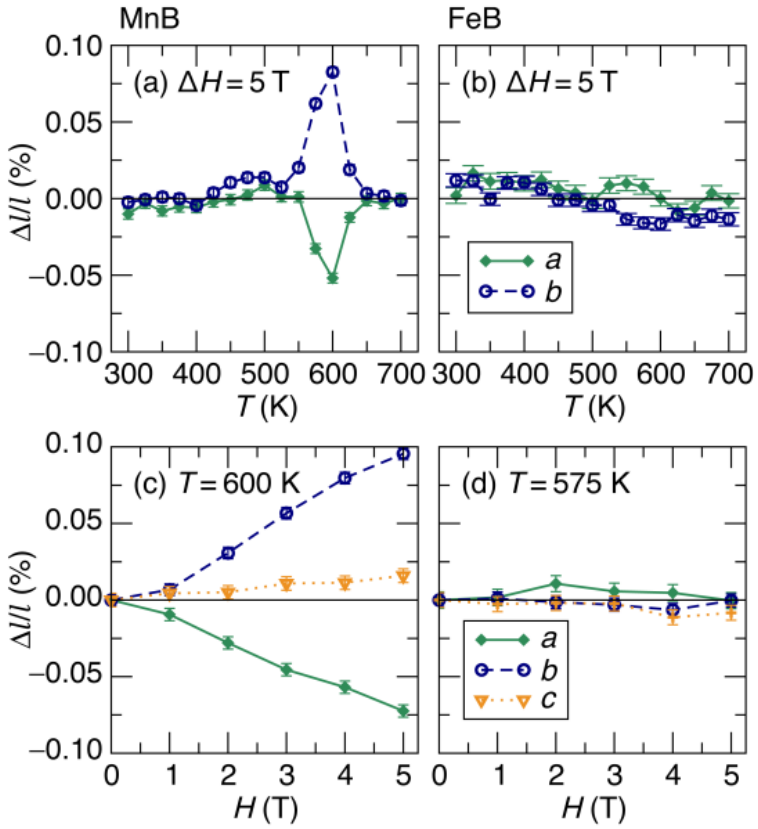

Figure 4.19.: Changes in lattice parameters induced by magnetic field. The top row shows the relative change in lattice parameters upon application of a 5 T field, monitored as a function of temperature. (a) MnB shows large induced magnetoelasticity around its magnetic transition temperature, with a positive change in the *b* lattice parameter and a negative change in the *a* lattice parameter. No changes are clearly resolvable above the noise in FeB (b). The bottom panel shows how the lattice parameters evolve with magnetic field at fixed temperature near the magnetic transition temperature. Once again, the changes are not clearly resolved in FeB (d), but are seen to be large in MnB (c).

Well above and well below the transition temperature, no consistent effect can be resolved above the noise. However, near the Curie temperature where the system is most susceptible to an external field, a substantial change in lattice parameters is seen upon application of the field in MnB, an effect which we will term “induced magnetoelasticity.” As with the thermal expansion, this effect is anisotropic: the *a* lattice parameter decreases upon application of the field, while the *b* lattice parameter increases by nearly 0.1%. In FeB, no induced

magnetoelasticity is resolvable. The observation of a maximum effect at 600 K in MnB as opposed to 570 K as seen in the magnetic measurements and synchrotron diffraction is most likely due to the large applied field increasing the transition temperature, as well as slight differences in the sample.

In the temperature-dependent experiment, the induced magnetoelasticity in the *c* lattice parameter was not determined as the *c* lattice parameter displayed a sample history dependence, presumably related to the build-up and release of strains in the material. However, the induced magnetoelasticity in all three lattice parameters was resolvable in isothermal experiments, where the sample was held at a constant temperature near the magnetic transition while fields ranging from 0 T to 5 T were applied. These results are shown in the bottom row of Figure 4.19. Once again, no lattice parameter changes could be resolved in FeB above the noise. In MnB at 600 K, on the other hand, the *b* lattice parameter expands upon the application of a magnetic field, reaching a maximum expansion of 0.095(4)% (or 950 ppm) at 5 T, while the *a* lattice parameter contracts, reaching a contraction of –0.072(4)%. The *c* lattice parameter shows a smaller expansion, which reaches 0.016(4)%. The *Q*-space resolution of the in-field diffractometer is insufficient to identify the two coexisting structural phases that were seen in the synchrotron diffraction, so it is somewhat ambiguous whether these large magnetoelasticities are caused by intrinsic effects in the two coexisting phases themselves or by the field transforming part of the sample from one phase to the other. However, because the lattice parameter changes are almost twice as large as the maximum difference in lattice parameter between the two phases in the temperature-dependent synchrotron diffraction experiment, we can conclude that intrinsic magnetoelasticity in the phases is at least partially responsible for the effect. This is also consistent with a visual inspection of the diffraction patterns (Supporting Information Figure 4.27), which shows that the diffraction peaks shift with applied field, rather than change shape. The observed lattice parameter changes are large compared to conventional Joule magnetostriction found in all magnets (typical measured in ppm), but are smaller than values would be observed at a giant first-order magnetostructural transition (often 1% or more). This behavior positions MnB in an intermediate regime in terms of magnetostructural coupling, suggesting that MnB is proximal to a magnetostructural tricritical point. The explains the large, but not hysteretic ΔS_M.

This observed anisotropic magnetovolume effect in MnB explains the strange thermal expansion behavior. As MnB is heated from low temperature, its magnetic moment falls as fluctuations set in, and therefore the moment's influence on structure is decreased. On the other hand, when an external magnetic field is applied, the moment strengthens and the inverse happens. Therefore, the changes in lattice upon application of a field provide information about the magnetic contribution to the observed thermal expansion. In FeB, this magnetostructural coupling is small, so the thermal expansion is more or less unaffected by the magnetism. In MnB on the other hand, the anisotropic magnetoelastic effect modifies the standard thermal expansion. In the *b* direction, the magnetoeleastic effect is positive and large, which overwhelms the standard positive thermal expansion and leads to a strong negative thermal expansion. In the *a* direction, the negative magnetoelastic effect strengthens the positive thermal expansion leading to an exceptionally large positive thermal expansion. In the *c* direction, the weaker positive effect offsets the thermal expansion leading to a fairly temperature-independent lattice parameter, as is the case in invar.

4.3.3.2. Competing Interactions and Magnetostructural Coupling

In order to understand the origins of the unconventional thermal expansion and magnetoelastic effect in MnB, we employ density functional theory (DFT) calculations on both MnB and FeB. Noting that the strongest bonds in the system are the covalent B–B bonds which run in a zig-zag chain along the *b* lattice parameter, we show the results of DFT calculations for FeB and MnB unit cells with expanded and contracted *b* lattice parameters in Figure 4.20. B–B bond strength (as indicated by the integrated Crystal Orbital Hamilton Population, iCOHP), Mn or Fe moment magnitude, and magnetic stabilization energy ($E_{mag} - E_{nonmag}$) are shown. In both compounds, contraction of the *b* lattice parameter (up to about 20%) leads to an increase in the B–B bond strength, indicating that the B–B are more elongated than they would prefer to be, absent of other forces in the structure.

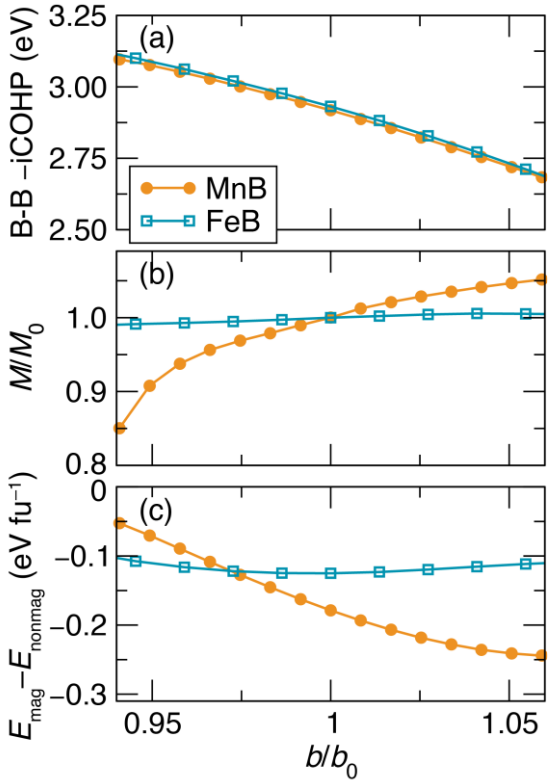

Figure 4.20.: Results of DFT calculations for MnB and FeB cells with contracted and expanded *b* lattice parameter. (a) Integrated crystal orbital Hamilton population (iCOHP) between B–B atoms in the chain, an indicator of the bond strength, with more negative values indicating greater stability. (b) Evolution of the local moment magnitudes (normalized to their equilibrium values M_0), which decrease as b is contracted in MnB but stay constant in FeB. Similarly, (c) shows that the energy stabilization from magnetization (difference in energy between a spin-polarized and non-spin-polarized calculations) decreases as *b* is contracted in MnB, but stays constant in FeB. These results demonstrate that MnB displays direct competition between Mn moment formation and B–B bond formation, while FeB does not.

On the other hand, contraction of the b lattice parameter leads to a decrease in moment magnitude and magnetic stabilization in MnB, indicating that the manganese magnetism would favor an expanded *b* lattice parameter. Therefore, the equilibrium lattice parameter in MnB can be understood as resulting from the result of a competition between moment magnitude and B–B bond strength. In FeB, on the other hand, the moment size and magnetic stabilization are virtually independent of *b* lattice parameter, and no such competition exists.

We propose that it is the competition between stabilizing the magnetism and the bonding in

MnB that leads to the strong and anisotropic magnetoelastic coupling. As temperature is increased and magnetic fluctuations set in, the magnetic stabilization weakens and the B–B bonds are able to exert their contractive forces on the structure, leading to negative thermal expansion in the *b* direction and a decrease in the B-B bond length and the closest Mn-B bond length. In this picture, the *a* lattice parameter responds to the driving forces in the *b* lattice direction with a positive Poisson ratio, alleviating some of the volumetric strain associated with the large decrease in *b* lattice parameter. This causes the negative magnetoelastic effect in the *a* direction. The *c* lattice direction is intermediate between these two cases since the B–B zigzag chains sit mostly in the *b*–*c* plane. In addition to explaining the thermal evolution of the lattice parameters, the competition-induced magnetostructural coupling in MnB can explain its extraordinary magnetocaloric effect. Because MnB sits in an active balance between magnetic and structural degrees of freedom, changes in magnetism or *b* lattice parameter can energetically compensate each other. This provides a low energy pathway for changing Mn moment magnitude, allowing a small stimulus (magnetic field) to cause a large change in magnetic state and therefore magnetic entropy.

FeB has a smaller transition metal cation than MnB, due to the increased nuclear charge as well as the lower magnetic moment. Comparing the room-temperature crystal structures, the unit cell volume and metal-B bond lengths are all larger in MnB than in FeB. However, the *b* lattice parameter and B–B bond lengths only show a small increase, suggesting that the larger size of MnB is straining against the available size of the metal site in the FeB structure, which is constrained by the strong B–B bonding. In fact, MnB sits at a phase boundary: moving one column to the left on the periodic table yields CrB, a transition metal monoboride with a modified structure (space group *Cmcm*) from the *Pnma* structure of the common forms of MnB, FeB, and CoB. In fact, MnB itself can be stabilized in either the *Pnma* (as studied presently) or a low-temperature *Cmcm* structure (317). Therefore, we expect that FeB does not show the moment-bonding competition, and associated magnetostructural coupling that MnB does because the smaller size of the Fe atoms is not straining the B–B bonds.

4.3.4. Conclusion

We have demonstrated that MnB shows anisotropic magnetoelastic coupling that is driven by competition between Mn moment formation and B–B bond strength. These results explain why MnB shows a large magnetocaloric effect of -10.7 J Kg^{-1} K^{-1} at 5 T, while isostructural FeB with otherwise similar magnetic properties shows a much smaller effect. While there is no change in the space group across the magnetic transition in MnB, coupling of magnetism and structure is evidently an important driver of the magnetocaloric performance. Based on this result, MnB appears to be proximal to a magnetostructural tricritical point which allows for a transition with a large ΔS_M while maintaining negligible hysteresis.

In addition, we have shown that the magnetic transition in MnB is in fact very subtly first-order with clear phase-coexistence at the magnetic transition, albeit the behavior of the transition is quite distinct from the giant first-order coupled magnetostructural transitions displayed by other magnetocalorics.

Supporting Information Additional details of the temperature- and field-dependent Rietveld refinements, additional magnetization data, and example data from the in-field diffractometer.

Acknowledgements This work was supported by the National Science Foundation (NSF) through DMR-1710638. Partial support by the NSF MRSEC Program under DMR 1720256 (IRG-1) is acknowledged. J.D.B. is supported by the NSF Graduate Research Fellowship Program

under 1650114. We also acknowledge the use of the facilities of the Center for Scientific Computing at UC Santa Barbara. Use of the Advanced Photon Source at Argonne National Laboratory was supported by the U. S. Department of Energy, Office of Science, Office of Basic Energy Sciences, under Contract No. DE-AC02-06CH11357. We thank Dr. Saul Lapidus (Beamline 11-BM) for assistance with the data collection and Professor Dr. Barbara Albert for helpful discussions on the subject of borides.

4.3.5. Appendix: Supporting Information

Table 4.2.: Refined crystal structure of MnB and FeB from room temperature high-resolution synchrotron diffraction data (λ = 0.414581 Å). GOF indicates the goodness of fit, which is defined as the ratio between the weighted profile *R* factor R_{wp}, and expected *R* factor, R_{exp}. Numbers in parentheses are standard uncertainties in the last given digit(s) from Rietveld refinement. The refined structures are also included in Crystallographic Information Files.

	MnB (300 K)	FeB (300 K)
spacegroup	*Pnma*	*Pnma*
a (Å)	5.5632	5.5020
b (Å)	2.9769	2.9482
c (Å)	4.1473	4.0596
V (Å^3)	68.682	65.852
GOF	1.93	1.57
metal		
x	0.17588(2)	0.17709(3)
y	0.25	0.25
z	0.12083(3)	0.11988(4)
B_{iso}	0.158(2)	0.162(2)
boron		
x	0.0341(2)	0.0363(2)
y	0.25	0.25
z	0.6128(3)	0.6141(3)
B_{iso}	0.35(1)	0.29(1)

Table 4.3.: Refined lattice parameters and weight fractions for the high-temperature phase of MnB from the temperature-dependent synchrotron diffraction data. Numbers in parentheses are standard uncertainties in the last given digit(s) from Rietveld refinement. The values for temperatures from 590.1 K to 580.1 K are from the single-phase parametric refinement, while the values for temperatures between 577.0 K and 557.7 K are from the two-phase parametric refinement, with the lattice parameters and weight fractions for the other (low temperature) phase given in Table 4.4.

T	*a* (Å)	*b* (Å)	*c* (Å)	*V* (Å^3)	weight fraction (%)
590.1	5.60293(1)	2.96463(1)	4.15299(1)	68.9836(1)	100
586.6	5.60221(1)	2.96490(1)	4.15287(1)	68.9790(1)	100
583.3	5.60149(1)	2.96522(1)	4.15278(1)	68.9761(1)	100
580.1	5.60059(1)	2.96566(1)	4.15272(1)	68.9744(1)	100
577.0	5.60014(1)	2.96586(1)	4.15300(1)	68.9781(2)	77.0(3)
573.8	5.59912(2)	2.96646(1)	4.15306(1)	68.9805(3)	59.0(3)
570.5	5.59771(3)	2.96742(2)	4.15314(2)	68.9868(6)	43.3(4)
567.7	5.59668(4)	2.96811(3)	4.15335(2)	68.9936(9)	27.2(5)
564.3	5.59596(6)	2.96865(4)	4.15353(3)	69.000(1)	18.7(5)
561.1	5.59536(7)	2.96909(5)	4.15355(4)	69.003(2)	13.4(4)
557.7	5.59492(8)	2.96977(5)	4.15181(5)	68.985(2)	10.3(4)

Table 4.4.: Lattice parameters and weight fractions refined for the low-temperature phase of MnB from the temperature-dependent synchrotron diffraction data. The values for temperatures from 577.0 K to 557.7 K are from the two-phase parametric refinement, with the lattice parameters and weight fractions for the other (high-temperature) phase given in Table 4.3. The values for temperatures from 554.3 K to 500.0 K are from the single-phase parametric refinement.

T	a (Å)	b (Å)	c (Å)	V (Å^3)	weight fraction (%)
577.0	5.59729(3)	2.96794(1)	4.15204(2)	68.9754(5)	23.0(3)
573.8	5.59619(2)	2.96834(1)	4.15252(1)	68.9791(3)	41.0(3)
570.5	5.59505(2)	2.96894(1)	4.15276(1)	68.9829(3)	56.7(4)
567.7	5.59400(1)	2.96952(1)	4.15280(1)	68.9842(3)	72.8(5)
564.3	5.59307(1)	2.97005(1)	4.15288(1)	68.9866(2)	81.3(5)
561.1	5.59215(1)	2.97051(1)	4.15289(1)	68.9859(2)	86.6(4)
557.7	5.59126(1)	2.97096(1)	4.15303(1)	68.9876(2)	89.7(4)
554.3	5.59070(1)	2.97130(1)	4.15296(1)	68.9876(1)	100
551.5	5.58991(1)	2.97163(1)	4.15291(1)	68.9845(1)	100
548.0	5.58914(1)	2.97196(1)	4.15286(1)	68.9820(1)	100
545.0	5.58845(1)	2.97227(1)	4.15282(1)	68.9798(1)	100
541.6	5.58782(1)	2.97253(1)	4.15278(1)	68.9775(1)	100
538.4	5.58718(1)	2.97278(1)	4.15272(1)	68.9743(1)	100
535.3	5.58656(1)	2.97300(1)	4.15265(1)	68.9707(1)	100
532.1	5.58601(1)	2.97321(1)	4.15261(1)	68.9682(1)	100
528.7	5.58547(1)	2.97343(1)	4.15256(1)	68.9658(1)	100
525.6	5.58499(1)	2.97362(1)	4.15253(1)	68.9636(1)	100
522.3	5.58443(1)	2.97376(1)	4.15243(1)	68.9584(1)	100
519.1	5.58393(1)	2.97393(1)	4.15237(1)	68.9550(1)	100
516.1	5.58345(1)	2.97409(1)	4.15233(1)	68.9524(1)	100
512.5	5.58301(1)	2.97426(1)	4.15228(1)	68.9498(1)	100
509.7	5.58248(1)	2.97437(1)	4.15218(1)	68.9443(1)	100
506.5	5.58202(1)	2.97450(1)	4.15210(1)	68.9404(1)	100
503.3	5.58159(1)	2.97463(1)	4.15204(1)	68.9371(1)	100
500.0	5.58140(1)	2.97470(1)	4.15202(1)	68.9359(1)	100

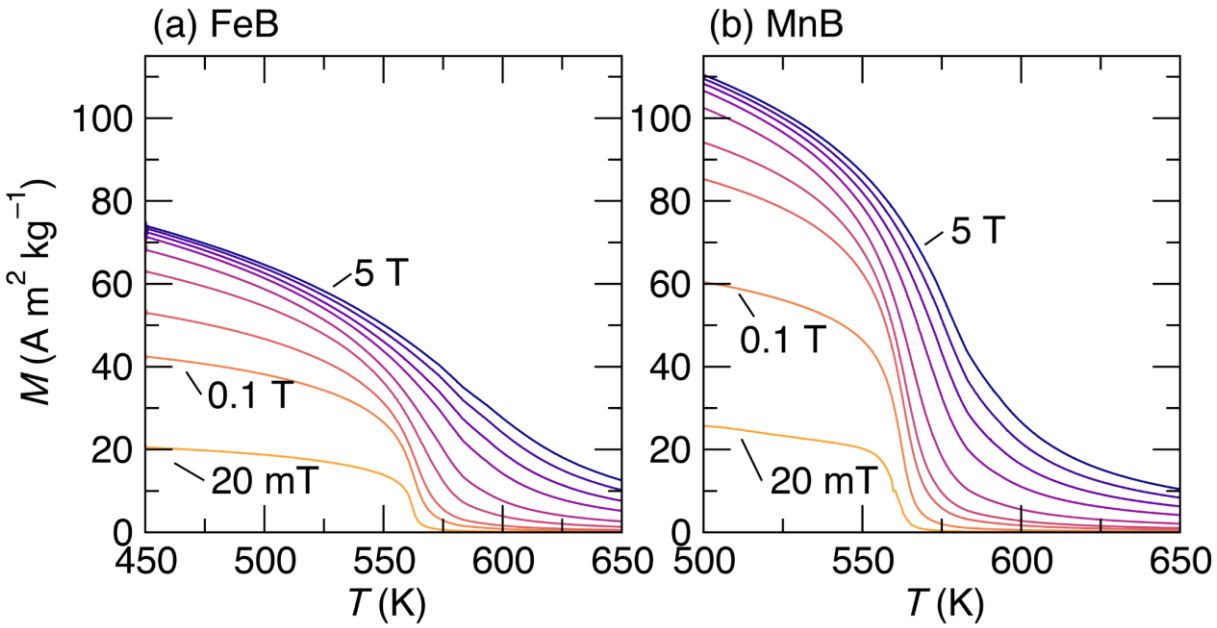

Figure 4.21.: Magnetization *vs.* temperature under nine applied fields for FeB (a), and MnB (b). These data are processed into the ΔS_M data presented in the main text Figure 4.15. At high field, the FeB $M(T)$ broadens out considerably while the MnB remains relatively sharp, leading to a much larger peak ΔS_M for MnB.

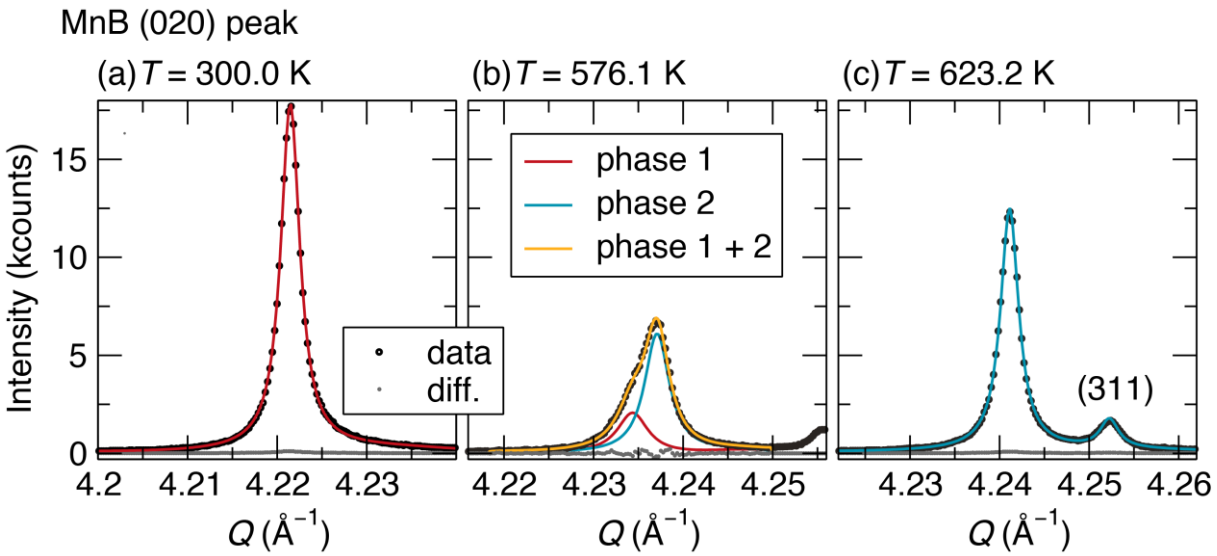

Figure 4.22.: MnB (020) synchrotron diffraction peak from patterns taken while equilibrated at temperatures well below the magnetic transition (a), near the magnetic transition (b), and well-above the magnetic transition (c). This data is similar to the data in the main text Figure 4.17, except that these patterns are taken at static temperature after temperature equilibration. In (a) and (c), the diffraction peaks can be fit with a single Lorentzian peak, while around the magnetic transition two Lorentzians are required, indicating phase coexistence of two phases.

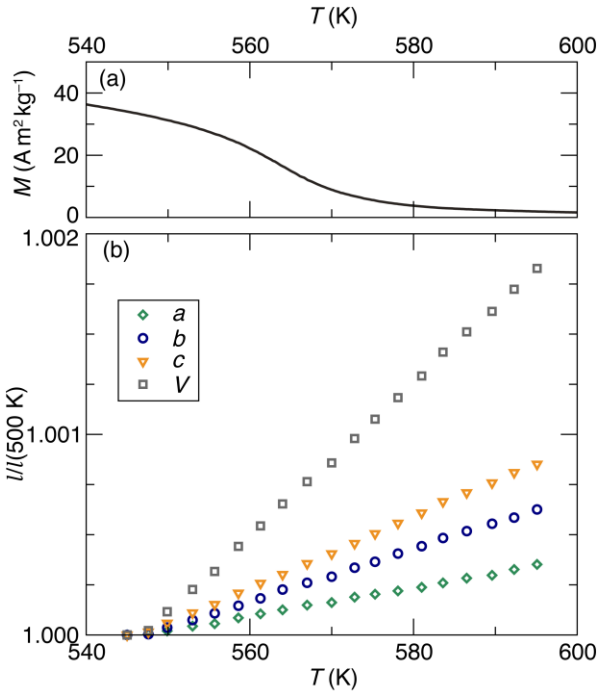

Figure 4.23.: Comparison of magnetic moment *vs.* temperature (a) and lattice parametric from parametric Rietveld refinement of temperature-dependent synchrotron diffraction data (b) for FeB. In contrast to MnB (main text Figure 4.18), the lattice parameters of FeB all show linear, moderate positive thermal expansion, with no obvious anomaly at the magnetic transition temperature. Some anisotropy in thermal expansion can be seen, evidenced by a larger coefficient of thermal expansion in the c direction than the a and b direction.

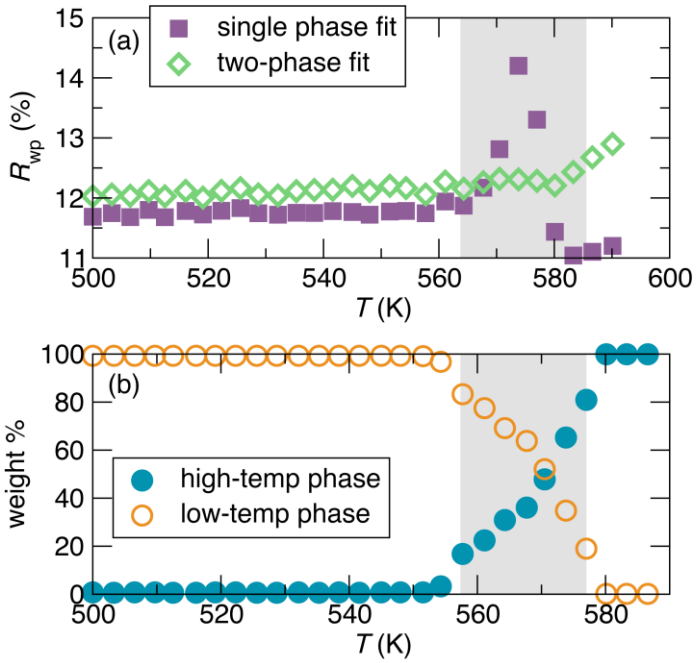

Figure 4.24.: (a) Quality of fit (R_{wp}) for parametric fit of temperature-dependent synchrotron diffraction data. The purple squares show that case when a single crystallographic phase is allowed, with the peak profile (Bragg peak widths) allowed to vary independently for each pattern. This case cannot adequately fit the Bragg peak splitting observed near the magnetic transition temperature, and a spike in R_{wp} is observed in the grey boxed region. On the other hand, when two phases with slightly different lattice parameters and each with a constant peak profile are included, the R_{wp} is constant through the magnetic transition. The weight fractions of the two phases refined from this fit are shown in (b), demonstrating that the magnetic transition is concurrent with the conversion from one crystallographic phase to the other, confirming a first-order transition.

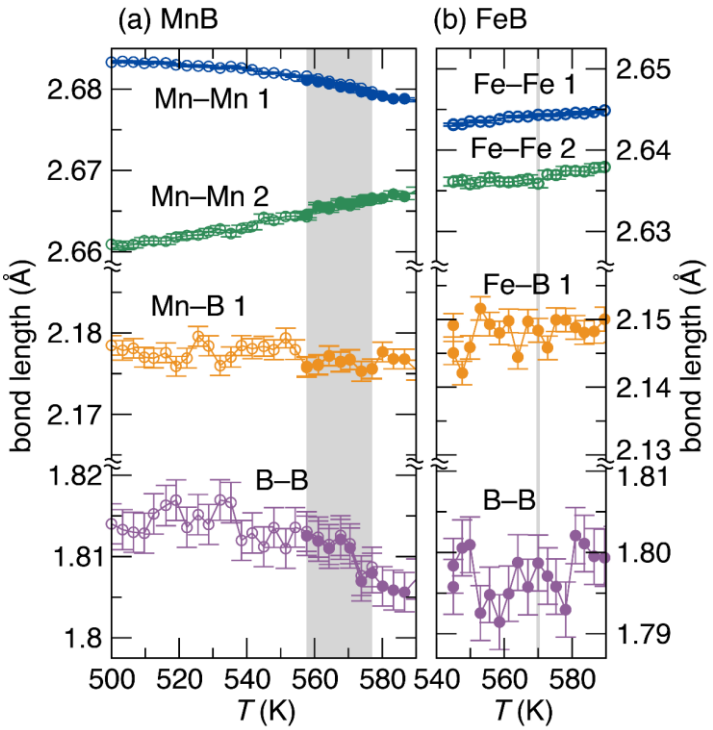

Figure 4.25.: Thermal evolution of selected bond lengths and contacts in MnB and FeB, as fit from the parametric refinements. For MnB, the high-temperature phase is indicated with solid symbols, and the low-temperature phase with empty symbols. The atomic positions were constrained to be the same in the two phases for the patterns where both phases exist, which is consistent with the positions above and below the transition. In each compound, there exist two distinct metal-metal contacts with length below 2.7 Å, seven distinct metal-boron contacts with length less than 2.3 Å (only the nearest is shown), and one distinct boron-boron contact. MnB shows anisotropic thermal expansion of its bonds, while FeB shows only mild increases in bond length as temperature is raised. Magnetic transition temperatures are represented as grey box for MnB (signifying the temperature range of phase co-existence), and a grey line for FeB.

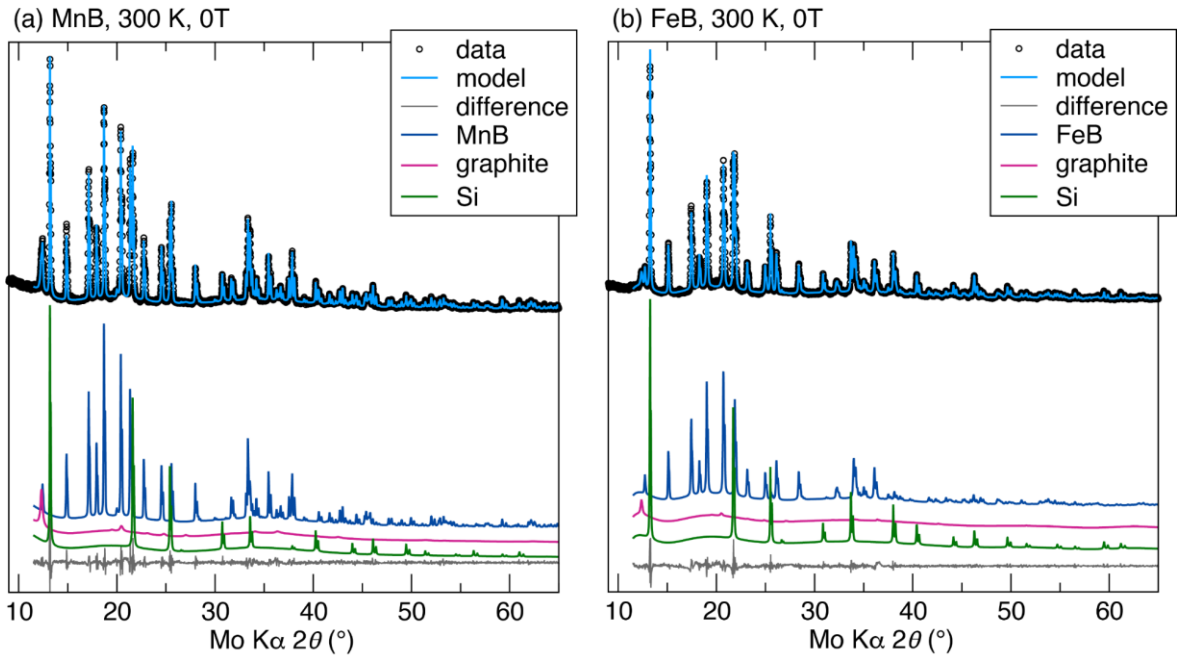

Figure 4.26.: Example Pawley fits of the diffraction data from the in-field, variable temperature X-ray diffractometer (in this case, taken at 300 K with no applied field). The samples (single phase MnB or FeB) have been mixed with NIST 640D standard reference silicon and mounted on a graphite support. Both silicon and graphite phases are

included in the Pawley refinement, and the known silicon lattice parameter is used to correct instrumental geometric errors.

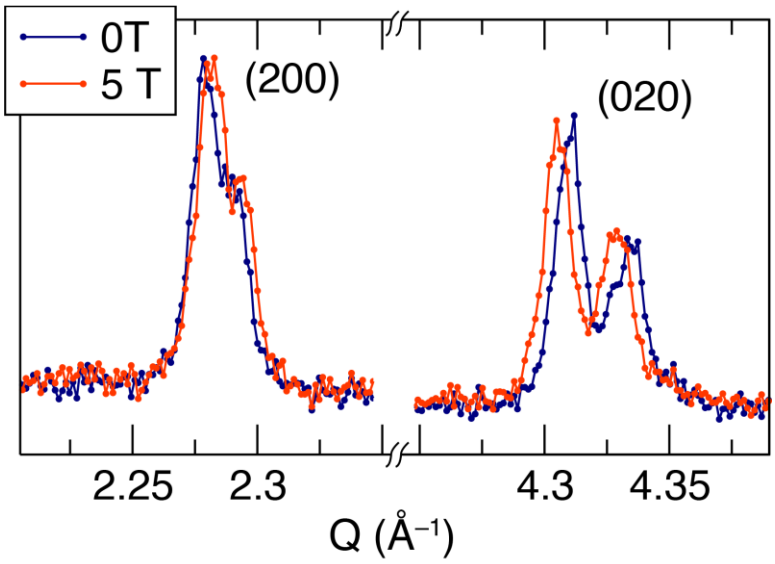

Figure 4.27.: Detailed view of the difference in MnB diffraction pattern under zero applied field and 5 T applied field, taken at 600 K. Only the (200) and (020) peaks are shown. The doublet peaks are from Mo $K_{\alpha 1}$ and $K_{\alpha 2}$ radiation. Upon application of the field, an anisotropic magneto-elastic effect is seen, with some lattice peaks with substantial *h* character moving to the right, and lattice peaks with substantial *k* character moving to the left. The full patterns (along with those taken at other fields) were fitted to give the data shown in the main text Figure 4.19(c).

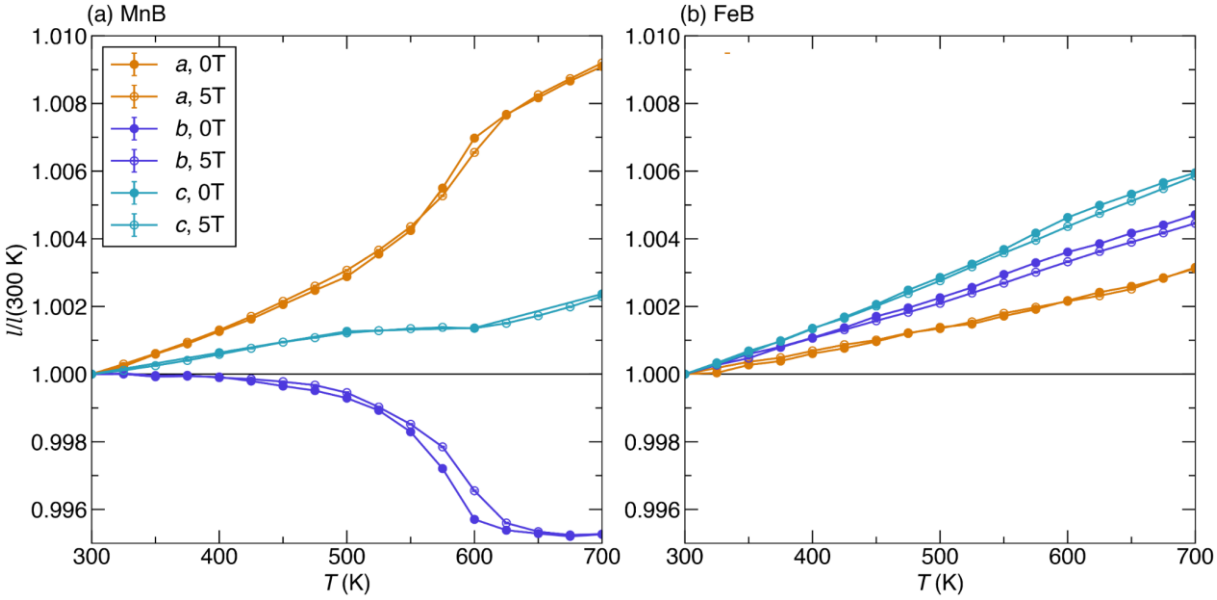

Figure 4.28.: Lattice parameters fit from temperature and field-dependent XRD patterns of MnB and FeB, normalized to their 300 K values at zero field. These refinements were used to generate the induced magnetoelasticity (difference in lattice parameters upon application of a magnetic field) data shown in the main text, Figure 4.19. Due to a sample history effects observed in MnB in the *c* lattice parameter, *c*, 0 T data are fit from a later run, after the sample had been cycled to remove any history. Error bars, which are in general smaller than the data points, represent standard uncertainties from the Pawley refinements.

5. Magnetic-field induced structural phase transition in the $La_{1-x}Ce_xFe_{12}B_6$ system

Publications D and E showcase the second set of case studies performed with the x-ray diffractometer with magnet assembled for this work. Investigations of the magnetic field-induced coupled magnetic and structural phase transitions in the (La,Ce)$Fe_{12}B_6$ system highlight the ability to decipher the mechanism behind their huge volume magnetostrictions and giant negative thermal expansion from XRD experiments. A crucial analysis technique during these investigations was the in-field x-ray diffraction at low temperatures.

5.1. Synopsis of Publications D and E

The aim of these studies was to investigate the magnetic-field induced first-order phase transition in the (La,Ce)$Fe_{12}B_6$ system, which was recently discovered in the parent compound $LaFe_{12}B_6$ (322, 323). This material class exhibits unusual step-wise magnetization changes (322–324) that were hypothesized to be linked to a magnetostructural phase transition, which was finally confirmed in this work. The x-ray diffractometer with magnet proved to be essential in these studies, as the phase transition only occurs under applied magnetic fields at low temperatures.

In previous studies it was found that the (La,Ce)$Fe_{12}B_6$ material class features a rich magnetic phase diagram. In the absence of an external magnetic field, (La,Ce)$Fe_{12}B_6$ has a first-order PM-AFM transition with $T_N \approx 35$ K, with a slight shift of T_N depending on the Ce content (324). If a magnetic field is applied, however, additional AFM-FM or PM-FM metamagnetic transitions can be induced. Both compositions investigated in these studies, $La_{0.9}Ce_{0.1}Fe_{12}B_6$ and $La_{0.85}Ce_{0.15}Fe_{12}B_6$, almost have the same Néel temperature, $T_N \approx 35$ K. However, each composition exhibits a slightly different response to external magnetic fields in the form of different critical transition fields for the PM/AFM-FM transition. Nevertheless, both compounds show very similar properties.

It was proposed that the unusual stepwise magnetization changes that occur in the (La,Ce)$Fe_{12}B_6$ material class after applying large magnetic fields at temperatures <10 K, *i.e.*, in the AFM phase, are the result of a martensitic phase transition (323, 324), similarly to the transitions observed in Gd_5Ge_4 (325), Ga-doped $CeFe_2$ (326), and Nd_5Ge_3 (327). As a consequence, the first-order field-induced metamagnetic phase transition in $La_{0.9}Ce_{0.1}Fe_{12}B_6$ and $La_{0.85}Ce_{0.15}Fe_{12}B_6$ would at the same time be a structural phase transition. In order to confirm this, XRD investigations under applied magnetic fields with the diffractometer assembled for this work were essential.

The magnetic-field-induced metamagnetic transition in $La_{0.9}Ce_{0.1}Fe_{12}B_6$ and $La_{0.85}Ce_{0.15}Fe_{12}B_6$ is accompanied by a huge macroscopic volume magnetostriction of up to $\Delta V/V = 1.15\%$ (25 K, 6 T), which was determined in this work. The magnetostriction was calculated for polycrystalline bulk samples in a capacitance dilatometer ($\Delta V/V = \Delta L/L_{//} + 2\Delta L/L_{\perp}$), so the determined values are isotropically averaged and contain only hints of anisotropic information related to the underlying microscopic phases and their crystal symmetry. Another macroscopic property that was determined from the magnetostriction measurements of $La_{0.9}Ce_{0.1}Fe_{12}B_6$ is a

huge negative thermal expansion (NTE) phenomenon over a temperature range of $\Delta T \approx 60$ K at 6 T applied magnetic field with an average linear thermal expansion coefficient $\alpha_L = (1/L)(\Delta L/\Delta T) = -37 \times 10^{-6}$ K^{-1}. Both effects, the huge volume magnetostriction and NTE effect that accompany the field-induced metamagnetic phase transition are direct evidence for strong magnetoelastic coupling in the investigated materials. Furthermore, the field-induced metamagnetic transition is accompanied by a huge negative magnetoresistance (MR) effect of up to −73% that was determined for $La_{0.85}Ce_{0.15}Fe_{12}B_6$.

The main achievement of Publications D and E, however, is revealing the mechanism behind the macroscopic, and therefore isotropically averaged, magnetostriction values obtained from dilatometry measurements. The key technique for these investigations is magnetic-field- and temperature-dependent XRD with the diffractometer assembled for this work. Not only is crystallographic information of the structure(s) involved in the metamagnetic phase transition accessible by XRD, but also additional anisotropic information in the form of unit cell parameters as function of temperature and magnetic field. With no applied magnetic field, the crystal structures of $La_{0.9}Ce_{0.1}Fe_{12}B_6$ and $La_{0.85}Ce_{0.15}Fe_{12}B_6$ are the rhombohedral $SrNi_{12}B_6$-type structure (space group $R\bar{3}m$) over the entire investigated temperature range, *i.e.*, between 300 and 15 K. The lattice parameters a and c decrease linearly (linear thermal expansion – LTE) in the range from 300 K to 125 K at a rate of $\alpha_a = 14.30 \times 10^{-6}$ K^{-1} and $\alpha_c = 7.29 \times 10^{-6}$ K^{-1}. Below 125 K, the lattice parameter decrease is damped, and, finally, almost constant below 50 K (25 K) for the a (c) axis. The thermal contraction being almost zero at low temperatures agrees with Grüneisen's law, and is a result of the phonon contribution becoming insignificant. The temperature difference ($\Delta T = 25$ K) at which a and c become constant is consistent with the anisotropy of the rhombohedral crystal symmetry.

This behavior changes drastically under applied magnetic fields. Above a certain critical field of $\mu_0 H \geq 1.75$ T (0.5 T) for $La_{0.9}Ce_{0.1}Fe_{12}B_6$ ($La_{0.85}Ce_{0.15}Fe_{12}B_6$) at 25 K, the reflections of the $SrNi_{12}B_6$-type structures in the XRD patterns begin to split, indicating the onset of a structural phase transition. The structure of the new phase was solved under the largest available magnetic field of $\mu_0 H = 5.5$ T. Although the phase transition is not complete – the highest phase fraction was later determined to be 90% (80%) for $La_{0.9}Ce_{0.1}Fe_{12}B_6$ ($La_{0.85}Ce_{0.15}Fe_{12}B_6$) at 25 K – solving the structure was possible using crystallographic group-subgroup relations. The structure was solved in the monoclinic space group $C2/m$, which means that the phase transition is accompanied by a symmetry reduction from the rhombohedral to the monoclinic crystal system. Space group $C2/m$ is a subgroup of $R\bar{3}m$, and as such the phase transition is not required to be of first order. However, a first-order character is clearly observed in the magnetization data in the form of a large hysteresis. This leads to the conclusion that it originates from the field-induced metamagnetic AFM-FM transition.

Correlation of phase fraction with the magnetization measurements indicated that the new phase is indeed FM. The AFM-FM transition in $La_{0.9}Ce_{0.1}Fe_{12}B_6$ and $La_{0.85}Ce_{0.15}Fe_{12}B_6$ is, therefore, a coupled magnetic and structural phase transition. This behavior distinguishes the $(La,Ce)Fe_{12}B_6$ material class, although also being an itinerant-electron metamagnet, fundamentally from the compounds reported in Chapter 4, *i.e.*, $LaFe_{11.6}Si_{1.4}$, MnB and FeB. These materials undergo (field-induced) metamagnetic transitions without a change in their crystal structure.

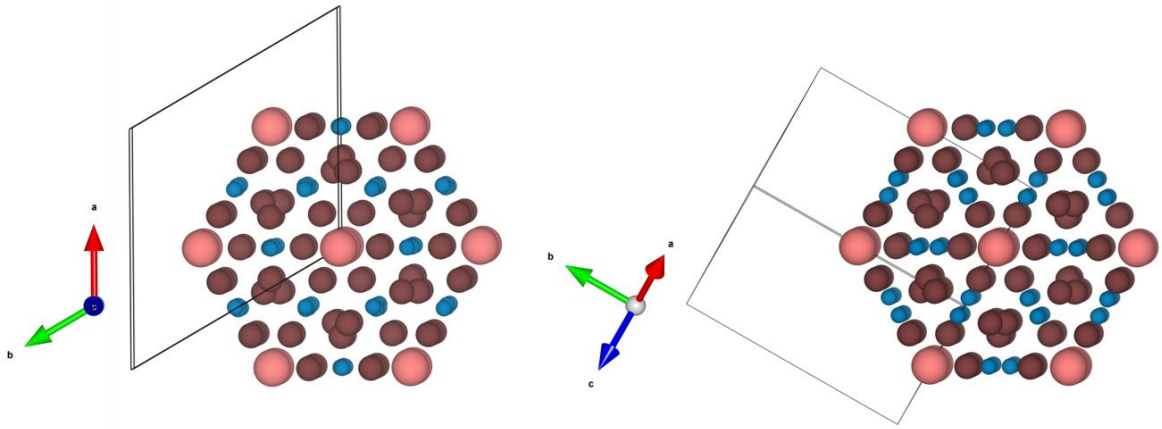

Figure 5.1: Models of the rhombohedral (left), and magnetic-field-induced monoclinic (right) crystal structure of (La,Ce)$Fe_{12}B_6$ along the (former) *c*-axis in the hexagonal coordinate system. The structure is comprised of two (four) distinct Fe atoms (brown), one (two) La atom(s) (salmon) with partial Ce occupation, and one (two) B atom(s) (turquoise).

A comparison of the rhombohedral and monoclinic structures of $La_{0.9}Ce_{0.1}Fe_{12}B_6$ and $La_{0.85}Ce_{0.15}Fe_{12}B_6$ is shown in Figure 5.1. The coordinate system of the monoclinic unit cell is different from the rhombohedral structure, but, if compared from equivalent viewing directions with respect to the former rhombohedral coordinate system, the similarity of the structures becomes apparent. Apart from a slight monoclinic distortion of the former rhombohedral unit cell, the main difference between the structures is a rearrangement of B atoms. The displacement of B atoms is similar to the shuffle displacement of atoms in martensitic transitions of Heusler alloys (231, 233, 328).

The structural phase transition is coupled with a huge unit cell expansion, *i.e.*, corresponds to a huge spontaneous magnetostriction. The crystallographic unit cell of the monoclinic structure, however, is smaller than the rhombohedral cell, due to the different lattice setting. The unit cell volumes can be compared using the following conversion: $V_{\mathrm{Mono}}(C/2m) = 2/3\, V_{\mathrm{Rhom}}(R\bar{3}m)$. After conversion of the unit cell volumes of each phase to contain exactly one formula unit of $La_{0.9}Ce_{0.1}Fe_{12}B_6$, the large difference in absolute unit cell volume becomes apparent, as shown in Figure 5.2(a).

The AFM-FM transition can be induced by applying a large enough magnetic field, regardless of using ZFCW or FCC protocol. A remarkable property of $La_{0.9}Ce_{0.1}Fe_{12}B_6$ and $La_{0.85}Ce_{0.15}Fe_{12}B_6$, however, is that overall unit cell volumes of AFM, PM and FM phases are almost constant in the two-phase region. Since the largest magnetic field that can be applied with the XRD setup with magnet (5.5 T) is not enough to complete the phase transition to the FM phase, all investigations in Publications D and E were carried out in the two-phase region. With the unit cell volumes of rhombohedral and monoclinic phases being constant as function of both temperature and magnetic field, see Figure 5.2(a) and (b), the huge volume magnetostriction that is measured macroscopically is effectively a direct measure of the monoclinic phase fraction. Volumetric thermal expansion for $La_{0.9}Ce_{0.1}Fe_{12}B_6$ ($La_{0.85}Ce_{0.15}Fe_{12}B_6$) is as large as $\alpha_V = -193 \times 10^{-6}\,K^{-1}$ ($-195 \times 10^{-6}\,K^{-1}$), placing it in the same order of magnitude as other itinerant-electron metamagnets, *e.g.*, (Hf,Ta)Fe_2 ($\alpha_V = -164 \times 10^{-6}$ K) (329, 330), $Mn_{0.98}CoGe$ ($\alpha_V = -423 \times 10^{-6}\,K^{-1}$) (331), and $Bi_{0.95}La_{0.05}NiO_3$ ($\alpha_V = -413 \times 10^{-6}\,K^{-1}$) (332).

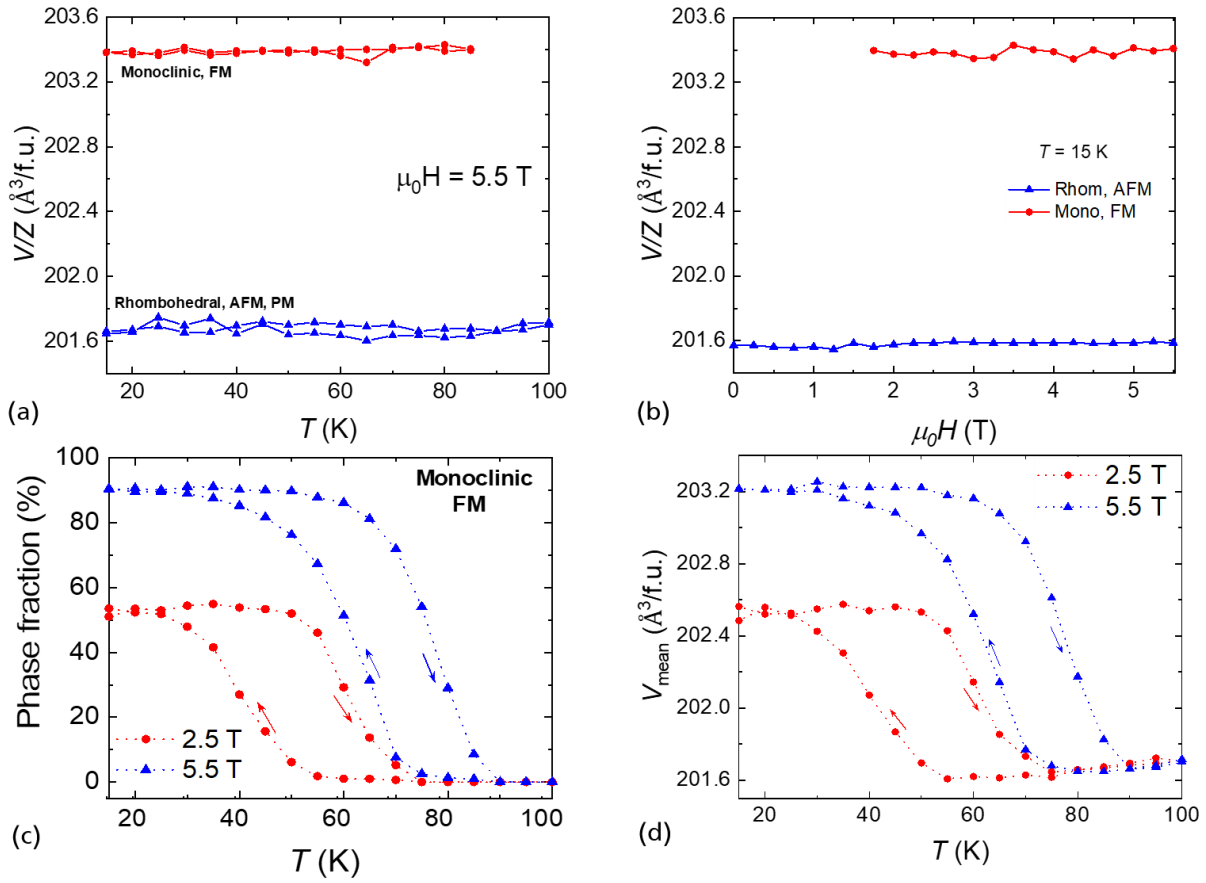

Figure 5.2.: (a) Temperature dependence of the cell volume per formula unit for $La_{0.9}Ce_{0.1}Fe_{12}B_6$ (both rhombohedral and monoclinic phases) determined from x-ray powder diffraction measurements during heating and cooling in $\mu_0 H$ = 5.5 T applied magnetic field. (b) Magnetic field dependence of the cell volume per chemical formula at 15 K. (c) Temperature dependence of the phase fraction of the monoclinic phase and (d) of the mean cell volume per formula unit determined from x-ray powder diffraction measurements during heating and cooling in $\mu_0 H$ = 2.5 and 5.5 T applied magnetic fields. Adapted from Publication D.

Analysis of the field- and temperature-dependent XRD patterns, however, provides a lot more useful information than unit cell volume and phase fraction. Information, that is not accessible by any other means from bulk sample measurements, *e.g.*, anisotropic magnetostriction for each involved crystallographic phase – simultaneously, as shown in Figure 5.3.

Single crystal investigations could yield similar information, but were not feasible as no single crystals of the required size and quality were available. Following the evolution of lattice parameters of AFM/PM and FM phases as function of temperature under 5.5 T applied field revealed a distinct hysteretic behavior. These lattice parameter hystereses are a feature of the first-order phase transition, and, hence, were expected to be present. A remarkable detail that could only be observed by XRD under magnetic fields is, however, that the thermal hysteresis region of the lattice parameters *a* and *c* is different for the rhombohedral, *i.e.*, AFM/PM, phase. The hysteresis in the *ab* basal plane of the rhombohedral phase is present in the temperature range between 30–60 K, whereas the *c* parameter remains hysteretic up to ~75 K. This anisotropy of the thermal hysteresis region is consistent with the rhombohedral symmetry of the low-volume, low-magnetization phase.

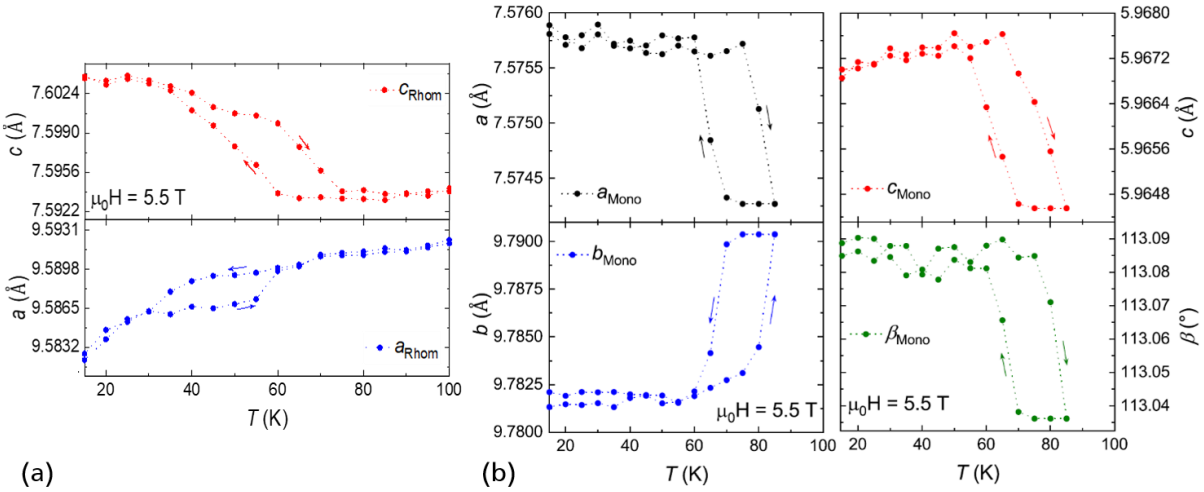

Figure 5.3.: Temperature dependences of (a) the lattice parameters *a* and *c* of the rhombohedral phase of $La_{0.9}Ce_{0.1}Fe_{12}B_6$ and (b) of the unit-cell dimensions *a*, *b*, and *c*, and Bragg angle β of the monoclinic phase determined from x-ray powder diffraction measurements during heating and cooling in $\mu_0 H = 5.5$ T applied magnetic field. Adapted from Publication D.

A distinct hysteresis was also present for the lattice parameters of the field-induced monoclinic phase, see Figure 5.3(b). Interestingly, the temperature range of thermal hysteresis was again different. All monoclinic unit cell parameters were hysteretic in the temperature region between 60 K and 80 K, which coincides with the hysteresis of monoclinic phase fraction, as seen in Figure 5.2(c). The rhombohedral lattice parameters are more affected by the magnetic field in the region where the FM phase is already the majority phase, whereas the monoclinic lattice parameters are almost constant in the same temperature region. This is a clear sign of the internal magnetic pressure that the magnetic field exerts on the AFM phase close to the critical field that would be needed for a complete conversion to FM phase. This feature of the field-induced magnetostructural transition is very similar to the metamagnetic transition of $LaFe_{11.6}Si_{1.4}$ reported in Publication B. In the two-phase region of $LaFe_{11.6}Si_{1.4}$, the lattice parameter of the PM phase is also highly dependent on the magnetic field, and temperature due to the internal magnetic pressure created by short-range magnetic correlations. However, the metamagnetic transition in $LaFe_{11.6}Si_{1.4}$ is not accompanied by a structural change, so the process of transition from one phase to another happens smoothly.

For $La_{0.9}Ce_{0.1}Fe_{12}B_6$ and $La_{0.85}Ce_{0.15}Fe_{12}B_6$, the mechanism of field-induced metamagnetic phase transition is different than for $LaFe_{11.6}Si_{1.4}$. Due to the large unit cell volume expansion, and structural distortion and rearrangement that accompany the phase transition, the FM phase is kinetically arrested in the AFM phase matrix. Seeds of FM phase form above the critical phase transition field, but they are hindered in growth by the strain of the untransformed matrix surrounding the grains. As the external field increases, the driving force acting on the magnetic moments increases, as well. The transition itself happens burst-like after reaching a certain critical field that is large enough to overcome the elastic strain energy. This phenomenon of kinetic arrest is often observed in martensitic phase transitions (159, 160), and is a main factor that contributes to the hysteresis of the martensite<->austenite transformations.

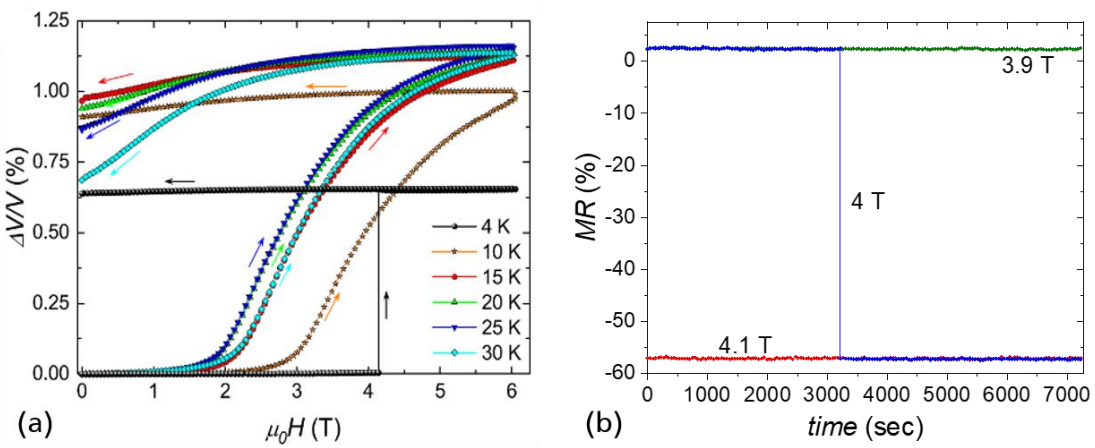

Figure 5.4.: (a) Volume magnetostriction isotherms of $La_{0.9}Ce_{0.1}Fe_{12}B_6$ measured between 4 and 30 K. (b) Time dependence of the magnetoresistance recorded at the indicated applied fields for $La_{0.85}Ce_{0.15}Fe_{12}B_6$ at 2.5 K. Adapted from Publications D and E.

Clear evidence for the martensitic-like character of the field-induced phase transition in $La_{0.9}Ce_{0.1}Fe_{12}B_6$ and $La_{0.85}Ce_{0.15}Fe_{12}B_6$ is the step-wise transformation behavior observed in several macroscopic material properties. At 4 K, there is a sudden burst-like volume expansion $\Delta V/V$ in the dilatometry measurements, see Figure 5.4(a). This was also observed in time dependent MR measurements, in which a sudden giant negative MR effect was detected at 4 T applied field after 3200 s incubation time. Applying 3.9 T would not induce the giant negative MR effect, but repeating the measurement under 4.1 T immediately induced the metamagnetic transition and, therefore, the giant negative MR effect. Many systems exhibiting this peculiar response to external fields were discovered in recent years (161, 325–327), and of particular interest were Heusler type alloys (159, 160, 239) for which the term kinetic arrest was coined initially.

These results show that XRD with magnetic field is a valuable tool for analyzing anisotropic magnetostriction of compounds. Information regarding phase-specific hysteresis of lattice parameters is crucial for understanding phase transformation mechanisms, and is information only accessible with XRD. Furthermore, it was shown that macroscopic properties can be understood using this analysis technique probing microscopic parameters.

5.2. Publication D: Evidence for a coupled magnetic-crystallographic transition in $La_{0.9}Ce_{0.1}Fe_{12}B_6$

Evidence for a coupled magnetic-crystallographic transition in $La_{0.9}Ce_{0.1}Fe_{12}B_6$

Léopold V.B. Diop[1], Tom Faske[2], Mehdi Amara[3], David Koch[2], Olivier Isnard[3], and Wolfgang Donner[2]
[1]Université de Lorraine, CNRS, IJL, F-54000 Nancy, France
[2]Institute of Materials Science, Technical University of Darmstadt, D-64287 Darmstadt, Germany
[3]Université Grenoble Alpes, CNRS, Institut NEEL, 25 rue des martyrs, F-38042 Grenoble, France

Correspondence email: leopold.diop@univ-lorraine.fr

Received 8 May 2021
Accepted 30 September 2021
DOI: 10.1103/PhysRevB.104.134412

Abstract Competition between antiferromagnetic (AFM), paramagnetic (PM), and ferromagnetic (FM) states in $La_{0.9}Ce_{0.1}Fe_{12}B_6$ compound is investigated by means of temperature- and magnetic field-dependent x-ray diffraction, magnetization, linear thermal expansion, and magnetostriction experiments. It is shown that both AFM and PM phases get converted into the FM phase via a first-order metamagnetic transition, which is accompanied by a huge forced-volume magnetostriction $\Delta V/V$ (25 K, 6 T) = 1.15%. X-ray powder diffraction reveals a magnetic field-induced crystallographic phase transition from a $R\bar{3}m$ rhombohedral (AFM, PM) to a $C2/m$ monoclinic (FM) structure. A peculiarly anisotropic lattice expansion as well as giant negative thermal expansion with a volumetric thermal expansion coefficient $\alpha_V = -193 \times 10^{-6}\ K^{-1}$ are observed. These findings point to the significance of magnetoelastic effects in this metamagnet and illustrate the strength of the coupling between lattice and spin degrees of freedom in the $La_{0.9}Ce_{0.1}Fe_{12}B_6$ intermetallic compound.

5.2.1. Introduction

A large number of solid systems display structural phase transitions when subject to changes in external applied pressure, temperature, and chemical composition. However, the occurrence of magnetic field-induced structure transformations is rather exceptional and a few examples are reported in the literature. An intensively investigated case is the transition-metal chalcogenide MnAs which exhibits a first-order structural transition from a hexagonal to an orthorhombic crystal symmetry upon heating through ≈313 K (ferromagnetic ordering temperature) (94, 260, 333). The structural transition observed in this compound can be stimulated, at a fixed temperature, by the application of an external magnetic field. For example at 327 K, the magnetic field required to accomplish the structural phase transformation amounts to 5.1 T (3.1 T) for increasing (decreasing) applied fields (94, 260, 333). A work by Asamitsu *et al.* (334), including striction, x-ray powder diffraction, and resistivity studies as a function of both external field and temperature, has revealed the existence of a magnetic field-induced structural phase transition in the (La,Sr)MnO_3 series of magnetoresistive compounds. The Gd_5Ge_4 alloy has been widely investigated due to a combination of intriguing physical phenomena and potentially important functionalities, such as magnetoresistance, anisotropic magnetostrictive effect, unconventional glasslike magnetic behavior, and unusual kinetic arrest of the magnetostructural phase transformation (335–337). The temperature alone cannot trigger the ferromagnetic ordering in Gd_5Ge_4 intermetallic system, yet a magnetic field induces the ferromagnetic phase through a first-order transition that is coupled with a considerable reshuffling of the crystallographic structure of the compound (54). The pseudo-binary $Gd_5(Si_xGe_{1-x})_4$ alloys within the concentration range $0.24 \leq x \leq 0.5$ are of particular interest; the crystallographic symmetry is no longer orthorhombic but monoclinic, giving rise to a dramatic change in the magnetic behavior (96, 338). These compounds undergo a field-induced magnetostructural transition from a high-temperature monoclinic (paramagnetic) to a low-temperature orthorhombic (ferromagnetic) phase, which is accompanied by large magnetoelastic and giant magnetocaloric effects (95, 338). Other systems, such as doped-$CeFe_2$ (339), (Hf,Nb)Fe_2 (340)], and FeRh (341–343) were found to exhibit a first-order magnetostructural phase transition from antiferromagnetic to ferromagnetic order. Currently, these different classes of materials featuring a strong coupling between the magnetic and crystal lattices are of significant importance from the fundamental research side as well as from the technological applications viewpoint. The understanding of the interplay between magnetic and crystallographic structures is a crucial challenge in condensed-matter physics. Solid systems with interconnected magnetic and structural degrees of freedom often present multifunctional properties such as giant magnetoresistance, colossal magnetostriction, and giant magnetocaloric effect. These prominent magnetoresponsive effects result from instabilities in crystallographic lattice and magnetic order (96). In other words, these emergent physical phenomena are particularly pronounced in the vicinity of a magnetostructural phase transformation, which in turn allows controlling the physical properties of the compound via several types of externally applied driving forces. These compounds constitute an exceptional playground for materials physics owing to the extreme sensitivity of their physical properties to moderate external stimuli.

Interestingly, unconventional multistep metamagnetic transitions were recently reported in (La,Ce)$Fe_{12}B_6$ series of compounds (322–324, 344). These peculiar metamagnetic phase transitions are featured by ultrasharp steps followed by plateaus leading to an unusual and even unique staircaselike magnetization process. The antiferromagnetic itinerant-electron compound $LaFe_{12}B_6$ occupies a special place among rare-earth iron-rich intermetallics; it exhibits exotic

magnetic and physical properties. The unusual amplitude-modulated spin configuration defined by a propagation vector k = (¼, ¼, ¼), remarkably weak Fe magnetic moment (0.43 μ_B) in the antiferromagnetic ground state, especially low magnetic ordering temperature T_N = 36 K for an Fe-rich phase, a multicritical point in the complex magnetic phase diagram (322), both normal and inverse magnetocaloric effects (345), colossal spontaneous magnetization jumps (323), and huge hydrostatic pressure effects (346) can be highlighted as the most relevant. These singular properties not only stimulate the development of theoretical models and experiments under extreme conditions for a deeper understanding of the striking phenomenology of this magnetic system (346–350), but also emphasize the potential interest of $LaFe_{12}B_6$ material in future low-temperature energy technologies. Among the $RT_{12}B_6$ family (where R stands for a rare-earth atom and T is a 3d transition-metal element), $LaFe_{12}B_6$ is the sole stable Fe-based phase of the 1:12:6 ternary system (349, 350). The first Fe-based member of the $RT_{12}B_6$ family to be identified, $NdFe_{12}B_6$ is metastable (351). On the other hand, the $RCo_{12}B_6$ alloys are stable along the entire rare-earth series (352). At room temperature, the intermetallic compounds $RT_{12}B_6$ crystallize in the rhombohedral $SrNi_{12}B_6$-type structure (space group $R\bar{3}m$) (353–355). Within the unit cell, there are two crystallographically inequivalent sites for T atoms (18g and 18h). The R and B atoms occupy the 3a and 18h Wyckoff positions, respectively. The $LaFe_{12}B_6$ compound is unique among the ternary system $RT_{12}B_6$ in having an antiferromagnetic ground state. The magnetic transition temperature of $LaFe_{12}B_6$ is much smaller than the Curie point of the Co-based $RCo_{12}B_6$ ferro- (R =Y, La-Sm) or ferri- (R = Gd-Tm) magnets (T_C =134−162 K) (352) and an order of magnitude smaller compared to the magnetic ordering temperature of any rare-earth iron-rich binary intermetallic. Extraordinary magnetotransport effects have been most recently discovered in $RT_{12}B_6$ compounds (356).

In this paper we report a thorough experimental study of the low-temperature first-order phase transition in $La_{0.9}Ce_{0.1}Fe_{12}B_6$ model compound by combining magnetization, linear thermal expansion, magnetostriction, and temperature- and magnetic field-dependent x-ray powder diffraction measurements. It is thus shown that the metamagnetic transition in question takes place simultaneously with a change of the crystal symmetry: a first-order structural transformation to a different monoclinic phase. This coupled magnetic-crystallographic phase transition is triggered by the external applied magnetic field, resulting in large magnetoelastic effects and therefore making this compound a potential candidate for magnetostrictive materials.

5.2.2. Experiment Details

The polycrystalline alloy of composition $La_{0.9}Ce_{0.1}Fe_{12}B_6$ was prepared by arc melting the mixture of high purity components (better than 99.9%) under an atmosphere of argon. To purify the argon atmosphere inside the arc melter, a piece of titanium was melted in an adjacent recess of the water-cooled copper hearth prior to the melting of the constituting elements. To promote compositional homogeneity, the alloy was melted several times with the button being flipped over after each re-melting. The so-obtained ingot was wrapped in tantalum foil, sealed in an evacuated fused silica tube and subsequently annealed in a furnace as follows. It was heated up to 1173 K at a rate of 5 K/min and kept at this temperature for 3 weeks. The analysis of the phase purity and the room-temperature crystallographic structure was carried out by standard x-ray diffraction using a Siemens D5000 powder diffractometer in reflection mode with the Bragg-Brentano geometry and Co-K_α radiation ($\lambda_{K\alpha1}$ = 1.78897 Å and $\lambda_{K\alpha2}$ = 1.79285 Å).

Magnetization curves were collected on a powder sample at temperatures ranging between 2 and 300 K with an extraction-type magnetometer. Temperature and field dependences of the magnetic moment were recorded in static magnetic fields of up to 10.5 T. The magnetometer was described in (357). Magnetization values were corrected for the presence of the minor ferromagnetic Fe_2B secondary phase.

Linear thermal expansion (LTE) and forced magnetostriction measurements were undertaken on the magnetostriction setup of the Néel Institut. This apparatus is based on a high-sensitivity capacitance dilatometer that operates in a magnetic field up to 6 T and over a temperature interval from 2.5 to 300 K. In terms of relative length variation, the sensitivity is better than 10^{-7}. The capacitance cell can be rotated around the vertical axis of the cryostat while the external magnetic field is applied along a fixed horizontal direction. Magnetostriction isotherms were recorded in both directions parallel and perpendicular to the applied magnetic field. For LTE and magnetostriction experiments, the polycrystal was first subject to mechanical shaping (roughly shaped into sphere) by grinding off sharp corners. Thereupon, it was run for several hours by a jet of compressed air inside a cylinder lined with fine sandpaper, until it became visually spherical. The polycrystalline sample was approximately a sphere of about 5 mm diameter. The LTE data were corrected for the cell thermal hysteresis.

Temperature- and magnetic field-dependent x-ray powder diffraction data were collected on a custom-built diffractometer in transmission geometry using Mo-K_α radiation ($\lambda_{K\alpha1}$ = 0.70932 Å and $\lambda_{K\alpha2}$ = 0.71340 Å) with an angular 2θ range from 7° to 57° and a scan step of 0.009°. $La_{0.9}Ce_{0.1}Fe_{12}B_6$ fine powder (particle size smaller than 20 μm) was uniformly mixed with a NIST standard reference Si powder 640d and then glued onto a carbon foil. The sample was dried in air. The carbon foil was mounted on a copper cold finger–serving as a sample holder– of a closed-cycle helium cryofurnace and transferred into a split-coil superconducting magnet that produces a homogeneous magnetic field of up to 5.5 T around the sample position with the magnetic field vector perpendicular to the scattering plane. A detailed description of the laboratory-based x-ray powder diffractometer can be found in (1). Zero-field cooled warming (ZFCW) and field cooled cooling (FCC) experimental procedures were employed for thermodiffraction measurements under various applied magnetic fields (isofield measurements). For ZFCW protocol, the sample is first cooled in zero magnetic field from room temperature down to the lowest measurement temperature; then, the magnetic field is applied after reaching thermal equilibrium, and diffraction patterns are recorded upon heating. The ZFCW data collection is immediately followed by cooling under the same applied magnetic field (FCC). Prior to the magnetic field-dependent diffraction measurements (isothermal measurements), the sample was cooled from room temperature to the temperature of the measurement with no magnetic field applied. For both isofield and isothermal measurements, the temperature of the sample was stabilized for ≈10 min before diffraction data acquisition. Rietveld analyses of the diffraction patterns were carried out using the *FULLPROF* suite software package (237). The unit-cell parameters and phase quantities, when two distinct crystallographic phases coexist in certain combinations of magnetic field and temperature, were determined. The sample employed in the present study is the same as that used in (324).

5.2.3. Results and Discussion

5.2.3.1. Magnetization

Figure 5.5 illustrates the thermomagnetic curves, *M(T),* of $La_{0.9}Ce_{0.1}Fe_{12}B_6$ in ZFCW and FCC measuring protocols at different applied magnetic fields from 0.75 to 10 T. The low-field magnetization curve ($\mu_0 H = 0.75$ T) displays a small broad peak around the Néel temperature $T_N = 35$ K which corresponds to an antiferromagnetic (AFM)–paramagnetic (PM) phase transition. In magnetic fields of $\mu_0 H = 7$ and 10 T at 2 K the alloy is already in the ferromagnetic (FM) state, and therefore the *M(T)* measurements reflect only the magnetic transition from FM order to PM state.

However, the magnetization shows considerably different thermal variation when measured in 3.5 T external field (Figure 5.5). It exhibits a bell-shaped anomaly with a pronounced divergence between ZFCW and FCC data. The steep rise in the magnetization by 650%, when temperature is increased by 5 K, indicates a sudden development of a high-magnetization phase stimulated by temperature change in an applied field of 3.5 T, whereas in 0.75 T $La_{0.9}Ce_{0.1}Fe_{12}B_6$ compound remains in a low-magnetization state. The spectacular increase of magnetization on the low-temperature side of the 3.5 T ZFCW curve is associated with the onset of ferromagnetic ordering. Throughout this phase transformation, both magnetically ordered phases, AFM and FM, coexist in $La_{0.9}Ce_{0.1}Fe_{12}B_6$, hence forming a magnetically heterogeneous state or magnetic-phase-segregated state in a chemically homogeneous compound. The bell-like feature correlates with the existence of both low-temperature AFM-FM and high-temperature FM-PM magnetic transitions. The intermetallic compound $La_{0.9}Ce_{0.1}Fe_{12}B_6$ transforms only partially into the FM state when cooled in a 3.5 T external magnetic field. This can be seen on Figure 5.5 from the intermediate magnetization plateau value of about 14 μ_B/f.u. During cooling, the magnetization increases as the temperature is lowered and then saturates demonstrating that the magnetic transformation in $La_{0.9}Ce_{0.1}Fe_{12}B_6$ depends on the direction of the temperature change. Furthermore, the maximum value of magnetization in the 3.5 T isofield curve is smaller for the FCC branch than for the ZFCW leg. This aspect is rather unusual for standard ferromagnetic materials in an external magnetic field as high as 3.5 T. A similar bell-like behavior was reported for $LaFe_{12}B_6$ in the magnetic field interval from 4.75 to 7 T (322). Another noteworthy experimental observation in the thermomagnetic data of Figure 5.5 is the large thermal hysteresis near the Curie point, which bears witness to the first-order character of the magnetic phase transition.

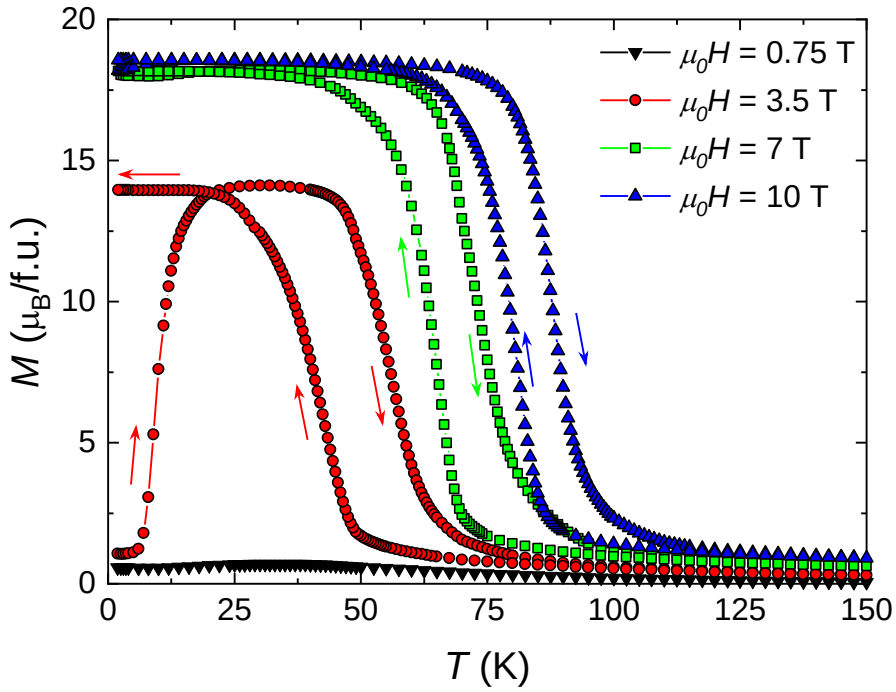

Figure 5.5.: Thermomagnetic curves of $La_{0.9}Ce_{0.1}Fe_{12}B_6$ in magnetic fields of 0.75, 3.5, 7, and 10 T. Both ZFCW and FCC data are marked by the same symbols. The arrows indicate the direction of the temperature change.

The isothermal magnetization curves, *M(H)*, of $La_{0.9}Ce_{0.1}Fe_{12}B_6$ at different fixed temperatures are displayed in Figure 5.6. For each isotherm, the applied magnetic field was cycled twice between 0 and the maximum attainable value of 10.5 T (measurements for the second field reduction are not presented in Figure 5.6 for the sake of clarity). Only a selection of the results of the measurements performed at some chosen representative temperatures in the different magnetic states are shown in Figure 5.6 (but all of the collected magnetization data were used to construct the magnetic phase diagram depicted in Figure 5.18). Each magnetization isotherm starts from the virgin state after zero magnetic-field cooling from the paramagnetic region. Figure 5.6(a) illustrates the data at temperatures of 2 and 10 K, and Figure 5.6(b) represents the isotherms taken at temperatures ranging between 20 and 65 K. The first magnetization curves (virgin curves) display a magnetic field-induced metamagnetic transition between the AFM ground state and the FM state below T_N and from the PM into FM states above T_N. This observed metamagnetic transition proceeds through a gradual transformation of the PM or AFM phases into FM domains with increasing magnetic field. The magnetization isotherms show a very large magnetic hysteresis, confirming the first-order nature of the metamagnetic phase transition. The width of the hysteresis amounts to 3.5 T at 10 K and progressively decreases with increasing temperature.

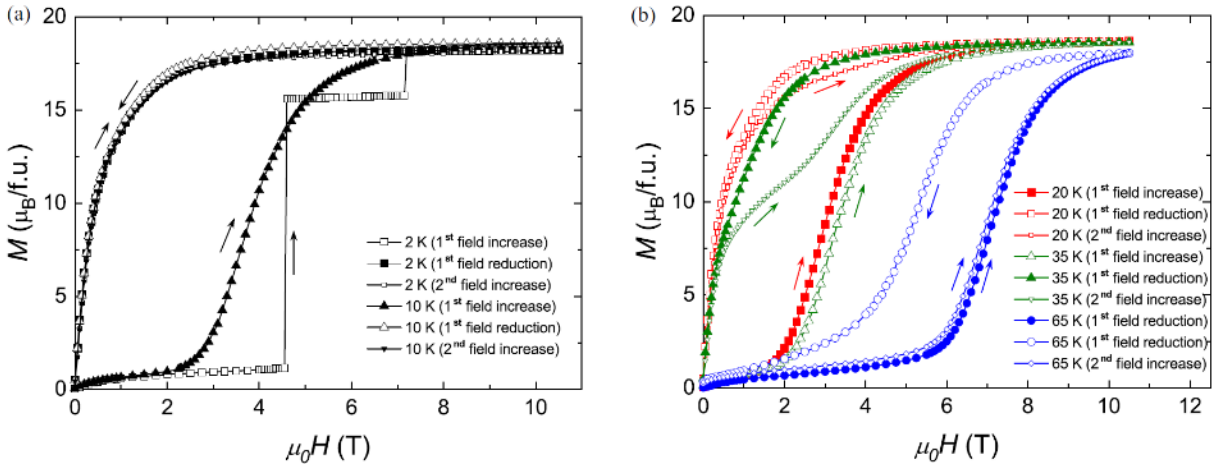

Figure 5.6.: Isothermal magnetization curves of $La_{0.9}Ce_{0.1}Fe_{12}B_6$ at (a) 2 and 10 K, and (b) 20, 35, and 65 K.

As can be seen from Figure 5.6, during the first application of the magnetic field, at 2 K the magnetization exhibits two sharp steps (at $\mu_0 H_{cr1} = 4.4$ T and $\mu_0 H_{cr2} = 7.1$ T) followed by plateaus, indicating a staircaselike metamagnetic transition similar to that evidenced in the parent compound $LaFe_{12}B_6$. This avalanchelike magnetization process arises from transformation of fraction of the specimen volume from the AFM state into the FM state. The first magnetization plateau observed at 2 K in Figure 5.6 represents a magnetically heterogeneous state corresponding to a mixture of the field-driven FM and original AFM phases (phase separated into AFM and FM domains). During the first step the total magnetic moment of the compound spontaneously increases from 1.15 to 15.59 μ_B/f.u. At the second metamagnetic jump it changes from 15.78 μ_B/f.u. to the saturation moment of the fully FM polarized state, 18.22 μ_B/f.u. In $La_{0.9}Ce_{0.1}Fe_{12}B_6$, the ultrasharp magnetization jumps are only seen in the virgin magnetization curve and are absent in the subsequent envelope. The multiple abrupt steps are restricted to very low temperatures and disappear at 8 K where the magnetization process becomes smooth.

During the second magnetic field increase in the temperature range between 2 and 25 K, the curve presents a conventional ferromagneticlike magnetization process and practically coincides with the first demagnetization loop. The first-order AFM-FM transformation is fully irreversible in this temperature region, *i.e.*, after the applied field is removed, almost 100% of the $La_{0.9}Ce_{0.1}Fe_{12}B_6$ alloy remains in the induced-FM state. In contrast, when the temperature is increased above 25 K and below 55 K, the shape of the *M(H)* curves during the second increase of the external field from 0 to 10.5 T is even more complex and quite unusual when compared to the behavior observed below 25 K. The magnetization shows a ferromagneticlike dependence (see the low magnetic field portion at 35 K) followed by a metamagnetic phase transformation. From ~25 to ~55 K, the magnetic field-induced AFM-FM and PM-FM transitions are partially reversible; a fraction of the sample volume recovers the initial AFM or PM state when the magnetic field is brought back to zero. Both reversible and irreversible transitions are present in the temperature interval between ~25 and ~55 K, and the fraction of the system, which undergoes the irreversible transformation, decreases with temperature. Beyond 55 K, the PM-FM metamagnetic transition becomes completely reversible, but accompanied with a magnetic hysteresis.

5.2.3.2. B. Thermal expansion and magnetostriction

$La_{0.9}Ce_{0.1}Fe_{12}B_6$ exhibits successive magnetic transformations and a remarkable metamagnetic transition which is characterized by an enormous magnetization variation and a huge hysteresis. Consequently, $La_{0.9}Ce_{0.1}Fe_{12}B_6$ is expected to display large magnetovolume effects across the magnetic transitions. To explore more profoundly the nature of this unusual magnetic behavior (first-order character of the AFM-FM and FM-PM transitions), LTE ($\Delta L/L$) was measured in various applied magnetic fields following the same experimental procedure as in the temperature dependence of the magnetization described above. The obtained results are presented in Figure 5.7. An anomaly is found at ≈33 K in the spontaneous ($\mu_0 H$ = 0 T) LTE curve; this value is in good agreement with the Néel temperature deduced from thermomagnetic measurements. No difference was detected between the heating and cooling protocols. In zero magnetic field, the compound expands upon heating (positive thermal expansion) at temperatures exceeding T_N; however, below the Néel temperature $\Delta L/L$ increases as the temperature is lowered (negative thermal expansion, NTE). No significant variation in $\Delta L/L$ was observed at T_N, suggesting weak magnetoelastic effects associated with the second-order AFM-PM transition.

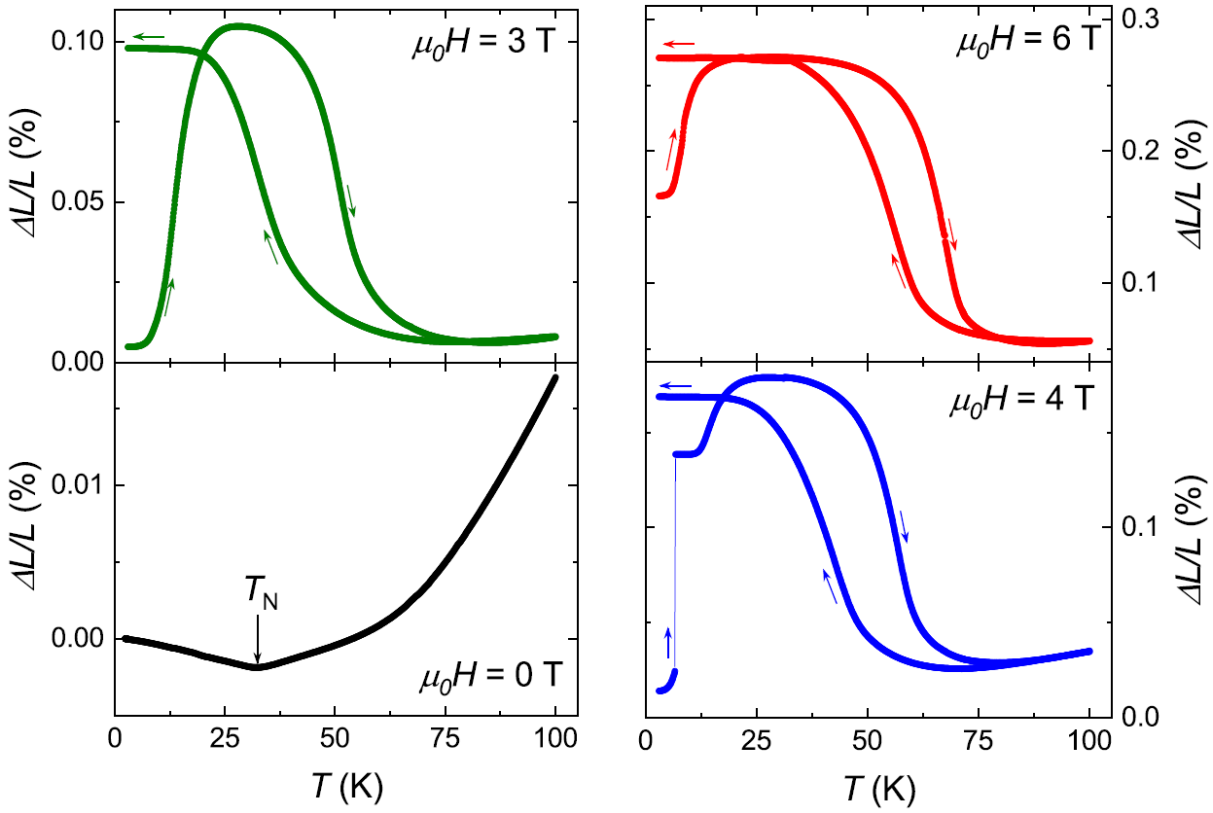

Figure 5.7.: Linear thermal expansion of $La_{0.9}Ce_{0.1}Fe_{12}B_6$ as a function of temperature recorded in magnetic fields of 0, 3, 4, and 6 T.

The LTE curve ($\mu_0 H$ = 3 T) manifests a bell-like behavior and magnetic events which are very much similar to the phase transitions found in the isofield magnetization data. Upon heating in a 3 T magnetic field, the zero-field cooled sample displays a crossover from positive to negative thermal expansion due to the AFM-FM and FM-PM transitions. During cooling ($\mu_0 H$ = 3 T), the lattice undergoes an expansion and then $\Delta L/L$ saturates at low temperatures. Interestingly, a sudden jump is detected in the 4 T LTE curve; $\Delta L/L$ varies abruptly from 0.025 to 0.14% when

the temperature changes by only 0.1 K. This result reveals that at 4 T, the increase in temperature triggers the AFM-FM magnetic phase transformation at low temperatures. Like the magnetization, the forced magnetostriction curves recorded in magnetic fields $\mu_0 H$ = 3, 4, and 6 T also show a pronounced splitting and a huge thermal hysteresis of ~15 K between the ZFCW and FCC modes. The large length variation and temperature hysteresis indicate the existence of important structural effects across the first-order AFM-FM and FM-PM transitions. In the 6 T ZFCW data, a NTE phenomenon is observed over a temperature interval of $\Delta T \sim 60$ K yielding an average linear thermal expansion coefficient $\alpha_L = (1/L)(\Delta L/\Delta T) = -37 \times 10^{-6}$ K^{-1}. Such a large NTE coefficient compares well with the value obtained for the itinerant-electron metamagnetic compound $LaFe_{10.5}CoSi_{1.5}$ $\alpha_L = -26 \times 10^{-6}$ K^{-1} (320). It is important to emphasize that the absolute value of α_L for $La_{0.9}Ce_{0.1}Fe_{12}B_6$ is about 4 times larger than that of ZrW_2O_8, $\alpha_L = -9 \times 10^{-6}$ K^{-1}, which is currently used as commercial NTE material (358).

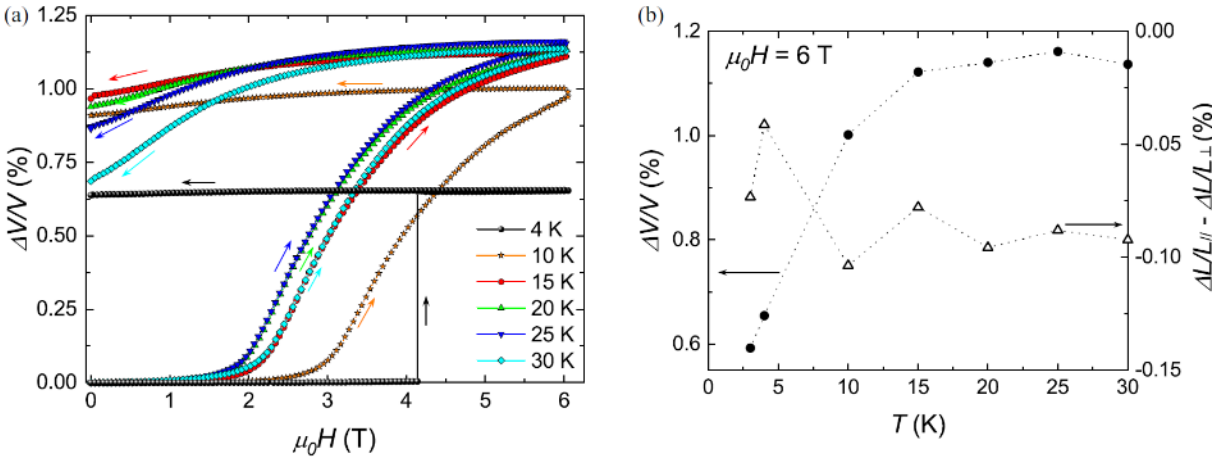

Figure 5.8.: (a) Volume magnetostriction isotherms measured between 4 and 30 K. (b) Temperature dependence of the volume ($\Delta V/V = \Delta L/L_{//} + 2\Delta L/L_\perp$) and anisotropic ($\Delta L/L_{//} - \Delta L/L_\perp$) magnetostriction measured for $La_{0.9}Ce_{0.1}Fe_{12}B_6$ at the maximum applied field of 6 T.

To clarify the volume change by the metamagnetic phase transition, longitudinal ($\Delta L/L_{//}$) and transverse ($\Delta L/L_\perp$) magnetostriction isotherms were recorded. Using these data, the volume magnetostriction ($\Delta V/V = \Delta L/L_{//} + 2\Delta L/L_\perp$) and the anisotropic magnetostriction ($\Delta L/L_{//} - \Delta L/L_\perp$) were assessed. In Figure 5.8(a) we present the forced-volume magnetostriction isotherms at various temperatures in the AFM region. For all isotherms the sample was cooled in zero magnetic field. At 4 K in the field-increasing branch, a sharp discontinuity of $\Delta V/V \approx 0.65\%$ occurs at a certain critical field $\mu_0 H_{cr} = 4.2$ T. No anomaly is detected in the reverse leg and $\Delta V/V$ keeps an almost constant value down to the zero magnetic field point, *i.e.*, the material remains in the final deformation state. This demonstrates the fully irreversible nature of the phase transition at 4 K. This strong magnetic field-induced irreversibility is an outstanding feature and consistent with the irreversibility observed in the isothermal magnetization curves. The jump present in the magnetostriction isotherm is similar to those seen in the virgin magnetization loops and proves the strong correlation between magnetic and elastic properties in $La_{0.9}Ce_{0.1}Fe_{12}B_6$ intermetallic compound. A huge magnetic hysteresis is evidenced, demonstrating that the phase transformation is of first-order type in nature. The magnetostriction results clearly attest that the metamagnetic phase transition is accompanied by large magnetovolume effects. In other words, the applied magnetic field induces a transition from a low-volume, low-magnetization phase to a high-volume, high-magnetization phase. The thermal variation of the volume and anisotropic magnetostriction at the maximum attainable

field of 6 T is depicted in Figure 5.8(b). In the present case a large anisotropic effect is observed, *i.e.*, the value of the longitudinal magnetostriction is lower than that of the transverse one ($\Delta L/L_{\perp} > \Delta L/L_{//}$). The anisotropic magnetostriction is as large as (10 K, 6 T) ≈ –0.10%, but the magnetostriction isotherms are not saturated even under 6 T. The maximum volume magnetostriction associated with the AFM-FM transition is estimated to be about $\Delta V/V$ (25 K, 6 T) ≈ 1.15%. When this later value is compared with the volume change calculated from LTE data of Figure 5.7, $\Delta V/V = 3\Delta L/L = 0.65\%$, one notices a significant discrepancy between them. This large difference in the observed relative volume variations, when taken into account concurrently with the presence of a huge anisotropic magnetostriction, likely reflects the role of anisotropy in describing the magnetoelastic effects of the compound. It is noteworthy that the relative volume change, $\Delta V/V$ (25 K, 6 T) ≈ 1.15%, in $La_{0.9}Ce_{0.1}Fe_{12}B_6$ is comparable in magnitude to the isotropic forced-volume magnetostriction due to the metamagnetic transition in iron-rich itinerant-electron compounds such as $La(Fe_xAl_{1-x})_{13}$ (359) and $La(Fe_xSi_{1-x})_{13}$ (252). Indeed, Irisawa *et al.* (359) reported a value of $\Delta V/V = 1\%$ for $La(Fe_{0.87}Al_{0.13})_{13}$. Volume changes of 0.9 and 1.5% were obtained for $La(Fe_{0.86}Si_{0.14})_{13}$ and $La(Fe_{0.88}Si_{0.12})_{13}$, respectively (252).

5.2.3.3. Temperature and magnetic field-dependent x-ray diffraction

The consistence found in the magnetostriction and magnetization data obviously reflects the strong coupling between lattice and spin degrees of freedom in $La_{0.9}Ce_{0.1}Fe_{12}B_6$. The magnetostriction data suggest strong structural effects associated with the magnetic transitions when the applied field exceeds the critical value. Therefore, the crystal structure of the field-induced FM phase cannot be inferred from zero magnetic field diffraction spectra since the temperature alone cannot trigger the transformation. Magnetic field-dependent x-ray powder diffraction appears to be the viable option to provide structural details at the atomic scale and to decipher how a crystal lattice is responsible for a specified magnetic behavior. In order to get a deeper insight into the nature of the low-temperature transformation in this intriguing material $La_{0.9}Ce_{0.1}Fe_{12}B_6$, x-ray diffraction measurements under applied magnetic fields were performed down to 15 K.

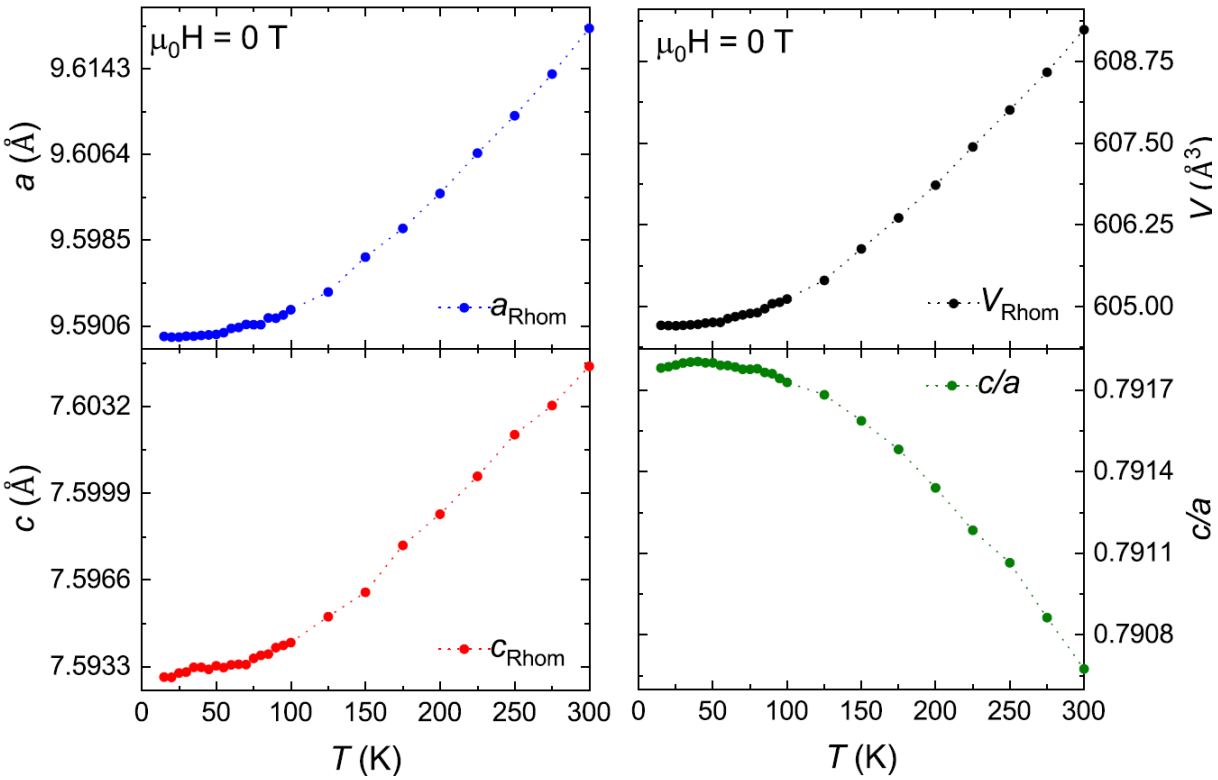

Figure 5.9.: Temperature dependence of the lattice parameters *a* and *c*, unit-cell volume *V*, and *c/a* ratio of the rhombohedral cell determined from Rietveld refinement of x-ray powder diffraction patterns measured during cooling in $\mu_0 H$ = 0 T.

The diffraction patterns recorded in zero magnetic field ($\mu_0 H = 0$ T) were identical in the temperature range from 300 to 15 K apart from an anisotropic shift of Bragg reflections due to thermal expansion. According to the Rietveld analyses the compound had the rhombohedral $SrNi_{12}B_6$-type structure (space group $R\bar{3}m$) over the entire investigated temperature range. The crystal symmetry is preserved down to 15 K, *i.e.*, the trigonal symmetry of the atomic arrangement is kept unchanged. No indication of a temperature-induced structural transition was detected down to the lowest temperature of the x-ray diffraction experiment. The lattice parameters *a* and *c*, unit-cell volume *V*, and *c/a* ratio of the rhombohedral cell are plotted against temperature in Figure 5.9. The zero-field thermodiffraction results reveal that both lattice constants are anisotropically reduced upon cooling, thus leading to a diminution in the cell volume. On the other hand, the *c/a* ratio increases as the temperature is lowered. At temperatures ranging from 300 to 125 K, the lattice constants vary linearly and the calculated coefficients of linear thermal expansion along the two principal crystallographic directions are $\alpha_a = 14.30 \times 10^{-6}$ K^{-1} and $\alpha_c = 7.29 \times 10^{-6}$ K^{-1}. Along the *a*-axis direction (in the basal plane) the thermal expansion is much larger than that along the threefold symmetry axis *c*. The crystallographic volume thermal expansion coefficient amounts to $\alpha_V = 36 \times 10^{-6}$ K^{-1}. Below 50 K, the unit-cell dimension *a* is basically constant and therefore the LTE along this particular crystallographic axis approaches zero, whereas the LTE along the high-symmetry direction *c* becomes almost negligible only below 25 K. Even though the practically zero thermal expansion found along the two principal crystallographic directions at low temperatures is in agreement with the normal phonon contribution becoming insignificant (consistent with Grüneisen's law), the difference in the temperature at which the LTE approaches zero is in accordance with the anisotropy of the crystal lattice. No perceptible anomaly of thermal expansion is observed around T_N in the temperature dependence of the unit-cell volume.

In order to examine the lattice response to the magnetic transitions, x-ray diffraction diagrams

were recorded at temperatures ranging between 15 and 100 K in a constant applied magnetic field. Diffractograms collected at 15 K in magnetic fields of 0 and 5.5 T are plotted in Figure 5.10(a). For clarity reasons, only the angular 2θ range 14°– 30° is displayed. From the visual inspection of the x-ray powder diffraction patterns, it is readily apparent that there are big differences between them. The diffraction profile is considerably altered as the applied magnetic field increases (above 1.75 T) and new Bragg reflections appear, indicating the occurrence of a structural phase transition. At 5.5 T, these new diffraction peaks become dominant and a coexistence of two crystallographically different $La_{0.9}Ce_{0.1}Fe_{12}B_6$ phases is observed, consistent with the first-order character of the phase transformation. The complete, fully refined x-ray spectra recorded at 15 K in 0 and 5.5 T applied field are shown in Figure 5.10(b) and Figure 5.10(c), respectively. As noted above, only the rhombohedral phase (henceforth called the Rhom phase) with $R\bar{3}m$ space group is present at 0 T in the AFM state at 15 K. The new Bragg lines seen in the diffraction pattern collected at 5.5 T can be indexed in a monoclinic cell adopting the $C2/m$ space group (henceforth called the Mono phase). A good refinement of the structure was achieved in $C2/m$ symmetry group. The Rietveld-refined structural parameters are summarized in Table 5.1. In the International Tables for Crystallography, all of the listed maximal nonisomorphic subgroups for $R\bar{3}m$ are trigonal except for one, which is the monoclinic space-group symmetry $C2/m$. This crystal symmetry, $C2/m$, is used to describe the lattice distortion and it fits very well the diffraction pattern shown in Fig 6(c). Therefore, it is likely to be the correct high magnetic field crystallographic structure of $La_{0.9}Ce_{0.1}Fe_{12}B_6$ compound. The threefold symmetry in the *ab* basal plane is broken in the magnetic field-induced state and such structural distortion lowers the lattice symmetry from trigonal to monoclinic.

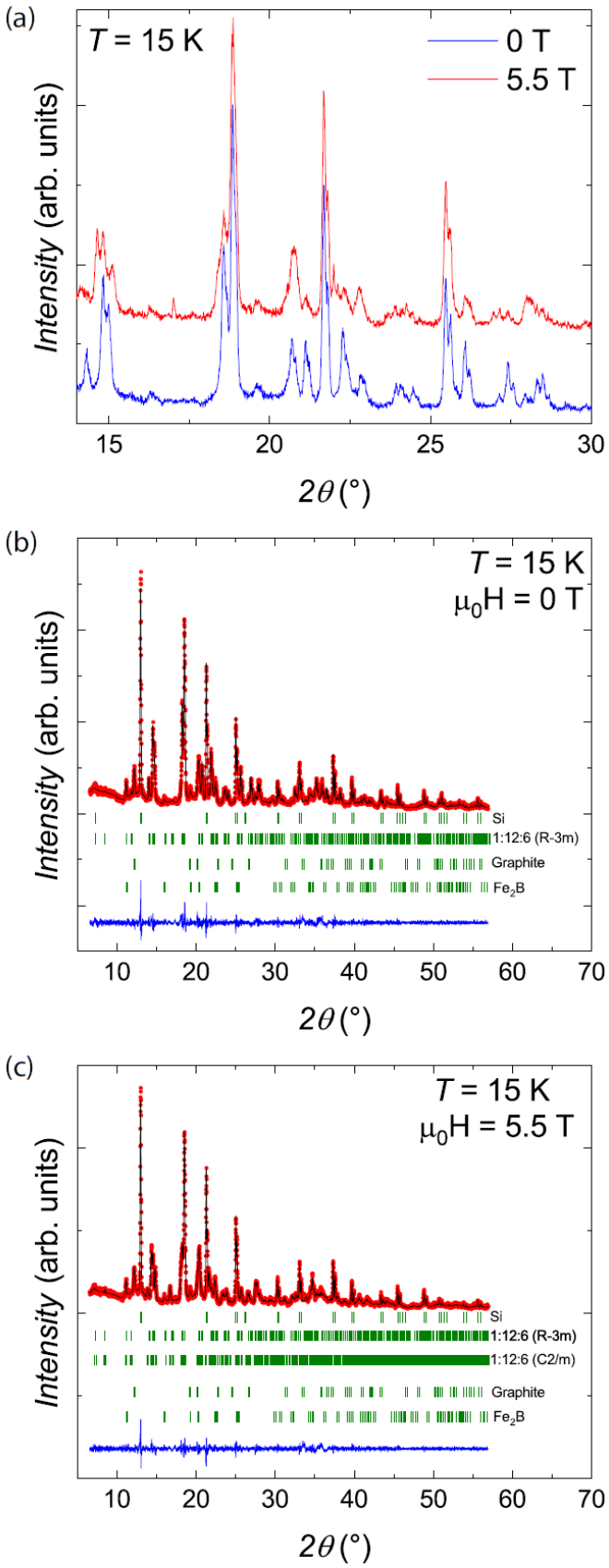

Figure 5.10.: (a) X-ray powder diffraction patterns collected at 15 K ($\lambda_{K\alpha1}$ = 0.70932 Å and $\lambda_{K\alpha2}$ = 0.71340 Å) in magnetic fields of 0 and 5.5 T. Only the diffraction angle range from 14° to 30° is shown to better illustrate development of phases with magnetic field. (b), (c) Rietveld refinements of the x-ray diffraction pattern collected at 15 K in magnetic field of $\mu_0 H$ = 0 T and $\mu_0 H$ = 5.5 T, respectively. The observed (red dots), calculated (black lines) patterns are shown. The blue line represents the difference $I_{obs} - I_{calc}$. The vertical bars (olive) indicate positions of Bragg peaks for the different phases.

Table 5.1.: Structural parameters of $La_{0.9}Ce_{0.1}Fe_{12}B_6$ obtained from Rietveld refinement of the x-ray powder diffraction patterns collected at $T = 15$ K in magnetic field of 0 and 5.5 T. Crystallographic space group, lattice parameters, and unit-cell volume are indicated.

	15 K 0 T	15 K 5.5 T	15 K 5.5 T
Space group	$R\bar{3}m$	$R\bar{3}m$	$C/2m$
a (Å)	9.5901(4)	9.5827(5)	7.5758(6)
b(Å)	9.5901(4)	9.5827(5)	9.7824(6)
c (Å)	7.5924(5)	7.5979(6)	5.9664(4)
β (°)	90	90	113.085(11)
V (Å^3)	604.72(5)	604.23(44)	406.76(7)

Let us describe briefly the relationship between the rhombohedral (in hexagonal setting) and monoclinic lattices. The space-group symmetry $C2/m$ is one of the maximal nonisomorphic subgroups of the parent $R\bar{3}m$ crystal symmetry group and the relation between the monoclinic unit cell and the rhombohedral (hexagonal) unit cell is as follows:

$$(\boldsymbol{abc})_{\mathrm{Mono}} = (\boldsymbol{abc})_{\mathrm{Rhom}} \begin{pmatrix} -1/3 & 1 & 1/3 \\ 1/3 & 1 & -1/3 \\ -2/3 & 0 & -1/3 \end{pmatrix}. \tag{5.1}$$

The rhombohedral and monoclinic unit-cell volumes are related in accordance with: $V_{\mathrm{Mono}}(C/2m) = 2/3\, V_{\mathrm{Rhom}}(R\bar{3}m)$. The observed crystal structure change to $C2/m$ is induced by magnetic field. Since $C2/m$ is a subgroup of $R\bar{3}m$ the first-order character of the transition is not obligatory and it originates from the magnetic transition from AFM ground state to field-induced FM state.

Considering that a different number of atoms are involved in the two crystallographically distinct structures and in order to compare directly their volumes, it is therefore necessary to normalize the cell volumes to a formula unit. The temperature dependence of the volume per chemical formula in an applied magnetic field of 5.5 T is illustrated in Figure 5.11 including the values of the two crystal structures. In association with the field-induced metamagnetic phase transition, the analysis of the x-ray diffraction diagrams demonstrates that in 5.5 T $La_{0.9}Ce_{0.1}Fe_{12}B_6$ exhibits an incomplete crystallographic transformation from a rhombohedral (AFM, PM) to a monoclinic (FM) structure. The powder diffraction results reveal the existence of a wide temperature interval of coexistence of the monoclinic and rhombohedral lattices. At 15 K, an applied magnetic field of 5.5 T is capable to induce ~90% of the structural alteration, and the field-driven Rhom to Mono crystallographic phase transition is accompanied by unit-cell volume change of 0.85%. At 70 K, the volume of the PM (Rhom) phase is about 0.86% smaller than that of the forced FM (Mono) phase. The volume changes at the first-order AFM-FM and FM-PM magnetic transitions are nearly the same. A symmetry-lowering crystallographic distortion takes place at the magnetic transitions.

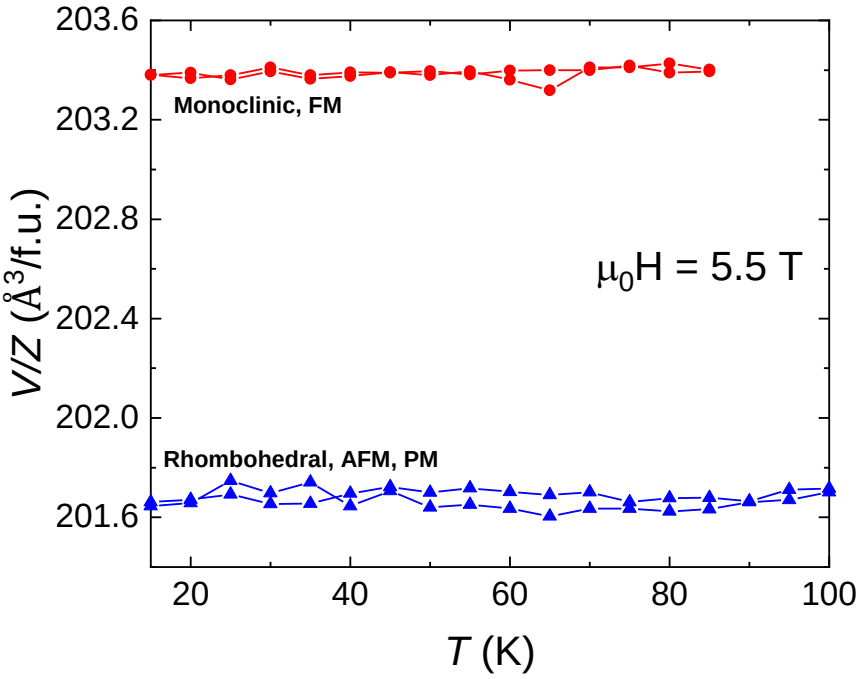

Figure 5.11.: Temperature dependence of the cell volume per formula unit for $La_{0.9}Ce_{0.1}Fe_{12}B_6$ (both rhombohedral and monoclinic phases) determined from x-ray powder diffraction measurements during heating and cooling in $\mu_0 H$ = 5.5 T applied magnetic field.

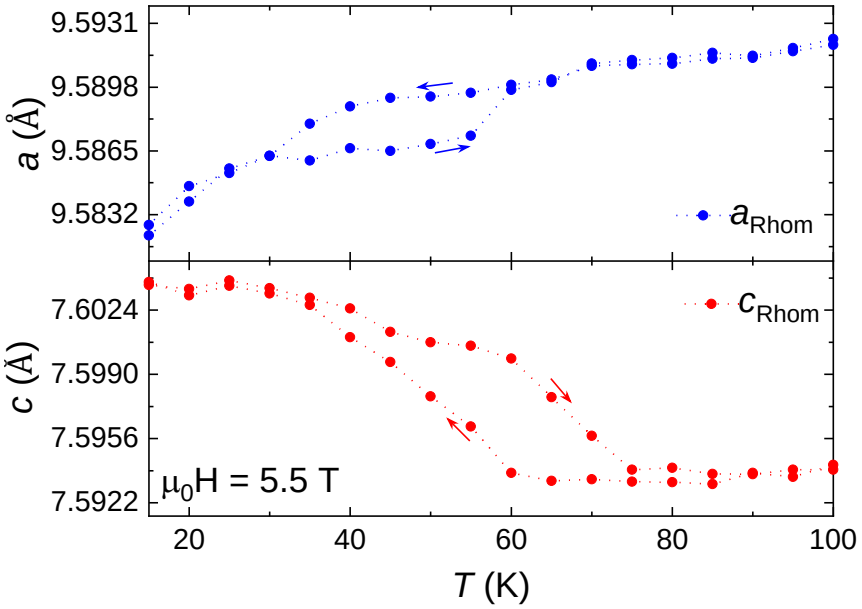

Figure 5.12.: Temperature dependence of the lattice parameters *a* and *c* of the rhombohedral cell determined from x-ray powder diffraction measurements during heating and cooling in $\mu_0 H$ = 5.5 T applied magnetic field.

The lattices parameters, *a* and *c*, of the rhombohedral structure are plotted as a function of temperature in Figure 5.12. From these data, it is easy to see that the unit-cell expansion in $La_{0.9}Ce_{0.1}Fe_{12}B_6$ proves highly anisotropic: the lattice expands in the basal plane while it shrinks along the threefold symmetry axis *c*. The results of Figure 5.12 reveal another interesting phenomenon, which is a large difference between the thermal hysteresis region in the *ab* basal plane and that along the *c* axis. The lattice constant *a* is hysteretic in the temperature range between ~30 and ~60 K, while hysteresis along the high-symmetry direction *c* persists up to ~75 K. This direction dependence of thermal hysteresis region is consistent with the anisotropy

of the rhombohedral lattice. Figure 5.13 shows the thermal variation of the structural parameters of the monoclinic cell. It is remarkable that the lattice constants *a*, *b*, and *c*, and the Bragg angle first evolve slowly at low temperatures and then exhibit very sharp changes at the transition point. The variation in cell dimensions presents strong anisotropy: in the vicinity of the magnetic transition both lattice parameters, *a* and *c*, decrease while the cell parameter, *b*, increases upon heating. In addition, the structural parameters of both $La_{0.9}Ce_{0.1}Fe_{12}B_6$ polymorphs display a large thermal hysteresis.

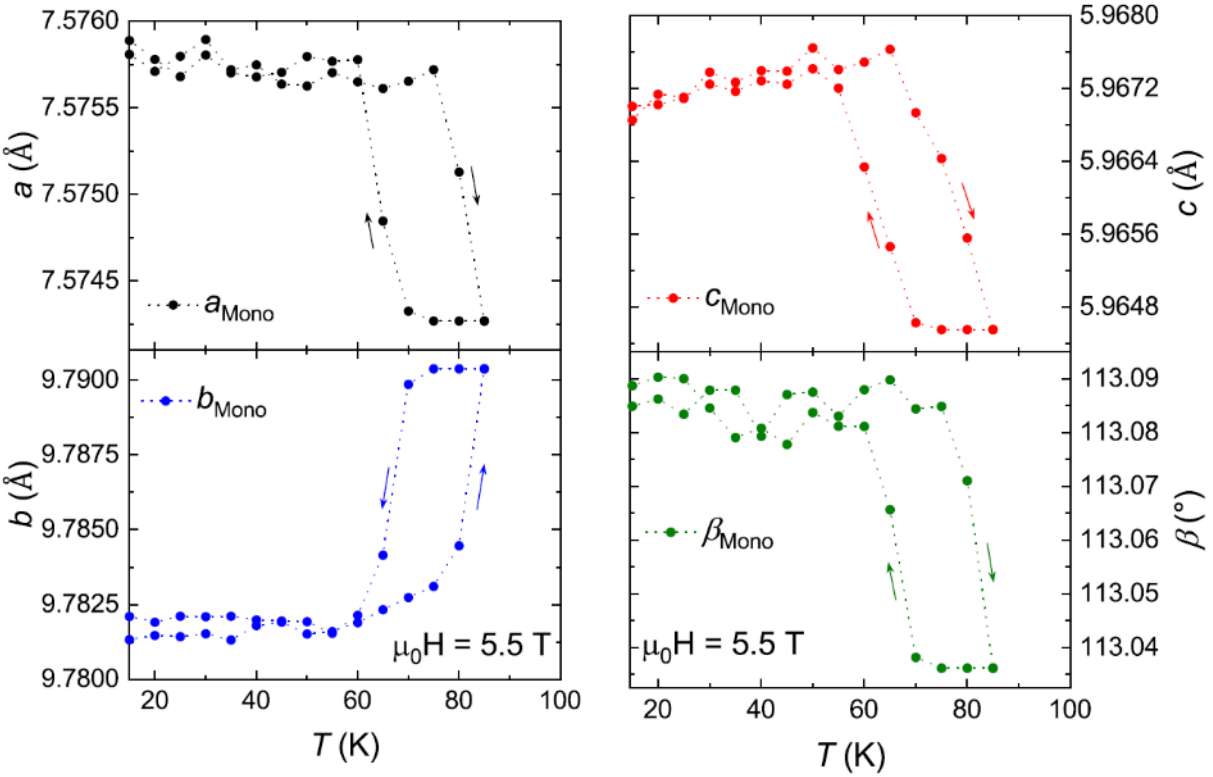

Figure 5.13.: Temperature dependence of the unit-cell dimensions *a*, *b*, and *c*, and Bragg angle of the monoclinic phase determined from x-ray powder diffraction measurements during heating and cooling in $\mu_0 H$ = 5.5 T applied magnetic field.

The variation of the concentration of the rhombohedral and monoclinic phases with temperature during both heating and cooling in magnetic fields of $\mu_0 H$ = 2.5 and 5.5 T is reported in Figure 5.14. A temperature hysteresis of 20 K is noticeable between the ZFCW and FCC data collected in 2.5 T. Upon heating, the fraction of induced monoclinic phase in 2.5 T applied field diminishes, amounting to less than 6% at 70 K. On decreasing the temperature, the transition in 2.5 T is incomplete with approximately 54% of the rhombohedral $La_{0.9}Ce_{0.1}Fe_{12}B_6$ converted into the monoclinic allotrope at 15 K. The system is partially transformed into the monoclinic structure, and the latter becomes the majority component (~90%) in the compound at 15 K and 5.5 T. The x-ray diffraction results clearly indicate that $La_{0.9}Ce_{0.1}Fe_{12}B_6$ presents crystallographic inhomogeneity (structurally heterogeneous state or coexistence of polymorphs) below T_C on heating and cooling in magnetic fields of 2.5 and 5.5 T. Beyond the Curie point the sample recovers homogeneity and sets fully in the rhombohedral crystallographic structure which is found at room temperature. The ratio between the low- and high- magnetic field crystallographic structures correlates very well with the percentage of the AFM, PM, and FM phases obtained from magnetization in the same applied fields. The data presented in Figure 5.14 result from the competition between the growth of the Rhom (AFM, PM) phase with increasing temperature and the diminution of the Mono (FM) component. The

ratio and the stability of the two different $La_{0.9}Ce_{0.1}Fe_{12}B_6$ polymorphs depends both on the strength of the applied magnetic field and the value of temperature, and the direction of the temperature variation. The magnetically and structurally heterogenous states observed in $La_{0.9}Ce_{0.1}Fe_{12}B_6$ are very similar to those found in some intermetallic alloys such as $Gd_5(Si_xGe_{1-x})_4$ (55, 96, 338, 360, 361), Si-doped $CeFe_2$ (339), and MnAs (94, 362) and also usually seen in the colossal magnetoresistive manganese-based perovskites, where they are often called “phase-segregated states” (363, 364).

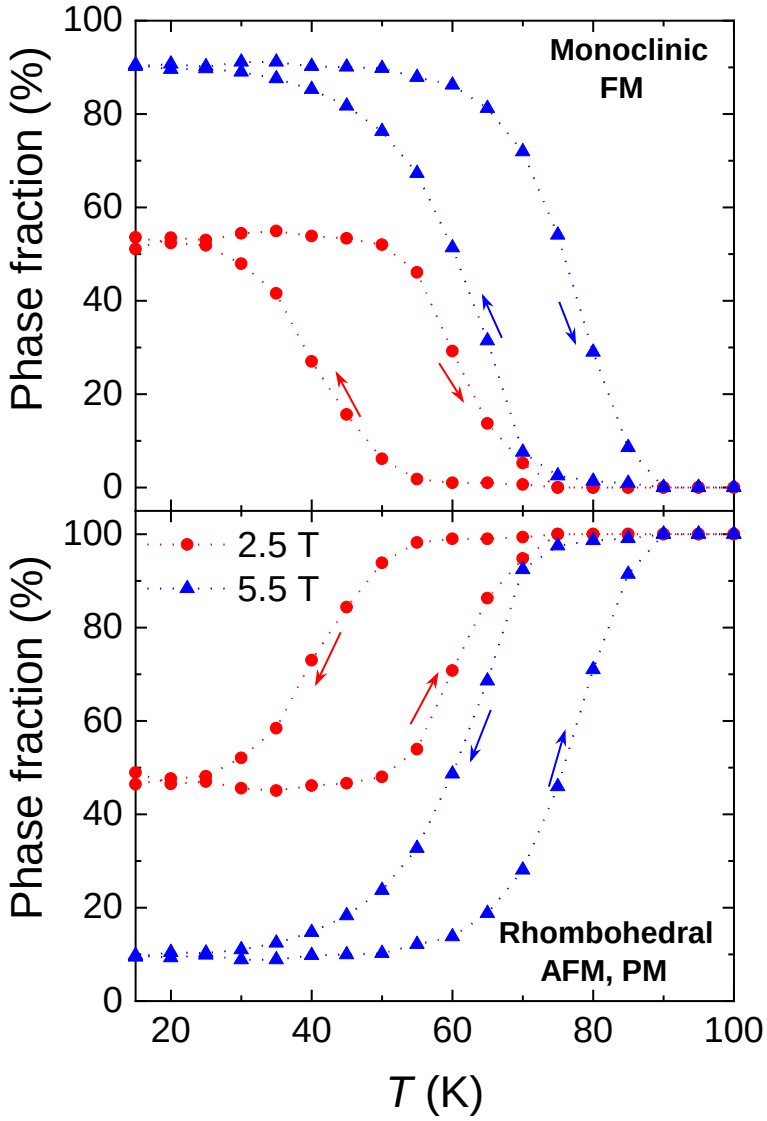

Figure 5.14.: Temperature dependence of the phase fractions of both rhombohedral and monoclinic crystal structures determined from x-ray powder diffraction measurements during heating and cooling in $\mu_0 H$ = 2.5 and 5.5 T applied magnetic fields.

The thermal dependence of the weighted mean cell volume in 2.5 and 5.5 T applied magnetic fields is illustrated in Figure 5.15. The weighted average volume undergoes a transition which is accompanied by a huge thermal hysteresis indicating first-order nature of the phase transition. There is a temperature interval in which the average volume shrinks with increasing temperature; namely, NTE effect occurs over this temperature range. Although the difference in volume between the two polymorphs (monoclinic and rhombohedral phases) is as large as 0.85%, the contraction of the mean volume between 50 and 90 K is about 0.77% in 5.5 T

magnetic field. The latter value compares well with the relative volume change obtained macroscopically from dilatometric LTE data $\Delta V/V = 3\Delta L/L = 0.65\%$, especially considering anisotropic effects. $La_{0.9}Ce_{0.1}Fe_{12}B_6$ exhibits a prominent NTE phenomenon over a temperature window of $\Delta T = 40$ K with an average volumetric thermal expansion coefficient $\alpha_V = -193 \times 10^{-6}$ K^{-1}. This large NTE effect is generated by the strong spin-lattice coupling. For comparison purposes it is worth noting that the volume thermal expansion coefficient reported for (Hf,Nb)Fe_2 (340) and (Hf,Ti)Fe_2 (365) is at least an order of magnitude smaller than the value obtained here for $La_{0.9}Ce_{0.1}Fe_{12}B_6$. Our volumetric NTE coefficient compares well with the giant negative thermal expansion observed in (Hf,Ta)Fe_2 itinerant-electron metamagnets ($\alpha_V = -164 \times 10^{-6}$ K) (329, 330) and is on the same order of magnitude as the colossal NTE discovered in $Mn_{0.98}CoGe$ ($\alpha_V = -423 \times 10^{-6}$ K^{-1}) (331) and $Bi_{0.95}La_{0.05}NiO_3$ ($\alpha_V = -413 \times 10^{-6}$ K^{-1}) (332).

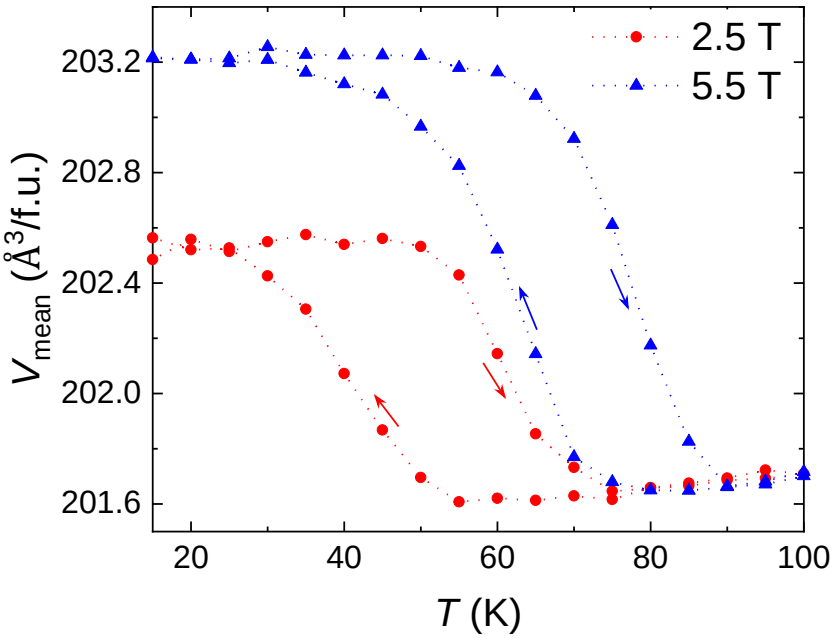

Figure 5.15.: Temperature dependence of the mean cell volume per formula unit determined from x-ray powder diffraction measurements during heating and cooling in $\mu_0 H$ = 2.5 and 5.5 T applied magnetic fields.

To further elucidate the field-induced metamagnetic transition observed in the magnetization and magnetostriction isotherms and in order to get a better understanding of the correlations between the structural and magnetic properties of $La_{0.9}Ce_{0.1}Fe_{12}B_6$, the magnetic field dependence of the crystallographic structure was also investigated at 15 K. For this study, the sample was cooled in zero magnetic field down to 15 K. After stabilization of the temperature, the external field was then raised at regular steps up to 5.5 T and x-ray powder diffraction patterns collected at each field step. At 15 K and $\mu_0 H < 1.75$ T, the diffractograms of the zero-field cooled $La_{0.9}Ce_{0.1}Fe_{12}B_6$ reflect the pure rhombohedral crystal structure. Even though, at all magnetic fields lower than 1.75 T, only the rhombohedral polymorph is detected, the Bragg peaks belonging to the monoclinic phase start to appear at higher applied fields, with dramatic changes of the diffractograms. When the Bragg reflections of the monoclinic structure emerge, the intensities of the diffraction lines that correspond to the rhombohedral phase are reduced.

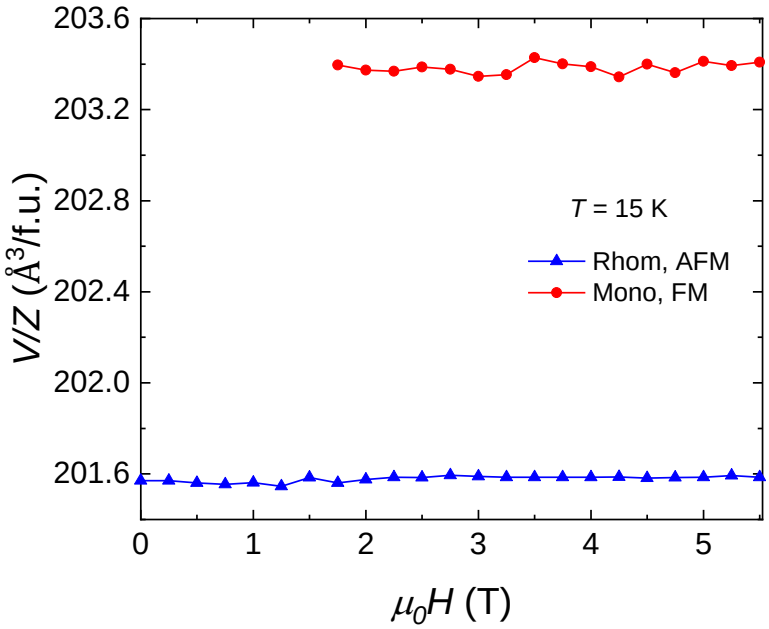

Figure 5.16.: Magnetic field dependence of the cell volume per chemical formula for $La_{0.9}Ce_{0.1}Fe_{12}B_6$ at 15 K.

The field dependences of the volume per chemical formula at 15 K are displayed in Figure 5.16. The Rietveld refinement results reveal that the structure is described solely by the $R\bar{3}m$ crystal symmetry group at low fields while at higher magnetic fields ($\mu_0 H \geq 1.75$ T) the x-ray diffraction profiles can be well fitted only by including a monoclinic structure. The $C2/m$ space-group symmetry is added to model the high-field x-ray powder diffraction data. The volumes for both Rhom (AFM) and Mono (FM) phases are nearly field independent as illustrated in Figure 5.16. The volume per formula unit of the AFM phase is smaller than that of FM phase. Our x-ray diffraction results reveal a change of the crystal symmetry at the AFM-FM first-order transition, *i.e.*, a coupled crystallographic-magnetic transformation from a Rhom (AFM) to a Mono (FM) state. In $La_{0.9}Ce_{0.1}Fe_{12}B_6$ intermetallic compound the crystal and magnetic sublattices are intimately coupled. Therefore, a modification of the magnetic order results in a concomitant change in the crystal lattice. The formation of the FM phase is accompanied by a symmetry-lowering lattice distortion.

As a means to follow more precisely the phase transformation, we show in Figure 5.17 the weighted mean volume (top panel) and its relative change (bottom panel) at 15 K as a function of magnetic field. Below 1.75 T, the weighted average volume is almost constant and then raises rapidly as the compound undergoes a magnetic transition just above 1.75 T. The magnetic field-induced metamagnetic transition is also distinctly visible in the relative variation of the volume. The relative change in the mean volume is negligible (approaches zero) at low fields, *i.e.*, very weak magnetoelastic effects are detected in the AFM ground state below 1.75 T. The forced-volume magnetostriction reaches a value of 0.83% at 5.5 T. This value is reasonably consistent with the relative volume change deduced from the 15 K dilatometric magnetostriction isotherm $\Delta V/V$ (5.5 T) $\approx$ 1.05%, particularly taking into account the anisotropic behavior. These experimental results reveal that the observed field-induced first-order AFM-FM transformation is concomitant with the symmetry-lowering rhombohedral to monoclinic structural phase transition.

At the local scale the observed martensitic-like transformation should involve different variants as it is expected upon lowering of the crystal symmetry. Due to the crystalline orientation of the

shearing-induced variants, several magnetic domains are expected. Further studies enabling to identify the different magnetic domains and crystal variant would be interesting.

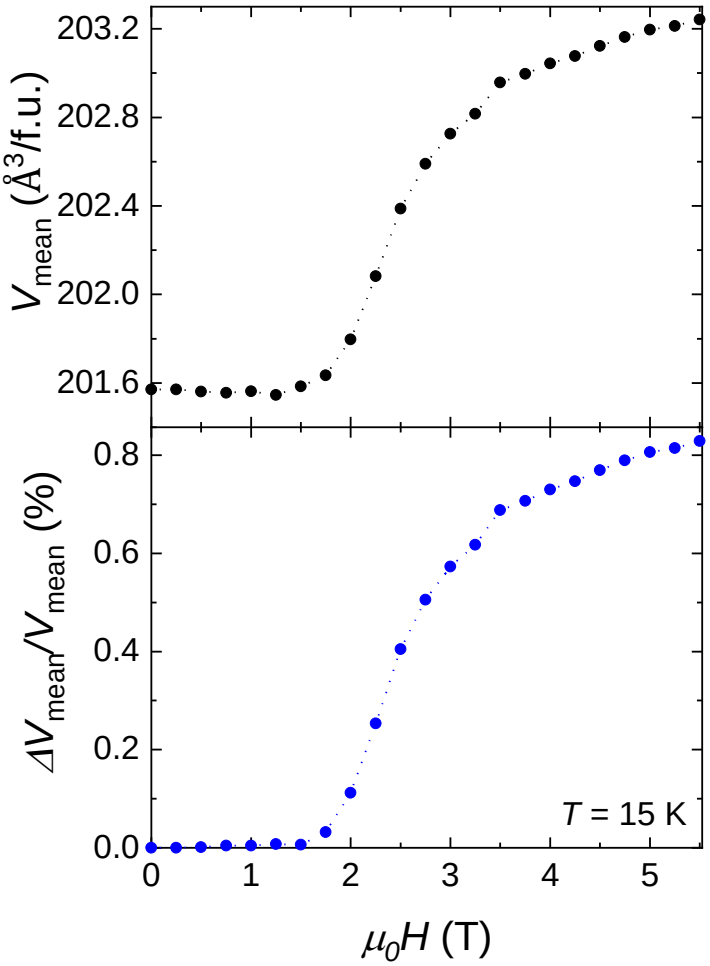

Figure 5.17.: Magnetic field dependence of the mean cell volume per chemical formula (top) and relative volume change (bottom) determined from x-ray powder diffraction measurements at 15 K.

5.2.3.4. Discussion

The compilation of the experimental results of the magnetization measurements and x-ray diffraction studies is presented in the magnetic-field ($\mu_0 H$)–temperature (T) phase diagram of $La_{0.9}Ce_{0.1}Fe_{12}B_6$ intermetallic compound (Figure 5.18). The critical transition field of the downward-field scan of the metamagnetic transition, $\mu_0 H_{cr,down}$, is approximately zero at 35 K and increases monotonically upon heating. However, the temperature dependence of the transition field obtained for the ascending-field process, $\mu_0 H_{cr,up}$, is nonmonotonic. Below 25 K $\mu_0 H_{cr,up}$ diminishes with increasing temperature while it exhibits the inverse trend at temperatures exceeding 25 K. Below 25 K, the critical field of the AFM-FM transition increases upon cooling because of the enhancement of the negative exchange interactions and the reduction of the thermal fluctuations of the moments and elasticity of the crystal structure in the AFM phase (322, 324, 366). This results in the increase of both the free-energy difference between the two magnetically ordered AFM and FM states, and the critical magnetic transition field required to complete the metamagnetic transition from one phase to another. In the paramagnetic temperature region, $\mu_0 H_{cr,up}$ evolves proportionally to the square of temperature T^2 (T^2 dependence) at low temperatures and presents a T dependence on the high-temperature side, in agreement with the spin-fluctuation theory for itinerant-electron metamagnetic systems

(37, 367, 368). It is worth to notice that the metamagnetic transition in $La_{0.9}Ce_{0.1}Fe_{12}B_6$ extends over a wide temperature range including below and well beyond T_N. The Néel temperature T_N (AFM-PM second-order phase transition) is weakly sensitive to the applied magnetic field. T_N slightly shifts to lower temperatures with increasing external field. The characteristic features of this phase diagram are large hysteresis associated with the magnetostructural transition in the magnetic data and a negative shift of the Néel temperature with applied magnetic field.

In addition to the three distinct magnetic phase regions–AFM, FM, and PM–another salient feature of the present phase diagram is the very-low-temperature region, where the intermetallic compound $La_{0.9}Ce_{0.1}Fe_{12}B_6$ may be in an AFM, phase mixture AFM+FM, or FM state depending on the thermal and magnetic history of the sample. For instance, when the sample is cooled in zero magnetic field from room temperature to 2 K and afterward magnetized by the application of a 4-T field, it will stay in the pure AFM ground state at 2 K and 4 T. When cooled from high temperatures down to 2 K in a 4-T magnetic field, the system will cross the onset AFM-FM phase boundary and undergo a partial AFM→FM order-order magnetic transformation; in such conditions the compound will remain in the phase mixture (or phase-segregated) AFM+FM state.

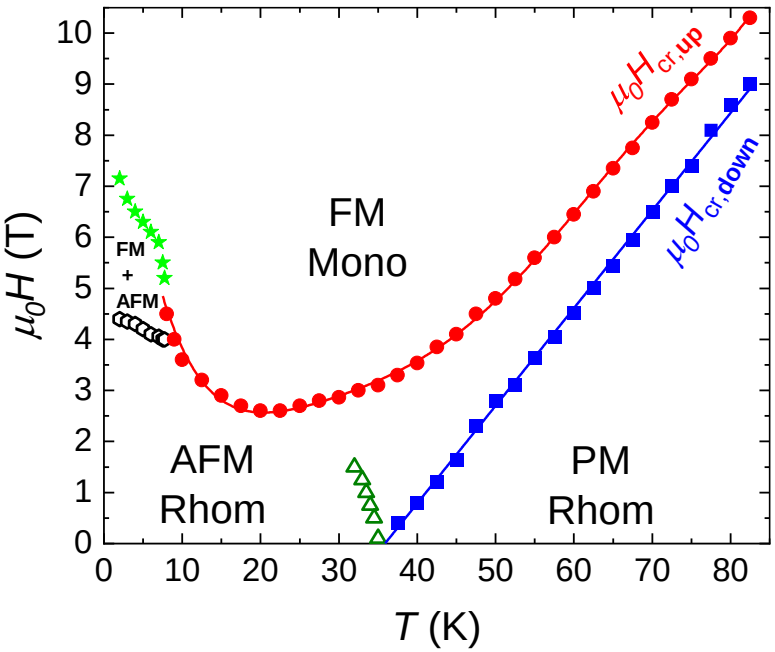

Figure 5.18.: Magnetic and crystallographic phase diagram of $La_{0.9}Ce_{0.1}Fe_{12}B_6$. AFM, PM, and FM label different magnetic phases, and Rhom and Mono denote different crystallographic structures, as defined throughout the text. The critical field for the upward ($\mu_0 H_{cr,up}$) and downward ($\mu_0 H_{cr,down}$) field variation as a function of temperature. The critical field has been derived from the maximum of the field derivative of the magnetization isotherms. The open hexagons and closed stars stand for the transition field of the first- and second-step transitions, respectively. The open triangles represent the Néel temperature, T_N.

At this point, the issue of the origin of the ultrasharp magnetization jumps, also seen in the magnetostriction data, must be taken into consideration. It is quite unambiguous that these unusual and anomalous features observed in $La_{0.9}Ce_{0.1}Fe_{12}B_6$ are not solely magnetic in origin. Our experimental findings undoubtedly prove that they possess a contribution from the strong spin-lattice coupling. Several interpretations have been suggested for the avalanchelike transitions phenomenon in intermetallic compounds and phase-separated oxides (manganese-based perovskites); however, a scenario based on the martensiticlike transition triggered by the

external magnetic field appears to be the most prominent one (325–327).
Let us depict the generation of field-induced staircaselike transitions in the magnetization process within the scope of such a martensiticlike transformation. The magnetic ground state of $La_{0.9}Ce_{0.1}Fe_{12}B_6$ is AFM with a rhombohedral crystallographic structure. When a suitable magnetic field is applied, FM phase (monoclinic) begins to grow inside the AFM matrix. The field-induced structural distortion (martensiticlike transformation) between the monoclinic and rhombohedral unit cells produces elastic strains at the AFM/FM interfaces. With the application of magnetic field, FM regions are likely to develop but the interfacial (martensitic) constraints obstruct the growth of the FM domains. As the external field is progressively raised, the driving force acting on the spins raises as well. When the magnetic force is strong enough to prevail over the elastic strain energy, the FM component grows catastrophically, giving rise to extremely sharp steps. These abrupt jumps can be considered as a burstlike development of the FM component within the AFM matrix. The magnetic field-induced lattice distortion which is driven by magnetoelastic coupling is likely responsible for the step-like metamagnetic transitions in this compound.
Similar sharp jumps and staircase-like transitions have been recently observed in other metamagnets such as FeRh-based systems (102, 369–371). Some authors attributed their origin to the AFM-FM phase boundary motion that is pinned by defects or inhibited by the stray field of the portions that have already converted (102); others proposed the combined effects of the transition hysteresis and the temperature dependence of the order parameter (369). Instead, Uhlíř *et al.* (371) suggested an alternative mechanism driven by the stronger exchange correlations of the long-range FM order compared to the AFM state, *i.e.*, the robustness of the FM exchange to local strain and disorder when compared with the AFM exchange. This should lead to residual FM domains at low temperatures that serve as seeds for the first-order AFM to FM metamagnetic phase transition.

5.2.4. Summary and Conclusions

In summary, we have carried out a detailed investigation of the magnetic, magnetoelastic and structural properties of $La_{0.9}Ce_{0.1}Fe_{12}B_6$. We discovered that the first-order AFM-FM transition occurs simultaneously with a crystallographic transition from a rhombohedral to a monoclinic structure. This field-induced symmetry-lowering structural distortion is driven by magnetoelastic effects. The FM order sets in the monoclinic crystal structure which can be described in $C2/m$ symmetry group, a subgroup of $R\bar{3}m$, the space group of the rhombohedral $SrNi_{12}B_6$-type crystallographic structure adopted by the AFM and PM phases. A huge volume magnetostriction, $\Delta V/V = 1.15\%$, was observed across the magnetic field-induced AFM-FM metamagnetic transition, making this intermetallic compound a potential candidate for magnetostrictive materials. Our experimental findings constitute direct evidence of the strong coupling between magnetic and crystallographic degrees of freedom in $La_{0.9}Ce_{0.1}Fe_{12}B_6$ system.

In order to establish the magnetic structure of the FM (monoclinic) phase and gain a deeper insight into the coupling between crystal lattice and magnetism in this intermetallic compound, neutron diffraction experiments in applied magnetic fields and further theoretical investigations and electronic band structure calculations are required.

5.3. Publication E: Magnetic-field-induced structural phase transition and giant magnetoresistance in $La_{0.85}Ce_{0.15}Fe_{12}B_6$

Magnetic-field-induced structural phase transition and giant magnetoresistance in $La_{0.85}Ce_{0.15}Fe_{12}B_6$

Léopold V.B. Diop[1], Tom Faske[2], Olivier Isnard[3], and Wolfgang Donner[2]
[1]Université de Lorraine, Centre national de la recherche scientifique (CNRS), Institut Jean Lamour (IJL), F-54000 Nancy, France
[2]Institute of Materials Science, Technical University of Darmstadt, D-64287 Darmstadt, Germany
[3]Université Grenoble Alpes, Institut NÉEL, CNRS, 25 rue des martyrs, F-38042 Grenoble, France

Correspondence email: leopold.diop@univ-lorraine.fr

Received 7 June 2021
Accepted 13 September 2021
DOI: 10.1103/PhysRevMaterials.5.104401

Abstract Magnetoelastic coupling, structural, magnetic, electronic transport, and magnetotransport properties of $La_{0.85}Ce_{0.15}Fe_{12}B_6$ have been studied by a combination of macroscopic [magnetization, electrical resistivity and magnetoresistance (MR)] and microscopic temperature- and magnetic-field-dependent x-ray powder diffraction measurements. The itinerant-electron system $La_{0.85}Ce_{0.15}Fe_{12}B_6$ exhibits an antiferromagnetic (AFM) ground state and multiple magnetic transitions, AFM-ferromagnetic (FM) and FM-paramagnetic (PM), triggered by changes in both temperature and magnetic fields. At low temperatures, the field-induced first-order AFM-FM metamagnetic phase transition is discontinuous, manifesting itself by extremely sharp steps in magnetization as well as in MR and is accompanied by large magnetic hysteresis. A remarkably large negative MR of -73% was discovered. In addition, the time evolution of the electrical resistivity displays a colossal spontaneous jump when both the applied magnetic field and temperature are constant. Diffraction data reveal a magnetic-field-induced structural phase transition associated with the AFM-FM and PM-FM transformations. The lattice distortion is driven by magneto-elastic coupling and converts the crystal structure from rhombohedral ($R\bar{3}m$) to monoclinic ($C2/m$). The AFM and PM states are related to the rhombohedral structure, whereas the FM order develops in the monoclinic symmetry. A huge volume magnetostriction of ~0.9% accompanies this symmetry-lowering lattice distortion. Meanwhile, a highly anisotropic thermal expansion involving giant negative thermal expansion with an average volumetric thermal expansion coefficient $\alpha_V = -195 \times 10^{-6}\,K^{-1}$ was observed. The consistency seen in these different experimental data constitutes a direct evidence of the strong correlations between charge, magnetic and crystallographic degrees of freedom in this material.

5.3.1. Introduction

It is general knowledge that many compounds may undergo structural phase transitions when subject to changes in hydrostatic pressure, temperature, and chemical composition. However, the occurrence of structure transformations induced by applied magnetic field is rather rare and only a few examples are discussed in the literature. Materials with interconnected lattice and spin degrees of freedom often exhibit multifunctional properties such as giant magnetoresistance (MR), colossal magnetostriction, and giant magnetocaloric effect (54, 94–96, 260, 333–338). These prominent magnetoresponsive physical properties of relevance result from instabilities in magnetic and crystallographic sublattices (96). That is, these emergent physical phenomena are particularly pronounced in the vicinity of a first-order magnetostructural phase transformation, which in turn allows controlling of the physical properties of the solid system via several types of externally applied driving forces. At present, the different families of materials featuring a strong magnetoelastic coupling are of great importance from the fundamental research side as well as from the technological applications viewpoint. Understanding the interplay between crystallographic and magnetic sublattices is a crucial challenge in condensed matter science. These magnetic systems form a phenomenal playground for materials physics due to the extreme sensitivity of their physical properties to reasonably weak external stimuli.

Most recently, discontinuous and unconventional staircase-like metamagnetic phase transitions were discovered in the (La,Ce)$Fe_{12}B_6$ system (322–324, 344). This singular multistep behavior is featured by steep magnetization jumps followed by plateaus leading to a unique and unusual avalanche like magnetization process. The itinerant-electron metamagnet $LaFe_{12}B_6$ occupies a special place among rare-earth iron-rich intermetallic compounds; it presents uncommon magnetic behavior and many intriguing physical properties among which the amplitude-modulated antiferromagnetic (AFM) structure is described by a propagation vector $k = (¼,¼,¼)$, especially weak Fe moment (0.43 μ_B) in the magnetically ordered ground state, remarkably low magnetic ordering temperature $T_N = 36$ K for an Fe-rich alloy, and a multicritical point in the complex magnetic phase diagram (322). In addition, both inverse and normal magnetocaloric effects (345), giant spontaneous magnetization steps (323), and large magnetovolume effects (346) can be emphasized as the most relevant intriguing physical properties. These peculiar features not only offer the development of experiments under extreme conditions and theoretical models for a better comprehension of the fascinating physics underlying the striking behavior of this compound (346–350), but also highlight the potential interest of the $LaFe_{12}B_6$ system in future low-temperature energy technologies. Within the ternary system $RT_{12}B_6$ (where R is a rare-earth atom and T stands for a 3d transition metal element Co or Fe), $LaFe_{12}B_6$ is the sole stable Fe-based compound of the 1:12:6 family (349, 350), whereas the $RCo_{12}B_6$ intermetallics are stable along the entire rare-earth series (352). Even though the $NdFe_{12}B_6$ alloy is the first Fe-based member of the $RT_{12}B_6$ ternary system to be identified, it is metastable (351). Among the 1:12:6 family, $LaFe_{12}B_6$ is the unique compound exhibiting an AFM ground state with an ordering temperature much lower than the Curie point of the Co-based $RCo_{12}B_6$ ferromagnets (R = Y, La-Sm) or ferrimagnets (R = Gd-Tm; $T_C = 134-162$ K) (352). The Néel temperature of $LaFe_{12}B_6$ is an order of magnitude smaller than the transition temperature of any rare-earth iron-rich binary alloy. Interestingly, extraordinary electronic transport and magnetotransport properties have been most recently discovered in $RCo_{12}B_6$ phases with R = Y, Gd and Ho (356).

In this paper, we report direct evidence of a coupled magnetic and structural phase transition stimulated by a magnetic field in the itinerant-electron metamagnet $La_{0.85}Ce_{0.15}Fe_{12}B_6$ as

investigated by means of macroscopic (magnetization, electrical resistivity and MR) and microscopic (temperature- and magnetic-field-dependent x-ray diffraction) experiments. In addition, we discovered that colossal spontaneous resistivity jumps occur in relaxation measurements, *i.e.*, in experimental conditions where both the applied magnetic field and temperature are kept constant.

5.3.2. Experimental Details

The $La_{0.85}Ce_{0.15}Fe_{12}B_6$ compound was synthetized by arc melting the mixture of high-purity constituent elements (better than 99.9%) under a protective argon gas atmosphere. To ensure compositional homogeneity, the alloy was arc melted several times with the button being turned over after each re-melting. The so-obtained ingot was wrapped in Ta foil, sealed in an evacuated silica tube and subsequently annealed at 1173 K for 21 days in a resistive furnace. The analysis of the phase purity and the room temperature crystal structure was performed by standard x-ray powder diffraction using a Siemens D5000 diffractometer in reflection mode with the Bragg-Brentano geometry and Co-K_α radiation ($\lambda_{K\alpha1}$ = 1.78897 Å and $\lambda_{K\alpha2}$ = 1.79285 Å).
Magnetic measurements were undertaken on a powder sample using an extraction-type magnetometer. Temperature and magnetic field dependences of the magnetization were measured in applied fields of up to 10.5 T. A detailed description of the magnetometer can be found in (357). Magnetization data were corrected for the presence of the minor ferromagnetic (FM) Fe_2B secondary phase to get the intrinsic magnetic properties of $La_{0.85}Ce_{0.15}Fe_{12}B_6$. Two different methods were used to determine the amount of Fe_2B impurity: (i) x-ray powder diffraction analysis and (ii) magnetization measurements. The latter measurements were realized just above the magnetic ordering temperature of $La_{0.85}Ce_{0.15}Fe_{12}B_6$ to remain far below the Curie point of Fe_2B, which is 1015 K. Therefore, the traces of Fe_2B impurity were considered as carrying a saturated magnetic moment simplifying the correction for its FM contribution. The impurity concentration is estimated to be ~6 wt.%.
The specimen for the resistivity and MR experiments was cut in parallelepiped form using a diamond saw, and then smooth and flat surfaces were prepared by polishing. The electrical connections on the surface of the sample were made by fixing thin platinum wires using silver paste. The measurements were performed using the conventional four-point contact method at a constant direct current (dc) of 10 mA at temperatures ranging between 2.5 and 150 K in a superconducting magnet providing a maximum magnetic field of 8 T. The magnetic field was applied perpendicular to the current orientation ($H \perp i$). To get rid of possible thermals, the electrical dc was applied in opposite polarities at each measurement. The temperature-dependent electrical resistivity curves were recorded at a heating/cooling rate of 1 K/min. The field dependence of electrical resistivity was measured at a sweep rate of 0.05 T/min.
X-ray diffraction as a function of both temperature and magnetic field was carried out on a custom-built powder diffractometer in transmission geometry using Mo-K_α radiation ($\lambda_{K\alpha1}$ = 0.70932 Å and $\lambda_{K\alpha2}$ = 0.71340 Å). Fine powder of $La_{0.85}Ce_{0.15}Fe_{12}B_6$ was uniformly mixed with a National Institute of Standards and Technology standard reference Si powder 640d and then glued onto a carbon foil. The carbon foil was fixed on a copper cold finger—serving as a sample holder—of a closed-cycle helium cryofurnace and transferred into a split-coil superconducting magnet that provided a homogeneous magnetic field of up to 5.5 T around the sample position with the magnetic field vector perpendicular to the scattering plane. The laboratory-based x-ray powder diffractometer was described in (1). Zero-field cooled (ZFC) and field cooled (FC) measuring protocols were employed for thermodiffraction measurements at various applied magnetic fields (isofield measurements). For ZFC mode, the sample was first

cooled in zero magnetic field from room temperature down to the lowest measurement temperature. Then the magnetic field was applied after reaching thermal equilibrium, and diffraction data were collected upon heating. The ZFC experimental procedure was immediately followed by cooling under the same applied field (FC). Before to the magnetic-field-dependent diffraction experiments (isothermal measurements), the sample was cooled from room temperature to the measurement temperature with no magnetic field applied. For both isofield and isothermal experiments, the temperature of the sample was stabilized for ≈10 min before data acquisition. Rietveld refinements of the x-ray powder diffraction patterns were performed using the *FULLPROF* program (237). Structural parameters and phase concentrations, when two structurally distinct phases coexisted in certain combinations of magnetic field and temperature, were determined. The sample used in this paper is from the same batch as that employed previously in magnetic relaxation experiments (324).

5.3.3. Results and Discussion

5.3.3.1. X-ray powder diffraction in zero magnetic field $\mu_0 H$ = 0 T

When the intermetallic compound $La_{0.85}Ce_{0.15}Fe_{12}B_6$ is cooled in zero magnetic field ($\mu_0 H = 0$ T) from room temperature down to 15 K, its x-ray powder diffraction diagrams remain identical except for an anisotropic shift of the Bragg lines toward higher diffraction angles consistent with thermal shrinkage. The Rietveld analyses indicated that as long as the alloy remains AFM below the Néel temperature or paramagnetic (PM) above, it possesses the rhombohedral $SrNi_{12}B_6$-type crystal structure with $R\bar{3}m$ space group (353–355). The lattice symmetry is preserved over the entire investigated temperature interval, *i.e.*, the trigonal symmetry of the atomic arrangement is kept unchanged. No signature of a temperature-induced structural phase transition was perceived down to 15 K. Within the unit-cell, Fe atoms are located on two inequivalent Wyckoff positions, namely, 18*g* and 18*h*. The B and La/Ce atoms reside on the 18*h* and *3a* sites, respectively. A Rietveld refinement of the diffraction pattern recorded at 25 K in zero magnetic field ($\mu_0 H = 0$ T) is shown in Figure 5.19, and the resulting parameters are summarized in Table 5.2.

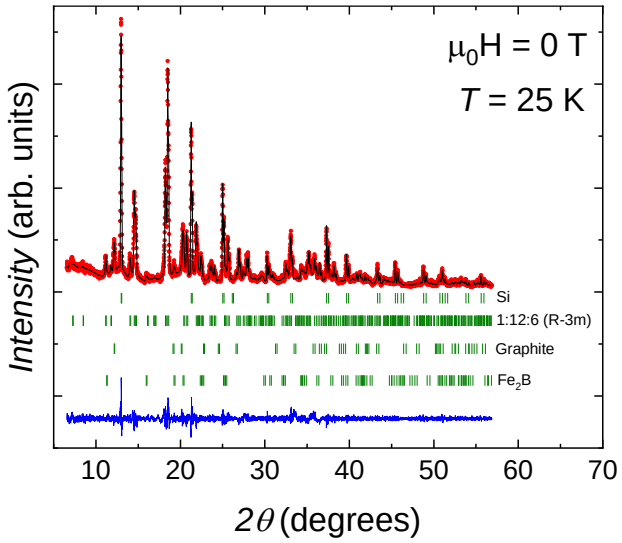

Figure 5.19.: Rietveld refinement of the x-ray powder diffraction pattern collected at 25 K in $\mu_0 H$ = 0 T for the $La_{0.85}Ce_{0.15}Fe_{12}B_6$ compound. The observed (red dots) and calculated (black lines) patterns are shown. The blue line represents the difference $I_{obs} - I_{calc}$. The vertical bars (olive) indicate positions of Bragg peaks for the different phases.

The unit-cell dimensions *a* and *c*, volume *V*, and *c/a* ratio of the rhombohedral structure are plotted in Figure 5.20 as a function of temperature. The zero magnetic field thermodiffraction results demonstrate that both lattice parameters are anisotropically decreased as the temperature is lowered, yielding a reduction in the unit-cell volume. By contrast, the c/a ratio shows the opposite trend upon cooling. At high temperatures, the structural parameters evolve nearly linearly and the determined coefficients of linear thermal expansion along the two principal crystallographic directions amount to $\alpha_a = 13.3 \times 10^{-6}\ K^{-1}$ and $\alpha_c = 4.9 \times 10^{-6}\ K^{-1}$. The thermal expansion along the high-symmetry direction *c* is much more than that along the *a* axis (basal plane). The crystallographic volume thermal expansion coefficient is estimated to be about $\alpha_V = 31.5 \times 10^{-6}\ K^{-1}$. In the temperature range below 60 K, the lattice parameter *a* remains basically constant and, consequently, the thermal expansion along this crystallographic direction approaches zero. On the other hand, the thermal expansion along the threefold symmetry axis *c* becomes almost negligible only below 30 K. This difference on the temperature at which a practically zero thermal expansion is observed along the two principal crystallographic axes is explainable by considering the anisotropy of the lattice. The flattening of the linear thermal expansion at low temperatures is in accord with the normal phonon contribution approaching zero (in agreement with Grüneisen's law). In the thermal variation of the volume, no discernible abnormality is detected at T_N associated with the second-order AFM-PM transition.

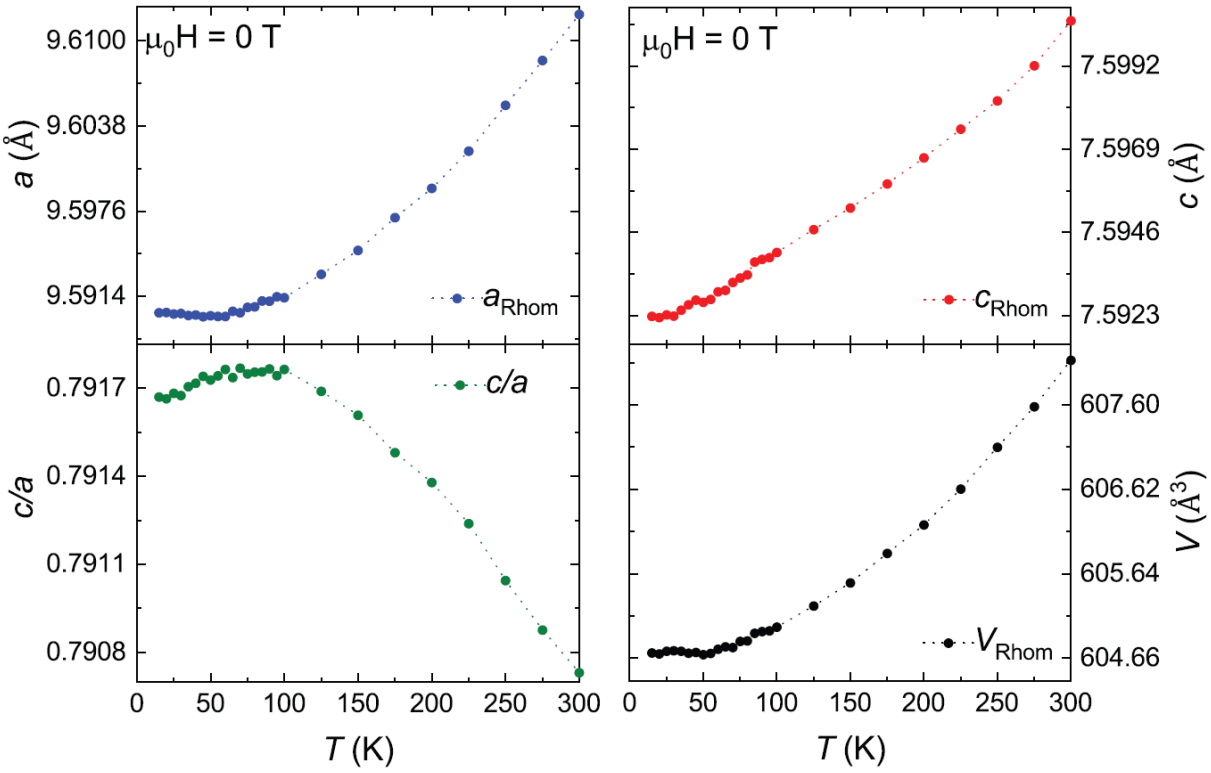

Figure 5.20.: Temperature dependence of the lattice parameters *a* and *c*, *c/a* ratio, and unit cell volume *V* of the rhombohedral cell for $La_{0.85}Ce_{0.15}Fe_{12}B_6$ as derived from Rietveld refinement of the diffraction patterns collected upon cooling in $\mu_0 H$ = 0 T. Dashed lines are guide for the eye.

5.3.3.2. Magnetization

Figure 4.16 displays the temperature-dependent magnetization curves *M(T)* measured under various applied magnetic fields between 0.1 and 9.5 T. The low-field thermomagnetic curve

[Figure 5.21(a)] presents a small peak around T_N = 35 K, indicating that $La_{0.85}Ce_{0.15}Fe_{12}B_6$ undergoes a second-order transition from an AFM to a PM phase. The *M(T)* measurements recorded in an applied field of 9.5 T [Figure 5.21(b)] reflect the magnetic transition from a typical FM phase to a PM state. The 4 T (6 T) thermomagnetic curve reveals that a large percentage ~74% (80%), of the sample volume is transformed into a FM phase at low temperatures, and the remaining fraction ~26% (20%) is in the AFM ground state. Note that the concentration of induced FM phase is strongly dependent on the strength of applied field, which favors the FM order over the AFM phase.

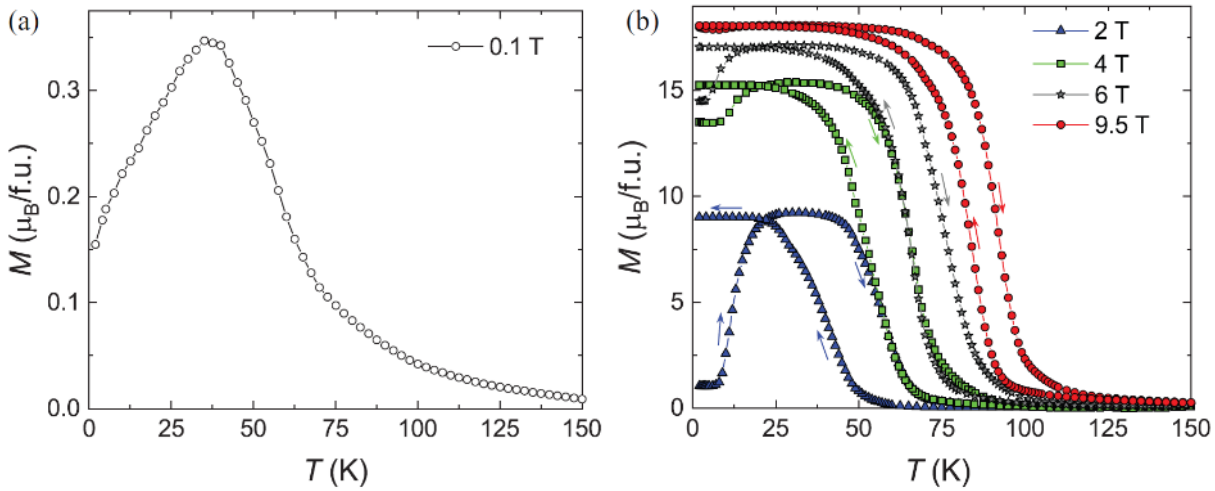

Figure 5.21.: Temperature dependence of the magnetization of $La_{0.85}Ce_{0.15}Fe_{12}B_6$: (a) magnetization measured using zero-field cooled (ZFC) protocol in 0.1 T applied magnetic field; (b) magnetization measured in applied magnetic fields of 2, 4, 6, and 9.5 T [both ZFC and field cooled (FC) data are marked by the same symbols. The arrows indicate the direction of the temperature change].

Nevertheless, the magnetization presents considerably different temperature dependence when conducted in 2 T magnetic field. The ZFC $M(T)$ curve ($\mu_0 H$ = 2 T) manifests a bell-shaped anomaly, and two magnetic events occur sequentially upon heating. The first one corresponds to an AFM-to-FM phase transition at low temperatures, and the second one is a FM-to-PM transformation at high temperatures. The spectacular increase in the magnetization by 550%, when temperature is raised by 8 K, is associated with the sudden formation of the FM order. Throughout this magnetic phase transition, both AFM and FM ordered states coexist, hence forming a magnetically heterogeneous state (magnetic-phase-segregated state). Cooling in a 2 T magnetic field converts $La_{0.85}Ce_{0.15}Fe_{12}B_6$ into a partially FM state. The 2 T curve shows a pronounced splitting between ZFC and FC modes and the maximum value of magnetization for ZFC measuring protocol is larger than for the FC branch. This last aspect is rather unusual for standard FM systems in an applied magnetic field as large as 2 T. A similar bell-like anomaly was evidenced in the parent compound $LaFe_{12}B_6$ within the magnetic field range between 4.75 and 7 T (322). Another salient feature of the isofield magnetization curves of $La_{0.85}Ce_{0.15}Fe_{12}B_6$ is the huge temperature hysteresis of ~12 K in the vicinity of the FM-PM magnetic phase transition, which is consistent with the first-order character of the transformation. Upon increasing the applied magnetic field, the Curie temperature T_C is strongly shifted to higher temperatures.

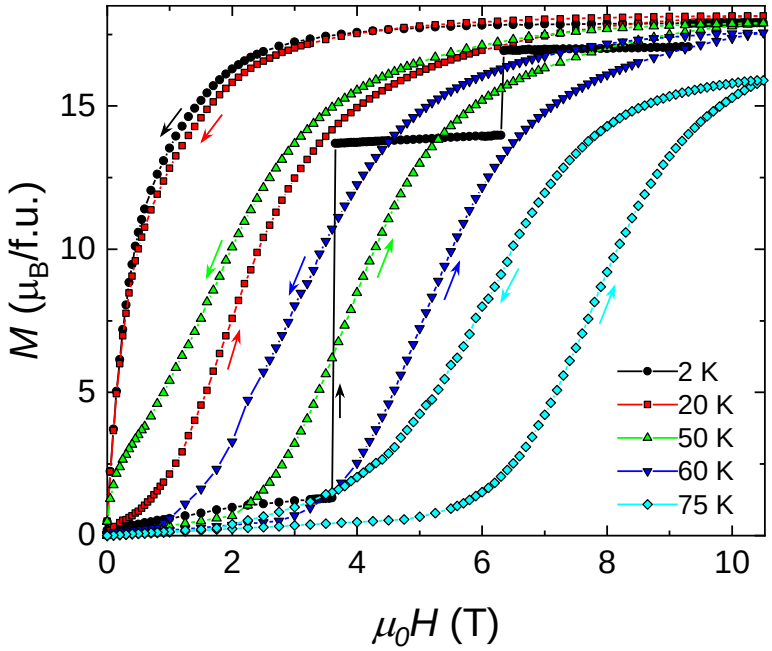

Figure 5.22.: Magnetization isotherms of $La_{0.85}Ce_{0.15}Fe_{12}B_6$ measured between 2 and 75 K.

To elucidate the magnetic states at different fixed temperatures and applied fields, isothermal magnetization curves *M(H)* were taken on the thermally demagnetized $La_{0.85}Ce_{0.15}Fe_{12}B_6$. Just the magnetization isotherms at some representative temperatures are displayed in Figure 5.22, but all the recorded data were used to construct the phase diagram depicted in Figure 5.23. At 2 K, the virgin curve (first magnetization curve) exhibits three ultrasharp jumps followed by plateaus; generating an avalanche-like metamagnetic process like that observed in $LaFe_{12}B_6$. These step-like transitions result from conversion of a fraction of the sample from the AFM state into the FM state. The first and second magnetization plateaus correspond to a mixed phase AFM+FM, *i.e.*, a magnetically heterogenous state. The saturation magnetization of the fully FM polarized state amounts to 17.9 μ_B/f.u. No abrupt steps nor transitions are seen in the demagnetization curve, which shows a conventional FM behavior, soft magnetism like with no remanent magnetization, and no significant coercivity. After the applied field is reduced to zero, 100% of the sample remains in the forced FM state, indicating that the AFM-FM phase transformation is completely irreversible at this temperature. The sharpness of the staircase-like transitions decreases with increasing temperature and vanishes at 8 K where the magnetization process becomes smooth. In $La_{0.85}Ce_{0.15}Fe_{12}B_6$, the magnetic-field-induced metamagnetic transition extends over a wide temperature interval, below and well above the Néel temperature, and proceeds beyond 8 K through a progressive conversion of the PM and AFM phases into FM domains upon increasing applied field. The field-driven AFM-FM and PM-FM phase transformations are accompanied by a large magnetic hysteresis, bearing witness to the first-order nature of the metamagnetic transition.

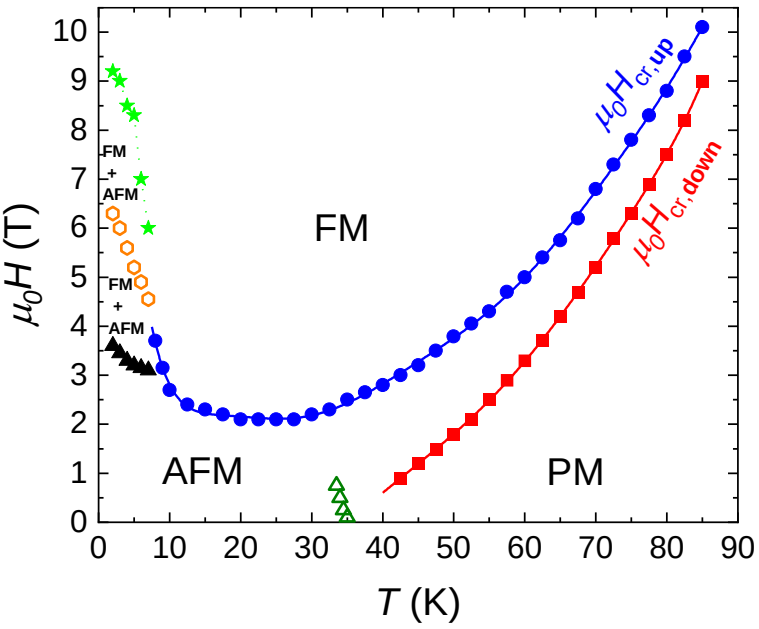

Figure 5.23.: Magnetic phase diagram of $La_{0.85}Ce_{0.15}Fe_{12}B_6$. The critical transition field for the upward ($\mu_0 H_{cr,up}$) and downward ($\mu_0 H_{cr,down}$) field scans as a function of temperature. The transition magnetic field has been derived from the maximum of the field derivative of the magnetization isotherms. The closed triangles, opened hexagons, and closed stars correspond to the critical field of the first, second, and third jump respectively observed on the isothermal magnetization curves. The open triangles represent the Néel temperature T_N.

The critical magnetic fields were defined as the peak of the derivative of magnetization with respect to the magnetic field, and the obtained values were used to elaborate the magnetic field ($\mu_0 H$)-temperature (T) phase diagram shown in Figure 5.23. The critical field of the demagnetization path $\mu_0 H_{cr,down}$ varies continuously with temperature. By contrast, the thermal evolution of the critical field obtained for the field-increasing leg $\mu_0 H_{cr,up}$ is nonmonotonic. Above 27.5 K, $\mu_0 H_{cr,up}$ increases upon heating, while it presents the opposite trend at lower temperatures. Below 27.5 K, the transition field of the first-order AFM-FM phase transition rises with lowering the temperature due to the strengthening of the negative exchange interactions and the diminution of the thermal fluctuations of the magnetic moments and elasticity of the crystal lattice in the AFM state (322, 324, 366). This leads to the increase of both the free energy difference between the two magnetically ordered AFM and FM phases, and the critical field needed to accomplish the magnetic transformation from one state to another. In the PM regime, the critical field $\mu_0 H_{cr,up}$ varies proportionally to the square of temperature T^2 (T^2 dependence) at low temperatures and exhibits a T dependence at high temperatures, in accord with the spin fluctuation theory for itinerant-electron metamagnetic systems (37, 367, 368). The Néel temperature slightly decreases with increasing applied magnetic field. In addition to the three relatively well-delineated magnetic regions—AFM, FM, and PM—another intriguing characteristic of this complex magnetic phase diagram is the low-temperature regime where the itinerant-electron metamagnetic compound $La_{0.85}Ce_{0.15}Fe_{12}B_6$ may be in an AFM, FM, or magnetically heterogeneous AFM + FM state depending on thermomagnetic history effects. For instance, when $La_{0.85}Ce_{0.15}Fe_{12}B_6$ is cooled in zero magnetic field from the PM region down to 2 K and subsequently a field of 3 T is applied, the sample will stay in the pure AFM ground state at 2 K and 3 T. When cooled from room temperature down to 2 K in an applied magnetic field of 3 T, the system will cross the AFM-FM phase boundary and endure a partial AFM → FM magnetic phase transformation; in such experimental conditions, the material will stay in the mixed phase (or phase separated) AFM + FM state.

5.3.3.3. Resistivity and MR

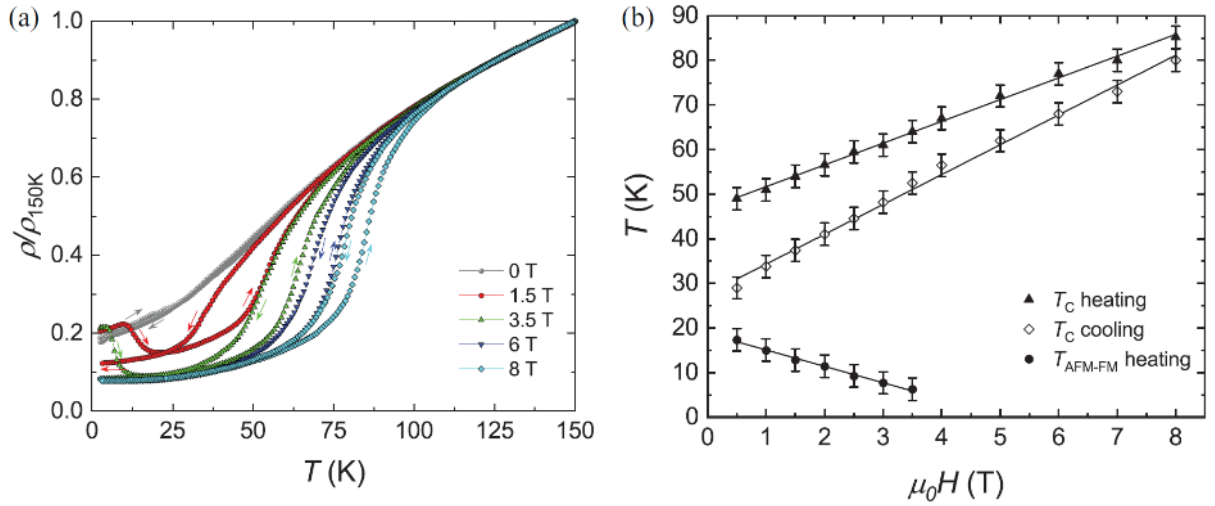

Figure 5.24.: Temperature dependence of the relative electrical resistivity of $La_{0.85}Ce_{0.15}Fe_{12}B_6$ on heating and cooling in various applied magnetic fields. Both zero-field cooled (ZFC) and field-cooled (FC) data are marked by the same symbols. The arrows indicate the direction of the temperature change. (b) Magnetic field dependence of the transition temperatures.

The temperature-dependent electrical resistivity curves *(T)* recorded during warming and cooling between 2.5 and 150 K under various magnetic fields are plotted in Figure 5.24(a). For each isofield *(T)* curve, the sample was first slowly cooled to 2.5 K in zero field. At this temperature of 2.5 K, the desired magnetic field is applied and resistivity data are collected as the system is heated up to 150 K. Subsequently the resistivity was measured by cooling the sample from 150 to 2.5 K under the same constant external field. All *(T)* plots display a strongly linear increase in resistivity at high temperatures, which is indicative of the metallic character, reflecting the dominance of the electron-phonon contribution. Such linear behavior is the general trend in the PM region whatever magnetic field strength is used here. In zero magnetic field, both electrical resistivity functions, heating and cooling, of $La_{0.85}Ce_{0.15}Fe_{12}B_6$ are practically identical, demonstrating that the mechanisms responsible for charge-carrier scattering and their concentration are not affected by the direction of the temperature change. A small anomaly is found at ≈33 K in the 0 T *(T)* curves. In magnetic field of 8 T (6 T), the dramatic increase in the resistivity at 85 K (77 K) upon heating arises from transition between the FM (low resistivity) and PM (high resistivity) phases. These transition temperature values are in excellent agreement with the Curie points derived from thermomagnetic measurements. The increase of external applied field lowers the resistivity around the magnetic ordering temperature T_C because the spin scattering is decreased by the magnetic-field-induced orientation of the local magnetic moments. The large anomaly in electrical resistivity in the vicinity of T_C indicates a strong interaction of Fe magnetic moments with conduction electrons. It is worth recalling that similar drop of the resistivity has been reported by Mesquita *et al.* (356) on FM $RCo_{12}B_6$ isotype compounds.

As it can be clearly seen from Figure 5.24(a), the behavior of the electrical resistivity measured in 1.5 and 3.5 T differs from that observed in zero and high magnetic fields. The *(T)* curves ($\mu_0 H$ = 1.5 and 3.5 T) show a strong divergence between ZFC and FC data and present an even more interesting thermal evolution: on heating from the AFM ground state at 2.5 K, the resistivity exhibits a rapid reduction followed by a plateau, and later, it increases at high temperatures. This peculiar change in resistivity correlates with the presence of both high-temperature FM-PM and low-temperature AFM-FM transitions. The onset of FM ordering is

featured by a large drop in resistivity. The thermal hysteresis accompanying the FM-PM transformation is remarkably large ≈15 K ($\mu_0 H$ = 1.5 T), and emphasizes the first-order nature of the phase transition. The pronounced change in resistivity across the order-order AFM → FM magnetic transformation can be ascribed to the difference in the strength of the scattering of the conduction electrons by the AFM and FM magnons and by the phonons. Our experimental results denote that the scattering in the FM structure is smaller than that in the AFM spin configuration because of a larger magnetic order.

The magnetic ordering temperatures T_C and $T_{AFM\text{-}FM}$ of $La_{0.85}Ce_{0.15}Fe_{12}B_6$ are plotted in Figure 5.24(b) as a function of the applied external field. The application of magnetic field leads to a nearly linear increase of T_C at a rate of 4.9 and 6.7 K/T upon heating and cooling, respectively. The other characteristic features of Figure 5.24(b) are large thermal hysteresis associated with the transformations and a strong negative shift of $T_{AFM\text{-}FM}$ with applied magnetic field. These results demonstrate that the magnetic field enhances the FM state.

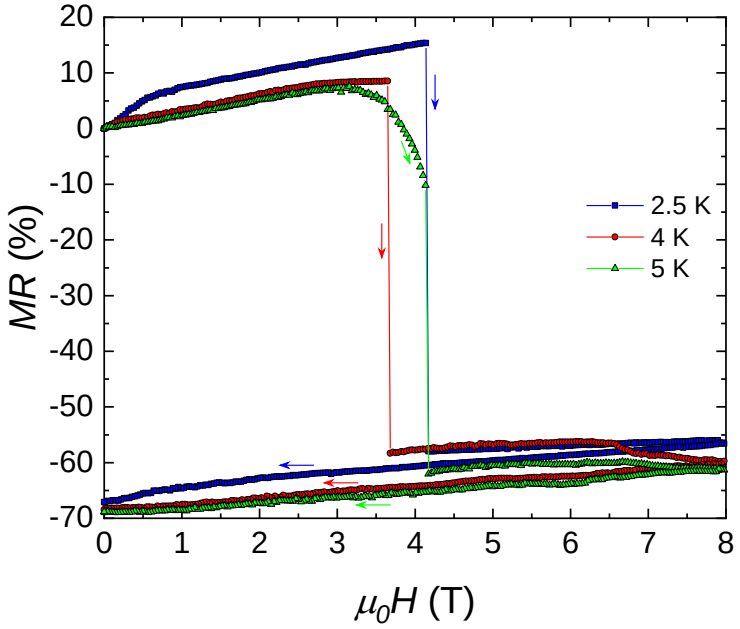

Figure 5.25.: Magnetic field dependence of the isothermal magnetoresistance of $La_{0.85}Ce_{0.15}Fe_{12}B_6$ measured at 2.5, 4 and 5 K.

To probe the correlations between the magnetic degrees of freedom and charge carriers, the magnetic field dependence of the resistivity was measured at various fixed temperatures. Using these data, the MR was assessed as $[\rho(\mu_0 H,T)-\rho(0,T)]/\rho(0,T)$. Isothermal MR curves are plotted in Figs. 7 and 8 at representative temperature intervals. Each isotherm begins from the virgin state after cooling the sample in zero field from the PM state. As follows from Figure 5.25, during the first field increase, the electrical resistivity initially increases and then exhibits a sharp discontinuity in the same magnetic field range where a pronounced stepwise behavior was observed in the magnetic data. This abrupt and substantial change in the resistivity corresponds to a transformation of $La_{0.85}Ce_{0.15}Fe_{12}B_6$ from an AFM into a FM phase, as proven by the magnetization measurements. The resistivity is larger in the AFM phase when compared with that in the field-driven FM state. The subsequent decreasing-field process shows no anomalies because the system stays in the forced FM state as mentioned above. The compound does not recover the initial value of the resistivity and a remanent (nonzero) MR appears after removal of the external field. The original AFM ground state and, thus, the initial resistivity value can be restored only after warming the sample above the FM ordering temperature and

subsequently cooling without an applied magnetic field. The behavior of the electrical resistivity of $La_{0.85}Ce_{0.15}Fe_{12}B_6$ supports the conclusion that the magnetic-field-induced phase transition is totally irreversible at very low temperature.

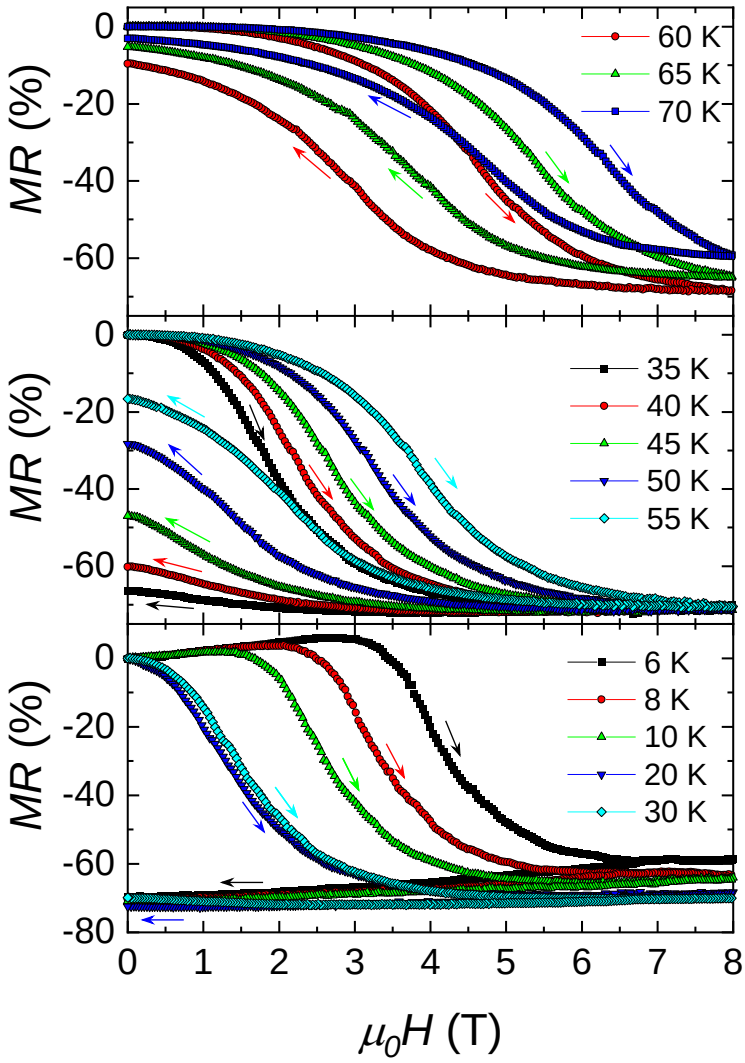

Figure 5.26.: Magnetoresistance isotherms of $La_{0.85}Ce_{0.15}Fe_{12}B_6$ at the indicated temperature ranging from 6 to 30 K (bottom panel), 35 to 55 K (middle panel) and 60 to 70 K (top panel).

At higher temperatures the resistivity shows gradual changes across both AFM-FM and PM-FM transformations unlike the steep jumps observed below 6 K. The MR isotherms display large hysteresis against the magnetic field scan, which is one of the signatures of a first-order transition. Moreover, the hysteretic character and the irreversible/reversible behavior are strongly dependent on a temperature range. We exemplify in Figure 5.26 the isothermal MR plots in three different representative temperature intervals: between 6 and 30 K (bottom panel), from 35 to 55 K (middle panel) and $T \geq 60$ K (top panel). In the AFM phase, below 35 K, the MR ratio is small at low magnetic fields but strikingly decreases above the critical field as the system undergoes a phase transition to the FM state and a giant negative MR effect is observed. The MR associated with the field-induced first-order AFM-FM metamagnetic phase transformation is estimated to be MR $= -73\%$ at 20 K. No transition is detected in the decreasing field scan, and the electrical resistivity remains nearly constant down to the zero magnetic field point, clearly pointing out the irreversible nature of the magnetic transition below 35 K. In the temperature range from 35 to 55 K, the decreasing field curve deviates from

the pure FM character, and a metamagnetic-like transition takes place at lower field, giving rise to a clear hysteresis between both magnetic field processes. From ~35 to ~55 K, the PM-FM phase transition is partially reversible; a fraction of the sample recovers the PM state when the applied field is reduced to zero. In other words, both irreversible and reversible magnetic transformations exist in this temperature interval. Beyond 60 K, the magnetic-field-induced metamagnetic transformation becomes completely reversible, but accompanied with a hysteresis.

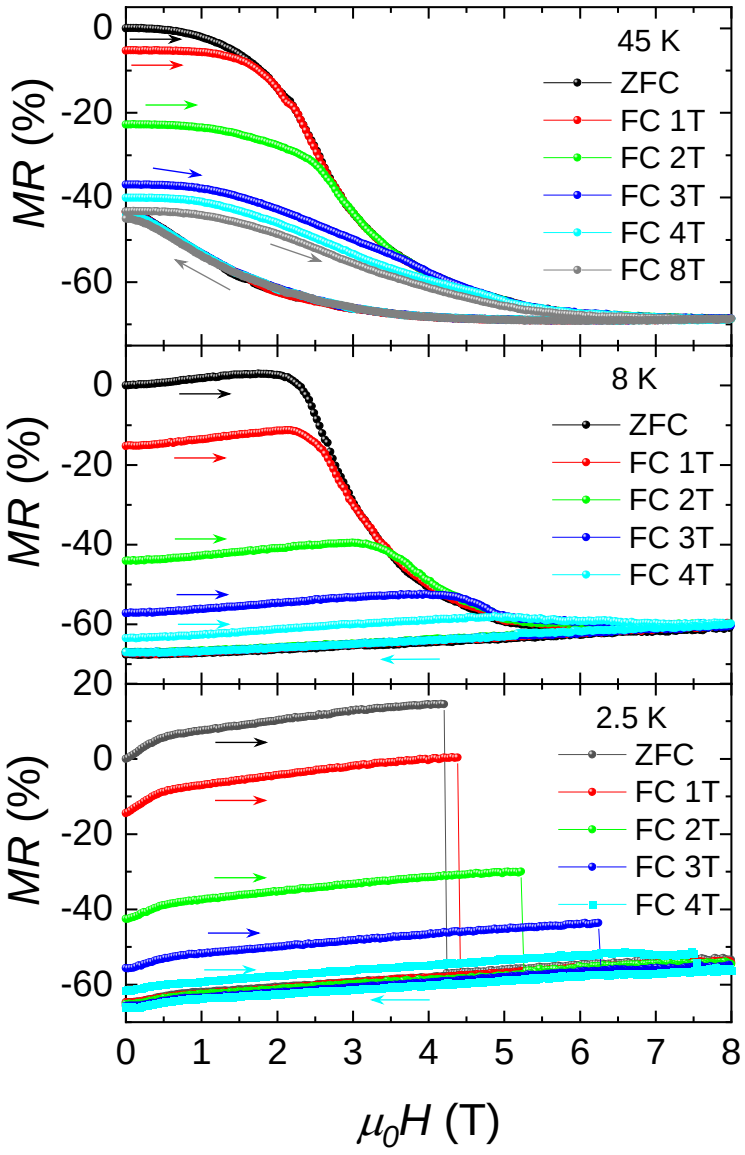

Figure 5.27.: Isothermal magnetoresistance of $La_{0.85}Ce_{0.15}Fe_{12}B_6$ at some selected temperatures of 2.5 K (bottom panel), 8 K (middle panel), and 45 K (top panel) taken after cooling the sample in different magnetic fields.

As discussed in our previous paper (324), field cooling alters the relative fraction of the different magnetic phases—AFM, FM, and PM. By analogy to the magnetic data, we investigated the influence of the magnetic field strength applied during cooling on the electrical resistivity. For these experiments, the sample was cooled in magnetic field ($\mu_0 H>0$) from high temperatures (PM region) down to the measurement temperature. After stabilizing the desired temperature, the cooling field was removed, and then the resistivity was recorded subsequently as a function of magnetic field up to 8 T and back to zero field. The corresponding MR results are illustrated

in Figure 5.27 for some selected temperatures of 2.5, 8, and 45 K after various field cooling procedures (between 0 and 8 T). At 2.5 K, such a magnetic field cooling process reduces the low-field resistivity due to the increase of the FM concentration in the sample at the expense of the AFM component. The critical field at which the step transition occurs is fully controlled by the FM phase content. Field cooling shifts the resistivity jump to higher magnetic fields. Cooling in an adequately high external field transforms the system into a fully FM polarized state, suppressing the sharp step. At 8 K (45 K), the transition field of the AFM-FM (PM-FM) transformation is hardly changed upon field cooling; however, the thermomagnetic history of the sample strongly affects the fraction of the FM phase and the low-field MR.

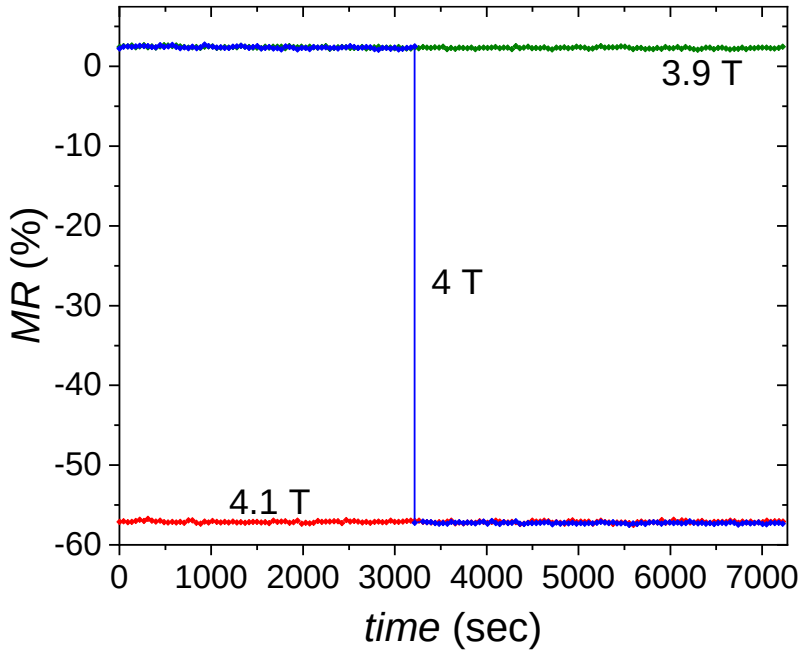

Figure 5.28.: Time dependence of the magnetoresistance recorded at the indicated applied fields for $La_{0.85}Ce_{0.15}Fe_{12}B_6$ at 2.5 K.

Considering the metastability of the different magnetic phases and the anomalous features observed in the data reported above, we further probe time-dependent phenomena (relaxation effect) to study more directly the dynamics of the resistivity abrupt change. The resistive relaxation measurements have been undertaken at 2.5 K and in magnetic fields slightly below and above the transition field corresponding to the steep jump seen in the MR isotherm. Before these time dependence measurements, the sample was cooled from 300 to 2.5 K in the absence of applied magnetic field. After the measurement temperature of 2.5 K is stabilized, a magnetic field is applied, and then the electrical resistivity is recorded vs time (duration of 7200 s). The same experimental protocol was repeated several times applying various fields in steps of 0.1 T, and the results are shown in Figure 5.28. For an applied magnetic field of 4 T, the curve displays giant resistive relaxation effects. The MR decreases abruptly from 2.5 to −57%, owing to, sudden formation of FM domains at the expense of the AFM phase. One can also emphasize that the spectacular and ultrasharp resistivity step occurs over a period smaller than the time interval separating two consecutive measurement points, *i.e.*, <40 s (which is required for averaging). The most salient feature in the present data is the huge spontaneous jump in electrical resistivity at a well-defined time when both external parameters (magnetic field and temperature) are kept constant. The transition time (incubation time) is found to be ~3260 s in $\mu_0 H = 4$ T. Remarkably, this exceptional resistive relaxation effect found in the

$La_{0.85}Ce_{0.15}Fe_{12}B_6$ intermetallic compound exhibits a similarity to the peculiar behavior seen in standard martensitic transitions. The time dependence of the electrical resistivity for the Fe-31.7 at. % Ni alloy (372) strikingly resembles Figure 5.28, *i.e.*, a sudden step is detected after an incubation time of 1020 s.

Although the spontaneous step is seen on both resistive and magnetic relaxation data for the $La_{0.85}Ce_{0.15}Fe_{12}B_6$ system, nevertheless, there is a discrepancy in the incubation time. The transition time differs from 3260 to 3810 s for resistive and magnetic (324) isothermal holding, respectively. This clearly demonstrates that the characteristic time associated with the sharp discontinuity is not a material constant. The phenomenal relaxation observed at 4 T is reminiscent of an explosive instability where the resistivity of the system endures a colossal change in a very short time interval (373). The consistence seen in the magnetotransport and magnetic properties obviously reveals the strong coupling between charge and spin degrees of freedom in the $La_{0.85}Ce_{0.15}Fe_{12}B_6$ compound.

5.3.3.4. X-ray powder diffraction in applied magnetic fields

The observation of anomalous features and multiple magnetic transitions by resistivity and magnetization characterizations urged us to carry out x-ray powder diffraction investigations to establish the crystallographic structures of $La_{0.85}Ce_{0.15}Fe_{12}B_6$ under various duplicated magnetic field and temperature conditions. Along with zero-field experiments, x-ray diffraction spectra were measured in a constant applied magnetic field at temperatures ranging from 15 and 100 K. The diffractograms recorded at 25 K in applied fields of 0 and 4 T are displayed in Figure 5.29. For the sake of clarity, only the region from 14° to 23° 2θ is depicted. Inspecting Figure 5.29, one can immediately observe big differences between the diffraction profiles at zero magnetic field and under applied field. In 4 T external field, the x-ray powder diffraction pattern is significantly modified with the appearance of new Bragg peaks, revealing the presence of a magnetic-field-induced structural transition. At 25 K and 4 T, two structurally distinct $La_{0.85}Ce_{0.15}Fe_{12}B_6$ phases coexist, which is consistent with the first-order character of the transformation.

The Rietveld refinement of the complete diffractogram measured at 25 K in 4 T magnetic field is illustrated in Figure 5.30. At 0 T (see Figure 5.19) in the AFM ground state, as previously mentioned, the diffraction pattern of the compound reflects the pure rhombohedral structure adopting the $R\bar{3}m$ symmetry group (from now on called the Rhom phase). The additional Bragg reflections seen in the 4 T x-ray diagram can be indexed in a monoclinic lattice with the $C2/m$ space group (Mono phase). A good structure refinement was achieved in $C2/m$ symmetry group. According to the International Tables for Crystallography, all listed maximal nonisomorphic subgroups for the $R\bar{3}m$ crystal symmetry group are trigonal except $C2/m$. This monoclinic space group symmetry fits very well the high field diffraction data and is employed to describe the observed structural distortion. Consequently, it is likely to be the correct high magnetic field crystallographic structure of the $La_{0.85}Ce_{0.15}Fe_{12}B_6$ intermetallic compound. Such a field-induced lattice distortion lowers the symmetry of the unit cell from trigonal to monoclinic, *i.e.*, a spontaneous loss of the three-fold symmetry in the *ab* basal plane.

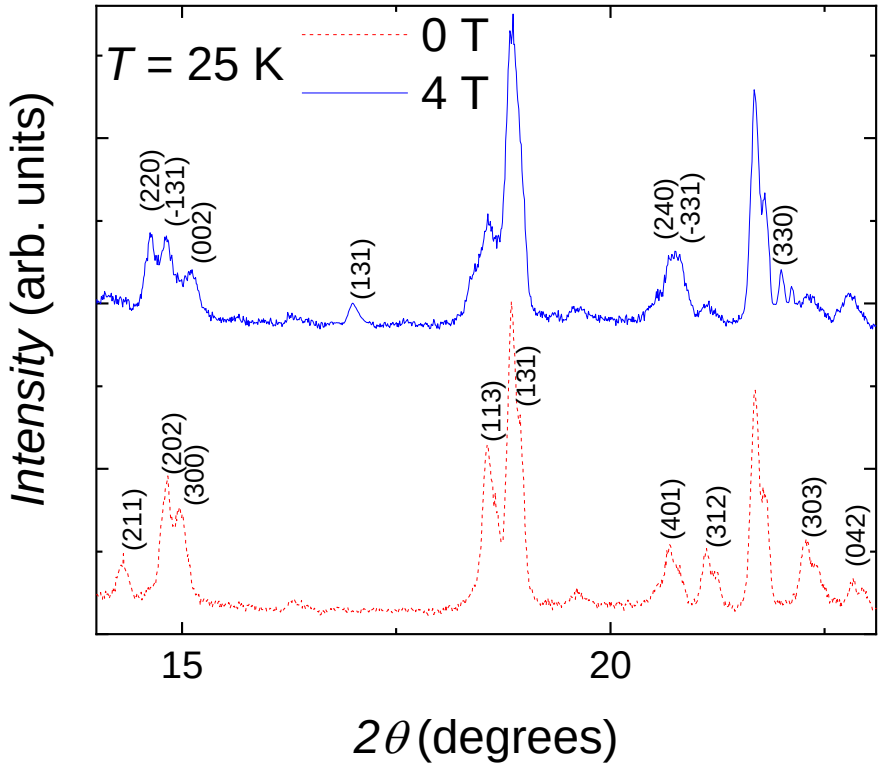

Figure 5.29.: Diffraction patterns measured at 25 K in magnetic fields of 0 and 4 T for the $La_{0.85}Ce_{0.15}Fe_{12}B_6$ compound. Only the low angle part (from 14° to 23°) of the diffraction pattern is shown to better illustrate development of phases with applied magnetic field.

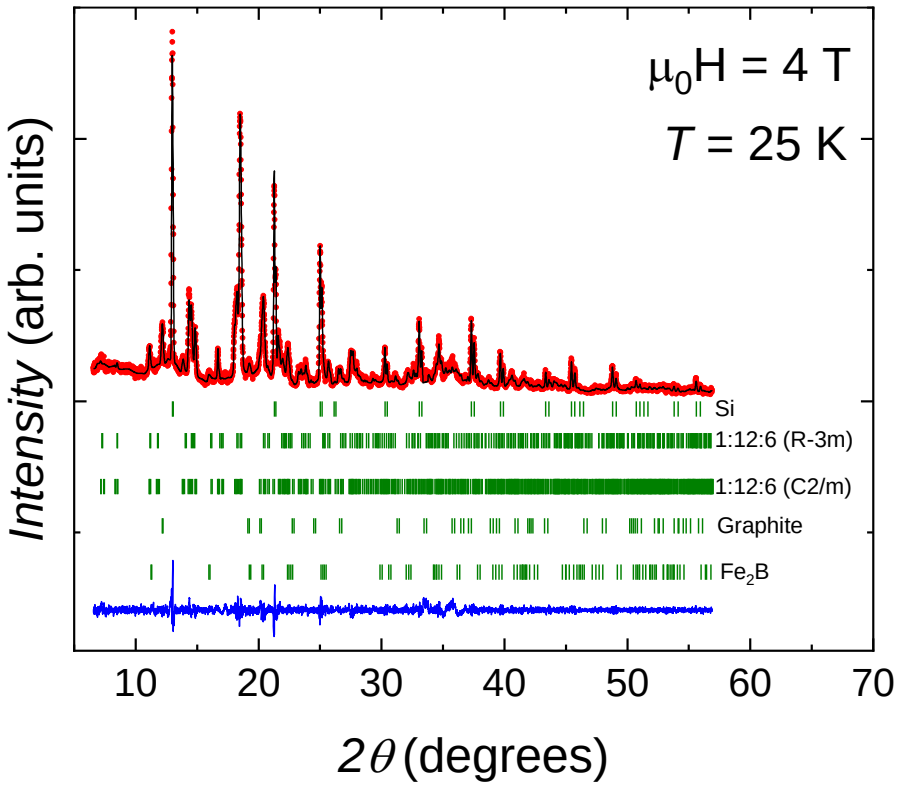

Figure 5.30.: Rietveld refinement of the x-ray powder diffraction pattern collected at 25 K in magnetic field of $\mu_0 H = 4$ T for the $La_{0.85}Ce_{0.15}Fe_{12}B_6$ compound. The observed (red dots) and calculated (black lines) patterns are shown. The blue line represents the difference $I_{obs} - I_{calc}$. The vertical bars (olive) indicated positions of Bragg peaks for the different phases.

The x-ray powder diffraction analyses reveal a change of the lattice symmetry across the magnetic-field-induced first-order AFM-FM transformation, in other words a magnetostructural or coupled crystallographic-magnetic transition from a Rhom (AFM) to a Mono (FM) phase. The structural parameters and reliability factors derived from the fits at 25 K in 0 and 4 T are given in Table 5.2. Temperature-dependent x-ray powder diffraction measurements were also undertaken at 2 T between 15 and 100 K; the obtained results were consistent with those at 4 T. Let us briefly describe the relationship between the monoclinic and rhombohedral lattices. The crystal lattice vectors of the two settings are connected according to $\mathbf{a}_{\mathrm{Mono}} = -\frac{1}{3}\mathbf{a}_{\mathrm{Rhom}} + \frac{1}{3}\mathbf{b}_{\mathrm{Rhom}} - \frac{2}{3}\mathbf{c}_{\mathrm{Rhom}}$; $\mathbf{b}_{\mathrm{Mono}} = \mathbf{a}_{\mathrm{Rhom}} + \mathbf{b}_{\mathrm{Rhom}}$; $\mathbf{c}_{\mathrm{Mono}} = \frac{1}{3}\mathbf{a}_{\mathrm{Rhom}} - \frac{1}{3}\mathbf{b}_{\mathrm{Rhom}} - \frac{1}{3}\mathbf{c}_{\mathrm{Rhom}}$; so that $\mathbf{b}_{\mathrm{Mono}} = \mathbf{a}_{\mathrm{Rhom}}$, and the rhombohedral crystallographic structure is described in the hexagonal triple cell. In the monoclinic crystal structure (space group $C2/m$), La/Ce atoms occupy one single Wyckoff position (2*c*), the Fe atoms are located on four inequivalent crystal sites (Fe1*A* in 4*i*, Fe1*B* in 8*j*, Fe2*A* in 8*j,* and Fe2*B* in 4*g*), and B atoms reside on two inequivalent positions (B1 in 4*i* and B2 in 8*j*). The monoclinic unit cell contains 2 f. u., and altogether it is composed of 38 atoms (24 Fe, 12 B and 2 La/Ce). The relationship between the two crystallographic arrangements is that each of the three 18-fold positions from the rhombohedral crystal structure, which are initially occupied by 18 B and 2 × 18 Fe, are split into pairs of independent eightfold and fourfold positions in the monoclinic atomic arrangement. The threefold site in the rhombohedral crystal system yields a twofold site in the monoclinic lattice.

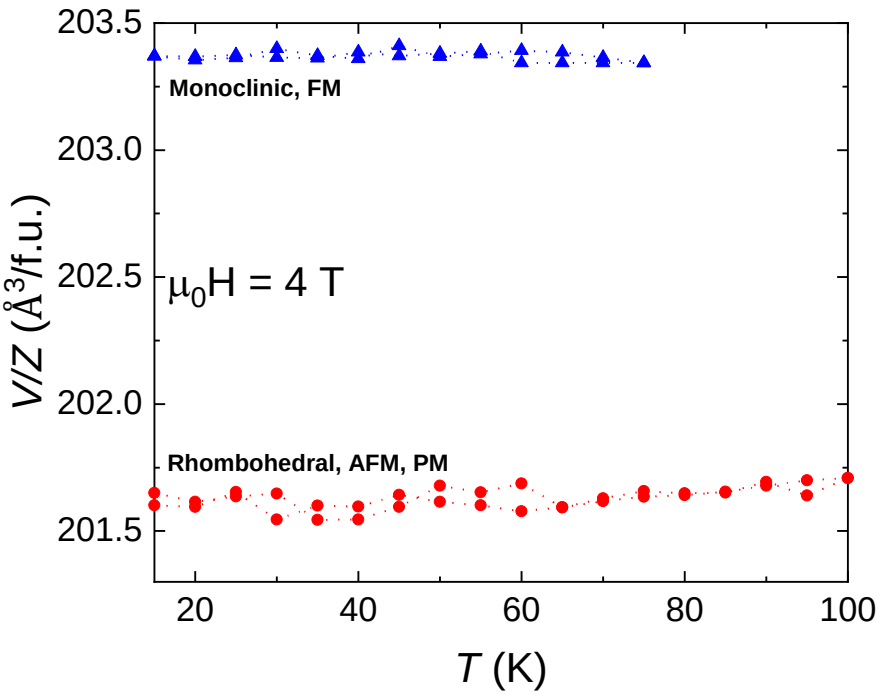

Figure 5.31.: Temperature dependence of the cell volume per formula unit for $La_{0.85}Ce_{0.15}Fe_{12}B_6$ (both rhombohedral and monoclinic phases) derived from x-ray diffraction measurements during heating and cooling in $\mu_0 H$ = 4 T applied magnetic field.

Table 5.2: Structural parameters of the $La_{0.85}Ce_{0.15}Fe_{12}B_6$ compound deduced from Rietveld refinement of the x-ray diffraction patterns collected at T = 25 K in magnetic field of 0 and 4 T. Crystallographic space group, lattice parameters, unit cell volume, number of chemical formulae in unit cell, phase fraction, fractional atomic coordinates, and reliability factors are indicated.

		25 K				25 K
		0T	4 T			4 T
Space group		$R\bar{3}m$	$R\bar{3}m$			$C2/m$
a (Å)		9.5903(3)	9.5903(1)			7.5755(9)
b(Å)		9.5903(3)	9.5903(1)			9.7817(8)
c (Å)		7.5923(4)	7.5944(2)			5.9667(6)
β (°)		90	90			113.089(12)
V (Å^3)		604.74(7)	604.91(22)			406.73(8)
Z		3	3			2
Wt. (%)		100	19.8			80.2
La/Ce (3a)	x	0.0000	0.0000	La/Ce (2c)	x	0.0000
	y	0.0000	0.0000		y	0.0000
	z	0.0000	0.0000		z	0.5000
Fe1 (18h)	x	0.4254(6)	0.4245(7)	Fe1A (4i)	x	0.5407
	y	−0.4254(6)	−0.4245(7)		y	0.0000
	z	0.0366(5)	0.0331(8)		z	0.3121
				Fe1B (8j)	x	0.1764
					y	0.3643
					z	0.0407
Fe2 (18g)	x	0.3698(3)	0.3691(5)	Fe2A (8j)	x	0.3158
	y	0.0000	0.0000		y	0.1842
	z	0.5000	0.5000		z	0.3684
				Fe2B (4g)	x	0.0000
					y	0.1316
					z	0.0000
B1 (18h)	x	0.1631(5)	0.1578(7)	B1A (4i)	x	0.2333
	y	−0.1631(5)	−0.1578(7)		y	0.0000
	z	0.0659(6)	0.0772(9)		z	0.1598
				B1B (8j)	x	0.0535
					y	0.2868
					z	0.2667
χ^2		1.62	1.54			1.54
R_{Bragg} (%)		4.88	4.97			4.72
R_{wp} (%)		9.03	8.63			8.63
R_p (%)		7.12	6.78			6.78
R_{exp} (%)		7.08	6.96			6.96

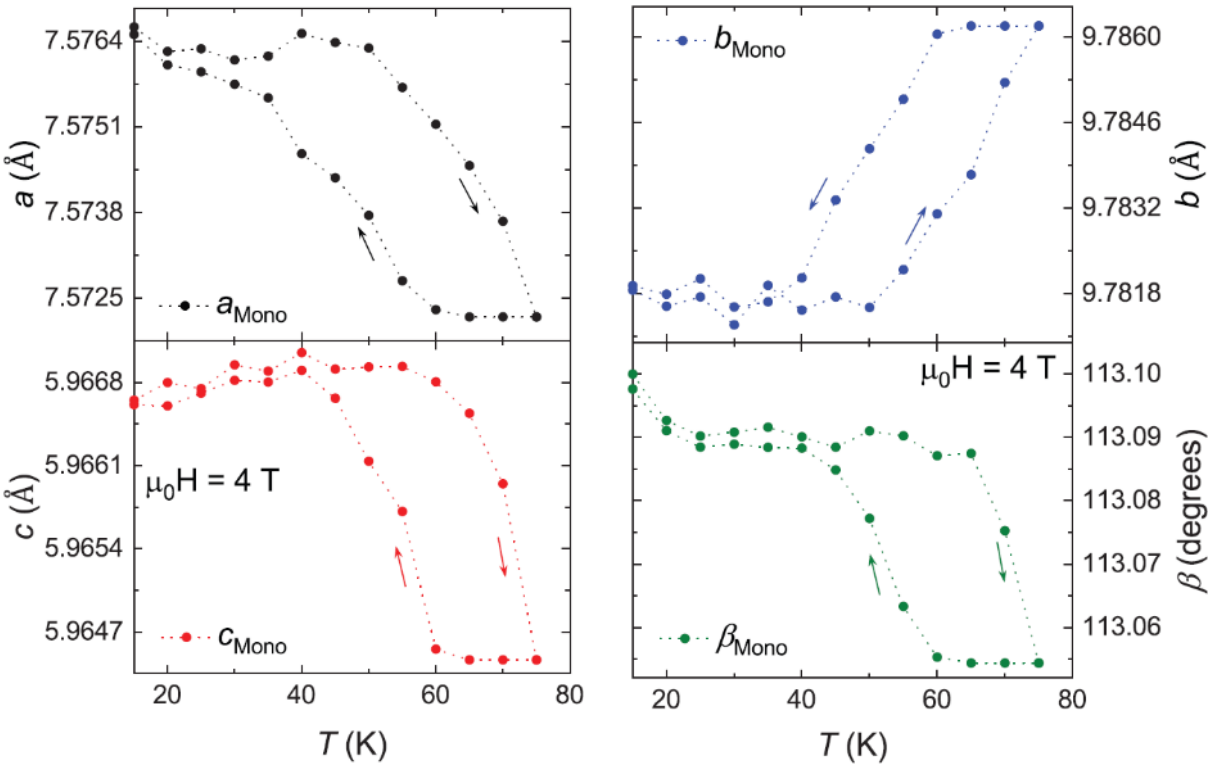

Figure 5.32.: Temperature dependence of the lattice parameters *a*, *b*, and *c*, and Bragg angle β of the monoclinic phase determined from x-ray powder diffraction measurements during heating and cooling in $\mu_0 H = 4$ T applied magnetic field.

The relationship between the rhombohedral (in hexagonal setting) and monoclinic cell volumes is as follows: V_{Mono} $(C2/m)$ = 2/3 V_{Rhom} ($R\bar{3}m$). To directly compare the volumes of the two different atomic arrangements, we normalized their cell volumes to a chemical formula since Z differs from one crystal structure to another. The thermal evolution of the normalized volumes in 4 T is reported in Figure 5.31 including the data upon heating and cooling. In an applied magnetic field of 4 T, the intermetallic compound $La_{0.85}Ce_{0.15}Fe_{12}B_6$ presents an incomplete structural transition from a rhombohedral (AFM, PM) to a monoclinic (FM) lattice; both crystal structures coexist over a wide temperature range. At the lowest measurement temperature (15 K), the application of a 4 T magnetic field triggers ~80% of the structural alteration, and the relative volume change associated with the field-driven magnetostructural transition amounts to 0.88%. At 65 K, the volume of the induced FM (Mono) phase is 0.89% larger than that of the PM (Rhom) one. The relative volume variations at the AFM-FM and FM-PM magnetic transitions are almost the same. The onset of the FM order in $La_{0.85}Ce_{0.15}Fe_{12}B_6$ is characterized by a symmetry-lowering lattice distortion and a simultaneous volume expansion. Figure 5.32 presents the thermal dependence of the monoclinic structural parameters. The cell dimensions vary slowly at low temperatures and show larger changes in the vicinity of the transition temperature. One can observe an extremely anisotropic cell expansion: the lattice expands along the *b* direction, while it contracts along the other two principal crystallographic *a* and *c* axes. Moreover, the lattice parameters *a*, *b*, and *c*, and the angle β exhibit a large temperature hysteresis.

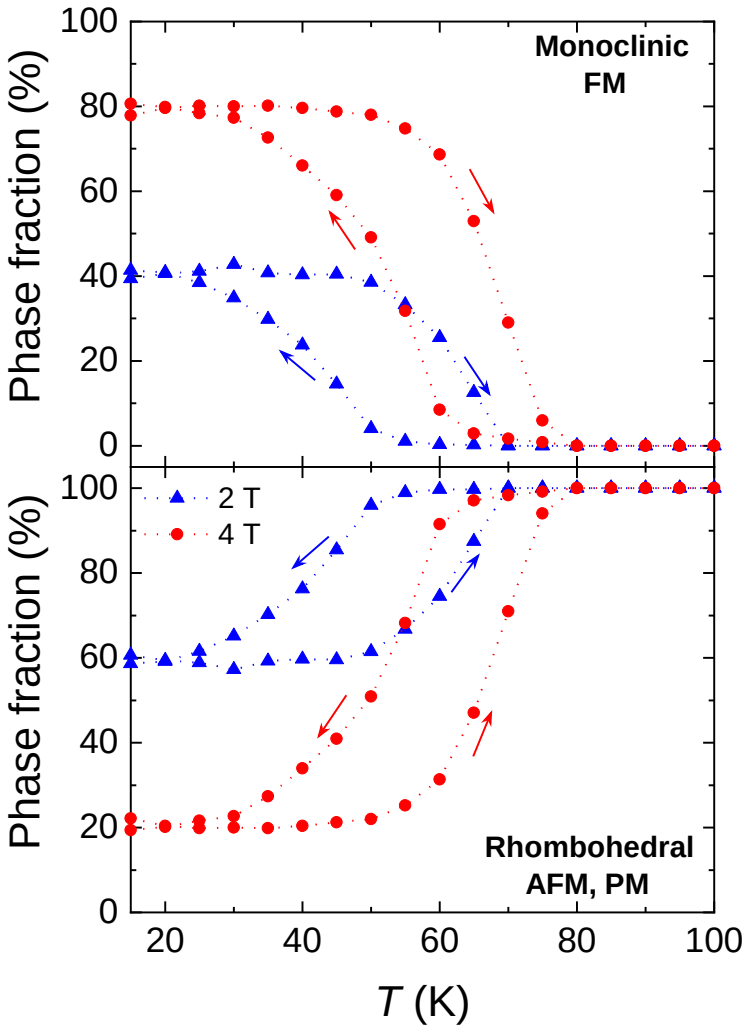

Figure 5.33.: Temperature dependence of the phase fractions of both rhombohedral and monoclinic crystal structures of $La_{0.85}Ce_{0.15}Fe_{12}B_6$ as determined from x-ray powder diffraction measurements during heating and cooling in $\mu_0 H$ = 2 and 4 T applied magnetic fields.

Figure 5.33 represents the evolution of the fractions of the monoclinic (upper panel) and rhombohedral (lower panel) phases with temperature upon warming and cooling in $\mu_0 H = 2$ and 4 T. From these results, it is obvious that the ratio between the rhombohedral and monoclinic phases depends strongly on the strength of the applied magnetic field. A huge thermal hysteresis of 15 K exists between ZFC and FC measuring protocols in 4 T. The behavior seen in Figure 5.33 follows from a competition between the growth of the Mono (FM) phase as the temperature is lowered and the reduction of the Rhom (AFM, PM) proportion. The transition is incomplete upon cooling in 2 T with 40% of the rhombohedral $La_{0.85}Ce_{0.15}Fe_{12}B_6$ transformed into the monoclinic polymorph at 15 K. In 2 T applied magnetic field, the rhombohedral allotrope remains the majority phase over the investigated temperature interval. The sample gets transformed partially into the monoclinic phase, which becomes dominant (~80%) in 4 T at 15 K. When heated and cooled in external fields of 2 and 4 T, $La_{0.85}Ce_{0.15}Fe_{12}B_6$ presents crystallographic inhomogeneity or structurally heterogeneous state (coexistence of polymorphs) below the Curie point. Above this temperature, the system adopts rhombohedral structure and recovers homogeneity. Similar structurally and magnetically inhomogeneous states were also observed in some intermetallic systems like $Gd_5(Si_xGe_{1-x})_4$ (55, 96, 338, 361), Si-doped $CeFe_2$ (339), MnAs (94, 362), and generally found in the colossal magnetoresistive manganese-based perovskites, where they are often called *phase-segregated states* (363, 364).

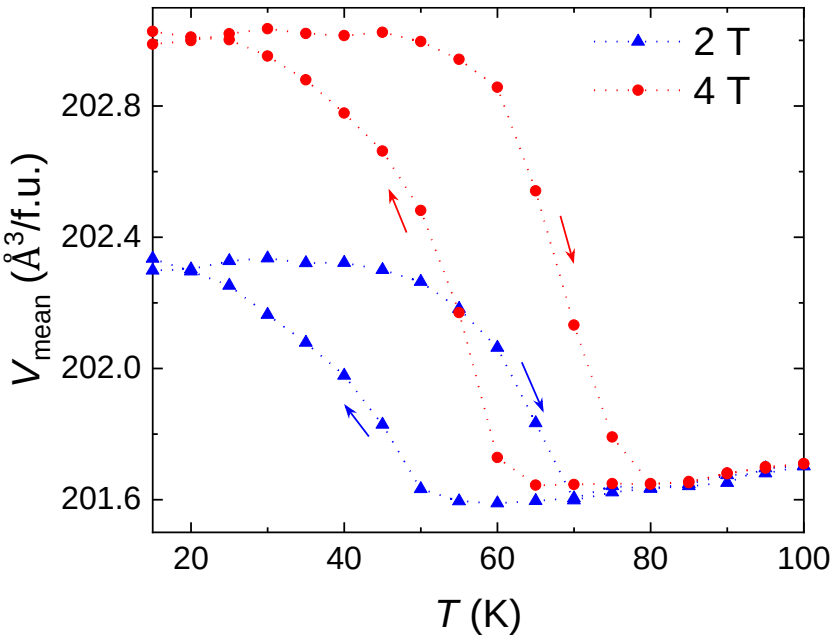

Figure 5.34.: Temperature dependence of the mean cell volume per formula unit determined from x-ray powder diffraction measurements during heating and cooling in $\mu_0 H$ = 2 and 4 T applied magnetic fields.

The weighted average cell volume in 2 and 4 T is plotted against temperature in Figure 5.34. The mean volume displays a transition accompanied by a temperature hysteresis which is consistent with a first-order phase transition. The reduction (growth) of the content of the monoclinic polymorph and the growth (reduction) of the concentration of the rhombohedral phase during heating (cooling) leads to a reduction (increase) of the average volume. For an applied magnetic field of 4 T, the weighted mean cell volume presents a negative thermal expansion (NTE) phenomenon over the temperature interval between 35 and 80 K with an average volumetric thermal expansion coefficient $\alpha_V = -195 \times 10^{-6}\ K^{-1}$. This huge NTE effect originates from the strong magneto-lattice coupling. It is worth noting that our experimental volumetric NTE coefficient compares well with the giant negative thermal expansion reported in (Hf,Ta)Fe_2 itinerant-electron metamagnets ($\alpha_V = -164 \times 10^{-6}$ K) (329, 330) and is on the same order of magnitude as the colossal NTE observed in $Mn_{0.98}CoGe$ ($\alpha_V = -423 \times 10^{-6}\ K^{-1}$) (331) and $Bi_{0.95}La_{0.05}NiO_3$ ($\alpha_V = -413 \times 10^{-6}\ K^{-1}$) (332).

The thermomagnetic behavior of Figure 5.19 may be directly correlated with the phase fractions derived from Rietveld refinements of the x-ray powder diffraction patterns by comparing the normalized magnetization data with the concentration of the monoclinic $La_{0.85}Ce_{0.15}Fe_{12}B_6$. The compilation of the results of x-ray diffraction studies and magnetic measurements is presented in Figure 5.35. The change of the monoclinic phase content with temperature agrees well with the percentage of the FM phase obtained from magnetization in the same applied fields and confirms the intimate coupling between magnetic ordering and the crystal structure in this intermetallic compound.

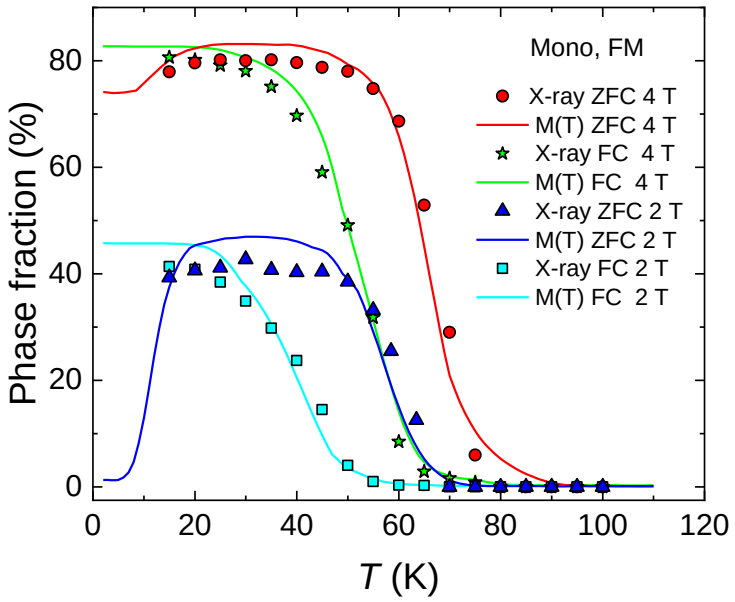

Figure 5.35.: Temperature dependence of the concentration of the monoclinic phase of $La_{0.85}Ce_{0.15}Fe_{12}B_6$ as determined from x-ray powder diffraction (symbols) and magnetization (lines) measurements during heating and cooling in $\mu_0 H$ = 2 and 4 T fields.

However, there are small discrepancies in values between the magnetic and x-ray powder diffraction data, which we attribute to arise from the following reasons: (i) the magnetization normalization yields some errors due to incompleteness of the transformation, and (ii) the intrinsic difference between the magnetization and x-ray diffraction experiments. In the magnetization measurement, a recorded signal reflects the alignment of magnetic moments and magnetic domains, as well as a structural change, while x-ray powder diffraction is only sensitive to a structural alteration. Furthermore, the PM and AFM states have nonzero magnetizations in nonzero external magnetic fields.

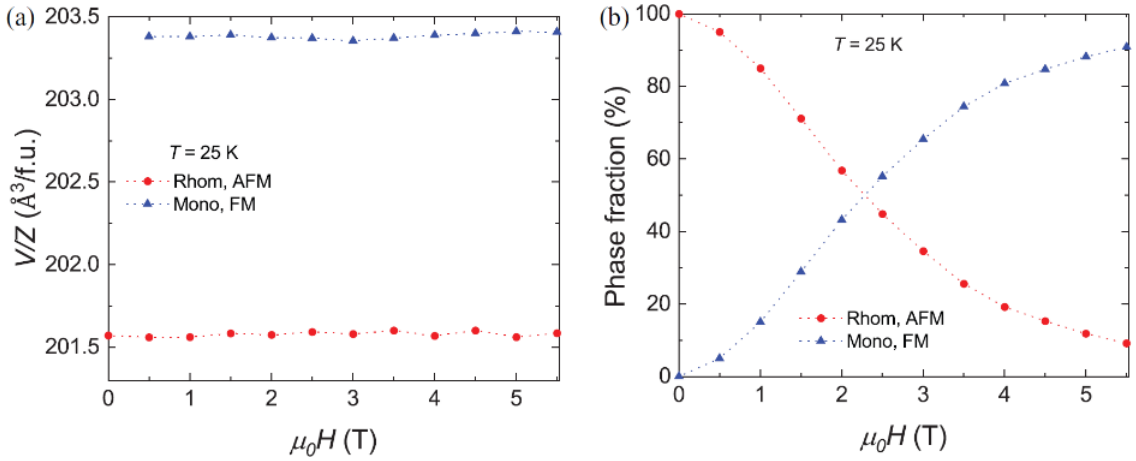

Figure 5.36.: Magnetic field dependence of the (a) cell volume per chemical formula for $La_{0.85}Ce_{0.15}Fe_{12}B_6$, and (b) phase fractions of both rhombohedral and monoclinic crystal structures determined from x-ray powder diffraction measurements at 25 K.

To further elucidate the lattice response at the metamagnetic transition seen in both magnetization and MR isotherms and as well to get a deeper insight into the correlations between the structural and magnetic properties of $La_{0.85}Ce_{0.15}Fe_{12}B_6$, the magnetic field dependence of the crystal structure was examined at a fixed temperature of 25 K (x-ray isotherm). For this experiment, the sample was thermally demagnetized at room temperature

and zero-field cooled down to 25 K. Thereafter, the field was increased between 0 and the maximum attainable value of 5.5 T at regular steps and diffraction patterns measured at every magnetic field step. The diffraction peaks, which correspond to the monoclinic crystal structure, emerge at $\mu_0 H \geq 0.5$ T. When the applied field increases, the intensities of the Bragg reflections corresponding to the rhombohedral phase are reduced, while those of the Bragg peaks of the monoclinic polymorph are increased. In the magnetic field range between 0.5 and 5.5 T, no other changes, except for the progressive reapportionment of intensities of the diffraction lines belonging to the two distinct $La_{0.85}Ce_{0.15}Fe_{12}B_6$ polymorphs, are detected in the x-ray spectra.
The magnetic field dependence of the normalized cell volumes at 25 K is presented in Figure 5.36(a). The Rietveld analysis of the x-ray isotherm indicates that the variations of the structural parameters of each allotrope during isothermal magnetization are very small; hence, the unit cell volumes of both phases are nearly field independent. However, the magnetostriction due to the crystallographic transition from Rhom to Mono is large. The cell volume of the Rhom phase is significantly smaller than that of the Mono phase. The maximum forced volume magnetostriction related to the Rhom (AFM)-Mono (FM) magnetostructural transformation is estimated to be 0.9% at 25 K and 5.5 T. The magnitude of the volume change in $La_{0.85}Ce_{0.15}Fe_{12}B_6$ compares well with the isotropic forced volume magnetostriction across the magnetic-field-induced metamagnetic transition in iron-rich intermetallic systems such as $La(Fe_xAl_{1-x})_{13}$ (359) and $La(Fe_xSi_{1-x})_{13}$ (252). Indeed, a relative volume variation as large as 1% was observed in the pseudo-binary $La(Fe_{0.87}Al_{0.13})_{13}$ alloy (359). Volume magnetostrictions of 0.9 and 1.5% were reported for $La(Fe_{0.86}Si_{0.14})_{13}$ and $La(Fe_{0.88}Si_{0.12})_{13}$, respectively (252). Figure 5.36(b) illustrates the field evolution of the proportion of each phase at 25 K, and the corresponding weighted mean cell volume is plotted in Figure 5.37. Upon increasing applied magnetic field, the amount of the Mono (FM) component gradually grows with the simultaneous decrease of the Rhom (AFM) phase. At a field of ≈2.25 T, the volume fraction of the two polymorphs is close to 1:1 ratio; a structurally and magnetically heterogeneous state. At the highest applied magnetic field of 5.5 T, 91% of the rhombohedral structure is converted to the Mono phase. At 25 K the average volume follows the changes of the concentration of the Mono phase. In the present compound, the magnetic field promotes the development of the high-volume FM phase.

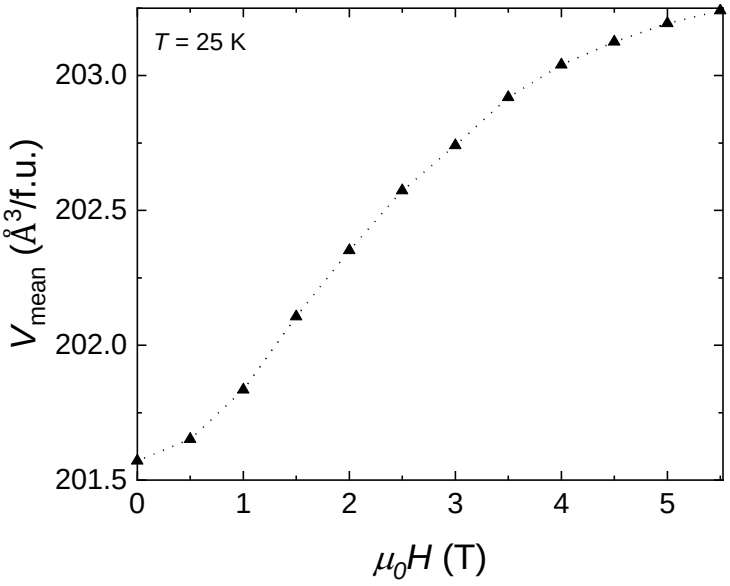

Figure 5.37.: Magnetic field dependence of the mean cell volume per chemical formula determined from powder diffraction measurements at 25 K for $La_{0.85}Ce_{0.15}Fe_{12}B_6$.

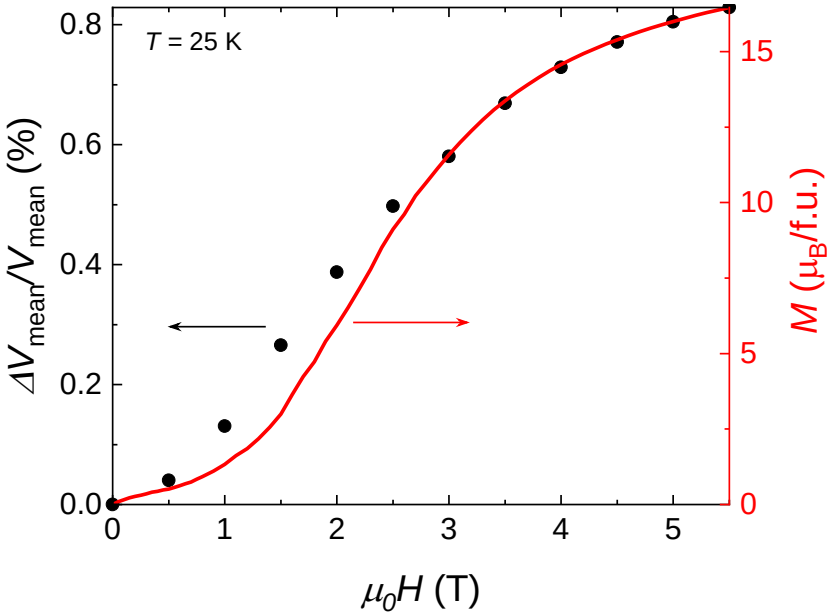

Figure 5.38.: Magnetic field dependence of the relative volume change and the magnetization at 25 K of $La_{0.85}Ce_{0.15}Fe_{12}B_6$.

The relative variation of the weighted mean volume is presented in Figure 5.38 together with the isothermal magnetization data collected at 25 K. Both curves show nearly the same behavior: the average cell volume increases quickly as the magnetization undergoes a magnetic transition. The metamagnetic process is unmistakably visible in the relative change of the mean volume. These data demonstrate that the metamagnetic transition is accompanied by large magnetovolume effects and shed light on the strong coupling between the crystal and magnetic lattices. The magnetic field stimulates a transformation from a low-volume, low-magnetization to a high-volume, high-magnetization phase.

5.3.3.5. Discussion

The experimental results presented in Sec. 5.3.3.2 and Sec. 5.3.3.3 reveal that the magnetic and magnetotransport behaviors of $La_{0.85}Ce_{0.15}Fe_{12}B_6$ are most interesting at very low temperature where the magnetization and MR isotherms display steep jumps. It is essential at this juncture to consider the issue of the origin of these sharp discontinuities. It is quite evident that the steplike transition phenomena observed in the itinerant-electron system $La_{0.85}Ce_{0.15}Fe_{12}B_6$ are not purely magnetic in origin, yet they have a contribution from the strong magneto-elastic coupling. Even though several explanations have been suggested for these unusual and anomalous features in oxides and intermetallics, the most plausible one appears to be a scenario based on the martensitic-like effect stimulated by external magnetic field (325–327).

Let us depict the occurrence of avalanchelike metamagnetic transitions in the magnetization and MR curves within the framework of such a martensitic-like process. Here, $La_{0.85}Ce_{0.15}Fe_{12}B_6$ exhibits an AFM ground state with a rhombohedral crystal structure. However, with the application of a suitable magnetic field, the FM phase (monoclinic cell) develops as a function of temperature, field, as well as time inside the AFM matrix. The magnetic-field-driven lattice distortion (martensiticlike transition) between the rhombohedral and monoclinic crystallographic structures generates elastic strains at the AFM/FM interfaces. Upon applying magnetic field, FM regions are likely to grow, but the interfacial (martensitic) constraints act

against this to block the development of the FM domains. Since the external applied field is gradually increased, the driving force acting on the magnetic moments raises as well. When the magnetic force is strong enough to overcome the elastic strain energy, the FM component evolves in a catastrophic manner, leading to an abrupt change of magnetization and resistivity. Consequently, the overall transition proceeds by successive sudden jumps separated by plateaus. These ultrasharp steps seen in the resistivity and magnetization data can be considered as a burst-like growth of the FM component within the AFM matrix. The field-induced structural distortion which is driven by magnetoelastic coupling, is likely responsible for the stepwise transitions in the $La_{0.85}Ce_{0.15}Fe_{12}B_6$ alloy.

5.3.4. Concluding Remarks

We have performed a detailed study of the structural, magnetic, and transport properties of $La_{0.85}Ce_{0.15}Fe_{12}B_6$ as a function of temperature, magnetic field, and time. Multiple steplike metamagnetic transitions were observed at low temperatures. X-ray powder diffraction indicated that the first-order AFM-FM and PM-FM phase transformations are associated with a symmetry-lowering rhombohedral-to-monoclinic structural transition. The magnetic state is intimately related to its crystallography: the AFM and PM states adopt the rhombohedral structure ($R\bar{3}m$), but the monoclinic symmetry ($C2/m$) is associated with the FM order. This simultaneous magnetic-crystallographic transformation is accompanied by large magnetoelastic and giant negative MR effects. A peculiarly anisotropic thermal expansion and giant NTE effect with a volumetric thermal expansion coefficient $\alpha_V = -195 \times 10^{-6}\,K^{-1}$ were found. At constant applied magnetic field and temperature a colossal spontaneous MR jump occurs after a very long incubation time of ~3260 s.

Magnetic-field-dependent neutron powder diffraction experiments are planned in the near future to establish the magnetic structure of the FM (monoclinic) phase and to gain a deeper understanding of the coupling between the magnetic and crystal lattices in this itinerant-electron metamagnetic compound. The field-induced crystallographic transition reported in this paper may turn out to be key in deciphering future electronic band structure calculations and theoretical studies of the physical properties of this intriguing system.

6. Conclusions and outlook

Magnetic-field-induced phase transitions and magnetostriction are two important fundamental aspects of magnetic materials. Understanding these concepts, and tuning these materials properties are important steps towards designing better materials for green technology, and were important aspects of this work. XRD is an excellent tool for investigation of these properties, but applying magnetic fields during an XRD experiment is not possible with x-ray diffractometers commercially available on the market. One solution is to perform these experiments at large-scale facilities, but access to these institutions is limited and rare. The main objective of this work, therefore, was to develop a lab-based x-ray diffractometer setup with magnet and non-ambient temperature capabilities. The successful assembly of this lab-based XRD system allowed for the investigation of several material classes exhibiting magnetovolume effects and magnetostructural phase transitions.

Of all lab-based x-ray diffractometer instruments with magnet installed worldwide, this works' setup is the most flexible, and allows for investigation of the widest sample parameter space. With a magnetic field of up to 5.5. T, many (potentially) technologically relevant materials with a magnetic-field-induced phase transition can be investigated. The installed sample cryostat features the widest temperature range (11–700 K) of all lab-based setups with magnet, and allows for seamless transitioning between heating and cooling experiments. Combined with the high-flux x-ray mirror optics, the noise-free position-sensitive Si strip detector covering 11 °2θ enables data collection of a complete diffraction pattern in a matter of minutes, with the highest peak resolution of all setups. This allows for quick data collections in a wide sample parameter space. Alternatively, a LiF monochromator that allows for Mo $K_{\alpha 1}$-only measurements can be installed in place of the mirror optics for even higher energy and reflection resolution. Transmission geometry coupled with a partial sample rotation allows for the most reliable relative reflection intensities of all setups, providing data quality of a level that even enables structure solution from powder XRD. Integration of all diffractometer parts into a control software allows for easy access to the system, and the use of convenient data collection macros for long-term measurements without intermittent user input.

The diffractometer with magnet proved to be an essential characterization tool for different kinds of magnetic materials. The investigated materials can be divided into two main groups: (i) magnetoelastic materials without structural phase transition, and (ii) materials undergoing coupled magnetostructural phase transitions.

Materials belonging to the first class that were thoroughly investigated in this work were MnB, FeB, and $LaFe_{11.6}Si_{1.4}$. They share the common feature of showing large magnetoelastic effects upon crossing their FM ordering temperature. $LaFe_{11.6}Si_{1.4}$ expands isotropically with a huge volume expansion upon reaching from cooling down to T_C at ~200 K. The isotropic nature of the expansion is given since it crystallizes in the cubic space group $Fm\bar{3}c$ in a $NaZn_{13}$-type crystal structure. MnB, which crystallizes in the orthorhombic space group *Pnma*, however, shows strong anisotropic, and non-linear behavior in the FM phase up to T_C of ~560 K. Its unit cell expands and contracts simultaneously along different crystallographic directions, and, as a

result, only a small overall unit cell volume change can be detected. FeB, although being isostructural to MnB, and having similar magnetic properties and ordering temperature, shows no lattice parameter anomaly crossing T_C. Magnetic field- and temperature-dependent XRD studies of these materials helped understanding the mechanism behind the corresponding magnetoelastic behavior, and was only possible with the XRD setup assembled for this work. Only the diffractometer setup from this work is able to reach the required temperatures (up to 700 K) to measure at and far above T_C of MnB and FeB. The limitation of the other lab-based setups with magnet for $LaFe_{11.6}Si_{1.4}$ lies in the fact that temperatures >320 K are typically only accessible with furnaces, which, however, cannot reach temperatures below RT. For $LaFe_{11.6}Si_{1.4}$ it proved essential to start the cooling measurement series at 400 K, which is far above its T_C of ~200 K. Otherwise, the fact that the lattice parameter evolution around RT, so still 100 K above T_C, is already non-linear due to intrinsic magnetic effects, would easily be missed. The question of why $LaFe_{11.6}Si_{1.4}$ and MnB show strong magnetoelastic coupling across their metamagnetic transitions is explained with the concept of spin fluctuations. Although referring to the same term – spin fluctuations – different phenomena describe the mechanism behind the large magnetoelasticity of $LaFe_{11.6}Si_{1.4}$ and MnB.

For $LaFe_{11.6}Si_{1.4}$, spin fluctuations are the driving force of the phase transition in the form of short-range correlated magnetic fluctuations in the PM phase. The correlated fluctuations are present as far as 100 K above T_C, and cause a tremendous internal magnetic pressure on the structure. This leads to a partial expansion of the unit cell, and a deviation from linear thermal contraction already around ~300 K. The correlation length of the spin fluctuations increases in the vicinity of T_C, and becomes infinite at T_C, *i.e.* FM order sets in, together with a huge spontaneous magnetostriction. Forced magnetostriction measurements revealed that the system follows Takahashi's SCR spin fluctuation theory.

In MnB, on the other hand, spin fluctuations affect the magnetoelasticity in a different way. Here, a pronounced competition between bonding and magnetism is present. Due to their large ionic radii, Mn atoms in the FM phase strain the neighboring B–B bonds beyond their relaxed state. Thermal spin fluctuations close to T_C tip the scale on the balance between magnetic and structural degrees of freedom, so that small changes in magnetism can lead to large elastic responses of the structure. This delicate competition between magnetism and bonding is not present in FeB, due to the smaller size of the Fe atoms. This results in the B–B bonds not being stretched, and therefore no magnetoelasticity is observable.

$LaFe_{11.6}Si_{1.}4$ and MnB both show large ΔS_{tot} at their metamagnetic transitions due to the large elastic entropy contribution in combination with the large magnetic entropy change. Furthermore, both systems have first-order transitions with almost negligible hysteresis that mainly arise from the fact that both materials are close to a tricritical point. The first-order character of the metamagnetic transitions was, nevertheless, proven by the appearance of distinct two-phase regions close to T_C, observed by the high-resolution synchrotron and neutron scattering studies. These scattering techniques proved to be vital tools for obtaining this information, as they yield phase-specific information, whereas methods like dilatometry or magnetization measurements only report averaged bulk sample results. The observed hysteresis is likely present due to particle size effects, and the large strain induced by the huge volume expansion at the metamagnetic transition. However, the hysteresis is comparatively small compared to many other GME materials due to the lack of kinetic arrest since there is no structural phase transition.

Investigated materials belonging to the second class, *i.e.*, having a coupled magnetostructural transition, were $La_{0.9}Ce_{0.1}Fe_{12}B_6$ and $La_{0.85}Ce_{0.15}Fe_{12}B_6$. The occurrence of a structural phase transition in these materials, however, was proven only during this work, as before it was only deduced indirectly. Reasons for this were the fact that the structural phase transition only occurs during the magnetic-field-induced metamagnetic PM/AFM-FM transition well below 100 K. Magnetization measurements hinted at the occurrence of a structural phase transition that is coupled with the magnetic-field-induced metamagnetic transition due to the presence of a large hysteresis, but could not have been verified without the x-ray diffractometer with magnet that was assembled for this work. The structure of the new FM phase was solved from the XRD data as monoclinic structure in space group $C2/m$, which is a subgroup of the rhombohedral AFM/PM phase crystallizing in space group $R\bar{3}m$. The structural phase transition is accompanied by a huge volume magnetostriction with an expansion of up to $\Delta V/V = 1.15\%$. The FM structure closely resembles the rhombohedral parent structure, but is monoclinically distorted. Furthermore, the most distinct structural difference is a shuffle-like displacement of B atoms in the FM phase, whereas the Fe and La substructures hardly change. Evaluation of phase-specific lattice parameter changes revealed the mechanism of spin alignment that occurs during the magnetostructural transition, and highlights another strength of XRD as material- and phase-sensitive analysis method.
Furthermore, unusual step-like magnetization, MR and macroscopic length changes were observed for $La_{0.9}Ce_{0.1}Fe_{12}B_6$ and $La_{0.85}Ce_{0.15}Fe_{12}B_6$ at temperatures below 10 K above certain critical magnetic fields. These sudden changes imply a burst-like growth of the FM phase under these conditions, and can be explained by the martensitic-like character of the structural phase transition. As commonly observed for martensitic phase transitions, the structural transformation is kinetically arrested by the stress induced by the matrix of neighboring grains. This is also the reason for the large thermal and isothermal hysteresis that clearly differentiates this material class from MnB/FeB and $LaFe_{11.6}Si_{1.4}$.

The number of different studies conducted with the x-ray diffractometer with magnet, and the range of material classes investigated highlight the large versatility of the instrument. Further research is, therefore, possible in many different directions in the vast field of magnetic materials. Even a modification of the sample holder to be able to accommodate samples in reflection geometry, like *e.g.*, thin films deposited on single crystal substrates, is conceivable, and has been demonstrated in a proof of concept measurement (374). A small limitation of the setup is the magnetic field with a maximum field strength of 5.5 T. This field strength is certainly enough to induce field effects in many magnetic materials. Phenomena like some spin-flop transitions (375, 376), or magnetic saturation of some hard magnet materials (17) are, however, not accessible with this work's setup. Many (potentially) technologically relevant magnetic materials, however, can be analyzed in-depth with this instrument, which might show a path for future research in the field of magnetocalorics.

7. Supplemental

7.1. Sample preparation

Sample preparation for the XRD experiments under magnetic fields proved crucial to achieve reliable, and reproducible results, so the following workflow was established.

1. Sample powder is ground and sieved to a particle size $<40\ \mu$m.

2. Sieved powder is mixed with NIST 640d standard reference Si. The weight percentage depends on absorption coefficient of the sample material.

3. Carbon sheet is compacted in a press to reduce the amount of non-sample material exposed to the x-ray beam in order to lower the background of the diffraction pattern.

4. Sample powder and reference Si material is thoroughly mixed and placed on the compacted carbon sheet.

5. The sample is dispersed in glue and spread to cover an area of $\sim$10 x 10 mm^2. The type of glue depends on the temperature range of interest:

- 9–400 K: super glue
- >400 K: high-temperature varnish

6. After drying, the sample is ready to be mounted in the cryofurnace sample holder, and can be recovered and stored afterwards.

7.2. Data transfer Python script

The following lists the Python script that is used for data conversion from the .raw file of the diffractometer control PC into an .xy file. Furthermore, a .stl file can be exported from a temperature- or magnetic-field-dependent measurement series for a 3D view of the diffractograms, and the possibility to 3D print the patterns.

```
#Messungsparameter
name="Terfenol_D"

#n=25
scans=[3, 4, 5, 6, 7, 8, 9, 10, 11, 12, 13]
#while n<62+1:
#    scans.append(n)
#    n+=1
#scans=scans=[1, 2, 3, 4, 5, 6, 7, 8, 9, 10, 11, 12, 13, 14, 15, 16, 17, 18, 19, 20, 21, 22, 23, 24, 25, 26, 27, 28, 29, 30, 31, 32, 33, 34, 35, 36, 37, 38, 39, 40, 41, 42, 43, 44, 45, 46, 47, 48, 49, 50, 51, 52, 53, 54, 55, 56, 57, 58, 59, 60, 61, 62, 63, 64, 65, 66, 67, 68, 69, 70, 71, 72, 73, 74, 75, 76, 77, 78, 79, 80, 81, 82, 83, 84, 85, 86, 87, 88, 89, 90, 91, 92, 93, 94, 95, 96, 97, 98, 99, 100, 101, 102, 103]
scan_continued=1#if there more than one scans with the same scan number type in the number of the scan starting at 1

resolution=0.009
plotten=True
saveplot=False
create_xy_files=True
create_stl=False
stl_file_name="DK050_750_450-110.stl"

Temp_as_name=True
B_as_name=False

#Justage
R=303.1523
th0=5.91267
C_center=615
p=0.05

left_boundary=50
right_boundary=50

# -*- coding: utf-8 -*-
Created on Wed Apr  4 16:04:40 2018

@author: Wansorra

import matplotlib.pyplot as plt
```

```
import numpy as np
from scipy.optimize import curve_fit
from stl import mesh

def th_funktion(th_start, channelnumber):
    channel_list=np.linspace(left_boundary, channelnumber-1-right_boundary, channelnumber-left_boundary-right_boundary)
    thlist = float(th_start)+(th0*((channel_list-C_center)/C_center))- np.arctan(p * (channel_list-C_center) / R)
    return thlist

def spec_to_list(infilename):
    """
    Splits spec file into single measurments and outputs as a list
    with the shape:
        [[[Zeile 1], [Zeile2], [...]],[Messung 2], [Messung 3]]

    infilename: Name of specfile as a string.
    """
    infile=open(infilename, "r")

    Messungen=[[]]
    n=0

    for lines in infile:
        if lines != "\n":
            wort=lines.split()
            Messungen[n].append(wort)
            linebrake=0

        elif linebrake==0:
            linebrake+=1
            Messungen.append([])
            n+=1


    infile.close()
    return Messungen

def transform_list(List, mca_list=True):
    """
    Transforms a List with the shape:
    [[[Zeile 1], [Zeile2], [...]],[Messung 2], [Messung 3]]
    to a shape:
    [[[Messparameter], [[Values as floats],[...]]],[Messung 2], [...]]
    and deletes comments.
```

```
    List: Input list as geneated with the funcition spec_to_list.

    mca_list: If mca_list is set to True, an other List is generated with
    the shape:
    [[[Messparameter], [[Values[values of mca channels]],[...]]],[Messung 2], [...]]
    """
    exitlist=[[]]

    n=0
    m=0
    o=0

    if mca_list==False:
        while n < len(List):
            if List[n][0][0]=="#S":
                exitlist.append([List[n][0]])
                exitlist+=[]
                m=0
                while m < len(List[n]):
                    if List[n][m][0]=="#L":
                        exitlist[n].append(List[n][m][:])
                        m+=1
                    elif List[n][m][0][0]=="#":
                        m+=1
                    elif List[n][m][-1][-1]=="\\":
                        m+=1
                        if List[n][m][-1][-1]!="\\":
                            m+=1
                        #mca eifügen!
                    else:
                        exitlist[-1].append(List[n][m])
                        m+=1
    #               print("m"+str(m))
            n+=1
#           print("n"+str(n))

    if mca_list==True:#Ändern: mca wird bisher nicht richtig berücksichtigt
        while n < len(List):
            if List[n][0][0]=="#S":
                exitlist.append([List[n][0]])
                exitlist+=[]
                o+=1
#               print("o",o)
                m=0
                while m < len(List[n]):
                    if List[n][m][0]=="#L":
                        exitlist[o].append(List[n][m][:])
```

```
                m+=1
#                 print("m",m)

            elif List[n][m][0][0]=="#":
                m+=1
            elif List[n][m][0]=="@A":
                exitlist[o][-1].append(List[n][m][:])
                exitlist[o][-1][-1][-1]=exitlist[o][-1][-1][-1][:-1]
                exitlist[o][-1][-1]=exitlist[o][-1][-1][1:]
                m+=1
                while List[n][m][-1][-1]=="\\":
                    exitlist[o][-1][-1]+=(List[n][m])
                    exitlist[o][-1][-1][-1]=exitlist[o][-1][-1][-1][:-1]
                    m+=1
                if List[n][m][-1][-1]!="\\":
                    exitlist[o][-1][-1]+=(List[n][m])
                    m+=1
                #mca eifügen!
            else:
                exitlist[-1].append(List[n][m])
                m+=1
  #              print("m"+str(m))
        n+=1
#         print("n",n)
        #print("n"+str(n))

  exitlist=exitlist[1:]
  return exitlist

def merge_scan_with_mca(List, scannumber, scan_continued, channelnumber=1280):
  exitlist=[[],[]]

  lastscancount=0

  m=0
  while m<scan_continued-1:
    check=float(List[lastscancount][0][1])
    if check > float(List[lastscancount+1][0][1]):
      m+=1
    lastscancount+=1

  scannumber+=lastscancount

  n=2

  while n < len(List[scannumber-1]):
    th_start=List[scannumber-1][n][0]
```

```
        exitlist[0].append(th_funktion(th_start, channelnumber))
        exitlist[1].append(List[scannumber-1][n][-1][left_boundary:channelnumber-
right_boundary])
        n+=1

    exitlist[0]=np.array(exitlist[0], dtype=float)
    exitlist[1]=np.array(exitlist[1], dtype=float)

    return exitlist

def gauss(x, pos,  sigma, i0, bg):
    Gauss=np.exp(-(x-pos)**2/2/sigma)*i0+bg
    return Gauss

def curve_fit_gauss(List):
    pos_list=[]
    sigma_list=[]
    i0_list=[]
    bg_list=[]
    n=0
    while n< len(List[0]):
        var, perr=curve_fit(gauss, List[0][n], List[1][n], p0=[1200, 2, 10, 0], bounds=([1, 1, 10,
0],[1280, 5, 10**20, 300]))
        pos_list.append(var[0])
        sigma_list.append(var[1])
        i0_list.append(var[2])
        bg_list.append(var[3])
        n+=1
        print(n)

    return [pos_list, sigma_list, i0_list, bg_list]

def transform_scan(List, resolution):
    middlelist=[[],[]]
    exitlist=[[],[]]

    n=0
    while n< len(List[0]):
        m=0
        while m < len(List[0][0]):
            middlelist[0].append(List[0][n][m])
            middlelist[1].append(List[1][n][m])
            m+=1
        n+=1
    middlearray=np.transpose(np.array(middlelist))
    middlelist=middlearray.tolist()
    middlelist.sort()
```

```
    exitarray=np.transpose(np.array(middlelist))

    middlelist2=[[],[]]
    n=0
    while n < len(exitarray[0])-1:
        middlelist2=[[],[]]
        m=0
        while exitarray[0][n+m]-exitarray[0][n] < resolution:
            middlelist2[0].append(exitarray[0][n+m])
            middlelist2[1].append(exitarray[1][n+m])
            m+=1
            if n+m >=len(exitarray[0]):
                break
        exitlist[0].append(round(sum(middlelist2[0])/len(middlelist2[0]), 5))
        exitlist[1].append(sum(middlelist2[1])/len(middlelist2[1]))
        n+=m

    return exitlist

def write_to_xy(List, scan):
    outfile=open(name+"_scan_"+str(scan)+".dat", "w")
    n=0
    while n < len(List[0]):
        outfile.write(str(List[0][n])+"    "+str(List[1][n])+"\n")
        n+=1
    outfile.close()
    return print("Scan data written in file '"+name+"_scan_"+str(scan)+".dat'")

def write_to_xy_with_name(List, name):
    outfile=open(name+".dat", "w")
    n=0
    while n < len(List[0]):
        outfile.write(str(List[0][n])+"    "+str(List[1][n])+"\n")
        n+=1
    outfile.close()
    return print("Scan data written in file '"+name+".dat'")

def create_stl_file(Matrix, bottom = -1):
    """
    Creates a .stl file from a Matrix of the type:
    [[list x values],[list y values],[list z values]]
    with a bottom plate of the thickness 'bottom'.
    The file is saved under the name 'data.stl'.

    Matrix: List that is used for the stl file.
    bottom: thickness of the bottom plate. Default = 1
    """
```

```
vertices1 = []
vertices = []

A0=[]
A1=[]
A2=[]

A0.append(list(Matrix[0][0]))
A0[0].insert(0,Matrix[0][0][0])
A0[0].insert(-1,Matrix[0][0][-1])

A1.append(list(Matrix[1][0]))
A1[0].insert(0,Matrix[1][0][0])
A1[0].insert(-1,Matrix[1][0][-1])

A2.append(list(np.zeros(len(Matrix[2][0]))+bottom))
A2[0].insert(0,bottom)
A2[0].insert(-1,bottom)

n=0
while n < len(Matrix[0]):
    A0.append(list(Matrix[0][n]))
    A0[-1].insert(0,Matrix[0][n][0])
    A0[-1].insert(-1,Matrix[0][n][-1])

    A1.append(list(Matrix[1][n]))
    A1[-1].insert(0,Matrix[1][n][0])
    A1[-1].insert(-1,Matrix[1][n][-1])

    A2.append(list(Matrix[2][n]))
    A2[-1].insert(0,bottom)
    A2[-1].insert(len(A2[-1]),bottom)
    n+=1

A0.append(list(Matrix[0][-1]))
A0[-1].insert(0,Matrix[0][-1][0])
A0[-1].insert(-1,Matrix[0][-1][-1])

A1.append(list(Matrix[1][-1]))
A1[-1].insert(0,Matrix[1][-1][0])
A1[-1].insert(-1,Matrix[1][-1][-1])

A2.append(list(np.zeros(len(Matrix[2][0]))+bottom))
A2[-1].insert(0,bottom)
A2[-1].insert(-1,bottom)

A0.append(list(Matrix[0][0]))
```

```
    A0[-1].insert(0,Matrix[0][0][0])
    A0[-1].insert(-1,Matrix[0][0][-1])

    A1.append(list(Matrix[1][0]))
    A1[-1].insert(0,Matrix[1][0][0])
    A1[-1].insert(-1,Matrix[1][0][-1])

    A2.append(list(np.zeros(len(Matrix[2][0]))+bottom))
    A2[-1].insert(0,bottom)
    A2[-1].insert(-1,bottom)

    A=[np.array(A0), np.array(A1), np.array(A2)]

    m=0

    while m < len(A[2][0]):
        vertices1.append([A[0][0][m], A[1][0][m], A[2][0][m]])
        m+=1

    n=0
    while n < len(A[2]):
        m=0
        while m < len(A[2][0]):
            vertices.append([A[0][n][m], A[1][n][m], A[2][n][m]])
            m+=1
        n+=1


    faces = []

    n=0
    while n < len(A[2])-1:
        m=0
        while m < len(vertices1)-1:
            faces.append([m+(n*len(vertices1)),                    m+1+n*len(vertices1),
m+((n+1)*len(vertices1))])
            faces.append([m+1+(n*len(vertices1)),                  ((n+1)*len(vertices1))+m+1,
m+((n+1)*len(vertices1))])
            m+=1
        n+=1

    vertices = np.array(vertices)
    faces = np.array(faces)

    # Create the mesh
    data = mesh.Mesh(np.zeros(faces.shape[0], dtype=mesh.Mesh.dtype))
    for i, f in enumerate(faces):
```

```
        for j in range(3):
            data.vectors[i][j] = vertices[f[j],:]



    data.save(stl_file_name)
    return

def rescale_matrix(Matrix, x_scale=1, y_scale=1, z_scale=1, Autoscale=False, Autoscalefactor=100, zlog=False):
    """
    Changes the scale of a Matrix with the Form:
        [[list with x-distances],[values of y-axis],[values of zaxis]]

    x_scale: Multiplier for the scale of the x-values
    y_scale: Multiplier for the scale of the y-values
    z_scale: Multiplier for the scale of the x-values
    Autoscale: If True, autoscaling the values to a maximum of 100 in each direction. Default: False
    Autoscalefactor: Final dimension of autoscaled axes. Default: 100
    zlog: If True, z-axis is transformed to logarithmic scale. Default: False
    """
    if zlog==True:
        try:
            Z=list(np.log10(np.array(Matrix[2], dtype="float")))
        except:
            Z=list(np.log10(np.array(Matrix[2], dtype="float")))
        print(Z)
    else:
        Z=Matrix[2]

xmax,ymax,zmax,xmin,ymin,zmin=0,0,0,float(Matrix[0][0][0]),float(Matrix[1][0][0]),float(Z[0][0])



    if Autoscale == True:
        n=0
        while n < len(Matrix[0]):
            m=0
            while m < len(Matrix[0][0]):
                if xmax < float(Matrix[0][n][m]):
                    xmax = float(Matrix[0][n][m])
                if ymax < float(Matrix[1][n][m]):
                    ymax = float(Matrix[1][n][m])
                if zmax < float(Z[n][m]):
                    zmax = float(Z[n][m])
```

```
            if xmin > float(Matrix[0][n][m]):
                xmin = float(Matrix[0][n][m])
            if ymin > float(Matrix[1][n][m]):
                ymin = float(Matrix[1][n][m])
            if zmin > float(Z[n][m]):
                zmin = float(Z[n][m])

            m+=1
        n+=1

    if x_scale==1:
        x_scale=Autoscalefactor/(xmax-xmin)
    if y_scale==1:
        try:
            y_scale=Autoscalefactor/(ymax-ymin)
        except:
            print("Y is not changing during the matrix. You have to choose a 3D Scan")
    if z_scale==1:
        z_scale=Autoscalefactor/(zmax-zmin)

  X=list(np.array(Matrix[0], dtype="float")*x_scale)
  Y=list(np.array(Matrix[1], dtype="float")*y_scale)
  Z=list(np.array(Z, dtype="float")*z_scale)

  return [X,Y,Z]

def reduce_data(A, summe):
  """
  Reduces the datapoints of a list with the form:
  [[list x values],[list y values],[list z values]]
  by a factor of 'summe'.

  A: List that is reduced
  summe: Number of points that are averaged
  """

  B=[[],[],[]]
  m=0
  while m < len(A[0]):
    B[0].append([])
    B[1].append([])
    B[2].append([])
    n=0
    while n < len(A[0][0]):
      if len(A[0][m][n:n+summe])==summe:
        zwischensumme1 = sum(A[0][m][n:n+summe])
        zwischensumme2 = sum(A[1][m][n:n+summe])
```

```
            zwischensumme3 = sum(A[2][m][n:n+summe])
            B[0][m].append(zwischensumme1/summe)
            B[1][m].append(zwischensumme2/summe)
            B[2][m].append(zwischensumme3/summe)
        n+=summe
    m+=1
  return B

if create_xy_files == True:
  if plotten==True:
    plt.figure()
  A=spec_to_list(name)
  B=transform_list(A)
  n=0
  while n<len(scans):


    C=merge_scan_with_mca(B, scans[n], scan_continued)
    D=transform_scan(C, resolution)
    if Temp_as_name==True:
      Temp=int(round(float(B[scans[n]-1][2][1]),0))
      if Temp==0.0:
        m=0
        while Temp == 0.0:
          Temp=int(round(float(B[scans[n]-1][3+m][1])))
          m+=1
          if m > len(B[scans[n]-1]):
            print("Error: Évery temp is 0 K. Please check the Temperature.")
            break
      name=str(Temp)+"K"
      write_to_xy_with_name(D, name)
    elif B_as_name==True:
      B_feld=float(B[scans[n]-1][2][3])
      name=str(B_feld)+"T"
      write_to_xy_with_name(D, name)
    else:
      write_to_xy(D, scans[n])

    if plotten==True:
      plt.plot(D[0], D[1])

    n+=1
  if saveplot==True:
    plt.savefig(name+"_scan"+str(scans[n])+".png")
  else:
    plt.show()
```

```
if create_stl == True:
    E=[[],[],[]]
    n=0
    while n<len(scans):

        A=spec_to_list(name)
        B=transform_list(A)
        Temp=float(B[scans[n]-1][2][1])
        if Temp==0.0:
            m=0
            while Temp == 0.0:
                Temp=float(B[scans[n]-1][3+m][1])
                m+=1
                if m > len(B[scans[n]-1]):
                    print("Error: Évery temp is 0 K. Please check the Temperature.")
                    break
        C=merge_scan_with_mca(B, scans[n], scan_continued)
        D=transform_scan(C, resolution)
        Temp_array=np.linspace(Temp, Temp, len(D[0])).tolist()
        D.insert(1, Temp_array)
        E[0].append(D[0])
        E[1].append(D[1])
        E[2].append(D[2])
#       write_to_xy(D, scans[n])
        n+=1
    F=reduce_data(E, 4)
    G=rescale_matrix(F,x_scale=10, Autoscale=True)
    create_stl_file(G)
    print(stl_file_name+" created.")
#plt.figure()
#n=0
#while n<len(C[0]):
#    plt.plot(C[0][n],C[1][n], linewidth=0.5)
#    n+=1
#plt.savefig("test.pdf")
```

7.3. Measurement macro example

The following is a measurement macro for a temperature series of XRD experiments with no applied magnetic field, followed by an isotherm in fields up to 5.0 T.

```
setpowder phi 15
motor_par(phi, "powder_slew", 4)
motor_par(phi, "powder_base", 4)

# 15 min exposure per frame

# heater range to HIGH
ls332range 1 3
ls332range 1 3

shopen

# 1st cooling 300 - 25 K

umv phi 118
settemp 300
settemp 300
sleep(1800)
ascan tth 12 62 5 1

umv phi 118
settemp 275
settemp 275
sleep(900)
ascan tth 12 62 5 1

umv phi 118
settemp 250
settemp 250
sleep(900)
ascan tth 12 62 5 1

umv phi 118
settemp 225
settemp 225
sleep(900)
ascan tth 12 62 5 1

umv phi 118
settemp 220
settemp 220
sleep(500)
ascan tth 12 62 5 1

umv phi 118
settemp 215
settemp 215
sleep(500)
```

```
ascan tth 12 62 5 1

umv phi 118
settemp 210
settemp 210
sleep(500)
ascan tth 12 62 5 1

umv phi 118
settemp 205
settemp 205
sleep(500)
ascan tth 12 62 5 1

umv phi 118
settemp 200
settemp 200
sleep(900)
ascan tth 12 62 5 1

umv phi 118
settemp 195
settemp 195
sleep(500)
ascan tth 12 62 5 1

umv phi 118
settemp 190
settemp 190
sleep(500)
ascan tth 12 62 5 1

umv phi 118
settemp 185
settemp 185
sleep(500)
ascan tth 12 62 5 1

umv phi 118
settemp 180
settemp 180
sleep(500)
ascan tth 12 62 5 1

umv phi 118
settemp 175
settemp 175
sleep(500)
ascan tth 12 62 5 1

umv phi 118
settemp 150
settemp 150
```

```
sleep(900)
ascan tth 12 62 5 1

umv phi 118
settemp 125
settemp 125
sleep(900)
ascan tth 12 62 5 1

umv phi 118
settemp 100
settemp 100
sleep(900)
ascan tth 12 62 5 1

umv phi 118
settemp 75
settemp 75
sleep(900)
ascan tth 12 62 5 1

umv phi 118
settemp 50
settemp 50
sleep(900)
ascan tth 12 62 5 1

umv phi 118
settemp 25
settemp 25
sleep(900)
ascan tth 12 62 5 1

# heating 25 - 300 K

settemp 300
settemp 300

sleep(3600)

# 1st Isotherm at 210 K 0 - 5.0 T

shopen

setpowder phi 15
motor_par(phi, "powder_slew", 4)
motor_par(phi, "powder_base", 4)

settemp 215
settemp 215
sleep(5400)

umv phi 118
```

```
settemp 210
settemp 210
sleep(500)


# 0 T

setpowder phi 15
motor_par(phi, "powder_slew", 4)
motor_par(phi, "powder_base", 4)
umv phi 118
settemp 210
settemp 210
sleep(3)
ascan tth 12 62 5 1

# 0.5 T
setpowder off
ascan kepco 0 19 11 3

setpowder phi 15
motor_par(phi, "powder_slew", 4)
motor_par(phi, "powder_base", 4)
umv phi 118
settemp 210
settemp 210
sleep(3)
ascan tth 12 62 5 1

# 1.0 T
setpowder off
ascan kepco 19 38 19 3

setpowder phi 15
motor_par(phi, "powder_slew", 4)
motor_par(phi, "powder_base", 4)
umv phi 118
settemp 210
settemp 210
sleep(3)
ascan tth 12 62 5 1

# 1.5 T
setpowder off
ascan kepco 38 57 19 3

setpowder phi 15
motor_par(phi, "powder_slew", 4)
motor_par(phi, "powder_base", 4)
umv phi 118
settemp 210
settemp 210
sleep(3)
```

```
ascan tth 12 62 5 1

# 2.0 T
setpowder off
ascan kepco 57 76 19 3

setpowder phi 15
motor_par(phi, "powder_slew", 4)
motor_par(phi, "powder_base", 4)
umv phi 118
settemp 210
settemp 210
sleep(3)
ascan tth 12 62 5 1

# 2.5 T
setpowder off
ascan kepco 76 95 19 3

setpowder phi 15
motor_par(phi, "powder_slew", 4)
motor_par(phi, "powder_base", 4)
umv phi 118
settemp 210
settemp 210
sleep(3)
ascan tth 12 62 5 1

# 3.0 T
setpowder off
ascan kepco 95 114 19 3

setpowder phi 15
motor_par(phi, "powder_slew", 4)
motor_par(phi, "powder_base", 4)
umv phi 118
settemp 210
settemp 210
sleep(3)
ascan tth 12 62 5 1

# 3.5 T
setpowder off
ascan kepco 114 133 19 3

setpowder phi 15
motor_par(phi, "powder_slew", 4)
motor_par(phi, "powder_base", 4)
umv phi 118
settemp 210
settemp 210
sleep(3)
ascan tth 12 62 5 1
```

```
# 4.0 T
setpowder off
ascan kepco 133 152 19 3

setpowder phi 15
motor_par(phi, "powder_slew", 4)
motor_par(phi, "powder_base", 4)
umv phi 118
settemp 210
settemp 210
sleep(3)
ascan tth 12 62 5 1

# 4.5 T
setpowder off
ascan kepco 152 171 19 3

setpowder phi 15
motor_par(phi, "powder_slew", 4)
motor_par(phi, "powder_base", 4)
umv phi 118
settemp 210
settemp 210
sleep(3)
ascan tth 12 62 5 1

# 5.0 T
setpowder off
ascan kepco 171 190 19 3

setpowder phi 15
motor_par(phi, "powder_slew", 4)
motor_par(phi, "powder_base", 4)
umv phi 118
settemp 210
settemp 210
sleep(3)
ascan tth 12 62 5 1

# 5.0 --> 0.0 T
setpowder off
ascan kepco 190 0 190 2

setpowder phi 15
motor_par(phi, "powder_slew", 4)
motor_par(phi, "powder_base", 4)

# warming up to 300 K
settemp 300
settemp 300
sleep(900)
```

7.4. *FULLPROF* example input file

In the following, an example input file for the *FULLPROF* software for a standard Rietveld refinement is listed. The input file contains parameters describing the diffraction geometry, a global background, correction of systematic angular shifts, and crystallographic information of all three phases present in the diffraction pattern (graphite from the carbon sheet used for sample preparation, Si as internal standard, and Terfenol sample):

```
! Current global Chi2 (Bragg contrib.) =      2.206
! Files => DAT-file: 300K.dat,  PCR-file: 300K
!Job Npr Nph Nba Nex Nsc Nor Dum Iwg Ilo Ias Res Ste Nre Cry Uni Cor Opt Aut
  0  12   3  81   0   0   0   1   0   4   1   0   0   0   0   0   0   1
!
!Ipr Ppl Ioc Mat Pcr Ls1 Ls2 Ls3 NLI Prf Ins Rpa Sym Hkl Fou Sho Ana
  0   0   1   0   1   0   4   0   0  -3  10  -4   0   0   0   1   0
!
! Lambda1  Lambda2    Ratio    Bkpos    Wdt    Cthm     muR   AsyLim   Rpolarz  2nd-muR -> Patt# 1
 0.709320 0.713400  0.65000   40.000 12.0000  0.9780  0.5000  100.00    0.0000  0.3000
!
VARY backgd
!
!NCY  Eps  R_at  R_an  R_pr  R_gl     Thmin       Step      Thmax    PSD    Sent0
 10  0.10  1.00  1.00  1.00  1.00      6.7173   0.009453    67.7923  45.000   0.000
!
!2Theta/TOF/E(Kev)   Background  for Pattern#  1
       6.9914       355.1756       101.00
       7.5395       333.7775       181.00
       8.3805       327.9862       961.00
       9.1365       322.3170       971.00
      10.4311       291.2709       981.00
      10.7429       265.6623       991.00
      11.4138       289.9545       191.00
      12.7461       271.4623       201.00
      13.0391       308.4684       211.00
      14.2769       287.2132       221.00
      14.5604       288.8112       231.00
      15.7416       261.2341       241.00
      16.5543       254.7798       251.00
      17.3399       205.2296       261.00
      17.9836       207.2293       271.00
      18.1726       192.5241       281.00
      19.4200       256.3347       291.00
      19.8830       284.1326       301.00
      20.5676       244.3335       311.00
      21.0736       229.8710       321.00
      21.5272       176.6960       331.00
      22.1792       186.2947       341.00
```

23.4643	150.0601	351.00
23.9556	161.6328	361.00
24.4564	151.7889	371.00
25.3258	166.9540	381.00
26.1952	195.6829	391.00
26.5449	200.6879	401.00
27.7746	210.1971	411.00
28.5979	206.8387	421.00
28.9853	191.7945	431.00
30.2232	189.6368	441.00
30.7618	194.0815	451.00
31.4705	174.3611	461.00
32.0469	174.6362	471.00
32.8501	187.2117	481.00
33.5021	183.9057	491.00
34.7210	189.4100	501.00
35.3825	156.6369	511.00
35.7416	184.8734	521.00
37.2170	190.6940	531.00
37.4722	136.3205	541.00
38.6357	151.0250	551.00
39.1460	140.3300	561.00
39.6562	139.2255	571.00
40.8374	127.9822	581.00
41.7162	118.2976	591.00
42.1319	125.0903	601.00
42.7745	130.5228	611.00
43.6816	115.5982	621.00
44.1163	107.7189	631.00
45.5243	113.0268	641.00
45.7889	110.9307	651.00
47.0658	125.5433	661.00
47.8230	130.9660	671.00
48.0876	127.0694	681.00
48.9381	114.4823	691.00
50.1949	105.9929	701.00
50.2137	101.7578	711.00
51.1681	106.8540	721.00
52.2642	101.4454	731.00
52.6611	92.4361	741.00
53.4832	103.5613	751.00
54.5320	93.0258	761.00
55.2313	82.6911	771.00
55.6471	81.6524	781.00
56.3842	94.6676	791.00
57.2737	83.3071	801.00
58.3805	81.9339	811.00

```
      59.3066       93.2032       821.00
      59.7318       77.0524       831.00
      60.6673       74.9910       841.00
      61.5933       86.4103       851.00
      62.0752       91.4908       861.00
      63.0013       90.5488       871.00
      63.3225       80.6903       881.00
      64.4565       77.3868       891.00
      65.3920       65.1651       901.00
      65.5432       68.3311       911.00
      66.6772       71.5689       921.00
      67.3670       74.4565       931.00
!
!
    99    !Number of refined parameters
!
!  Zero    Code    SyCos    Code   SySin    Code  Lambda     Code MORE ->Patt# 1
  0.01920   21.0  0.00000    0.0  1.18168   61.0 0.709320    0.00   0
!-------------------------------------------------------------------------------
!  Data for PHASE number:   1  ==> Current R_Bragg for Pattern#  1:     4.64
!-------------------------------------------------------------------------------
Si
!
!Nat Dis Ang Pr1 Pr2 Pr3 Jbt Irf Isy Str Furth       ATZ     Nvk Npr More
  1   0   0 1.0 0.0 0.0   0   0   0   0   0         56.154   0  12   0
!
!
F d 3 m                 <--Space group symbol
!Atom   Typ       X        Y        Z     Biso       Occ     In Fin N_t Spc /Codes
Si     Si      0.12500  0.12500  0.12500  0.53568   0.02083   0   0   0    0
               0.00     0.00     0.00     71.00      0.00
!-------> Profile Parameters for Pattern #  1
!  Scale        Shape1      Bov      Str1      Str2      Str3    Strain-Model
 0.20450E-02   0.29334   0.00000   0.00000   0.00000   0.00000       0
   11.00000    41.000     0.000     0.000     0.000     0.000
!       U         V         W         X         Y        GauSiz   LorSiz Size-Model
  0.021551   0.010442   0.004881  -0.000514   0.000000   0.000000   0.000000    0
   141.000    131.000    121.000    111.000      0.000      0.000      0.000
!     a         b         c        alpha      beta       gamma      #Cell Info
  5.431330   5.431330   5.431330  90.000000  90.000000  90.000000
   0.00000    0.00000    0.00000    0.00000    0.00000    0.00000
!  Pref1    Pref2      Asy1     Asy2     Asy3     Asy4
 0.00000  0.00000  0.00000  0.00000  0.00000  0.00000
    0.00     0.00     0.00     0.00     0.00     0.00
!Additional asymmetry parameters (S_L, D_L)
  0.01258    0.00   0.01200    0.00           Shape: Shp1 CShp1 & Shp2 CShp2
!-------------------------------------------------------------------------------
```

```
!  Data for PHASE number:   2  ==> Current R_Bragg for Pattern#  1:     5.95
!-------------------------------------------------------------------------------
Terfenol
!
!Nat Dis Ang Pr1 Pr2 Pr3 Jbt Irf Isy Str Furth       ATZ    Nvk Npr More
  3   0   0 0.0 0.0 1.0   0   0   0   0   0       2184.954   0  12   0
!
!
227                    <--Space group symbol
!Atom   Typ       X        Y        Z     Biso       Occ     In Fin N_t Spc /Codes
Fe     Fe      0.00000  0.00000  0.00000 0.42672   0.08333   0   0   0    0
               0.00     0.00     0.00    91.00      0.00
Tb     Tb      0.37500  0.37500  0.37500 0.29433   0.01250   0   0   0    0
               0.00     0.00     0.00    81.00      0.00
Dy     Dy      0.37500  0.37500  0.37500 0.29433   0.02917   0   0   0    0
               0.00     0.00     0.00    81.00      0.00
!-------> Profile Parameters for Pattern #  1
!  Scale        Shape1       Bov       Str1       Str2       Str3    Strain-Model
 0.14822E-04    0.29229    0.00000    0.00000    0.00000    0.00000       0
  171.00000   941.000      0.000      0.000      0.000      0.000
!      U          V          W          X          Y        GauSiz   LorSiz Size-Model
 -0.015148   0.038359  -0.000245   0.019631   0.000000   0.000000   0.000000    0
    0.000      0.000      0.000      0.000      0.000      0.000      0.000
!    a          b          c        alpha       beta       gamma      #Cell Info
  7.338471   7.338471   7.338471  90.000000  90.000000  90.000000
  51.00000   51.00000   51.00000    0.00000    0.00000    0.00000
!  Pref1    Pref2      Asy1      Asy2      Asy3      Asy4
 0.00000  0.00000  0.00000  0.00000  0.00000  0.00000
   0.00     0.00     0.00     0.00     0.00     0.00
!Additional asymmetry parameters (S_L, D_L)
  0.01258    0.00   0.01200    0.00          Shape: Shp1 CShp1 & Shp2 CShp2
!-------------------------------------------------------------------------------
!  Data for PHASE number:   3  ==> Current R_Bragg for Pattern#  1:     7.30
!-------------------------------------------------------------------------------
Graphite
!
!Nat Dis Ang Pr1 Pr2 Pr3 Jbt Irf Isy Str Furth       ATZ    Nvk Npr More
  2   0   0 1.0 0.0 0.0   0   0   0   0   0        48.040   0  12   0
!
!
194                    <--Space group symbol
!Atom   Typ       X        Y        Z     Biso       Occ     In Fin N_t Spc /Codes
C1     C       0.00000  0.00000  0.25000  0.50000   0.08333   0   0   0    0
               0.00     0.00     0.00     0.00       0.00
C2     C       0.33333  0.66666  0.25000  0.50000   0.08333   0   0   0    0
               0.00     0.00     0.00     0.00       0.00
!-------> Profile Parameters for Pattern #  1
```

```
!  Scale        Shape1       Bov       Str1       Str2       Str3    Strain-Model
 0.89369E-02   0.64959    0.00000    0.00000    0.00000    0.00000       0
    31.00000   951.000      0.000      0.000      0.000      0.000
!       U         V         W         X         Y        GauSiz    LorSiz Size-Model
   0.004102   0.005123   0.036820   0.026888   0.000000   0.000000   0.000000    0
      0.000      0.000      0.000      0.000      0.000      0.000      0.000
!     a         b         c        alpha      beta       gamma       #Cell Info
   2.459569   2.459569   6.720825  90.000000  90.000000 120.000000
  161.00000  161.00000  151.00000    0.00000    0.00000  161.00000
!  Pref1     Pref2      Asy1      Asy2      Asy3      Asy4
  0.00000   0.00000   0.00000   0.00000   0.00000   0.00000
     0.00      0.00      0.00      0.00      0.00      0.00
!Additional asymmetry parameters (S_L, D_L)
   0.01258    0.00   0.01200    0.00           Shape: Shp1 CShp1 & Shp2 CShp2
!  2Th1/TOF1    2Th2/TOF2  Pattern to plot
       8.718      57.791       1
```

References

1. T. Faske, W. Donner, X-ray diffractometer for the investigation of temperature- and magnetic field-induced structural phase transitions. *J Appl Crystallogr*. **51** (2018), doi:10.1107/S1600576718004892.
2. T. Faske, I. A. Radulov, M. Hölzel, O. Gutfleisch, W. Donner, Direct observation of paramagnetic spin fluctuations in LaFe13-x Si x. *Journal of physics: Condensed matter*. **32**, 115802 (2020), doi:10.1088/1361-648X/ab5a99.
3. J. D. Bocarsly, E. E. Levin, S. A. Humphrey, T. Faske, W. Donner, S. D. Wilson, R. Seshadri, Magnetostructural Coupling Drives Magnetocaloric Behavior. *Chem. Mater.* (2019), doi:10.1021/acs.chemmater.9b01476.
4. L. V. B. Diop, T. Faske, M. Amara, D. Koch, O. Isnard, W. Donner, Evidence for a coupled magnetic-crystallographic transition in La0.9Ce0.1Fe12B6. *Phys. Rev. B*. **104** (2021), doi:10.1103/PhysRevB.104.134412.
5. L. V. B. Diop, T. Faske, O. Isnard, W. Donner, Magnetic-field-induced structural phase transition and giant magnetoresistance in La0.85Ce0.15Fe12B6. *Phys. Rev. Materials*. **5** (2021), doi:10.1103/PhysRevMaterials.5.104401.
6. L. Allen, A. O'Connell, V. Kiermer, How can we ensure visibility and diversity in research contributions? How the Contributor Role Taxonomy (CRediT) is helping the shift from authorship to contributorship. *Learned Publishing*. **32**, 71–74 (2019), doi:10.1002/leap.1210.
7. W. C. Röntgen, ON A NEW KIND OF RAYS. *Science*. **3**, 227–231 (1896), doi:10.1126/science.3.59.227.
8. R. E. Dinnebier, S. J. L. Billinge, *Powder diffraction*, *Theory and practice / editors, Robert E. Dinnebier and Simon Billinge* (Royal Society of Chemistry, Cambridge, 2008).
9. J. A. Kaduk, S. J. L. Billinge, R. E. Dinnebier, N. Henderson, I. Madsen, R. Černý, M. Leoni, L. Lutterotti, S. Thakral, D. Chateigner, Powder diffraction. *Nat Rev Methods Primers*. **1** (2021), doi:10.1038/s43586-021-00074-7.
10. W. I. F. David, K. Shankland, Structure determination from powder diffraction data. *Acta crystallographica. Section A, Foundations of crystallography*. **64**, 52–64 (2008), doi:10.1107/S0108767307064252.
11. E. J. Mittemeijer, U. Welzel, The "state of the art" of the diffraction analysis of crystallite size and lattice strain. *Zeitschrift für Kristallographie*. **223** (2008), doi:10.1524/zkri.2008.1213.
12. M. Casas-Cabanas, J. Rodríguez-Carvajal, J. Canales-Vázquez, Y. Laligant, P. Lacorre, M. R. Palacín, Microstructural characterisation of battery materials using powder diffraction data. *Journal of Power Sources*. **174**, 414–420 (2007), doi:10.1016/j.jpowsour.2007.06.216.
13. S. Vives, E. Gaffet, C. Meunier, X-ray diffraction line profile analysis of iron ball milled powders. *Materials Science and Engineering: A*. **366**, 229–238 (2004), doi:10.1016/S0921-5093(03)00572-0.
14. J.-P. Wang, Environment-friendly bulk Fe16N2 permanent magnet: Review and prospective. *Journal of Magnetism and Magnetic Materials*. **497**, 165962 (2020), doi:10.1016/j.jmmm.2019.165962.

15. V. Ly, X. Wu, L. Smillie, T. Shoji, A. Kato, A. Manabe, K. Suzuki, Low-temperature phase MnBi compound: A potential candidate for rare-earth free permanent magnets. *Journal of Alloys and Compounds*. **615**, S285-S290 (2014), doi:10.1016/j.jallcom.2014.01.120.
16. B. Fayyazi, K. P. Skokov, T. Faske, D. Y. Karpenkov, W. Donner, O. Gutfleisch, Bulk combinatorial analysis for searching new rare-earth free permanent magnets. *Acta Materialia*. **141**, 434–443 (2017), doi:10.1016/j.actamat.2017.09.036.
17. D. Y. Karpenkov, K. P. Skokov, M. B. Lyakhova, I. A. Radulov, T. Faske, Y. Skourski, O. Gutfleisch, Intrinsic magnetic properties of hydrided and non-hydrided Nd 5 Fe 17 single crystals. *Journal of Alloys and Compounds*. **741**, 1012–1020 (2018), doi:10.1016/j.jallcom.2018.01.239.
18. K. Fukamichi, A. Fujita, S. Fujieda, Large magnetocaloric effects and thermal transport properties of La(FeSi)13 and their hydrides. *Journal of Alloys and Compounds*. **408-412**, 307–312 (2006), doi:10.1016/j.jallcom.2005.04.022.
19. S. Fujieda, A. Fujita, K. Fukamichi, Large magnetocaloric effect in La(FexSi1−x)13 itinerant-electron metamagnetic compounds. *Appl. Phys. Lett.* **81**, 1276–1278 (2002), doi:10.1063/1.1498148.
20. L. Pfeuffer, T. Gottschall, T. Faske, A. Taubel, F. Scheibel, A. Y. Karpenkov, S. Ener, K. P. Skokov, O. Gutfleisch, Influence of the martensitic transformation kinetics on the magnetocaloric effect in Ni-Mn-In. *Phys. Rev. Materials*. **4** (2020), doi:10.1103/PhysRevMaterials.4.111401.
21. L. Pfeuffer, A. Gràcia-Condal, T. Gottschall, D. Koch, T. Faske, E. Bruder, J. Lemke, A. Taubel, S. Ener, F. Scheibel, K. Durst, K. P. Skokov, L. Mañosa, A. Planes, O. Gutfleisch, Influence of microstructure on the application of Ni-Mn-In Heusler compounds for multicaloric cooling using magnetic field and uniaxial stress. *Acta Materialia*. **217**, 117157 (2021), doi:10.1016/j.actamat.2021.117157.
22. A. Taubel, T. Gottschall, M. Fries, T. Faske, K. P. Skokov, O. Gutfleisch, Influence of magnetic field, chemical pressure and hydrostatic pressure on the structural and magnetocaloric properties of the Mn–Ni–Ge system. *J. Phys. D: Appl. Phys.* **50**, 464005 (2017), doi:10.1088/1361-6463/aa8e89.
23. J. Lai, X. You, J. Law, V. Franco, B. Huang, D. Bessas, M. Maschek, D. Zeng, N. van Dijk, E. Brück, Ultra-low Hysteresis in Giant Magnetocaloric Mn1-V Fe0.95(P,Si,B) Compounds. *Journal of Alloys and Compounds*, 167336 (2022), doi:10.1016/j.jallcom.2022.167336.
24. M. Ait Haddouch, N. Abboushi, N. Sharma, A. Eich, A. Grzechnik, C. Li, M. Tolkiehn, H. Alsamamra, J. Voigt, K. Friese, Site dependence of the magnetocaloric effect in Mn 5− x Fe x Si 3. *J Appl Crystallogr*. **55**, 1164–1172 (2022), doi:10.1107/S1600576722007440.
25. J. Akiyama, H. Iwasaki, S. Yatabe, S. Chiba, Magnetic read-out head using induced RF permeability variation. *IEEE Trans. Magn.* **22**, 692–694 (1986), doi:10.1109/TMAG.1986.1064351.
26. A. Yamaguchi, Y. Suzuki, K. Tanase, S. Sumi, K. Torazawa, S. Ohnuki, N. Ohta, Magnetic expansion read-out of MSR disk with double in-plane magnetic layers. *IEEE Trans. Magn.* **33**, 3217–3219 (1997), doi:10.1109/20.617896.
27. H. J. Williams, R. C. Sherwood, F. G. Foster, E. M. Kelley, Magnetic Writing on Thin Films of MnBi. *J. Appl. Phys.* **28**, 1181–1184 (1957), doi:10.1063/1.1722603.
28. P. M. Braganca, J. A. Katine, N. C. Emley, D. Mauri, J. R. Childress, P. M. Rice, E. Delenia, D. C. Ralph, R. A. Buhrman, A Three-Terminal Approach to Developing Spin-Torque Written Magnetic Random Access Memory Cells. *IEEE Trans. Nanotechnology*. **8**, 190–195 (2009), doi:10.1109/TNANO.2008.2005187.

29. C. C. Hong, Application of a magnetostrictive actuator. *Materials & Design (1980-2015)*. **46**, 617–621 (2013), doi:10.1016/j.matdes.2012.11.013.
30. S. Karunanidhi, M. Singaperumal, Design, analysis and simulation of magnetostrictive actuator and its application to high dynamic servo valve. *Sensors and Actuators A: Physical*. **157**, 185–197 (2010), doi:10.1016/j.sna.2009.11.014.
31. A. Grunwald, A. G. Olabi, Design of a magnetostrictive (MS) actuator. *Sensors and Actuators A: Physical*. **144**, 161–175 (2008), doi:10.1016/j.sna.2007.12.034.
32. X. Tan, J. S. Baras, Modeling and control of hysteresis in magnetostrictive actuators. *Automatica*. **40**, 1469–1480 (2004), doi:10.1016/j.automatica.2004.04.006.
33. J. Nagamatsu, N. Nakagawa, T. Muranaka, Y. Zenitani, J. Akimitsu, Superconductivity at 39 K in magnesium diboride. *Nature*. **410**, 63–64 (2001), doi:10.1038/35065039.
34. M. E. Jones, R. E. Marsh, The Preparation and Structure of Magnesium Boride, MgB 2. *Journal of the American Chemical Society*. **76**, 1434–1436 (1954), doi:10.1021/ja01634a089.
35. T. Moriya, A. Kawabata, Effect of Spin Fluctuations on Itinerant Electron Ferromagnetism. *J. Phys. Soc. Jpn.* **34**, 639–651 (1973), doi:10.1143/JPSJ.34.639.
36. T. Moriya, Y. Takahashi, Spin Fluctuation Theory of Itinerant Electron Ferromagnetism –A Unified Picture. *J. Phys. Soc. Jpn.* **45**, 397–408 (1978), doi:10.1143/JPSJ.45.397.
37. T. Moriya, *Spin Fluctuations in Itinerant Electron Magnetism* (Springer Berlin Heidelberg, Berlin, Heidelberg, 1985).
38. K. R. A. Ziebeck, J. G. Boom, P. J. Brown, H. Capellmann, J. A. C. Bland, Observation of spatial magnetic correlations in the paramagnetic phase of chromium using polarised neutrons and polarisation analysis. *Z. Physik B - Condensed Matter*. **48**, 233–239 (1982), doi:10.1007/BF01420585.
39. T. Sakon, Y. Hayashi, N. Fujimoto, T. Kanomata, H. Nojiri, Y. Adachi, Forced magnetostriction of ferromagnetic Heusler alloy Ni 2 MnGa at the Curie temperature. *Journal of Applied Physics*. **123**, 213902 (2018), doi:10.1063/1.5036558.
40. T. Sakon, J. Yamazaki, T. Komori, T. Kanomata, Y. Narumi, M. Hagiwara, H. Nojiri, Y. Adachi, The Forced Magnetostrictions and Magnetic Properties of Ni2MnX (X = In, Sn) Ferromagnetic Heusler Alloys. *Materials (Basel, Switzerland)*. **13** (2020), doi:10.3390/ma13092017.
41. T. Krenke, M. Acet, E. F. Wassermann, X. Moya, L. Mañosa, A. Planes, Ferromagnetism in the austenitic and martensitic states of Ni−Mn−In alloys. *Phys. Rev. B*. **73** (2006), doi:10.1103/PhysRevB.73.174413.
42. V. V. Vorobev, V. S. Belovol, V. A. Finkel, X-Ray Diffraction Study of Magnetostriction and Phase Transitions in a Field in Rare Earth Metals and Some Alloys. *phys. stat. sol. (b)*. **82**, 213–219 (1977), doi:10.1002/pssb.2220820122.
43. L. Petrás, A. Preisinger, K. Mereiter, Magnetostriction Studied with Precise High Temperature Powder Diffraction. *MSF*. **228-231**, 393–398 (1996), doi:10.4028/www.scientific.net/MSF.228-231.393.
44. Z. Nie, S. Yang, Y. Wang, Z. Wang, D. Liu, Y. Ren, T. Chang, R. Zhang, In-situ studies of low-field large magnetostriction in Tb1−xDyxFe2 compounds by synchrotron-based high-energy x-ray diffraction. *Journal of Alloys and Compounds*. **658**, 372–376 (2016), doi:10.1016/j.jallcom.2015.10.244.
45. J. Mada, K. Yamaguchi, Measurements of magnetostriction constants of epitaxial garnet films by double-crystal x-ray diffraction. *Journal of Applied Physics*. **53**, 596–600 (1982), doi:10.1063/1.329925.

46. X. Moya, L. E. Hueso, F. Maccherozzi, A. I. Tovstolytkin, D. I. Podyalovskii, C. Ducati, L. C. Phillips, M. Ghidini, O. Hovorka, A. Berger, M. E. Vickers, E. Defay, S. S. Dhesi, N. D. Mathur, Giant and reversible extrinsic magnetocaloric effects in La0.7Ca0.3MnO3 films due to strain. *Nature materials*. **12**, 52–58 (2013), doi:10.1038/nmat3463.
47. A. Çak ı r, L. Righi, F. Albertini, M. Acet, M. Farle, S. Aktürk, Extended investigation of intermartensitic transitions in Ni-Mn-Ga magnetic shape memory alloys. *Journal of Applied Physics*. **114**, 183912 (2013), doi:10.1063/1.4831667.
48. A. Çakır, L. Righi, F. Albertini, M. Acet, M. Farle, Intermartensitic transitions and phase stability in Ni50Mn50−xSnx Heusler alloys. *Acta Materialia*. **99**, 140–149 (2015), doi:10.1016/j.actamat.2015.07.072.
49. A. Shahee, S. Sharma, K. Singh, N. P. Lalla, Infield X-ray diffraction studies of field and temperature driven structural phase transition in Nd 0.49 Sr 0.51 MnO 3+ δ . *Journal of Magnetism and Magnetic Materials*. **434**, 174–180 (2017), doi:10.1016/j.jmmm.2017.03.052.
50. A. Shahee, S. Sharma, K. Singh, N. P. Lalla, Studies on magnetic field and temperature driven magneto-structural phase transition in La 0.5 Sr 0.5 MnO 3+ δ . *Journal of Alloys and Compounds*. **708**, 734–742 (2017), doi:10.1016/j.jallcom.2016.12.251.
51. Y. Mitsui, K. Koyama, W. Ito, R. Y. Umetsu, R. Kainuma, K. Watanabe, Observation of Reverse Transformation in Metamagnetic Shape Memory Alloy $Ni_{40}Co_{10}Mn_{34}Al_{16}$ by High-Field X-Ray Diffraction Measurements. *Mater. Trans.* **51**, 1648–1650 (2010), doi:10.2320/matertrans.M2010150.
52. Y. Mitsui, K. Koyama, M. Ohtsuka, R. Umetsu, R. Kainuma, K. Watanabe, High Field X-ray Diffraction Study for Ni46.4Mn38.8In12.8Co2.0 Metamagnetic Shape Memory Film. *Metals*. **7**, 364 (2017), doi:10.3390/met7090364.
53. N. K. Singh, Y. Mudryk, V. K. Pecharsky, K. A. Gschneidner, In situ X-ray powder diffraction study of Ho 5 Ge 4. *Journal of Applied Physics*. **115**, 17E105 (2014), doi:10.1063/1.4853215.
54. V. K. Pecharsky, A. P. Holm, K. A. Gschneidner, JR, R. Rink, Massive magnetic-field-induced structural transformation in Gd5Ge4 and the nature of the giant magnetocaloric effect. *Physical review letters*. **91**, 197204 (2003), doi:10.1103/PhysRevLett.91.197204.
55. Y. Mudryk, A. P. Holm, K. A. Gschneidner, V. K. Pecharsky, Crystal structure-magnetic property relationships of Gd5Ge4 examined by in situ x-ray powder diffraction. *Phys. Rev. B*. **72** (2005), doi:10.1103/PhysRevB.72.064442.
56. K. Tajima, H. Ohsumi, Y. Kida, K. Hayashi, Magnetostriction of Dy and Ho studied by X-ray diffraction. *Journal of Alloys and Compounds*. **303-304**, 276–279 (2000), doi:10.1016/S0925-8388(00)00673-3.
57. O. Gutfleisch, T. Gottschall, M. Fries, D. Benke, I. Radulov, K. P. Skokov, H. Wende, M. Gruner, M. Acet, P. Entel, M. Farle, Mastering hysteresis in magnetocaloric materials. *Philosophical transactions. Series A, Mathematical, physical, and engineering sciences*. **374** (2016), doi:10.1098/rsta.2015.0308.
58. K. Katsumata, Synchrotron X-Ray Diffraction Studies of Magnetic Materials under Extreme Conditions. *Phys. Scr.* **71**, CC7-CC13 (2005), doi:10.1238/Physica.Regular.071a00CC7.
59. Kiryukhin, Keimer, Hill, Coad, Paul, Synchrotron x-ray-scattering study of magnetic-field-induced transitions in Cu1-x(Zn, Ni)xGeO3. *Physical review. B, Condensed matter*. **54**, 7269–7278 (1996), doi:10.1103/physrevb.54.7269.
60. Y. Narumi, K. Katsumata, Y. Tabata, S. Kimura, Y. Tanaka, T. Nakamura, S. Shimomura, M. Matsuda, I. Harada, Y. Nishiyama, T. Ishikawa, H. Kitamura, T. Hara, T. Tanaka, K.

Tamasaku, M. Yabashi, S. Goto, H. Ohashi, K. Takeshita, T. Ohata, T. Matsushita, T. Bizen, Synchrotron X-ray Diffraction Studies of the Incommensurate Phase of a Spin–Peierls System CuGeO 3 in Strong Magnetic Fields. *J. Phys. Soc. Jpn.* **73**, 2650–2653 (2004), doi:10.1143/JPSJ.73.2650.

61. Y. D. Wang, E. W. Huang, Y. Ren, Z. H. Nie, G. Wang, Y. D. Liu, J. N. Deng, H. Choo, P. K. Liaw, D. E. Brown, L. Zuo, In situ high-energy X-ray studies of magnetic-field-induced phase transition in a ferromagnetic shape memory Ni–Co–Mn–In alloy. *Acta Materialia*. **56**, 913–923 (2008), doi:10.1016/j.actamat.2007.10.045.
62. D. C. Tennant, N. Kerley, N. Killoran, Horizontal field magnet cryostat and specimen positioning assembly for neutron scattering experiments. *Review of Scientific Instruments*. **60**, 136–138 (1989), doi:10.1063/1.1140570.
63. H. Nojiri, K. Takahashi, T. Fukuda, M. Fujita, M. Arai, M. Motokawa, 25 T repeating pulsed magnetic fields system for neutron diffraction experiments. *Physica B: Condensed Matter*. **241-243**, 210–212 (1997), doi:10.1016/S0921-4526(97)00864-8.
64. K. Prokeš, M. Meissner, P. Smeibidl, C. Fritsche, K.-D. Ohloff, P. Daniels, Neutron scattering in magnetic fields: extending the possibilities. *Physica B: Condensed Matter*. **294-295**, 691–695 (2001), doi:10.1016/S0921-4526(00)00745-6.
65. M. Steiner, D. A. Tennant, P. Smeibidl, New high field magnet for neutron scattering at Hahn-Meitner Institute. *J. Phys.: Conf. Ser.* **51**, 470–474 (2006), doi:10.1088/1742-6596/51/1/108.
66. Y. H. Matsuda, Y. Ueda, H. Nojiri, T. Takahashi, T. Inami, K. Ohwada, Y. Murakami, T. Arima, Application of a portable pulsed magnet to synchrotron radiation experiments. *Physica B: Condensed Matter*. **346-347**, 519–523 (2004), doi:10.1016/j.physb.2004.01.139.
67. T. Inami, K. Ohwada, Y. H. Matsuda, Y. Ueda, H. Nojiri, Y. Murakami, T. Arima, H. Ohta, W. Zhang, K. Yoshimura, X-ray diffraction experiments under pulsed magnetic fields above 30 T. *Nuclear Instruments and Methods in Physics Research Section B: Beam Interactions with Materials and Atoms*. **238**, 233–236 (2005), doi:10.1016/j.nimb.2005.06.053.
68. Y. H. Matsuda, T. Inami, K. Ohwada, Y. Murata, H. Nojiri, Y. Murakami, H. Ohta, W. Zhang, K. Yoshimura, High field x-ray diffraction study on a magnetic-field-induced valence transition in YbInCu4. *J. Phys. Soc. Jpn.* **75**, 24710 (2006), doi:10.1143/JPSJ.75.024710.
69. P. Frings, J. Vanacken, C. Detlefs, F. Duc, J. E. Lorenzo, M. Nardone, J. Billette, A. Zitouni, W. Bras, G. L. J. A. Rikken, Synchrotron x-ray powder diffraction studies in pulsed magnetic fields. *Review of Scientific Instruments*. **77**, 63903 (2006), doi:10.1063/1.2216914.
70. P. J. E. M. van der Linden, O. Mathon, C. Strohm, M. Sikora, Miniature pulsed magnet system for synchrotron x-ray measurements. *Review of Scientific Instruments*. **79**, 75104 (2008), doi:10.1063/1.2949873.
71. Z. Islam, J. P. C. Ruff, H. Nojiri, Y. H. Matsuda, K. A. Ross, B. D. Gaulin, Z. Qu, J. C. Lang, A portable high-field pulsed-magnet system for single-crystal x-ray scattering studies. *The Review of scientific instruments*. **80**, 113902 (2009), doi:10.1063/1.3251273.
72. Z. Islam, D. Capatina, J. P. C. Ruff, R. K. Das, E. Trakhtenberg, H. Nojiri, Y. Narumi, U. Welp, P. C. Canfield, A single-solenoid pulsed-magnet system for single-crystal scattering studies. *The Review of scientific instruments*. **83**, 35101 (2012), doi:10.1063/1.3688251.
73. J. Billette, F. Duc, P. Frings, M. Nardone, A. Zitouni, C. Detlefs, T. Roth, W. Crichton, J. E. Lorenzo, G. L. J. A. Rikken, A 30 T pulsed magnet with conical bore for synchrotron powder diffraction. *The Review of scientific instruments*. **83**, 43904 (2012), doi:10.1063/1.3701830.
74. Y. H. Matsuda, T. Inami, X-ray Diffraction and Absorption Spectroscopy in Pulsed High Magnetic Fields. *J. Phys. Soc. Jpn.* **82**, 21009 (2013), doi:10.7566/JPSJ.82.021009.

75. F. Duc, X. Fabrèges, T. Roth, C. Detlefs, P. Frings, M. Nardone, J. Billette, M. Lesourd, L. Zhang, A. Zitouni, P. Delescluse, J. Béard, J. P. Nicolin, G. L. J. A. Rikken, A 31 T split-pair pulsed magnet for single crystal x-ray diffraction at low temperature. *The Review of scientific instruments*. **85**, 53905 (2014), doi:10.1063/1.4878915.
76. A. P. Holm, V. K. Pecharsky, K. A. Gschneidner, R. Rink, M. N. Jirmanus, X-ray powder diffractometer for in situ structural studies in magnetic fields from 0 to 35 kOe between 2.2 and 315 K. *Review of Scientific Instruments*. **75**, 1081–1088 (2004), doi:10.1063/1.1667253.
77. Y. Mitsui, K. Koyama, K. Takahashi, K. Watanabe, Development of an x-ray diffraction camera used in magnetic fields up to 10 T. *The Review of scientific instruments*. **82**, 125104 (2011), doi:10.1063/1.3663839.
78. S. Wang, A. E. Kovalev, A. V. Suslov, T. Siegrist, A facility for X-ray diffraction in magnetic fields up to 25 T and temperatures between 15 and 295 K. *The Review of scientific instruments*. **86**, 123902 (2015), doi:10.1063/1.4936969.
79. A. Shahee, S. Sharma, D. Kumar, P. Yadav, P. Bhardwaj, N. Ghodke, K. Singh, N. P. Lalla, P. Chaddah, Low-temperature high magnetic field powder x-ray diffraction setup for field-induced structural phase transition studies from 2 to 300 K and at 0 to 8-T field. *The Review of scientific instruments*. **87**, 105110 (2016), doi:10.1063/1.4963843.
80. K. Watanabe, Y. Watanabe, S. Awaji, M. Fujiwara, N. Kobayashi, T. Hasebe, in *Advances in Cryogenic Engineering Materials*, U. B. Balachandran *et al.*, Eds. (Springer US, Boston, MA, 1998), pp. 747–752.
81. Y. Mitsui, K. Koyama, K. Watanabe, X-ray diffraction measurements in high magnetic fields and at high temperatures. *Science and technology of advanced materials*. **10**, 14612 (2009), doi:10.1088/1468-6996/10/1/014612.
82. B. Fultz, *Phase Transitions in Materials* (Cambridge University Press, 2020).
83. H. E. Karaca, I. Karaman, B. Basaran, Y. Ren, Y. I. Chumlyakov, H. J. Maier, Magnetic Field-Induced Phase Transformation in NiMnCoIn Magnetic Shape-Memory Alloys-A New Actuation Mechanism with Large Work Output. *Adv. Funct. Mater.* **19**, 983–998 (2009), doi:10.1002/adfm.200801322.
84. S. Y. Dan'kov, A. M. Tishin, V. K. Pecharsky, K. A. Gschneidner, Magnetic phase transitions and the magnetothermal properties of gadolinium. *Physical review. B, Condensed matter*. **57**, 3478–3490 (1998), doi:10.1103/PhysRevB.57.3478.
85. J. M. Yeomans, *Statistical Mechanics of Phase Transitions* (Clarendon Press, 1992).
86. F. Guillou, A. K. Pathak, D. Paudyal, Y. Mudryk, F. Wilhelm, A. Rogalev, V. K. Pecharsky, Non-hysteretic first-order phase transition with large latent heat and giant low-field magnetocaloric effect. *Nature communications*. **9**, 2925 (2018), doi:10.1038/s41467-018-05268-4.
87. E. Stern-Taulats, T. Castán, L. Mañosa, A. Planes, N. D. Mathur, X. Moya, Multicaloric materials and effects. *MRS Bull.* **43**, 295–299 (2018), doi:10.1557/mrs.2018.72.
88. C. Zimm, A. Jastrab, A. Sternberg, V. Pecharsky, K. Gschneidner, M. Osborne, I. Anderson, in *Advances in cryogenic engineering*, P. Kittel, Ed. (Springer Science+Business Media, New York, 1998), pp. 1759–1766.
89. T. Gottschall, K. P. Skokov, R. Burriel, O. Gutfleisch, On the S(T) diagram of magnetocaloric materials with first-order transition. *Acta Materialia*. **107**, 1–8 (2016), doi:10.1016/j.actamat.2016.01.052.
90. T. Gottschall, K. P. Skokov, B. Frincu, O. Gutfleisch, Large reversible magnetocaloric effect in Ni-Mn-In-Co. *Appl. Phys. Lett.* **106**, 21901 (2015), doi:10.1063/1.4905371.

91. J. Liu, T. Gottschall, K. P. Skokov, J. D. Moore, O. Gutfleisch, Giant magnetocaloric effect driven by structural transitions. *Nature materials*. **11**, 620–626 (2012), doi:10.1038/nmat3334.
92. T. Krenke, E. Duman, M. Acet, E. F. Wassermann, X. Moya, L. Manosa, A. Planes, Inverse magnetocaloric effect in ferromagnetic Ni-Mn-Sn alloys. *Nature materials*. **4**, 450–454 (2005), doi:10.1038/nmat1395.
93. H. Wada, Y. Tanabe, Giant magnetocaloric effect of MnAs1−xSbx. *Appl. Phys. Lett.* **79**, 3302–3304 (2001), doi:10.1063/1.1419048.
94. J. Mira, F. Rivadulla, J. Rivas, A. Fondado, T. Guidi, R. Caciuffo, F. Carsughi, P. G. Radaelli, J. B. Goodenough, Structural transformation induced by magnetic field and "colossal-like" magnetoresistance response above 313 K in MnAs. *Physical review letters*. **90**, 97203 (2003), doi:10.1103/PhysRevLett.90.097203.
95. V. K. Pecharsky, J. K. A. Gschneidner, Giant Magnetocaloric Effect in Gd5(Si2Ge2). *Physical review letters*. **78**, 4494–4497 (1997), doi:10.1103/PhysRevLett.78.4494.
96. V. K. Pecharsky, K. A. Gschneidner Jr., Gd5(SixGe1-x)4: An Extremum Material. *Adv. Mater.* **13**, 683–686 (2001), doi:10.1002/1521-4095(200105)13:9<683::AID-ADMA683>3.0.CO;2-O.
97. C. L. Zhang, H. F. Shi, E. J. Ye, Y. G. Nie, Z. D. Han, D. H. Wang, Magnetostructural transition and magnetocaloric effect in MnCoGe–NiCoGe system. *Journal of Alloys and Compounds*. **639**, 36–39 (2015), doi:10.1016/j.jallcom.2015.03.118.
98. Y.-Y. Zhao, F. Hu, L.-F. Bao, J. Wang, H. Wu, Q.-Z. Huang, R.-R. Wu, Y. Liu, F.-R. Shen, H. Kuang, M. Zhang, W.-L. Zuo, X.-Q. Zheng, J. Sun, B. Shen, Giant negative thermal expansion in bonded MnCoGe-based compounds with Ni2In-type hexagonal structure. *Journal of the American Chemical Society*. **137**, 1746–1749 (2015), doi:10.1021/ja510693a.
99. Asamitsu, Moritomo, Kumai, Tomioka, Tokura, Magnetostructural phase transitions in La1-xSrxMnO3 with controlled carrier density. *Physical review. B, Condensed matter*. **54**, 1716–1723 (1996), doi:10.1103/physrevb.54.1716.
100. S. A. Nikitin, G. Myalikgulyev, A. M. Tishin, M. P. Annaorazov, K. A. Asatryan, A. L. Tyurin, The magnetocaloric effect in Fe49Rh51 compound. *Physics Letters A*. **148**, 363–366 (1990), doi:10.1016/0375-9601(90)90819-A.
101. M. P. Annaorazov, S. A. Nikitin, A. L. Tyurin, K. A. Asatryan, A. K. Dovletov, Anomalously high entropy change in FeRh alloy. *J. Appl. Phys.* **79**, 1689–1695 (1996), doi:10.1063/1.360955.
102. A. M. Chirkova, K. P. Skokov, Y. Skourski, F. Scheibel, A. Y. Karpenkov, A. S. Volegov, N. V. Baranov, K. Nielsch, L. Schultz, K.-H. Müller, T. G. Woodcock, O. Gutfleisch, Magnetocaloric properties and specifics of the hysteresis at the first-order metamagnetic transition in Ni-doped FeRh. *Phys. Rev. Materials*. **5** (2021), doi:10.1103/PhysRevMaterials.5.064412.
103. L. H. Lewis, C. H. Marrows, S. Langridge, Coupled magnetic, structural, and electronic phase transitions in FeRh. *J. Phys. D: Appl. Phys.* **49**, 323002 (2016), doi:10.1088/0022-3727/49/32/323002.
104. B. S. Wang, P. Tong, Y. P. Sun, W. Tang, L. J. Li, X. B. Zhu, Z. R. Yang, W. H. Song, Structural, magnetic properties and magnetocaloric effect in Ni-doped antiperovskite compounds GaCMn3−xNix (0≤x≤0.10). *Physica B: Condensed Matter*. **405**, 2427–2430 (2010), doi:10.1016/j.physb.2010.03.001.
105. D. Fruchart, E. F. Bertaut, Magnetic Studies of the Metallic Perovskite-Type Compounds of Manganese. *J. Phys. Soc. Jpn.* **44**, 781–791 (1978), doi:10.1143/JPSJ.44.781.

106. A. Fujita, K. Fukamichi, Giant volume magnetostriction due to the itinerant electron metamagnetic transition in La(Fe-Si)/sub 13/ compounds. *IEEE Trans. Magn.* **35**, 3796–3798 (1999), doi:10.1109/20.800668.
107. A. T. Saito, T. Kobayashi, H. Tsuji, Magnetocaloric effect of new spherical magnetic refrigerant particles of La(Fe1−x−yCoxSiy)13 compounds. *Journal of Magnetism and Magnetic Materials*. **310**, 2808–2810 (2007), doi:10.1016/j.jmmm.2006.10.1058.
108. K. Löwe, J. Liu, K. Skokov, J. D. Moore, H. Sepehri-Amin, K. Hono, M. Katter, O. Gutfleisch, The effect of the thermal decomposition reaction on the mechanical and magnetocaloric properties of La(Fe,Si,Co)13. *Acta Materialia*. **60**, 4268–4276 (2012), doi:10.1016/j.actamat.2012.04.027.
109. I. A. Radulov, K. P. Skokov, D. Y. Karpenkov, T. Gottschall, O. Gutfleisch, On the preparation of La(Fe,Mn,Si)13Hx polymer-composites with optimized magnetocaloric properties. *Journal of Magnetism and Magnetic Materials*. **396**, 228–236 (2015), doi:10.1016/j.jmmm.2015.08.044.
110. I. A. Radulov, D. Y. Karpenkov, K. P. Skokov, A. Y. Karpenkov, T. Braun, V. Brab?nder, T. Gottschall, M. Pabst, B. Stoll, O. Gutfleisch, Production and properties of metal-bonded La(Fe,Mn,Si) 13 H x composite material. *Acta Materialia*. **127**, 389–399 (2017), doi:10.1016/j.actamat.2017.01.054.
111. E. Brück, M. Ilyn, A. M. Tishin, O. Tegus, Magnetocaloric effects in MnFeP1−xAsx-based compounds. *Journal of Magnetism and Magnetic Materials*. **290-291**, 8–13 (2005), doi:10.1016/j.jmmm.2004.11.152.
112. F. Guillou, H. Yibole, G. Porcari, L. Zhang, N. H. van Dijk, E. Brück, Magnetocaloric effect, cyclability and coefficient of refrigerant performance in the MnFe(P, Si, B) system. *J. Appl. Phys.* **116**, 63903 (2014), doi:10.1063/1.4892406.
113. Y. Nishihara, Y. Yamaguchi, Magnetic Phase Transitions in Itinerant Electron Magnets Hf 1- x Ta x Fe 2. *J. Phys. Soc. Jpn.* **52**, 3630–3636 (1983), doi:10.1143/JPSJ.52.3630.
114. Radaelli, Cox, Marezio, Cheong, Schiffer, Ramirez, Simultaneous structural, magnetic, and electronic transitions in La1-xCaxMnO3 with x=0.25 and 0.50. *Physical review letters*. **75**, 4488–4491 (1995), doi:10.1103/PhysRevLett.75.4488.
115. A. S. Chernyshov, Y. Mudryk, D. Paudyal, V. K. Pecharsky, K. A. Gschneidner, D. L. Schlagel, T. A. Lograsso, Magnetostructural transition in Gd5Sb0.5Ge3.5. *Phys. Rev. B*. **80** (2009), doi:10.1103/PhysRevB.80.184416.
116. K. Morrison, L. F. Cohen, Overview of the Characteristic Features of the Magnetic Phase Transition with Regards to the Magnetocaloric Effect: the Hidden Relationship Between Hysteresis and Latent Heat. *Metallurgical and Materials Transactions E*. **1**, 153–159 (2014), doi:10.1007/s40553-014-0015-8.
117. A. R. Dinesen, S. Linderoth, S. Mørup, Direct and indirect measurement of the magnetocaloric effect in La 0.67 Ca 0.33− x Sr x MnO 3 ± δ . *J. Phys.: Condens. Matter*. **17**, 6257–6269 (2005), doi:10.1088/0953-8984/17/39/011.
118. V. Provenzano, A. J. Shapiro, R. D. Shull, Reduction of hysteresis losses in the magnetic refrigerant Gd5Ge2Si2 by the addition of iron. *Nature*. **429**, 853–857 (2004), doi:10.1038/nature02657.
119. I. Titov, M. Acet, M. Farle, D. González-Alonso, L. Mañosa, A. Planes, T. Krenke, Hysteresis effects in the inverse magnetocaloric effect in martensitic Ni-Mn-In and Ni-Mn-Sn. *Journal of Applied Physics*. **112**, 73914 (2012), doi:10.1063/1.4757425.
120. L. F. Cohen, Contributions to Hysteresis in Magnetocaloric Materials. *phys. stat. sol. (b)*. **255**, 1700317 (2018), doi:10.1002/pssb.201700317.

121. T. Gottschall, D. Benke, M. Fries, A. Taubel, I. A. Radulov, K. P. Skokov, O. Gutfleisch, A Matter of Size and Stress. *Adv. Funct. Mater.* **27**, 1606735 (2017), doi:10.1002/adfm.201606735.
122. L. Morellon, Z. Arnold, C. Magen, C. Ritter, O. Prokhnenko, Y. Skorokhod, P. A. Algarabel, M. R. Ibarra, J. Kamarad, Pressure enhancement of the giant magnetocaloric effect in Tb5Si2Ge2. *Physical review letters*. **93**, 137201 (2004), doi:10.1103/PhysRevLett.93.137201.
123. K. Morrison, J. D. Moore, K. G. Sandeman, A. D. Caplin, L. F. Cohen, Capturing first- and second-order behavior in magnetocaloric CoMnSi0.92Ge0.08. *Phys. Rev. B*. **79** (2009), doi:10.1103/PhysRevB.79.134408.
124. Y. Takahashi, *Spin fluctuation theory of itinerant electron magnetism* (Springer, Heidelberg, 2013).
125. J. Kusz, S. Juszczyk, J. Warczewski, An X-ray diffraction study of magnetostriction in Zn 1− x Cu x Cr 2 Se 4 (0·2< x <1·0). *J Appl Crystallogr*. **21**, 898–901 (1988), doi:10.1107/S0021889888005151.
126. J. P. Joule, XVII. On the effects of magnetism upon the dimensions of iron and steel bars. *The London, Edinburgh, and Dublin Philosophical Magazine and Journal of Science*. **30**, 76–87 (1847), doi:10.1080/14786444708645656.
127. H. D. Chopra, M. Wuttig, Non-Joulian magnetostriction. *Nature*. **521**, 340–343 (2015), doi:10.1038/nature14459.
128. H. D. Chopra, A. Ravishankar, M. S. Pacifico, M. L. Forst, Non-Joulian Magnetostriction and Non-Joulian Magnetism. *phys. stat. sol. (b)*. **255**, 1800214 (2018), doi:10.1002/pssb.201800214.
129. H. D. Chopra, M. Wuttig, Addendum: Non-Joulian magnetostriction. *Nature*. **538**, 416 (2016), doi:10.1038/nature19064.
130. H. Brooks, Ferromagnetic Anisotropy and the Itinerant Electron Model. *Phys. Rev.* **58**, 909–918 (1940), doi:10.1103/PhysRev.58.909.
131. H. S. Jarrett, W. H. Cloud, R. J. Bouchard, S. R. Butler, C. G. Frederick, J. L. Gillson, Evidence for Itinerant d -Electron Ferromagnetism. *Physical review letters*. **21**, 617–620 (1968), doi:10.1103/PhysRevLett.21.617.
132. Y. Takahashi, T. Moriya, Quantitative Aspects of the Theory of Weak Itinerant Ferromagnetism. *J. Phys. Soc. Jpn.* **54**, 1592–1598 (1985), doi:10.1143/JPSJ.54.1592.
133. T. Moriya, A. Kawabata, Effect of Spin Fluctuations on Itinerant Electron Ferromagnetism. II. *J. Phys. Soc. Jpn.* **35**, 669–676 (1973), doi:10.1143/JPSJ.35.669.
134. Y. Takahashi, Theoretical Development in Itinerant Electron Ferromagnetism. *J. Phys.: Conf. Ser.* **868**, 12002 (2017), doi:10.1088/1742-6596/868/1/012002.
135. Y. Takahashi, On the Origin of the Curie-Weiss Law of the Magnetic Susceptibility in Itinerant Electron Ferromagnetism. *J. Phys. Soc. Jpn.* **55**, 3553–3573 (1986), doi:10.1143/JPSJ.55.3553.
136. E. P. Wohlfarth, Thermodynamic aspects of itinerant electron magnetism. *Physica B+C*. **91**, 305–314 (1977), doi:10.1016/0378-4363(77)90199-1.
137. D. M. Edwards, E. P. Wohlfarth, Magnetic Isotherms in the Band Model of Ferromagnetism. *Proceedings of the Royal Society A: Mathematical, Physical and Engineering Sciences*. **303**, 127–137 (1968), doi:10.1098/rspa.1968.0043.
138. T. Moriya, K. Usami, Magneto-volume effect and invar phenomena in ferromagnetic metals. *Solid State Communications*. **34**, 95–99 (1980), doi:10.1016/0038-1098(80)91241-7.

139. Y. Takahashi, H. Nakano, Magnetovolume effect of itinerant electron ferromagnets. *J. Phys.: Condens. Matter*. **18**, 521–556 (2006), doi:10.1088/0953-8984/18/2/013.
140. H. Wada, H. Nakamura, E. Fukami, K. Yoshimura, M. Shiga, Y. Nakamura, Spin fluctuations of Y(Mn1−xAlx)2 and Y1−xScxMn2. *Journal of Magnetism and Magnetic Materials*. **70**, 17–19 (1987), doi:10.1016/0304-8853(87)90350-7.
141. V. S. Amaral, J. S. Amaral, Magnetoelastic coupling influence on the magnetocaloric effect in ferromagnetic materials. *Journal of Magnetism and Magnetic Materials*. **272-276**, 2104–2105 (2004), doi:10.1016/j.jmmm.2003.12.870.
142. M. Zarifi, P. Kameli, M. Mansouri, H. Ahmadvand, H. Salamati, Magnetocaloric effect and critical behavior in La 0.8-x Pr x Sr 0.2 MnO 3 (x = 0.2, 0.4, 0.5) manganites. *Solid State Communications*. **262**, 20–28 (2017), doi:10.1016/j.ssc.2017.06.007.
143. X. F. Miao, L. Caron, J. Cedervall, P. C. M. Gubbens, P. D. d. Réotier, A. Yaouanc, F. Qian, A. R. Wildes, H. Luetkens, A. Amato, N. H. van Dijk, E. Brück, Short-range magnetic correlations and spin dynamics in the paramagnetic regime of (Mn,Fe)2(P,Si). *Phys. Rev. B*. **94**, 14426 (2016), doi:10.1103/PhysRevB.94.014426.
144. X. F. Miao, L. Caron, P. Gubbens, A. Yaouanc, P. Dalmas de Réotier, H. Luetkens, A. Amato, N. H. van Dijk, E. Brück, Spin correlations in (Mn,Fe)2(P,Si) magnetocaloric compounds above Curie temperature. *Journal of Science: Advanced Materials and Devices*. **1**, 147–151 (2016), doi:10.1016/j.jsamd.2016.06.002.
145. T. Kanomata, T. Sasaki, H. Nishihara, H. Yoshida, T. Kaneko, S. Hane, T. Goto, N. Takeishi, S. Ishida, Magnetic properties of ferromagnetic Heusler alloy Co2ZrAl. *Journal of Alloys and Compounds*. **393**, 26–33 (2005), doi:10.1016/j.jallcom.2004.09.071.
146. I. Shigeta, Y. Fujimoto, R. Ooka, Y. Nishisako, M. Tsujikawa, R. Y. Umetsu, A. Nomura, K. Yubuta, Y. Miura, T. Kanomata, M. Shirai, J. Gouchi, Y. Uwatoko, M. Hiroi, Pressure effect on the magnetic properties of the half-metallic Heusler alloy Co2TiSn. *Phys. Rev. B*. **97** (2018), doi:10.1103/PhysRevB.97.104414.
147. T. Sakon, Y. Yamasaki, H. Kodama, T. Kanomata, H. Nojiri, Y. Adachi, The Characteristic Properties of Magnetostriction and Magneto-Volume Effects of Ni2MnGa-Type Ferromagnetic Heusler Alloys. *Materials (Basel, Switzerland)*. **12** (2019), doi:10.3390/ma12223655.
148. G. Krauss, Martensite in steel: strength and structure. *Materials Science and Engineering: A*. **273-275**, 40–57 (1999), doi:10.1016/S0921-5093(99)00288-9.
149. S. K. Park, Y. Diao, Martensitic transition in molecular crystals for dynamic functional materials. *Chemical Society reviews*. **49**, 8287–8314 (2020), doi:10.1039/d0cs00638f.
150. V. Soolshenko, N. Lanska, K. Ullakko, Structure and twinning stress of martensites in non-stoichiometric Ni 2 MnGa single crystal. *J. Phys. IV France*. **112**, 947–950 (2003), doi:10.1051/jp4:20031037.
151. H. Maeda, T. Fukuda, T. Kakeshita, Effect of hydrostatic pressure on martensitic transformation in a ferromagnetic shape memory alloy Ni2MnGa. *Journal of Alloys and Compounds*. **509**, 7840–7843 (2011), doi:10.1016/j.jallcom.2011.05.039.
152. I. Takeuchi, O. O. Famodu, J. C. Read, M. A. Aronova, K.-S. Chang, C. Craciunescu, S. E. Lofland, M. Wuttig, F. C. Wellstood, L. Knauss, A. Orozco, Identification of novel compositions of ferromagnetic shape-memory alloys using composition spreads. *Nature materials*. **2**, 180–184 (2003), doi:10.1038/nmat829.
153. P. Entel, V. D. Buchelnikov, M. E. Gruner, A. Hucht, V. V. Khovailo, S. K. Nayak, A. T. Zayak, Shape Memory Alloys. *MSF*. **583**, 21–41 (2008), doi:10.4028/www.scientific.net/MSF.583.21.

154. A. T. Zayak, P. Entel, K. M. Rabe, W. A. Adeagbo, M. Acet, Anomalous vibrational effects in nonmagnetic and magnetic Heusler alloys. *Phys. Rev. B*. **72** (2005), doi:10.1103/PhysRevB.72.054113.
155. M. A. Azeem, D. Dye, Lattice instability during the martensitic transformation in the high temperature shape memory alloy Zr(Cu0.5Co0.25Ni0.25). *Journal of Alloys and Compounds*. **618**, 469–474 (2015), doi:10.1016/j.jallcom.2014.08.141.
156. S. M. Shapiro, P. Vorderwisch, K. Habicht, K. Hradil, H. Schneider, Observation of phasons in the magnetic shape memory alloy Ni 2 MnGa. *Europhys. Lett.* **77**, 56004 (2007), doi:10.1209/0295-5075/77/56004.
157. M. E. Gruner, R. Niemann, P. Entel, R. Pentcheva, U. K. Rößler, K. Nielsch, S. Fähler, Modulations in martensitic Heusler alloys originate from nanotwin ordering. *Scientific reports*. **8**, 8489 (2018), doi:10.1038/s41598-018-26652-6.
158. M. K. Chattopadhyay, S. B. Roy, P. Chaddah, Kinetic arrest of the first-order ferromagnetic-to-antiferromagnetic transition in Ce(Fe0.96Ru0.04)2 : Formation of a magnetic glass. *Phys. Rev. B*. **72** (2005), doi:10.1103/PhysRevB.72.180401.
159. W. Ito, K. Ito, R. Y. Umetsu, R. Kainuma, K. Koyama, K. Watanabe, A. Fujita, K. Oikawa, K. Ishida, T. Kanomata, Kinetic arrest of martensitic transformation in the NiCoMnIn metamagnetic shape memory alloy. *Appl. Phys. Lett.* **92**, 21908 (2008), doi:10.1063/1.2833699.
160. A. Tekgül, M. Acet, M. Farle, N. Ünal, Kinetic arrest of the ferrimagnetic state in indium-doped Mn1.82Co0.18Sb. *Journal of Alloys and Compounds*. **695**, 418–425 (2017), doi:10.1016/j.jallcom.2016.11.093.
161. D. J. Keavney, Y. Choi, M. V. Holt, V. Uhlíř, D. Arena, E. E. Fullerton, P. J. Ryan, J.-W. Kim, Phase Coexistence and Kinetic Arrest in the Magnetostructural Transition of the Ordered Alloy FeRh. *Scientific reports*. **8**, 1778 (2018), doi:10.1038/s41598-018-20101-0.
162. N. M. Bruno, D. Salas, S. Wang, I. V. Roshchin, R. Santamarta, R. Arroyave, T. Duong, Y. I. Chumlyakov, I. Karaman, On the microstructural origins of martensitic transformation arrest in a NiCoMnIn magnetic shape memory alloy. *Acta Materialia*. **142**, 95–106 (2018), doi:10.1016/j.actamat.2017.08.037.
163. J. W. Edwards, R. Speiser, H. L. Johnston, High Temperature Structure and Thermal Expansion of Some Metals as Determined by X-Ray Diffraction Data. I. Platinum, Tantalum, Niobium, and Molybdenum. *J. Appl. Phys.* **22**, 424–428 (1951), doi:10.1063/1.1699977.
164. G. Teufer, The crystal structure of tetragonal ZrO2. *Acta Cryst*. **15**, 1187 (1962), doi:10.1107/S0365110X62003114.
165. K. KURIBAYASHI, M. YOSHIMURA, T. OHTA, T. SATA, High-Temperature Phase Relations in the System Y2O3-Y2O3.WO3. *J American Ceramic Society*. **63**, 644–647 (1980), doi:10.1111/j.1151-2916.1980.tb09853.x.
166. U. Benedict, C. Dufour, K. Mayne, Low temperature XRD study of actinide metals and compounds. *J. Phys. Colloques*. **40**, C4-103-C4-105 (1979), doi:10.1051/jphyscol:1979432.
167. C.-J. Chang, Y. Zhu, J. Wang, H.-C. Chen, C.-W. Tung, Y.-C. Chu, H. M. Chen, In situ X-ray diffraction and X-ray absorption spectroscopy of electrocatalysts for energy conversion reactions. *J. Mater. Chem. A*. **8**, 19079–19112 (2020), doi:10.1039/D0TA06656G.
168. A. D. Katsenis, A. Puškarić, V. Štrukil, C. Mottillo, P. A. Julien, K. Užarević, M.-H. Pham, T.-O. Do, S. A. J. Kimber, P. Lazić, O. Magdysyuk, R. E. Dinnebier, I. Halasz, T. Friščić, In situ X-ray diffraction monitoring of a mechanochemical reaction reveals a unique topology metal-organic framework. *Nature communications*. **6**, 6662 (2015), doi:10.1038/ncomms7662.

169. P. J. Chupas, M. F. Ciraolo, J. C. Hanson, C. P. Grey, In situ X-ray diffraction and solid-state NMR study of the fluorination of gamma-Al(2)O(3) with HCF(2)Cl. *Journal of the American Chemical Society*. **123**, 1694–1702 (2001), doi:10.1021/ja0032374.
170. C. Aparicio, J. Filip, L. Machala, From Prussian blue to iron carbides: high-temperature XRD monitoring of thermal transformation under inert gases. *Powder Diffr.* **32**, S207-S212 (2017), doi:10.1017/S0885715617000471.
171. I. A. Courtney, J. R. Dahn, Electrochemical and In Situ X-Ray Diffraction Studies of the Reaction of Lithium with Tin Oxide Composites. *J. Electrochem. Soc.* **144**, 2045–2052 (1997), doi:10.1149/1.1837740.
172. N. A. Cañas, P. Einsiedel, O. T. Freitag, C. Heim, M. Steinhauer, D.-W. Park, K. A. Friedrich, Operando X-ray diffraction during battery cycling at elevated temperatures: A quantitative analysis of lithium-graphite intercalation compounds. *Carbon*. **116**, 255–263 (2017), doi:10.1016/j.carbon.2017.02.002.
173. W. Zhu, D. Liu, A. Paolella, C. Gagnon, V. Gariépy, A. Vijh, K. Zaghib, Application of Operando X-ray Diffraction and Raman Spectroscopies in Elucidating the Behavior of Cathode in Lithium-Ion Batteries. *Front. Energy Res.* **6** (2018), doi:10.3389/fenrg.2018.00066.
174. S.-M. Bak, Z. Shadike, R. Lin, X. Yu, X.-Q. Yang, In situ/operando synchrotron-based X-ray techniques for lithium-ion battery research. *NPG Asia Mater*. **10**, 563–580 (2018), doi:10.1038/s41427-018-0056-z.
175. G. Marra, G. Artioli, A. Fitch, M. Milanesio, C. Lamberti, Orthorhombic to monoclinic phase transition in high-Ti-loaded TS-1: an attempt to locate Ti in the MFI framework by low temperature XRD. *Microporous and Mesoporous Materials*. **40**, 85–94 (2000), doi:10.1016/S1387-1811(00)00244-4.
176. N. Narayanan, A. Senyshyn, D. Mikhailova, T. Faske, T. Lu, Z. Liu, B. Weise, H. Ehrenberg, R. A. Mole, W. D. Hutchison, H. Fuess, G. J. McIntyre, Y. Liu, D. Yu, Magnetic structure and spin correlations in magnetoelectric honeycomb Mn4Ta2O9. *Phys. Rev. B*. **98**, 628 (2018), doi:10.1103/PhysRevB.98.134438.
177. H. C. Wu, P. J. Sun, D. J. Hsieh, H. J. Chen, D. C. Kakarla, L. Z. Deng, C. W. Chu, H. D. Yang, Observation of skyrmion-like magnetism in magnetic Weyl semimetal Co3Sn2S2. *Materials Today Physics*. **12**, 100189 (2020), doi:10.1016/j.mtphys.2020.100189.
178. M. Hirschberger, T. Nakajima, S. Gao, L. Peng, A. Kikkawa, T. Kurumaji, M. Kriener, Y. Yamasaki, H. Sagayama, H. Nakao, K. Ohishi, K. Kakurai, Y. Taguchi, X. Yu, T.-H. Arima, Y. Tokura, Skyrmion phase and competing magnetic orders on a breathing kagomé lattice. *Nature communications*. **10**, 5831 (2019), doi:10.1038/s41467-019-13675-4.
179. H. C. Wu, T. Y. Wei, K. D. Chandrasekhar, T. Y. Chen, H. Berger, H. D. Yang, Unexpected observation of splitting of skyrmion phase in Zn doped Cu2OSeO3. *Scientific reports*. **5**, 13579 (2015), doi:10.1038/srep13579.
180. S. Das, Y. L. Tang, Z. Hong, M. A. P. Gonçalves, M. R. McCarter, C. Klewe, K. X. Nguyen, F. Gómez-Ortiz, P. Shafer, E. Arenholz, V. A. Stoica, S.-L. Hsu, B. Wang, C. Ophus, J. F. Liu, C. T. Nelson, S. Saremi, B. Prasad, A. B. Mei, D. G. Schlom, J. Íñiguez, P. García-Fernández, D. A. Muller, L. Q. Chen, J. Junquera, L. W. Martin, R. Ramesh, Observation of room-temperature polar skyrmions. *Nature*. **568**, 368–372 (2019), doi:10.1038/s41586-019-1092-8.
181. J. Cedervall, M. S. Andersson, T. Sarkar, E. K. Delczeg-Czirjak, L. Bergqvist, T. C. Hansen, P. Beran, P. Nordblad, M. Sahlberg, Magnetic structure of the magnetocaloric compound

AlFe 2 B 2. *Journal of Alloys and Compounds*. **664**, 784–791 (2016), doi:10.1016/j.jallcom.2015.12.111.
182. M. E. Gruner, S. Fähler, P. Entel, Magnetoelastic coupling and the formation of adaptive martensite in magnetic shape memory alloys. *phys. stat. sol. (b)*. **251**, 2067–2079 (2014), doi:10.1002/pssb.201350397.
183. M. E. Gruner, W. Keune, J. Landers, S. Salamon, M. Krautz, J. Zhao, M. Y. Hu, T. Toellner, E. E. Alp, O. Gutfleisch, H. Wende, Moment-Volume Coupling in La(Fe 1 −x Si x) 13. *phys. stat. sol. (b)*. **255**, 1700465 (2018), doi:10.1002/pssb.201700465.
184. Z. W. Ouyang, Y. H. Matsuda, H. Nojiri, T. Inami, K. Ohwada, M. Tsubota, T. Sakon, T. Fukuda, T. Kakeshita, Direct observation of field-induced variant transformation in Fe3Pt using pulsed magnetic field x-ray diffraction. *J. Appl. Phys.* **102**, 113917 (2007), doi:10.1063/1.2822278.
185. S. Sharma, A. E. Kovalev, D. J. Rebar, D. Mann, V. Yannello, M. Shatruk, A. V. Suslov, J. H. Smith, T. Siegrist, Magnetostriction of AlFe2B2 in high magnetic fields. *Phys. Rev. Materials*. **5** (2021), doi:10.1103/PhysRevMaterials.5.064409.
186. E. Arakawa, K. Maruyama, K. Mori, H. Nishigaitsu, N. Aizawa, Magnetostriction observed by X-ray diffraction in iron. *IEEE Trans. Magn.* **41**, 3718–3720 (2005), doi:10.1109/TMAG.2005.854922.
187. F. Yokaichiya, A. Krimmel, V. Tsurkan, I. Margiolaki, P. Thompson, H. N. Bordallo, A. Buchsteiner, N. Stüßer, D. N. Argyriou, A. Loidl, Spin-driven phase transitions in ZnCr2Se4 and ZnCr2S4 probed by high-resolution synchrotron x-ray and neutron powder diffraction. *Phys. Rev. B*. **79** (2009), doi:10.1103/PhysRevB.79.064423.
188. Y. Narumi, K. Katsumata, Y. Tanaka, T. Nakamura, S. Shimomura, Y. Tabata, S. Kimura, M. Matsuda, Synchrotron X-ray diffraction studies on magnetic materials in high magnetic fields. *Physica B: Condensed Matter*. **346-347**, 11–14 (2004), doi:10.1016/j.physb.2004.01.011.
189. J. Potticary, M. P. Avery, D. Mills, S. R. Hall, DONALD: A 2.5 T wide sample space permanent magnet. *HardwareX*. **3**, 39–48 (2018), doi:10.1016/j.ohx.2018.01.002.
190. T. J. Sumner, J. M. Pendlebury, K. F. Smith, Convectional magnetic shielding. *J. Phys. D: Appl. Phys.* **20**, 1095–1101 (1987), doi:10.1088/0022-3727/20/9/001.
191. K. D. M. Harris, M. Tremayne, B. M. Kariuki, Contemporary Advances in the Use of Powder X-Ray Diffraction for Structure Determination. *Angew. Chem. Int. Ed.* **40**, 1626–1651 (2001), doi:10.1002/1521-3773(20010504)40:9<1626::AID-ANIE16260>3.0.CO;2-7.
192. S. Vortmann, J. Rius, S. Siegmann, H. Gies, Ab Initio Structure Solution from X-ray Powder Data at Moderate Resolution: Crystal Structure of a Microporous Layer Silicate. *J. Phys. Chem. B*. **101**, 1292–1297 (1997), doi:10.1021/jp962162g.
193. S. G. Zhukov, V. V. Chernyshev, E. V. Babaev, E. J. Sonneveld, H. Schenk, Application of simulated annealing approach for structure solution of molecular crystals from X-ray laboratory powder data. *Zeitschrift für Kristallographie - Crystalline Materials*. **216**, 5–9 (2001), doi:10.1524/zkri.216.1.5.18998.
194. P. Sanphui, G. Bolla, A. Nangia, V. Chernyshev, Acemetacin cocrystals and salts: structure solution from powder X-ray data and form selection of the piperazine salt. *IUCrJ*. **1**, 136–150 (2014), doi:10.1107/S2052252514004229.
195. K. Ufer, H. Stanjek, G. Roth, R. Dohrmann, R. Kleeberg, S. Kaufhold, Quantitative phase analysis of bentonites by the Rietveld method. *Clays Clay Miner.* **56**, 272–282 (2008), doi:10.1346/CCMN.2008.0560210.

196. G. Le Saoût, V. Kocaba, K. Scrivener, Application of the Rietveld method to the analysis of anhydrous cement. *Cement and Concrete Research*. **41**, 133–148 (2011), doi:10.1016/j.cemconres.2010.10.003.
197. L. Lutterotti, H. Pillière, C. Fontugne, P. Boullay, D. Chateigner, Full-profile search-match by the Rietveld method. *J Appl Crystallogr*. **52**, 587–598 (2019), doi:10.1107/S160057671900342X.
198. H. M. Rietveld, A profile refinement method for nuclear and magnetic structures. *J Appl Crystallogr*. **2**, 65–71 (1969), doi:10.1107/S0021889869006558.
199. J. G. M. van Berkum, G. J. M. Sprong, T. H. de Keijser, R. Delhez, E. J. Sonneveld, The optimum standard specimen for X-ray diffraction line-profile analysis. *Powder Diffr.* **10**, 129–139 (1995), doi:10.1017/S0885715600014512.
200. Y. H. Matsuda, Y. Kakita, F. Iga, The Temperature Dependence of the Magnetization Process of the Kondo Insulator YbB12. *Crystals*. **10**, 26 (2020), doi:10.3390/cryst10010026.
201. O. Young, G. Balakrishnan, P. Manuel, D. Khalyavin, A. Wildes, O. Petrenko, Field-Induced Transitions in Highly Frustrated SrHo2O4. *Crystals*. **9**, 488 (2019), doi:10.3390/cryst9100488.
202. C. Dong, R. Chen, Y. Liu, C. Liu, H. Zhu, J. Ke, W. Liu, M. Yang, J. Wang, Field-Induced Magnetic Phase Transitions and Rich Phase Diagram of HoMnO3 Single Crystal. *Crystals*. **9**, 419 (2019), doi:10.3390/cryst9080419.
203. H. S. Nair, K. R. Kumar, B. Sahu, S. P. Xhakaza, P. Mishra, D. Samal, S. K. Ghosh, B. R. Sekhar, A. M. Strydom, Field-Independent Features in the Magnetization and Specific Heat of Sm3Co4Ge13. *Crystals*. **9**, 322 (2019), doi:10.3390/cryst9060322.
204. J. Kusz, H. Böhm, E. Talik, X-ray investigation and discussion of the magnetostriction of Gd 3T (T = Ni, Rh, Ir x) single crystals. *J Appl Crystallogr*. **33**, 213–217 (2000), doi:10.1107/S0021889899014922.
205. M.-Y. Zeng, Q. Tang, Z.-W. Mei, C.-Y. Lu, Y.-M. Tang, X. Li, Y. He, Z.-P. Guo, Magnetostriction and spin reorientation in ferromagnetic Laves phase Pr(Ga x Fe 1–x) 1.9 compounds*. *Chinese Phys. B*. **30**, 67504 (2021), doi:10.1088/1674-1056/abe1a3.
206. K. Tajima, N. Suzuki, K. Oguchi, Superconducting Electromagnet for X-Ray Diffraction. *Jpn. J. Appl. Phys.* **29**, 986–987 (1990), doi:10.1143/JJAP.29.986.
207. F. Guillou, H. Yibole, Z. Q. Ou, E. Brück, O. Tegus, Large recalescence-like event at the first cooling across the magnetic transition of (Mn,Fe)2(P,Si) magnetocaloric materials. *Scripta Materialia*. **160**, 81–85 (2019), doi:10.1016/j.scriptamat.2018.10.002.
208. E. Brück, Developments in magnetocaloric refrigeration. *J. Phys. D: Appl. Phys.* **38**, R381-R391 (2005), doi:10.1088/0022-3727/38/23/R01.
209. W. Hanggai, O. Tegus, H. Yibole, F. Guillou, Structural and magnetic phase diagrams of MnFe0.6Ni0.4(Si,Ge) alloys and their giant magnetocaloric effect probed by heat capacity measurements. *Journal of Magnetism and Magnetic Materials*. **494**, 165785 (2020), doi:10.1016/j.jmmm.2019.165785.
210. S. T. Anderson, Economics, Helium, and the U.S. Federal Helium Reserve: Summary and Outlook. *Nat Resour Res*. **27**, 455–477 (2018), doi:10.1007/s11053-017-9359-y.
211. S. Nakagawa, Y. Mitsui, R. Kobayashi, R. Y. Umetsu, K. Takahashi, K. Koyama, Magnetic-field-induced decomposition in Cu2MnAl Heusler alloys. *Journal of Magnetism and Magnetic Materials*. **540**, 168411 (2021), doi:10.1016/j.jmmm.2021.168411.
212. R. Santamarta, J. Font, J. Muntasell, F. Masdeu, J. Pons, E. Cesari, J. Dutkiewicz, Effect of ageing on the martensitic transformation of Ni–Fe–Ga alloys. *Scripta Materialia*. **54**, 1105–1109 (2006), doi:10.1016/j.scriptamat.2005.11.062.

213. A. Bergamaschi, A. Cervellino, R. Dinapoli, F. Gozzo, B. Henrich, I. Johnson, P. Kraft, A. Mozzanica, B. Schmitt, X. Shi, The MYTHEN detector for X-ray powder diffraction experiments at the Swiss Light Source. *Journal of synchrotron radiation*. **17**, 653–668 (2010), doi:10.1107/S0909049510026051.
214. H. W. King, E. A. Payzant, An Experimental Examination of Error Functions for Bragg-Brentano Powder Diffractometry. *Adv. x-ray anal.* **36**, 663–670 (1992), doi:10.1154/S0376030800019327.
215. F. Bai, N. Wang, J. Li, D. Viehland, P. M. Gehring, G. Xu, G. Shirane, X-ray and neutron diffraction investigations of the structural phase transformation sequence under electric field in 0.7Pb(Mg1⁄3Nb2⁄3)-0.3PbTiO3 crystal. *J. Appl. Phys.* **96**, 1620–1627 (2004), doi:10.1063/1.1766087.
216. M. Knapp, V. Joco, C. Baehtz, H. Brecht, A. Berghaeuser, H. Ehrenberg, H. von Seggern, H. Fuess, Position-sensitive detector system OBI for High Resolution X-Ray Powder Diffraction using on-site readable image plates. *Nuclear Instruments and Methods in Physics Research Section A: Accelerators, Spectrometers, Detectors and Associated Equipment*. **521**, 565–570 (2004), doi:10.1016/j.nima.2003.10.100.
217. G. Swislow, *SPEC, Software for Diffraction* (certified scientific software, 2017).
218. DECTRIS Ltd., *DECTRIS MYTHEN2 User Manual* (2021) (available at https://media.dectris.com/210127-User_Manual-DECTRIS_MYTHEN2.pdf).
219. A. Terwey, M. E. Gruner, W. Keune, J. Landers, S. Salamon, B. Eggert, K. Ollefs, V. Brabänder, I. Radulov, K. Skokov, T. Faske, M. Y. Hu, J. Zhao, E. E. Alp, C. Giacobbe, O. Gutfleisch, H. Wende, Influence of hydrogenation on the vibrational density of states of magnetocaloric LaFe11.4Si1.6H1.6. *Phys. Rev. B.* **101** (2020), doi:10.1103/PhysRevB.101.064415.
220. T. Hashimoto, T. Numasawa, M. Shino, T. Okada, Magnetic refrigeration in the temperature range from 10 K to room temperature. *Cryogenics*. **21**, 647–653 (1981), doi:10.1016/0011-2275(81)90254-X.
221. V. K. Pecharsky, K. A. Gschneidner Jr, Magnetocaloric effect and magnetic refrigeration. *Journal of Magnetism and Magnetic Materials*. **200**, 44–56 (1999), doi:10.1016/S0304-8853(99)00397-2.
222. B. Yu, Q. Gao, B. Zhang, X. Meng, Z. Chen, Review on research of room temperature magnetic refrigeration. *International Journal of Refrigeration*. **26**, 622–636 (2003), doi:10.1016/S0140-7007(03)00048-3.
223. L. Mañosa, A. Planes, M. Acet, Advanced materials for solid-state refrigeration. *J. Mater. Chem. A*. **1**, 4925 (2013), doi:10.1039/c3ta01289a.
224. J. Romero Gómez, R. Ferreiro Garcia, A. de Miguel Catoira, M. Romero Gómez, Magnetocaloric effect. *Renewable and Sustainable Energy Reviews*. **17**, 74–82 (2013), doi:10.1016/j.rser.2012.09.027.
225. F. Wang, G. Wang, F. Hu, A. Kurbakov, B. Shen, Z. Cheng, Strong interplay between structure and magnetism in the giant magnetocaloric intermetallic compound LaFe 11.4 Si 1.6. *Journal of physics. Condensed matter : an Institute of Physics journal*. **15**, 5269–5278 (2003), doi:10.1088/0953-8984/15/30/309.
226. T. Krenke, E. Duman, M. Acet, E. F. Wassermann, X. Moya, L. Mañosa, A. Planes, E. Suard, B. Ouladdiaf, Magnetic superelasticity and inverse magnetocaloric effect in Ni-Mn-In. *Phys. Rev. B*. **75** (2007), doi:10.1103/PhysRevB.75.104414.

227. S. Singh, J. Bednarcik, S. R. Barman, C. Felser, D. Pandey, Premartensite to martensite transition and its implications for the origin of modulation in Ni2MnGa ferromagnetic shape-memory alloy. *Phys. Rev. B*. **92** (2015), doi:10.1103/PhysRevB.92.054112.
228. D. M. Pooke, V. Chamritski, M. Fee, S. Gibson, B. T. King, J. L. Tallon, M. Meissner, R. Feyerherm, S. R. Olsen, S. J. Kennedy, R. A. Robinson, HTS 5 Tesla Synchrotron and Neutron Beamline Magnets. *IEEE Trans. Appl. Supercond.* **19**, 1372–1375 (2009), doi:10.1109/TASC.2009.2018806.
229. X. Moya, L. Mañosa, A. Planes, T. Krenke, M. Acet, E. F. Wassermann, Martensitic transition and magnetic properties in Ni–Mn–X alloys. *Materials Science and Engineering: A*. **438-440**, 911–915 (2006), doi:10.1016/j.msea.2006.02.053.
230. J. Pons, V. A. Chernenko, R. Santamarta, E. Cesari, Crystal structure of martensitic phases in Ni–Mn–Ga shape memory alloys. *Acta Materialia*. **48**, 3027–3038 (2000), doi:10.1016/S1359-6454(00)00130-0.
231. L. RIGHI, F. ALBERTINI, L. PARETI, A. PAOLUZI, G. CALESTANI, Commensurate and incommensurate “5M” modulated crystal structures in Ni–Mn–Ga martensitic phases. *Acta Materialia*. **55**, 5237–5245 (2007), doi:10.1016/j.actamat.2007.05.040.
232. L. Righi, F. Albertini, S. Fabbrici, A. Paoluzi, Crystal Structures of Modulated Martensitic Phases of FSM Heusler Alloys. *MSF*. **684**, 105–116 (2011), doi:10.4028/www.scientific.net/MSF.684.105.
233. L. RIGHI, F. ALBERTINI, E. Villa, A. PAOLUZI, G. CALESTANI, V. Chernenko, S. Besseghini, C. Ritter, F. Passaretti, Crystal structure of 7M modulated Ni–Mn–Ga martensitic phase. *Acta Materialia*. **56**, 4529–4535 (2008), doi:10.1016/j.actamat.2008.05.010.
234. A. Sozinov, A. A. Likhachev, N. Lanska, K. Ullakko, Giant magnetic-field-induced strain in NiMnGa seven-layered martensitic phase. *Appl. Phys. Lett.* **80**, 1746–1748 (2002), doi:10.1063/1.1458075.
235. V. Petříček, M. Dušek, J. Plášil, Crystallographic computing system Jana2006. *Zeitschrift für Kristallographie - Crystalline Materials*. **231** (2016), doi:10.1515/zkri-2016-1956.
236. A. Fujita, S. Fujieda, K. Fukamichi, H. Mitamura, T. Goto, Itinerant-electron metamagnetic transition and large magnetovolume effects in La(FexSi1−x)13 compounds. *Phys. Rev. B*. **65**, 131 (2001), doi:10.1103/PhysRevB.65.014410.
237. J. Rodríguez-Carvajal, Recent advances in magnetic structure determination by neutron powder diffraction. *Physica B: Condensed Matter*. **192**, 55–69 (1993), doi:10.1016/0921-4526(93)90108-I.
238. H. P. Klug, L. E. Alexander, *X-ray Diffraction Procedures for Polycrystalline and Amorphous Materials* (Wiley-Interscience, S.l., ed. 2, 1974).
239. V. K. Sharma, M. K. Chattopadhyay, S. B. Roy, Kinetic arrest of the first order austenite to martensite phase transition in Ni50Mn34In16. *Phys. Rev. B*. **76** (2007), doi:10.1103/PhysRevB.76.140401.
240. K. Momma, F. Izumi, VESTA 3 for three-dimensional visualization of crystal, volumetric and morphology data. *J Appl Crystallogr*. **44**, 1272–1276 (2011), doi:10.1107/S0021889811038970.
241. V. Franco, J. Y. Law, A. Conde, V. Brabander, D. Y. Karpenkov, I. Radulov, K. Skokov, O. Gutfleisch, Predicting the tricritical point composition of a series of LaFeSi magnetocaloric alloys via universal scaling. *J. Phys. D: Appl. Phys.* **50**, 414004 (2017), doi:10.1088/1361-6463/aa8792.

242. M. F. J. Boeije, M. Maschek, X. F. Miao, N. V. Thang, N. H. van Dijk, E. Brück, Mixed magnetism in magnetocaloric materials with first-order and second-order magnetoelastic transitions. *J. Phys. D: Appl. Phys.* **50**, 174002 (2017), doi:10.1088/1361-6463/aa5db9.
243. J. Y. Law, V. Franco, L. M. Moreno-Ramírez, A. Conde, D. Y. Karpenkov, I. Radulov, K. P. Skokov, O. Gutfleisch, A quantitative criterion for determining the order of magnetic phase transitions using the magnetocaloric effect. *Nature communications*. **9**, 2680 (2018), doi:10.1038/s41467-018-05111-w.
244. L. M. Moreno-Ramírez, J. S. Blázquez, I. A. Radulov, K. P. Skokov, O. Gutfleisch, V. Franco, A. Conde, Combined kinetic and Bean–Rodbell approach for describing field-induced transitions in LaFe 11.6 Si 1.4 alloys. *J. Phys. D: Appl. Phys.* **54**, 135003 (2021), doi:10.1088/1361-6463/abd583.
245. M. Janoschek, M. Garst, A. Bauer, P. Krautscheid, R. Georgii, P. Böni, C. Pfleiderer, Fluctuation-induced first-order phase transition in Dzyaloshinskii-Moriya helimagnets. *Phys. Rev. B*. **87** (2013), doi:10.1103/PhysRevB.87.134407.
246. O. Cépas, A. P. Young, B. S. Shastry, Degeneracy and strong fluctuation-induced first-order phase transition in the dipolar pyrochlore antiferromagnet. *Phys. Rev. B*. **72** (2005), doi:10.1103/PhysRevB.72.184408.
247. N. Biniskos, K. Schmalzl, S. Raymond, S. Petit, P. Steffens, J. Persson, T. Brückel, Spin Fluctuations Drive the Inverse Magnetocaloric Effect in Mn_{5}Si_{3}. *Physical review letters*. **120**, 257205 (2018), doi:10.1103/PhysRevLett.120.257205.
248. Z. Zhang, H. Zhou, R. Mole, C. Yu, Z. Zhang, X. Zhao, W. Ren, D. Yu, B. Li, F. Hu, B. Shen, Z. Zhang, Intense ferromagnetic fluctuations preceding magnetoelastic first-order transitions in giant magnetocaloric LaFe13−xSix. *Phys. Rev. Materials*. **5** (2021), doi:10.1103/PhysRevMaterials.5.L071401.
249. K. A. Gschneidner, V. K. Pecharsky, Magnetic refrigeration materials (invited). *Journal of Applied Physics*. **85**, 5365–5368 (1999), doi:10.1063/1.369979.
250. V. K. Pecharsky, K. A. Gschneidner, Some common misconceptions concerning magnetic refrigerant materials. *J. Appl. Phys.* **90**, 4614–4622 (2001), doi:10.1063/1.1405836.
251. H. Yamada, Metamagnetic transition and susceptibility maximum in an itinerant-electron system. *Phys. Rev. B*. **47**, 11211–11219 (1993), doi:10.1103/PhysRevB.47.11211.
252. A. Fujita, Y. Akamatsu, K. Fukamichi, Itinerant electron metamagnetic transition in La(FexSi1−x)13 intermetallic compounds. *Journal of Applied Physics*. **85**, 4756–4758 (1999), doi:10.1063/1.370471.
253. L. Jia, G. J. Liu, J. R. Sun, H. W. Zhang, F. X. Hu, C. Dong, G. H. Rao, B. G. Shen, Entropy changes associated with the first-order magnetic transition in LaFe13−xSix. *Journal of Applied Physics*. **100**, 123904 (2006), doi:10.1063/1.2404468.
254. A. Fujita, H. Yako, Stability of metallic, magnetic and electronic states in NaZn13-type La(FexSi1−x)13 magnetocaloric compounds. *Scripta Materialia*. **67**, 578–583 (2012), doi:10.1016/j.scriptamat.2012.03.033.
255. M. Rosca, M. Balli, D. Fruchart, D. Gignoux, E. K. Hlil, S. Miraglia, B. Ouladdiaf, P. Wolfers, Neutron diffraction study of LaFe11.31Si1.69 and LaFe11.31Si1.69H1.45 compounds. *Journal of Alloys and Compounds*. **490**, 50–55 (2010), doi:10.1016/j.jallcom.2009.10.093.
256. A. Fujita, Relation between paramagnetic entropy and disordered local moment in La(Fe 0.88 Si 0.12) 13 magnetocaloric compound. *APL Materials*. **4**, 64108 (2016), doi:10.1063/1.4953434.

257. T. Palstra, J. A. Mydosh, G. J. Nieuwenhuys, A. M. van der Kraan, K. Buschow, Study of the critical behaviour of the magnetization and electrical resistivity in cubic La(Fe, Si)13 compounds. *Journal of Magnetism and Magnetic Materials*. **36**, 290–296 (1983), doi:10.1016/0304-8853(83)90128-2.
258. A. Fujita, K. Fukamichi, M. Yamada, T. Goto, Pressure-induced anomalies in itinerant-electron metamagnetic properties around the critical end point in La(Fe0.89Si0.11)13. *Phys. Rev. B*. **73**, 167 (2006), doi:10.1103/PhysRevB.73.104420.
259. A. Fujita, H. Yako, M. Kano, Contribution of paramagnetic entropy to magnetocaloric effect in La(Fe x Si 1−x) 13. *Journal of Applied Physics*. **113**, 17A924 (2013), doi:10.1063/1.4796191.
260. C. P. Bean, D. S. Rodbell, Magnetic Disorder as a First-Order Phase Transformation. *Phys. Rev.* **126**, 104–115 (1962), doi:10.1103/PhysRev.126.104.
261. D. Wagner, E. P. Wohlfarth, Arrott plots of magnetic systems with strong spin fluctuations. *Physics Letters A*. **118**, 29–31 (1986), doi:10.1016/0375-9601(86)90529-3.
262. P. Mohn, D. Wagner, E. P. Wohlfarth, Magnetoelastic anomalies due to spin fluctuations in weakly itinerant ferromagnetic systems. *J. Phys. F: Met. Phys.* **17**, L13-L18 (1987), doi:10.1088/0305-4608/17/1/003.
263. G. L. Squires, *Introduction to the theory of thermal neutron scattering* (Cambridge University Press, Cambridge, ed. 3, 2012).
264. M. Krautz, K. Skokov, T. Gottschall, C. S. Teixeira, A. Waske, J. Liu, L. Schultz, O. Gutfleisch, Systematic investigation of Mn substituted La(Fe,Si)13 alloys and their hydrides for room-temperature magnetocaloric application. *Journal of Alloys and Compounds*. **598**, 27–32 (2014), doi:10.1016/j.jallcom.2014.02.015.
265. M. Hoelzel, A. Senyshyn, N. Juenke, H. Boysen, W. Schmahl, H. Fuess, High-resolution neutron powder diffractometer SPODI at research reactor FRM II. *Nuclear Instruments and Methods in Physics Research Section A: Accelerators, Spectrometers, Detectors and Associated Equipment*. **667**, 32–37 (2012), doi:10.1016/j.nima.2011.11.070.
266. S. Fujieda, A. Fujita, K. Fukamichi, Y. Yamaguchi, K. Ohoyama, Neutron Diffraction and Isotropic Volume Expansion Caused by Deuterium Absorption into La(Fe 0.88 Si 0.12) 13. *J. Phys. Soc. Jpn.* **77**, 74722 (2008), doi:10.1143/JPSJ.77.074722.
267. T. Moriya, Recent progress in the theory of itinerant electron magnetism. *Journal of Magnetism and Magnetic Materials*. **14**, 1–46 (1979), doi:10.1016/0304-8853(79)90201-4.
268. T. Moriya, Theory of itinerant electron magnetism. *Journal of Magnetism and Magnetic Materials*. **100**, 261–271 (1991), doi:10.1016/0304-8853(91)90824-T.
269. J. Kübler, *Theory of Itinerant Electron Magnetism* (OUP Oxford, 2017).
270. T. Chatterji, *Neutron scattering from magnetic materials* (Elsevier, Amsterdam, Boston, 2006).
271. R. Kubo, The fluctuation-dissipation theorem. *Rep. Prog. Phys.* **29**, 255–284 (1966), doi:10.1088/0034-4885/29/1/306.
272. Z. B. Guo, Y. W. Du, J. S. Zhu, H. Huang, W. P. Ding, D. Feng, Large Magnetic Entropy Change in Perovskite-Type Manganese Oxides. *Physical review letters*. **78**, 1142–1145 (1997), doi:10.1103/PhysRevLett.78.1142.
273. Choe, Pecharsky, Gschneidner, JR, Young, JR, Miller, Making and breaking covalent bonds across the magnetic transition in the giant magnetocaloric material Gd5(Si2Ge2). *Physical review letters*. **84**, 4617–4620 (2000), doi:10.1103/PhysRevLett.84.4617.

274. W. Choe, G. J. Miller, J. Meyers, S. Chumbley, A. O. Pecharsky, “Nanoscale Zippers” in the Crystalline Solid. Structural Variations in the Giant Magnetocaloric Material Gd 5 Si 1.5 Ge 2.5. *Chem. Mater.* **15**, 1413–1419 (2003), doi:10.1021/cm020928l.
275. G. J. Miller, Complex rare-earth tetrelides, RE5(SixGe(1-x))4: new materials for magnetic refrigeration and a superb playground for solid state chemistry. *Chemical Society reviews*. **35**, 799–813 (2006), doi:10.1039/b208133b.
276. J. Yao, P. Wang, Y. Mozharivskyj, Tuning Magnetic and Structural Transitions through Valence Electron Concentration in the Giant Magnetocaloric Gd 5– x Eu x Ge 4 Phases. *Chem. Mater.* **24**, 552–556 (2012), doi:10.1021/cm203148e.
277. O. Tegus, E. Bruck, K. H. J. Buschow, F. R. de Boer, Transition-metal-based magnetic refrigerants for room-temperature applications. *Nature*. **415**, 150–152 (2002), doi:10.1038/415150a.
278. E. Brück, O. Tegus, L. Zhang, X. W. Li, F. R. de Boer, K. Buschow, Magnetic refrigeration near room temperature with Fe2P-based compounds. *Journal of Alloys and Compounds*. **383**, 32–36 (2004), doi:10.1016/j.jallcom.2004.04.042.
279. D. T. Cam Thanh, E. Brück, N. T. Trung, J. C. P. Klaasse, K. H. J. Buschow, Z. Q. Ou, O. Tegus, L. Caron, Structure, magnetism, and magnetocaloric properties of MnFeP1−xSix compounds. *J. Appl. Phys.* **103**, 07B318 (2008), doi:10.1063/1.2836958.
280. M. F. J. Boeije, P. Roy, F. Guillou, H. Yibole, X. F. Miao, L. Caron, D. Banerjee, N. H. van Dijk, R. A. de Groot, E. Brück, Efficient Room-Temperature Cooling with Magnets. *Chem. Mater.* **28**, 4901–4905 (2016), doi:10.1021/acs.chemmater.6b00518.
281. J. H. Grebenkemper, J. D. Bocarsly, E. E. Levin, G. Seward, C. Heikes, C. Brown, S. Misra, F. Seeler, K. Schierle-Arndt, S. D. Wilson, R. Seshadri, Rapid Microwave Preparation and Composition Tuning of the High-Performance Magnetocalorics (Mn,Fe)2(P,Si). *ACS applied materials & interfaces*. **10**, 7208–7213 (2018), doi:10.1021/acsami.7b16988.
282. B. G. Shen, J. R. Sun, F. X. Hu, H. W. Zhang, Z. H. Cheng, Recent Progress in Exploring Magnetocaloric Materials. *Adv. Mater.* **21**, 4545–4564 (2009), doi:10.1002/adma.200901072.
283. G. V. Brown, Magnetic heat pumping near room temperature. *J. Appl. Phys.* **47**, 3673–3680 (1976), doi:10.1063/1.323176.
284. R. A. Kishore, S. Priya, A review on design and performance of thermomagnetic devices. *Renewable and Sustainable Energy Reviews*. **81**, 33–44 (2018), doi:10.1016/j.rser.2017.07.035.
285. T. Christiaanse, E. Brück, Proof-of-Concept Static Thermomagnetic Generator Experimental Device. *Metallurgical and Materials Transactions E*. **1**, 36–40 (2014), doi:10.1007/s40553-014-0006-9.
286. R. A. Kishore, S. Priya, Low-grade waste heat recovery using the reverse magnetocaloric effect. *Sustainable Energy Fuels*. **1**, 1899–1908 (2017), doi:10.1039/C7SE00182G.
287. N. H. Dung, L. Zhang, Z. Q. Ou, E. Brück, From first-order magneto-elastic to magneto-structural transition in (Mn,Fe) 1.95 P 0.50 Si 0.50 compounds. *Appl. Phys. Lett.* **99**, 92511 (2011), doi:10.1063/1.3634016.
288. F. Guillou, G. Porcari, H. Yibole, N. van Dijk, E. Brück, Taming the first-order transition in giant magnetocaloric materials. *Adv. Mater.* **26**, 2671-5, 2615 (2014), doi:10.1002/adma.201304788.
289. I. Takeuchi, K. Sandeman, Solid-state cooling with caloric materials. *Physics Today*. **68**, 48–54 (2015), doi:10.1063/PT.3.3022.

290. K. Mandal, A. Yan, P. Kerschl, A. Handstein, O. Gutfleisch, K.-H. Müller, The study of magnetocaloric effect in R 2 Fe 17 (R = Y, Pr) alloys. *J. Phys. D: Appl. Phys.* **37**, 2628–2631 (2004), doi:10.1088/0022-3727/37/19/002.
291. S. Singh, L. Caron, S. W. D'Souza, T. Fichtner, G. Porcari, S. Fabbrici, C. Shekhar, S. Chadov, M. Solzi, C. Felser, Large Magnetization and Reversible Magnetocaloric Effect at the Second-Order Magnetic Transition in Heusler Materials. *Adv. Mater.* **28**, 3321–3325 (2016), doi:10.1002/adma.201505571.
292. K. G. Sandeman, Magnetocaloric materials: The search for new systems. *Scripta Materialia*. **67**, 566–571 (2012), doi:10.1016/j.scriptamat.2012.02.045.
293. X. Tan, P. Chai, C. M. Thompson, M. Shatruk, Magnetocaloric effect in AlFe2B2: toward magnetic refrigerants from earth-abundant elements. *Journal of the American Chemical Society*. **135**, 9553–9557 (2013), doi:10.1021/ja404107p.
294. R. Barua, B. T. Lejeune, B. A. Jensen, L. Ke, R. W. McCallum, M. J. Kramer, L. H. Lewis, Enhanced room-temperature magnetocaloric effect and tunable magnetic response in Ga- and Ge-substituted AlFe2B2. *Journal of Alloys and Compounds*. **777**, 1030–1038 (2019), doi:10.1016/j.jallcom.2018.10.206.
295. Songlin, Dagula, O. Tegus, E. Brück, F. de Boer, K. Buschow, Magnetic and magnetocaloric properties of Mn5Ge3−Sb. *Journal of Alloys and Compounds*. **337**, 269–271 (2002), doi:10.1016/S0925-8388(01)01935-1.
296. X. Zhang, Y. Chen, L. Lü, Z. Li, A potential oxide for magnetic refrigeration application: CrO 2 particles. *J. Phys.: Condens. Matter*. **18**, L559-L566 (2006), doi:10.1088/0953-8984/18/44/L01.
297. J. D. Bocarsly, E. E. Levin, C. A. C. Garcia, K. Schwennicke, S. D. Wilson, R. Seshadri, A Simple Computational Proxy for Screening Magnetocaloric Compounds. *Chem. Mater.* **29**, 1613–1622 (2017), doi:10.1021/acs.chemmater.6b04729.
298. M. Fries, Z. Gercsi, S. Ener, K. P. Skokov, O. Gutfleisch, Magnetic, magnetocaloric and structural properties of manganese based monoborides doped with iron and cobalt – A candidate for thermomagnetic generators. *Acta Materialia*. **113**, 213–220 (2016), doi:10.1016/j.actamat.2016.05.005.
299. J. F. Elliott, S. Legvold, F. H. Spedding, Some Magnetic Properties of Gadolinium Metal. *Phys. Rev.* **91**, 28–30 (1953), doi:10.1103/PhysRev.91.28.
300. T. Shigematsu, T. Kanaizuka, K. Kosuge, M. Shiga, Y. Nakamura, S. Kachi, Thermal expansion anomaly of MnB. *Physics Letters A*. **53**, 385–386 (1975), doi:10.1016/0375-9601(75)90041-9.
301. T. Kanaizuka, Invar like properties of transition metal monoborides Mn1−xCrxB and Mn1−xFexB. *Materials Research Bulletin*. **16**, 1601–1608 (1981), doi:10.1016/0025-5408(81)90033-7.
302. J. Park, Y.-K. Hong, H.-K. Kim, W. Lee, C.-D. Yeo, S.-G. Kim, M.-H. Jung, C.-J. Choi, O. N. Mryasov, Electronic structures of MnB soft magnet. *AIP Advances*. **6**, 55911 (2016), doi:10.1063/1.4943240.
303. A. Gueddouh, The effects of magnetic moment collapse under high pressure, on physical properties in mono-borides TMB (TM = Mn, Fe): a first-principles. *Phase Transitions*. **90**, 984–1000 (2017), doi:10.1080/01411594.2017.1302088.
304. S. Ma, K. Bao, Q. Tao, P. Zhu, T. Ma, B. Liu, Y. Liu, T. Cui, Manganese mono-boride, an inexpensive room temperature ferromagnetic hard material. *Scientific reports*. **7**, 43759 (2017), doi:10.1038/srep43759.

305. J. J. Stickel, Data smoothing and numerical differentiation by a regularization method. *Computers & Chemical Engineering*. **34**, 467–475 (2010), doi:10.1016/j.compchemeng.2009.10.007.
306. J. D. Bocarsly, R. F. Need, R. Seshadri, S. D. Wilson, Magnetoentropic signatures of skyrmionic phase behavior in FeGe. *Phys. Rev. B*. **97** (2018), doi:10.1103/PhysRevB.97.100404.
307. G. W. Stinton, J. S. O. Evans, Parametric Rietveld refinement. *J Appl Crystallogr*. **40**, 87–95 (2007), doi:10.1107/S0021889806043275.
308. Kresse, Furthmüller, Efficient iterative schemes for ab initio total-energy calculations using a plane-wave basis set. *Physical review. B, Condensed matter*. **54**, 11169–11186 (1996), doi:10.1103/physrevb.54.11169.
309. Blöchl, Projector augmented-wave method. *Physical review. B, Condensed matter*. **50**, 17953–17979 (1994), doi:10.1103/physrevb.50.17953.
310. G. Kresse, D. Joubert, From ultrasoft pseudopotentials to the projector augmented-wave method. *Physical review. B, Condensed matter*. **59**, 1758–1775 (1999), doi:10.1103/PhysRevB.59.1758.
311. Perdew, Burke, Ernzerhof, Generalized Gradient Approximation Made Simple. *Physical review letters*. **77**, 3865–3868 (1996), doi:10.1103/PhysRevLett.77.3865.
312. R. Dronskowski, P. E. Bloechl, Crystal orbital Hamilton populations (COHP): energy-resolved visualization of chemical bonding in solids based on density-functional calculations. *J. Phys. Chem.* **97**, 8617–8624 (1993), doi:10.1021/j100135a014.
313. V. L. Deringer, A. L. Tchougréeff, R. Dronskowski, Crystal orbital Hamilton population (COHP) analysis as projected from plane-wave basis sets. *The journal of physical chemistry. A*. **115**, 5461–5466 (2011), doi:10.1021/jp202489s.
314. S. Maintz, V. L. Deringer, A. L. Tchougréeff, R. Dronskowski, Analytic projection from plane-wave and PAW wavefunctions and application to chemical-bonding analysis in solids. *Journal of computational chemistry*. **34**, 2557–2567 (2013), doi:10.1002/jcc.23424.
315. S. Maintz, V. L. Deringer, A. L. Tchougréeff, R. Dronskowski, LOBSTER: A tool to extract chemical bonding from plane-wave based DFT. *Journal of computational chemistry*. **37**, 1030–1035 (2016), doi:10.1002/jcc.24300.
316. S. Maintz, M. Esser, R. Dronskowski, Efficient Rotation of Local Basis Functions Using Real Spherical Harmonics. *Acta Phys. Pol. B*. **47**, 1165 (2016), doi:10.5506/APhysPolB.47.1165.
317. T. Kanaizuka, Phase diagram of pseudobinary CrB・MnB and MnB・FeB systems: Crystal structure of the low-temperature modification of FeB. *Journal of Solid State Chemistry*. **41**, 195–204 (1982), doi:10.1016/0022-4596(82)90202-X.
318. P. Mohn, D. G. Pettifor, The calculated electronic and structural properties of the transition-metal monoborides. *J. Phys. C: Solid State Phys.* **21**, 2829–2839 (1988), doi:10.1088/0022-3719/21/15/015.
319. P. W. Stephens, Phenomenological model of anisotropic peak broadening in powder diffraction. *J Appl Crystallogr*. **32**, 281–289 (1999), doi:10.1107/S0021889898006001.
320. R. Huang, Y. Liu, W. Fan, J. Tan, F. Xiao, L. Qian, L. Li, Giant negative thermal expansion in NaZn13-type La(Fe, Si, Co)13 compounds. *Journal of the American Chemical Society*. **135**, 11469–11472 (2013), doi:10.1021/ja405161z.
321. F. Hu, F. Shen, J. Hao, Y. Liu, J. Wang, J. Sun, B. Shen, Negative Thermal Expansion in the Materials With Giant Magnetocaloric Effect. *Frontiers in chemistry*. **6**, 438 (2018), doi:10.3389/fchem.2018.00438.

322. L. V. B. Diop, O. Isnard, J. Rodríguez-Carvajal, Ultrasharp magnetization steps in the antiferromagnetic itinerant-electron system LaFe12B6. *Phys. Rev. B*. **93**, 80 (2016), doi:10.1103/PhysRevB.93.014440.
323. L. V. B. Diop, O. Isnard, Giant spontaneous magnetization jumps in LaFe 12 B 6. *Appl. Phys. Lett.* **108**, 132401 (2016), doi:10.1063/1.4944904.
324. L. V. B. Diop, O. Isnard, Multiple magnetization steps and plateaus across the antiferromagnetic to ferromagnetic transition in La1−xCexFe12B6. *Phys. Rev. B*. **97**, 80 (2018), doi:10.1103/PhysRevB.97.014436.
325. V. Hardy, S. Majumdar, S. J. Crowe, M. R. Lees, D. M. Paul, L. Hervé, A. Maignan, S. Hébert, C. Martin, C. Yaicle, M. Hervieu, B. Raveau, Field-induced magnetization steps in intermetallic compounds and manganese oxides: The martensitic scenario. *Phys. Rev. B*. **69** (2004), doi:10.1103/PhysRevB.69.020407.
326. A. Haldar, K. G. Suresh, A. K. Nigam, Magnetism in gallium-doped CeFe2 : Martensitic scenario. *Phys. Rev. B*. **78** (2008), doi:10.1103/PhysRevB.78.144429.
327. B. Maji, K. G. Suresh, A. K. Nigam, Observation of spontaneous magnetization jump and field-induced irreversibility in Nd 5 Ge 3. *Europhys. Lett.* **91**, 37007 (2010), doi:10.1209/0295-5075/91/37007.
328. L. Righi, F. Albertini, A. Paoluzi, S. Fabbrici, E. Villa, G. Calestani, S. Besseghini, Incommensurate and Commensurate Structural Modulation in Martensitic Phases of FSMA. *MSF*. **635**, 33–41 (2009), doi:10.4028/www.scientific.net/MSF.635.33.
329. L. Diop, O. Isnard, M. Amara, F. Gay, J. P. Itié, Giant negative thermal expansion across the first-order magnetoelastic transition in Hf0.86Ta0.14Fe2. *Journal of Alloys and Compounds*. **845**, 156310 (2020), doi:10.1016/j.jallcom.2020.156310.
330. B. Li, X. H. Luo, H. Wang, W. J. Ren, S. Yano, C.-W. Wang, J. S. Gardner, K.-D. Liss, P. Miao, S.-H. Lee, T. Kamiyama, R. Q. Wu, Y. Kawakita, Z. D. Zhang, Colossal negative thermal expansion induced by magnetic phase competition on frustrated lattices in Laves phase compound (Hf,Ta) Fe2. *Phys. Rev. B*. **93** (2016), doi:10.1103/PhysRevB.93.224405.
331. J. Lin, P. Tong, K. Zhang, H. Tong, X. Guo, C. Yang, Y. Wu, M. Wang, S. Lin, L. Chen, W. Song, Y. Sun, Colossal negative thermal expansion with an extended temperature interval covering room temperature in fine-powdered Mn 0.98 CoGe. *Appl. Phys. Lett.* **109**, 241903 (2016), doi:10.1063/1.4972234.
332. M. Azuma, W. Chen, H. Seki, M. Czapski, S. Olga, K. Oka, M. Mizumaki, T. Watanuki, N. Ishimatsu, N. Kawamura, S. Ishiwata, M. G. Tucker, Y. Shimakawa, J. P. Attfield, Colossal negative thermal expansion in BiNiO3 induced by intermetallic charge transfer. *Nature communications*. **2**, 347 (2011), doi:10.1038/ncomms1361.
333. A. Zięba, Y. Shapira, S. Foner, Magnetic phase diagram of MnAs: Effect of magnetic field on structural and magnetic transitions. *Physics Letters A*. **91**, 243–245 (1982), doi:10.1016/0375-9601(82)90482-0.
334. A. Asamitsu, Y. Moritomo, Y. Tomioka, T. Arima, Y. Tokura, A structural phase transition induced by an external magnetic field. *Nature*. **373**, 407–409 (1995), doi:10.1038/373407a0.
335. E. M. Levin, V. K. Pecharsky, K. A. Gschneidner, G. J. Miller, Electrical resistivity, electronic heat capacity, and electronic structure of Gd5Ge4. *Phys. Rev. B*. **64** (2001), doi:10.1103/PhysRevB.64.235103.
336. C. Magen, L. Morellon, P. A. Algarabel, C. Marquina, M. R. Ibarra, Magnetoelastic behaviour of Gd 5 Ge 4. *J. Phys.: Condens. Matter*. **15**, 2389–2397 (2003), doi:10.1088/0953-8984/15/14/314.

337. S. B. Roy, M. K. Chattopadhyay, P. Chaddah, J. D. Moore, G. K. Perkins, L. F. Cohen, K. A. Gschneidner, V. K. Pecharsky, Evidence of a magnetic glass state in the magnetocaloric material Gd5Ge4. *Phys. Rev. B*. **74** (2006), doi:10.1103/PhysRevB.74.012403.
338. L. Morellon, P. A. Algarabel, M. R. Ibarra, J. Blasco, B. García-Landa, Z. Arnold, F. ALBERTINI, Magnetic-field-induced structural phase transition in Gd5(Si1.8Ge2.2). *Phys. Rev. B*. **58**, R14721-R14724 (1998), doi:10.1103/PhysRevB.58.R14721.
339. A. Haldar, N. K. Singh, Y. Mudryk, K. G. Suresh, A. K. Nigam, V. K. Pecharsky, Temperature and magnetic field induced structural transformation in Si-doped : An in-field X-ray diffraction study. *Solid State Communications*. **150**, 879–883 (2010), doi:10.1016/j.ssc.2010.01.045.
340. H. Yibole, A. K. Pathak, Y. Mudryk, F. Guillou, N. Zarkevich, S. Gupta, V. Balema, V. K. Pecharsky, Manipulating the stability of crystallographic and magnetic sub-lattices: A first-order magnetoelastic transformation in transition metal based Laves phase. *Acta Materialia*. **154**, 365–374 (2018), doi:10.1016/j.actamat.2018.05.048.
341. M. Fallot, R. Hocart, Sur l'apparition du ferromagnétisme par élévation de température dans des alliages de fer et de rhodium. *Rev. Sci.* **77**, 498 (1939).
342. G. Shirane, R. Nathans, C. W. Chen, Magnetic Moments and Unpaired Spin Densities in the Fe-Rh Alloys. *Phys. Rev.* **134**, A1547-A1553 (1964), doi:10.1103/PhysRev.134.A1547.
343. J. A. Arregi, O. Caha, V. Uhlíř, Evolution of strain across the magnetostructural phase transition in epitaxial FeRh films on different substrates. *Phys. Rev. B*. **101** (2020), doi:10.1103/PhysRevB.101.174413.
344. S. Fujieda, K. Fukamichi, S. Suzuki, Itinerant-electron metamagnetic transition in LaFe12B6. *Journal of Magnetism and Magnetic Materials*. **421**, 403–408 (2017), doi:10.1016/j.jmmm.2016.08.039.
345. L. V. B. Diop, O. Isnard, Inverse and normal magnetocaloric effects in LaFe 12 B 6. *J. Appl. Phys.* **119**, 213904 (2016), doi:10.1063/1.4953235.
346. L. Diop, O. Isnard, Z. Arnold, J. P. Itié, J. Kastil, J. Kamarad, High pressure structural and magnetic studies of LaFe 12 B 6. *Solid State Communications*. **252**, 29–32 (2017), doi:10.1016/j.ssc.2017.01.010.
347. G. I. Miletić, Ž. Blažina, Theoretical study of magnetism in RM12B6 compounds (R=Y, La or Ce; M=Fe, Co). *Journal of Magnetism and Magnetic Materials*. **323**, 2340–2347 (2011), doi:10.1016/j.jmmm.2011.03.035.
348. G. I. Miletić, Ž. Blažina, Possible role of two iron sites in the metamagnetic transition observed in LaFe12 B6. *Journal of Alloys and Compounds*. **430**, 9–12 (2007), doi:10.1016/j.jallcom.2006.04.062.
349. M. Rosenberg, T. Sinnernann, M. Mittag, K. Buschow, Magnetic properties and 57Fe Mössbauer spectroscopy of rare earth compounds of the type RFe12-x Cox B6. *Journal of Alloys and Compounds*. **182**, 145–156 (1992), doi:10.1016/0925-8388(92)90582-T.
350. Q. A. Li, C. H. de Groot, F. R. de Boer, K. Buschow, Metamagnetic behaviour of La1 − xGdxFe12B6 compounds. *Journal of Alloys and Compounds*. **256**, 82–85 (1997), doi:10.1016/S0925-8388(96)03100-3.
351. K. Buschow, D. B. de Mooij, H. M. van Noort, Properties of metastable ternary compounds and amorphous alloys in the Nd-Fe-B system. *Journal of the Less Common Metals*. **125**, 135–146 (1986), doi:10.1016/0022-5088(86)90088-3.
352. M. Mittag, M. Rosenberg, K. Buschow, A magnetization study of RCo12B6 intermetallics. *Journal of Magnetism and Magnetic Materials*. **82**, 109–117 (1989), doi:10.1016/0304-8853(89)90070-X.

353. K. Niihara, S. Yajima, A New Ternary Compound in Rare Earth-Cobalt-Boron System. *Chem. Lett.* **1**, 875–876 (1972), doi:10.1246/cl.1972.875.
354. Y. Kuz'ma, G. V. Chernyak, N. F. Chaban, New borides of rare earths with the structure of the SrNi12B6 type. *Dopovidi Akademii Nauk Ukrains'koj RSR. Seriya A, Fiziko-Tekhnichni ta Matematichni Nauki*, 80–83 (1981).
355. W. Jung, D. Quentmeier, Darstellung und Kristallstruktur der ternären Boride SrNi 12 B 6 und BaNi 12 B 6. *Zeitschrift für Kristallographie - Crystalline Materials*. **151**, 121–128 (1980), doi:10.1524/zkri.1980.151.1-2.121.
356. F. Mesquita, S. G. Magalhaes, P. Pureur, L. V. B. Diop, O. Isnard, Electrical magnetotransport properties in RCo12B6 compounds (R=Y , Gd, and Ho). *Phys. Rev. B*. **101** (2020), doi:10.1103/PhysRevB.101.224414.
357. A. Barlet, J. C. Genna, P. Lethuillier, Insert for regulating temperatures between 2 and 1000 K in a liquid helium dewar: Description and cryogenic analysis. *Cryogenics*. **31**, 801–805 (1991), doi:10.1016/0011-2275(91)90138-M.
358. A. W. Sleight, Compounds That Contract on Heating. *Inorganic chemistry*. **37**, 2854–2860 (1998), doi:10.1021/ic980253h.
359. K. Irisawa, A. Fujita, K. Fukamichi, M. Yamada, H. Mitamura, T. Goto, K. Koyama, Transition between antiferromagnetic and ferromagnetic states in itinerant-electron La(FexAl1−x)13 compounds. *Phys. Rev. B*. **70** (2004), doi:10.1103/PhysRevB.70.214405.
360. L. Morellon, J. Blasco, P. A. Algarabel, M. R. Ibarra, Nature of the first-order antiferromagnetic-ferromagnetic transition in the Ge-rich magnetocaloric compounds Gd5(SixGe1−x)4. *Phys. Rev. B*. **62**, 1022–1026 (2000), doi:10.1103/PhysRevB.62.1022.
361. Y. Mudryk, D. Paudyal, V. K. Pecharsky, K. A. Gschneidner, Magnetostructural transition in Gd5Si0.5Ge3.5 : Magnetic and x-ray powder diffraction measurements, and theoretical calculations. *Phys. Rev. B*. **77** (2008), doi:10.1103/PhysRevB.77.024408.
362. F. Ishikawa, K. Koyama, K. Watanabe, H. Wada, Field Induced Structural Transformation in MnAs. *Jpn. J. Appl. Phys.* **42**, L918-L920 (2003), doi:10.1143/JJAP.42.L918.
363. A. I. Kurbakov, V. A. Ryzhov, V. V. Runov, E. O. Bykov, I. I. Larionov, V. V. Deriglazov, C. Martin, A. Maignan, Study of phase separation phenomena in half-doped manganites with isovalent substitution of rare-earth cations on example of Sm0.32Pr0.18Sr0.5MnO3. *Phys. Rev. B*. **100** (2019), doi:10.1103/PhysRevB.100.184424.
364. K. A. Gschneidner, J.-C. G. Bünzli, V. K. Pecharsky, Eds., *Handbook on the physics and chemistry of rare earths* (Elsevier Science, Amsterdam, 2003).
365. Y. Qiao, Y. Song, K. Lin, X. Liu, A. Franz, Y. Ren, J. Deng, R. Huang, L. Li, J. Chen, X. Xing, Negative Thermal Expansion in (Hf,Ti)Fe2 Induced by the Ferromagnetic and Antiferromagnetic Phase Coexistence. *Inorganic chemistry*. **58**, 5380–5383 (2019), doi:10.1021/acs.inorgchem.8b03600.
366. E. M. Levin, K. A. Gschneidner, V. K. Pecharsky, Magnetic correlations induced by magnetic field and temperature in Gd5Ge4. *Phys. Rev. B*. **65** (2002), doi:10.1103/PhysRevB.65.214427.
367. H. Yamada, T. Goto, Itinerant-electron metamagnetism and giant magnetocaloric effect. *Phys. Rev. B*. **68**, 44 (2003), doi:10.1103/PhysRevB.68.184417.
368. T. Goto, K. Fukamichi, H. Yamada, Itinerant electron metamagnetism and peculiar magnetic properties observed in 3d and 5f intermetallics. *Physica B: Condensed Matter*. **300**, 167–185 (2001), doi:10.1016/S0921-4526(01)00579-8.

369. J. del Valle, N. Ghazikhanian, Y. Kalcheim, J. Trastoy, M.-H. Lee, M. J. Rozenberg, I. K. Schuller, Resistive asymmetry due to spatial confinement in first-order phase transitions. *Phys. Rev. B*. **98** (2018), doi:10.1103/PhysRevB.98.045123.
370. J. A. Arregi, M. Horký, K. Fabianová, R. Tolley, E. E. Fullerton, V. Uhlíř, Magnetization reversal and confinement effects across the metamagnetic phase transition in mesoscale FeRh structures. *J. Phys. D: Appl. Phys.* **51**, 105001 (2018), doi:10.1088/1361-6463/aaaa5a.
371. V. Uhlíř, J. A. Arregi, E. E. Fullerton, Colossal magnetic phase transition asymmetry in mesoscale FeRh stripes. *Nature communications*. **7**, 13113 (2016), doi:10.1038/ncomms13113.
372. T. Kakeshita, J. Katsuyama, T. Fukuda, T. Saburi, Time-dependent nature of displacive transformations in Fe–Ni and Fe–Ni–Mn alloys under magnetic field and hydrostatic pressure. *Materials Science and Engineering: A*. **312**, 219–226 (2001), doi:10.1016/S0921-5093(00)01878-5.
373. V. Hardy, A. Maignan, S. Hébert, C. Yaicle, C. Martin, M. Hervieu, M. R. Lees, G. Rowlands, D. M. K. Paul, B. Raveau, Observation of spontaneous magnetization jumps in manganites. *Phys. Rev. B*. **68** (2003), doi:10.1103/PhysRevB.68.220402.
374. Ö. Özgün, D. Koch, A. Çakır, T. Tavsanoglu, W. Donner, M. Farle, M. Acet, Magnetic properties of the FCC- and sigma-phases in equiatomic and off-equiatomic high-entropy Cantor alloys. *submitted* (2022).
375. D. Li, Z. Han, J. G. Zheng, X. L. Wang, D. Y. Geng, J. Li, Z. D. Zhang, Spin canting and spin-flop transition in antiferromagnetic Cr2O3 nanocrystals. *J. Appl. Phys.* **106**, 53913 (2009), doi:10.1063/1.3213100.
376. R. Basnet, A. Wegner, K. Pandey, S. Storment, J. Hu, Highly sensitive spin-flop transition in antiferromagnetic van der Waals material MPS3 (M=Ni and Mn). *Phys. Rev. Materials*. **5** (2021), doi:10.1103/PhysRevMaterials.5.064413.

List of figures

List of tables